Spring 1-1-2017

Quantum State-Resolved Collision Dynamics of Nitric Oxide at Ionic Liquid and Molten Metal Surfaces

Amelia Marie Zutz
University of Colorado at Boulder, mia.zutz@gmail.com

Quantum State-Resolved Collision Dynamics of Nitric Oxide at Ionic Liquid and Molten Metal Surfaces

by

Amelia Marie Zutz

B.A., Carleton College, 2010

A thesis submitted to the

Faculty of the Graduate School of the

University of Colorado in partial fulfillment

of the requirement for the degree of

Doctor of Philosophy

Department of Chemistry and Biochemistry

2017

This thesis entitled:

Quantum State-Resolved Collision Dynamics
of Nitric Oxide at Ionic Liquid and Molten Metal Surfaces

written by Amelia M. Zutz

has been approved for the program of Chemical Physics by:

_____

David J. Nesbitt

_____

W. Carl Lineberger

Date _____

The final copy of this thesis has been examined by both the signatories, and we find that both the content and the form meet acceptable presentation standards of scholarly work in the above mentioned discipline.

Zutz, Amelia M. (Ph.D., Chemical Physics)

Quantum State-Resolved Collision Dynamics of Nitric Oxide at Ionic Liquid and Molten Metal Surfaces

Thesis directed by Professor David J. Nesbitt

Detailed molecular scale interactions at the gas–liquid interface are explored with quantum state-to-state resolved scattering of a jet-cooled beam of NO($^2\Pi_{1/2}$; $N = 0$) from ionic liquid and molten metal surfaces. The scattered distributions are probed via laser-induced fluorescence methods, which yield rotational and spin-orbit state populations that elucidate the dynamics of energy transfer at the gas-liquid interface. These collision dynamics are explored as a function of incident collision energy, surface temperature, scattering angle, and liquid identity, all of which are found to substantially affect the degree of rotational, electronic and vibrational excitation of NO via collisions at the liquid surface.

Rotational distributions observed reveal two distinct scattering pathways, (i) molecules that trap, thermalize and eventually desorb from the surface (trapping-desorption, TD), and (ii) those that undergo prompt recoil (impulsive scattering, IS) prior to complete equilibration with the liquid surface. Thermally desorbing NO molecules are found to have rotational temperatures close to, but slightly cooler than the surface temperature, indicative of rotational dependent sticking probabilities on liquid surfaces. Nitric oxide is a radical with multiple low-lying electronic states that serves as an ideal candidate for exploring nonadiabatic state-changing collision dynamics at the gas-liquid interface, which induce significant excitation from ground ($^2\Pi_{1/2}$) to excited ($^2\Pi_{3/2}$) spin–orbit states. Molecular beam scattering of supersonically cooled NO from hot molten metals (Ga and Au, $T_s = 300 – 1400$ K) is also explored, which provide preliminary evidence for vibrational excitation of NO mediated by thermally populated electron-

hole pairs in the hot, conducting liquid metals. The results highlight the presence of electronically nonadiabatic effects and build toward a more complete characterization of energy transfer dynamics at gas-liquid interfaces.

To Andy

ACKNOWLEDGMENTS

I have many people to thank for not only helping me during my Ph.D., but also prior to my arrival in Boulder. I started my undergraduate degree at Carleton with many possible majors in mind, but eventually Will Hollingsworth and Marion Cass piqued my interest in Physical Chemistry. Their passion for science and endless curiosity was infectious, as they were always excited to explore new ideas and even created a new class for myself and four other students who wanted to learn more about molecular reaction dynamics.

I want to thank David Nesbitt, my research advisor and mentor, who has constantly pushed me to think more deeply about my data and to understand underlying fundamental principles of a problem. David has shown me the importance of distilling complex ideas down to simple physical pictures, as well as the power of clear communication and scientific storytelling.

To my thesis committee—Eric Cornell, Barney Ellison, Heather Lewandowski, and Carl Lineberger—thank you for taking the time to learn about and provide feedback on my research. I want to further express my appreciation to Eric, Barney and Carl for tracking my progress over the last few years and bringing an outside perspective to my research.

Over my time here at JILA, the support and assistance of the entire JILA staff has been invaluable. The machine shop and electronics shop staffs have helped me consider, discuss and solve countless problems with their extensive knowledge and constant willingness to help. In particular, Kyle was incredibly helpful in designing and building new components for my experiment, as well as Hans for his enthusiasm and skill in brainstorming and tackling every

conceivable problem. The computing support and supply staff have also proven to be crucial in helping to keep my experiment up and running.

The Nesbitt group has been an intellectually stimulating and scientifically diverse environment, which has been incredibly rewarding. Many fellow Nesbitt group members have helped immensely throughout my Ph.D. Mike Ziemkiewicz built up this experiment and was an invaluable teacher and mentor. I learned so much working with him, especially from the multitude of angles from which he attacks problems. Thank you also to Nick Dupuis, Grant Buckingham, Rob Roscioli, Kevin Early, Monika Grutter, Andrej Grubisic, Melanie Reber, Erik Holmstrom, Tim Livingston-Large, Jake Pettine, and Mikhail Ryazanov for countless scientific and nonscientific discussions.

I am incredibly grateful for the support of all my friends and family and am especially appreciative of the community of friends I've gathered in Boulder with whom I ski and play soccer/squash/ultimate frisbee. All of my friends outside of Colorado have continued to provide support from afar, in particular both my brothers. Mom and Dad, thank you for all the opportunities you've made available to me and for your boundless love and support. Finally, Andy, thank for all your relentless support throughout this process, for being there always and for bringing so much joy to my life.

CONTENTS

FIGURES

TABLES

Chapter 1

Introduction

The gas-liquid interface is a complex and remarkably important chemical environment, yet the chemical physics community is still seeking a comprehensive understanding of the chemical dynamics occurring at a molecular level. The interaction of gases with liquid surfaces is fundamental to many atmospheric, environmental, biological and catalytic processes,[1-7] however it is still not possible to predict how individual gas molecules will interact with a liquid surface. As a gas molecule approaches a surface, there are many properties that govern whether a molecule sticks to or bounces away from the surface. Are there barriers for molecules adsorbing on the surface? Do these barriers depend on angle of approach, rotational state, vibrational state, molecular orientation, or surface temperature? For molecules that do stick, how long do they take to thermally equilibrate, or do the molecules escape before fully thermalizing? Does an adsorbed molecule on the surface remain intact, migrate across the surface and possibly dissolve? If the probe molecule is chemically reactive, does it have sufficient time to react with the surface before desorbing? Additionally, if the molecule bounces away from the surface, how is energy transferred between the liquid surface and gas molecules? What degrees of freedom (i.e., rotational, translational, vibrational, electronic) are involved in this process? By isolating individual gas-liquid systems, we can build a more detailed molecular level picture of energy

transfer at gas-liquid interfaces and develop a more predictive understanding of collision dynamics and adsorption/solvation of gases into the liquid phase.

The interfacial layer of a liquid next to a gas looks and behaves fundamentally differently from the bulk of the liquid. Depending on the gas-liquid combination, the interfacial region extends several monolayers into the liquid, ranging from several angstroms to a few nanometers, and has a preferred orientation due to the gas-liquid interfacial asymmetry.[8] Many experiments can now characterize the structure and composition of liquid surfaces,[9-14] with experimental techniques that include: sum frequency generation spectroscopy (SFG),[10, 15, 16] surface tension measurements,[17] angle-resolved X-ray photoelectron spectroscopy (ARXPS),[18] X-ray diffraction,[19, 20] low energy ion scattering (LEIS),[21] metastable atom electron spectroscopy (MAES),[22] and neutron reflectivity.[23, 24] All of these experimental techniques have varying levels of surface sensitivity, ranging from the topmost surface layer to a region that extends several monolayers deep. Additionally, these techniques are all capable of extracting a variety of gas-liquid interface specific information. For example, SFG yields information on molecular composition and orientation in the interfacial region, whereas ARXPS, MAES and LEIS offer insight into atomic composition at the surface. These experiments, combined with theoretical efforts,[25-32] paint a physical picture of how molecules arrange at liquid surfaces.

In order to explore gases adsorption on and solvation into liquid surfaces, a number of other experiments have examined solubilities and rates of trace gases dissolving in liquids,[33] such as droplet train flow reactors, wetted wall flow reactors, and bubble train reactors. In these experiments, gas molecules are brought into contact with a liquid surface in a controlled way, such that the amount of gas dissolved in the liquid over a known time can be determined. While these experiments yield important information on mass accommodation rates and bulk

solubilities of gases for liquids, they are unable to address the fundamental processes that govern the adsorption of gases on liquid surfaces.

Molecular and atomic scattering experiments, however, provide insight on the dynamical processes occurring at gas-liquid interfaces and help to elucidate the elementary steps involved in collisions of gases at liquid surfaces. The first gas-liquid scattering experiments were performed by Hurlbut and Beck in 1959,[34] who investigated Ar and N_2 interactions with molten gallium and indium surfaces. The field was expanded further by Fenn,[35, 36] Cohen,[37-39] and Nathanson[40, 41] who continued to develop and explore atomic and molecular scattering from low vapor pressure liquid surfaces. In general, most scattering experiments involve a well characterized incident molecular or atomic beam, which is directed at a clean liquid surface in vacuum. Scattered molecules are then detected either via time of flight-mass spectrometry (TOF-MS)[26, 32, 41-45] or laser based quantum state resolved techniques (e.g., laser induced fluorescence,[46-51] direct IR absorption spectroscopy,[52-56] resonant multiphoton ionization + velocity map imaging[57-60]). These experiments extract information from gas-molecule interactions with the topmost surface layer, which allow investigation of energy transfer between gas molecules and the liquid surface.

In addition to the Nesbitt group, current research by the groups of Nathanson, McKendrick and Minton have explored gas-liquid interfaces via inelastic and reactive scattering of molecules and atoms.[26, 32, 40-69] Scattering experiments have been performed with a wide range of molecular and atomic probes, including inert gases (Ar, Ne, Xe),[41, 44, 62, 63] reactive atoms (O, F),[32, 49-51, 68, 69] diatomics (NO, N_2, HCl, DCl)[42, 46, 47, 57, 59, 61] and larger polyatomic molecules (CO_2, CH_4 NH_3, D_2O)[52-56, 65]. The liquids studied have traditionally been low vapor pressure liquids like squalane ($C_{30}H_{62}$), squalene ($C_{30}H_{50}$), perfluoropolyether (PFPE), glycerol, room

temperature ionic liquids (RTILs), and molten metals. Collectively, results from these experiments have built a more complete picture of chemical dynamics at the gas-liquid interface by studying energy transfer into and out of internal molecular degrees of freedom (i.e. rotational, translational, vibrational and electronic). This energy transfer has been explored as function of (i) incident and final scattering angles,[26, 54, 55] (ii) incident collision energy,[28, 52] (iii) mass/identity of atomic or molecular probe,[42, 44, 65] and (iv) surface temperature[41, 46, 53, 62]. From these experiments, a number of parameters have been found to influence sticking probabilities. For example, compared to atoms, molecules adsorb more readily on surfaces due to their additional rotational and vibrational degrees of freedom that facilitate energy transfer between the gas and the liquid surface. Heavier incident projectiles can more efficiently dissipate translational energy into the liquid, allowing them to trap more easily on surfaces. Additionally, incident molecules with more momentum normal to the surface are more likely to trap and thermalize on the surface, which include molecules with higher collision energies and projectiles approaching the surface at less glancing angles. Finally, hotter liquids with larger amplitude fluctuations at the surface create rougher surfaces that increase the trapping probability for incident molecules.

Reactive scattering experiments probe both the atomic composition as well as the chemical reactivities at the topmost liquid surface layer. For example, hydrogen abstraction experiments (F + squalane → HF and O + RTILs/squalane/squalene → OH) have been able to probe relative concentrations of H atoms at surfaces by comparing the yield of OH and HF between different liquids.[32, 49, 51, 68, 70] In more recent work, high vapor pressure liquids are studied in microjet experiments where gas molecules are investigated after evaporating and/or scattering from a ~10-20 μm diameter narrow stream of liquid.[13, 42, 63, 64] Liquids with vapor pressures as high as several Torr can be studied using liquid microjets. The simple reason for this

is that the vapor density decreases with distance from a liquid jet more rapidly than from a planar liquid surface, thus suppressing collisions of the molecular probe with evaporated gas phase molecules and enabling detection of collision dynamics occurring at the gas-liquid surface. This is a capability not previously possible, which points to a new and exciting direction in the field that will allow species such as NO and HCl evaporated from critically relevant liquids like water to be studied with quantum state resolution.

In the experiments described in this thesis, nitric oxide is used as the molecular probe of liquid surfaces and its internal rovibronic states are probed with laser induced fluorescence (LIF). The experimental setup, described in detail in Chapter 2, involves a supersonically cooled beam of NO ($^2\Pi_{1/2}$, J= 0.5) directed at a clean liquid surface in vacuum with quantum state resolved detection of scattered molecules (Figure 1.1). These state-to-state resolved scattering experiments investigate energy transfer and collision dynamics occurring at gas-liquid interfaces by comparing the internal molecular quantum states between incoming vs. outgoing NO molecules. NO is an ideal molecular probe with a well-characterized LIF spectrum on the $A^2\Sigma^+ \leftarrow X^2\Pi$ γ band that has strong transition probabilities. Moreover, as a radical with multiple low lying electronic states, the use of NO facilitates the investigation of collisional energy transfer into the electronic degrees of freedom.

The $^2\Pi$ electronic state of NO is split by spin-orbit coupling into the $^2\Pi_{1/2}$ ground and $^2\Pi_{3/2}$ excited states, which are separated by a spin-orbit splitting of E_{so} =120 cm^{-1} at J=1.5.[71] Each spin-orbit state is also further split into two lambda-doublet states of opposite spectroscopic parity, with energy spacings of ~0.01 cm^{-1} for lowest rotational state. These small electronic energy spacings invite the investigation of surface-hopping between electronic states from collisions at conductive liquid surfaces, like ionic liquids and molten metals. Each of these

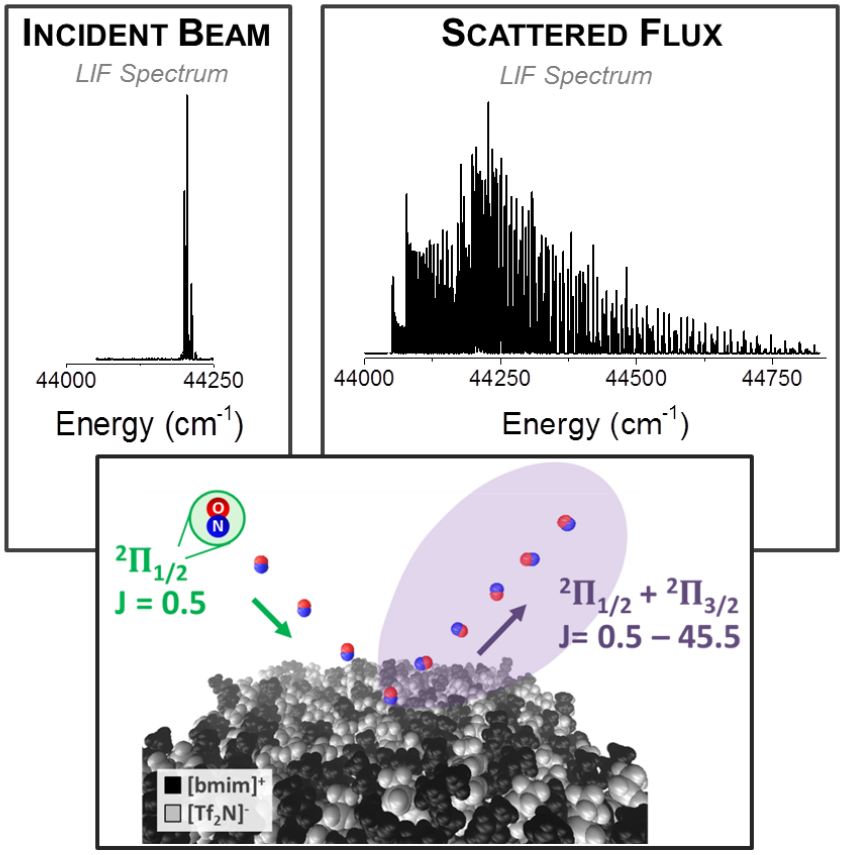

Figure 1.1 Molecular scattering of supersonically cooled NO ($^2\Pi_{1/2}$, J = 0.5) from a room-temperature ionic liquid surface ([bmim][Tf_2N]). Scattered NO molecules are detected via LIF with quantum state resolution, where collisions excite both spin-orbit states and rotational states up to J = 50.5. The LIF spectra are shown for the incident jet-cooled beam and the scattered flux. The liquid surface is generated from molecular dynamics simulations by Schatz et al.[72]

electronic states, as well as the rotational distributions within each state, can be probed independently with LIF detection.

Many molecular scattering experiments have produced rotational and translational distributions of scattered molecules that provide evidence for two simple physical pathways,[40, 41, 51, 53, 57, 73] whereby incident gas molecules interact and transfer energy with a liquid surface and can (i) trap and thermalize on the surface before desorbing (trapping desorption, TD), or (ii)

scatter directly from the surface (impulsive scattering, IS), as illustrated in Figure 1.2. Molecular dynamics simulations reveal the presence of IS scattering pathways, whereby incident molecules collide once or twice with the liquid surface before scattering away at near specular scattering angles, whereas molecules that thermalize typically do so in multiple collisions with the surface. By the time such thermalized gas molecules desorb, it is reasonable to assume that they have lost memory of the incident collision conditions and, in the absence of exit channel barriers, often leave the surface in near $\cos(\theta_s)$ distributions. While it seems reasonable to expect a continuum of scattering pathways in between these two limits, as suggested by trajectory simulations,[25, 27, 28, 30, 74] this bimodal picture empirically fits data from our NO molecular beam scattering experiments over a dynamical range of more than two orders of magnitude in rotational state distributions and offers useful quantitative parameters with which to characterize rotational excitation.

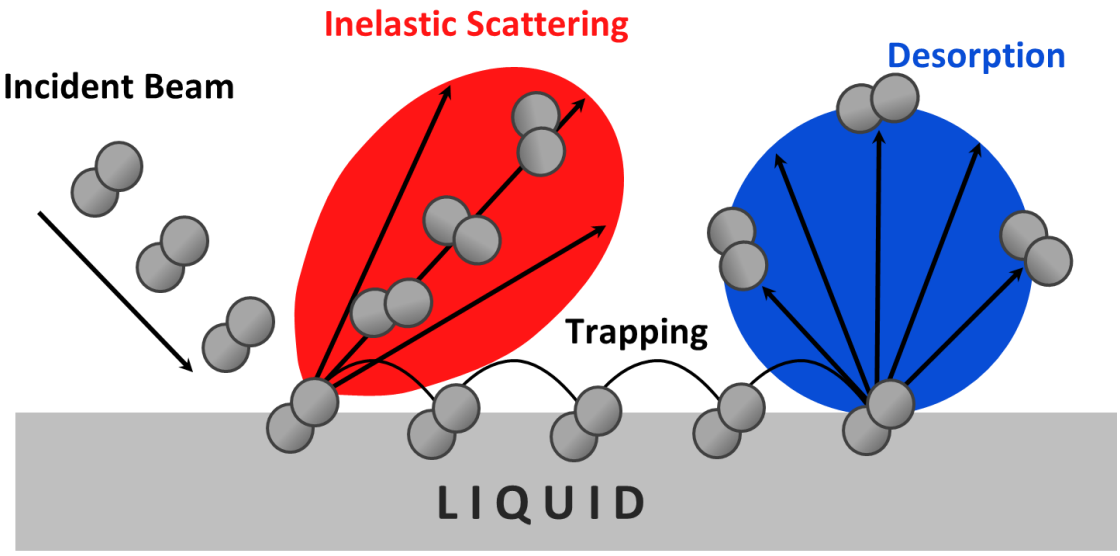

Figure 1.2 Molecular scattering pathways whereby incident molecules can either directly scatter (impulsively scattering, IS) or trap and thermalize on the surface before desorbing (trapping/thermal-desorption, TD).

In the thermal desorption scattering pathway, decades of gas-liquid scattering experiments have supported a simple physical picture where molecules thermalize/trap on the surface and subsequently desorb back into the gas phase with translational and rotational distributions that are described by the surface temperature. This can be understood with the subtle, yet remarkably powerful concept of detailed balance,[75] which is most easily described by considering a system of gas molecules in equilibrium with a liquid surface. In order for this system at equilibrium *to remain* at equilibrium, the flux of gas phase molecules approaching the surface must be equal to the flux of molecules leaving the surface. Therefore, if we assume unity sticking coefficients for all molecules striking the liquid, then all molecules leaving the surface must be thermally desorbing from the surface with rotational and translational temperature distributions characteristic of the surface temperature. These ideas still hold true for molecular scattering experiments in vacuum even though the system is not in equilibrium. The basic reason why is that, once a molecule has thermalized on the surface, it can't "know" in advance whether a thermal distribution of gas or vacuum conditions are situated above it, therefore these thermalized molecules on the surface must behave as they would under equilibrium conditions. These ideas are discussed in more detail in Chapters 3 and 5 where nonunity sticking probabilities are also considered, which can arise from the presence of dynamical barriers to adsorption/desorption at the surface.

Room temperature ionic liquids (RTILs) are a novel class of green, designer solvents with various applications spanning environmental, biological, electrochemical, and industrial processes.[76, 77] These liquids are molten salts, in that they consist only of ions, yet unlike the familiar table salt, these RTILs are liquid at or near room temperature. The presence of interfacial ions makes these liquids an intriguing surface to explore nonadiabatic surface hopping

effects, which might arise from partial electron transfer with incident NO molecules. RTILs are remarkably versatile, with low vapor pressures, high solubilities, and chemical/thermal stability.[78-80] These RTILs are also known as "designer solvents", since by changing the identity of either the anion or cation, these liquids can be tuned to solvate specific species with more than 10^6 possible combinations.[77] RTILs are being developed for solar cells,[81, 82] Li-ion batteries,[83, 84] drug delivery,[85] catalytic reactions,[86-88] and many extraction schemes.[89-91] For example, the tunability of RTILs is being used to engineer ionic liquids as CO_2 scrubbers[92-94] and also to separate H_2 from CO in steam gas reformation.[95] For these applications, molecular beam scattering experiments can help us to develop an understanding of what parameters promote specific gas molecules to trap and dissolve into a liquid, while inhibiting other gases from solvating. The liquid surface acts as a barrier to solvation for an approaching gas molecule, thus the investigation of collision dynamics at the gas-liquid interface represents a crucial first step toward a predictive understanding of gas solvation processes in RTILs.

Imidazolium-based ionic liquids, in particular, are relevant in many of the applications mentioned above. The cation of these RTILs has its charge delocalized over an imidazolium ring, with nonpolar alkyl side chains on each of the nitrogen atoms. The specific cations studied here are referred to as 1-alkyl-3-methylimidazolium, or [$C_n$mim], and are pictured in Figure 1.3. Common anion pairings are often inorganic molecules like $[BF_4]^-$, $[TF_2N]^-$ (bis(trifluoromethylsulfonyl)imide, $N(CF_3SO_2)_2^-$), and Cl^-, which are also illustrated in Figure 1.3. A number of gas-RTIL interface studies have investigated the atomic composition at these liquid surfaces, which have found both anions and cations present at the surface.[12, 22, 51, 72, 96-100] The studies presented in Chapters 3-6 of this thesis focus on collision dynamics at the surface of

these imidazolium based ionic liquids and how the atomic composition of these varied RTILs affects the interfacial dynamics.

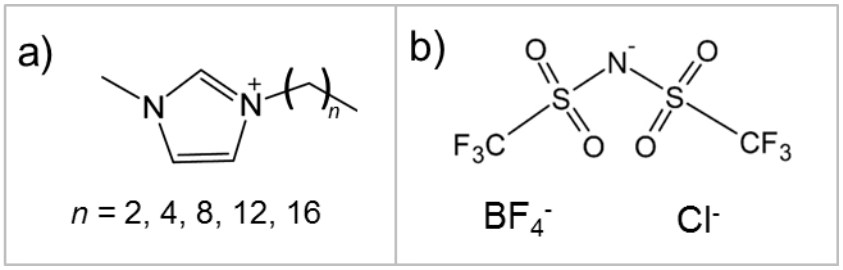

Figure 1.3 RTIL molecular structures of a) 1-alkyl-3-methylimidazolium cation ($[C_n mim]^+$) and b) $[TF_2N]^-$, $[BF_4]^-$, and Cl^- anions

Molten metal surfaces represent another intriguing opportunity to explore nonadiabatic collision dynamics with NO. Metals have a continuum of electronic states that allow electron hole pair (ehp) formation to be resonant with any vibrational or spin-orbit excitation in an NO molecule. This means that ehp formation can couple to degrees of freedom in incoming/outgoing gas phase molecules via nonadiabatic mechanisms such as surface-hopping. Many experimental[101-105] and theoretical studies[106, 107] have examined scattering dynamics of vibrationally excited NO (v = 12 and v = 15) from solid crystalline surfaces like Au(111) and Cu(111), which have demonstrated evidence of ehp mediated energy transfer in gas-surface collisions. Specifically, research by Wodtke and coworkers[101, 103, 104] has demonstrated these effects lead to multiquanta vibrational excitation and relaxation of NO from Au(111), a process which is not present in insulting surfaces such as LiF. Molecular and atomic scattering experiments have also been performed from liquid metallic surfaces. Nathanson et. al. has scattered inert gases from Ga, In, and Bi liquid surfaces[44, 108] to investigate the effects of surface

mass and surface tension on scattering dynamics. Additionally, in previous work in the Nesbitt group, surface temperature dependent studies were performed on NO scattering from liquid Ga from T_s = 300 to 600 K, where both efficient rotation and spin-orbit excitation were detected.[46] These spin-orbit changing collision dynamics observed necessitate surface-hopping between two electronic potential energy surfaces. There are many opportunities to further explore these nonadiabatic collision dynamics from molten metal surfaces, especially via energy transfer into the vibrational degree of freedom, which will be presented in the final chapter of this thesis.

The organization of this thesis is as follows. Chapter 2 provides a detailed description of the experimental apparatus, in addition to data collection and analysis. Recent changes to the experiment that allow studies of molecular scattering from molten metal surfaces at $T_s \leq 1400$ K are also presented. Experimental results are first introduced in Chapter 3, which examine NO scattering from [bmim][Tf_2N] at varying surface temperatures and collision energies. The simple physical picture of thermally desorbing molecules with rotational and translational distributions reflective of the surface temperature has been supported in scattering experiments of CO_2 from perfluoropolyether (PFPE)[53] and HCl from a liquid-mimetic self-assembled monolayers (SAMs).[57] Nitric oxide, however, exhibits subthermal rotational and spin-orbit temperatures at low collision energies in these experiments, consistent with rotational/spin-orbit dependent sticking coefficients of NO adsorption/desorption on liquid surfaces. This chapter also presents scattering results at higher incident collision energies, where both the TD and IS scattering pathways are populated, to explore the thermal accommodation coefficient, α, as the surface temperature is varied.

In Chapter 4, dynamics at the gas-RTIL interface are investigated as a function of the cation alkyl chain length, with a specific focus on [$C_n$mim][Tf_2N] RTILs, where n = 2, 4, 8, 12,

16 and *n* represents the number of carbon atoms in the hydrocarbon chain on the cation (Figure 1.3). The complexities of the intermolecular interactions (i.e., hydrogen bonding, van der Waals forces, Coulomb attraction between ions, and π-stacking) govern how the molecules organize in the bulk and at the liquid surface. The relative strength of these interactions change as the hydrocarbon chains are lengthened. For example, the dispersion forces between alkyl chains start to dominate for RTILs with longer chains ($n \geq 6$), resulting in bilayer formation in the bulk where alternating layers of nonpolar hydrocarbons form between layers of charged anions and imidazolium rings. Additionally, longer hydrocarbon chains are preferentially located at the surface and tend to protrude out into the vacuum. As the cationic alkyl chains are lengthened and the RTIL liquid surface is altered, the experiments in this chapter explore how these changes affect NO collision dynamics from RTIL surfaces. The results in Chapter 4 show a distinct shift in scattering dynamics from shorter ($n \leq 4$) to longer ($n \geq 8$) hydrocarbons, which is the range of alkyl chain lengths over which the most significant changes in surface composition take place.

Angle resolved scattering of NO is investigated in Chapter 5. These studies are motivated by the observation of subthermal NO rotational distributions presented in Chapters 3 and 4, in order to determine if molecules thermally desorbing at all scattering angle have the same rotational temperatures. Additionally, these experiments explore whether or not all molecules are thermalizing on the surface at low collision energies and if there are incident angle or rotational state dependent sticking coefficients. Scattered molecules are detected at backward and forward scattering angles of θ_s = -60º, -30º, 0º, 30º, 45º and 60º with respect to surface normal, while he incident angle is kept constant at θ_{inc} = 45º. Collision dynamics are investigated at the liquid surfaces of squalane, PFPE, and [bmim][Tf_2N] to determine whether NO scattering trends persist at different, more insulating liquid surfaces.

In Chapter 6, unpublished studies are presented of incident energy dependence on NO scattered from a [bmim][Tf_2N] liquid surface. Rotational distributions of scattered NO are explored as the incident collision energy is tuned. Additionally, a series of low collision energies are also examined to investigate translational energy dependence on the sticking coefficient in the thermal desorption scattering channel.

Finally, molecular scattering of NO from molten metal surfaces is presented in Chapter 7. A new heating setup has been built (Chapter 2) to investigate scattering dynamics at molten Au and Ga surfaces, with heating capabilities up to T_s = 1400 K. The molten metal surface temperatures are hotter than have previously been explored in molecular scattering experiments[44, 46, 108] and represent first molecular scattering experiments performed from molten gold. Vibrationally excited NO is detected from both molten Ga and Au metal surfaces, suggestive of electron hole pair formation at the NO-molten metal interface. Additionally, scattering experiments from liquid gold are compared to the extensive molecular scattering studies of NO from Au(111), which demonstrate differences in how molecules scatter from solid and liquid surfaces.

References for Chapter 1

1. J. P. D. Abbatt, *Chem. Rev.*, 2003, **103**, 4783-4800.

2. G. B. Ellison, A. F. Tuck and V. Vaida, *J. Geophys. Res.-Atmos.*, 1999, **104**, 11633-11641.

3. P. Davidovits, C. E. Kolb, L. R. Williams, J. T. Jayne and D. R. Worsnop, *Chem. Rev.*, 2006, **106**, 1323-1354.

4. B. J. Gertner and J. T. Hynes, *Science*, 1996, **271**, 1563-1566.

5. C. P. Mehnert, R. A. Cook, N. C. Dispenziere and M. Afeworki, *J. Am. Chem. Soc.*, 2002, **124**, 12932-12933.

6. M. Kanakidou, J. H. Seinfeld, S. N. Pandis, I. Barnes, F. J. Dentener, M. C. Facchini, R. Van Dingenen, B. Ervens, A. Nenes, C. J. Nielsen, E. Swietlicki, J. P. Putaud, Y. Balkanski, S. Fuzzi, J. Horth, G. K. Moortgat, R. Winterhalter, C. E. L. Myhre, K. Tsigaridis, E. Vignati, E. G. Stephanou and J. Wilson, *Atmos. Chem. Phys.*, 2005, **5**, 1053-1123.

7. R. M. Hewick, M. W. Hunkapiller, L. E. Hood and W. J. Dreyer, *J. Biol. Chem.*, 1981, **256**, 7990-7997.

8. Y. R. Shen, *Appl. Phys. B*, 1999, **68**, 295-300.

9. G. M. Nathanson, P. Davidovits, D. R. Worsnop and C. E. Kolb, *J. Phys. Chem.*, 1996, **100**, 13007-13020.

10. G. L. Richmond, *Annu. Rev. Phys. Chem.*, 2001, **52**, 357-389.

11. G. M. Nathanson, *Annu. Rev. Phys. Chem.*, 2004, **55**, 231-255.

12. C. S. Santos and S. Baldelli, *Chem. Soc. Rev.*, 2010, **39**, 2136-2145.

13. J. A. Faust and G. M. Nathanson, *Chem. Soc. Rev.*, 2016, **45**, 3609-3620.

14. M. A. Tesa-Serrate, E. J. Smoll, T. K. Minton and K. G. McKendrick, *Annu. Rev. Phys. Chem.*, 2016, **67**, 515-540.

15. D. E. Gragson and G. L. Richmond, *J. Phys. Chem. B*, 1998, **102**, 3847-3861.

16. G. L. Richmond, *Chem. Rev.*, 2002, **102**, 2693-2724.

17. C. Kolbeck, J. Lehmann, K. R. J. Lovelock, T. Cremer, N. Paape, P. Wasserscheid, A. P. Froba, F. Maier and H. P. Steinruck, *J. Phys. Chem. B*, 2010, **114**, 17025-17036.

18. V. Lockett, R. Sedev, C. Bassell and J. Ralston, *Phys. Chem. Chem. Phys.*, 2008, **10**, 1330-1335.

19. A. H. Narten, M. D. Danford and H. A. Levy, *Faraday Discuss.*, 1967, 97.

20. E. Bodo, L. Gontrani, R. Caminiti, N. V. Plechkova, K. R. Seddon and A. Triolo, *J. Phys. Chem. B*, 2010, **114**, 16398.

21. I. J. Villar-Garcia, S. Fearn, G. F. De Gregorio, N. L. Ismail, F. J. V. Gschwend, A. J. S. McIntosh and K. R. J. Lovelock, *Chem. Sci.*, 2014, **5**, 4404-4418.

22. T. Iwahashi, T. Nishi, H. Yamane, T. Miyamae, K. Kanai, K. Seki, D. Kim and Y. Ouchi, *J. Phys. Chem. C*, 2009, **113**, 19237.

23. J. Penfold and R. K. Thomas, *J. Phys. Condens. Matter*, 1990, **2**, 1369-1412.

24. J. Bowers, M. C. Vergara-Gutierrez and J. R. P. Webster, *Langmuir*, 2004, **20**, 309-312.

25. D. Kim and G. C. Schatz, *J. Phys. Chem. A*, 2007, **111**, 5019-5031.

26. B. H. Wu, J. M. Zhang, T. K. Minton, K. G. McKendrick, J. M. Slattery, S. Yockel and G. C. Schatz, *J. Phys. Chem. C*, 2010, **114**, 4015-4027.

27. T. Y. Yan, W. L. Hase and J. R. Barker, *Chem. Phys. Lett.*, 2000, **329**, 84-91.

28. J. J. Nogueira, S. A. Vazquez, O. A. Mazyar, W. L. Hase, B. G. Perkins, D. J. Nesbitt and E. Martinez-Nunez, *J. Phys. Chem. A*, 2009, **113**, 3850-3865.

29. J. J. Nogueira, Z. Homayoon, S. A. Vazquez and E. Martinez-Nunez, *J. Phys. Chem. C*, 2011, **115**, 23817-23830.

30. E. Martinez-Nunez, A. Rahaman and W. L. Hase, *J. Phys. Chem. C*, 2007, **111**, 354-364.

31. B. G. Perkins and D. J. Nesbitt, *J. Phys. Chem. A*, 2009, **113**, 4613-4625.

32. M. A. Tesa-Serrate, B. C. Marshall, E. J. Smoll, S. M. Purcell, M. L. Costen, J. M. Slattery, T. K. Minton and K. G. McKendrick, *J. Phys. Chem. C*, 2015, **119**, 5491-5505.

33. J. S. Vieceli and D. J. Tobias, *Abstr. Pap. Am. Chem. S.*, 2004, **227**, U1003-U1003.

34. F. C. Hurlbut and D. E. Beck, *U.C. Eng. Proj. Report HE-150-166*, 1959.

35. S. L. Lednovich and J. B. Fenn, *AIChE J.*, 1977, **23**, 454-459.

36. M. Sinha and J. B. Fenn, Proc. 5th Int. Symp. Molecular Beams, Nice, 1975.

37. S. R. Cohen, R. Naaman and G. G. Balintkurti, *Chem. Phys.*, 1989, **134**, 119-126.

38. S. R. Cohen, R. Naaman and G. G. Balintkurti, *Chem. Phys. Lett.*, 1988, **152**, 269-273.

39. S. R. Cohen, R. Naaman and J. Sagiv, *J. Chem. Phys.*, 1988, **88**, 2757-2763.

40. M. E. Saecker, S. T. Govoni, D. V. Kowalski, M. E. King and G. M. Nathanson, *Science*, 1991, **252**, 1421-1424.

41. M. E. King, M. E. Saecker and G. M. Nathanson, *J. Chem. Phys.*, 1994, **101**, 2539-2547.

42. J. A. Faust, T. B. Sobyra and G. M. Nathanson, *J. Phys. Chem. Lett.*, 2016, **7**, 730-735.

43. M. E. King, G. M. Nathanson, M. A. Hanninglee and T. K. Minton, *Phys. Rev. Lett.*, 1993, **70**, 1026-1029.

44. M. Manning, J. A. Morgan, D. J. Castro and G. M. Nathanson, *J. Chem. Phys.*, 2003, **119**, 12593-12604.

45. J. P. Wiens, G. M. Nathanson, W. A. Alexander, T. K. Minton, S. Lakshmi and G. C. Schatz, *J. Am. Chem. Soc.*, 2014, **136**, 3065-3074.

46. M. P. Ziemkiewicz, J. R. Roscioli and D. J. Nesbitt, *J. Chem. Phys.*, 2011, **134**, 234703.

47. M. P. Ziemkiewicz, A. Zutz and D. J. Nesbitt, *J. Phys. Chem. C*, 2012, **116**, 14284-14294.

48. K. L. King, G. Paterson, G. E. Rossi, M. Iljina, R. E. Westacott, M. L. Costen and K. G. McKendrick, *Phys. Chem. Chem. Phys.*, 2013, **15**, 12852-12863.

49. G. M. Sweeney, A. Watson and K. G. McKendrick, *J. Chem. Phys.*, 1997, **106**, 9172-9181.

50. M. A. Tesa-Serrate, K. L. King, G. Paterson, M. L. Costen and K. G. McKendrick, *Phys. Chem. Chem. Phys.*, 2014, **16**, 173-183.

51. C. Waring, P. A. J. Bagot, J. M. Slattery, M. L. Costen and K. G. McKendrick, *J. Phys. Chem. A*, 2010, **114**, 4896-4904.

52. B. G. Perkins and D. J. Nesbitt, *J. Phys. Chem. B*, 2006, **110**, 17126-17137.

53. B. G. Perkins and D. J. Nesbitt, *J. Phys. Chem. B*, 2008, **112**, 507-519.

54. B. G. Perkins and D. J. Nesbitt, *J. Phys. Chem. A*, 2008, **112**, 9324-9335.

55. B. G. Perkins and D. J. Nesbitt, *Phys. Chem. Chem. Phys.*, 2010, **12**, 14294-14308.

56. B. G. Perkins and D. J. Nesbitt, *P. Natl. Acad. Sci. USA*, 2008, **105**, 12684-12689.

57. C. H. Hoffman and D. J. Nesbitt, *J. Phys. Chem. C*, 2016, **120**, 16687–16698.

58. J. R. Roscioli and D. J. Nesbitt, *J. Phys. Chem. A*, 2011, **115**, 9764-9773.

59. J. R. Roscioli and D. J. Nesbitt, *Faraday Discuss.*, 2011, **150**, 471-479.

60. J. R. Roscioli and D. J. Nesbitt, *J. Phys. Chem. Lett.*, 2010, **1**, 674-678.

61. I. Chorny, I. Benjamin and G. M. Nathanson, *J. Phys. Chem. B*, 2004, **108**, 995-1002.

62. M. E. King, K. M. Fiehrer, G. M. Nathanson and T. K. Minton, *J. Phys. Chem. A*, 1997, **101**, 6556-6561.

63. D. K. Lancaster, A. M. Johnson, D. K. Burden, J. P. Wiens and G. M. Nathanson, *J. Phys. Chem. Lett.*, 2013, **4**, 3045-3049.

64. D. K. Lancaster, A. M. Johnson, K. Kappes and G. M. Nathanson, *J. Phys. Chem. C*, 2015, **119**, 14613-14623.

65. M. E. Saecker and G. M. Nathanson, *J. Chem. Phys.*, 1993, **99**, 7056-7075.

66. A. W. Gisler and D. J. Nesbitt, *Faraday Discuss.*, 2012, **157**, 297-305.

67. M. Ziemkiewicz and D. J. Nesbitt, *J. Chem. Phys.*, 2009, **131**.

68. A. M. Zolot, P. J. Dagdigian and D. J. Nesbitt, *J. Chem. Phys.*, 2008, **129**, 194705.

69. S. P. K. Kohler, M. Allan, H. Kelso, D. A. Henderson and K. G. McKendrick, *J. Chem. Phys.*, 2005, **122**, 24712.

70. J. M. Zhang, H. P. Upadhyaya, A. L. Brunsvold and T. K. Minton, *J. Phys. Chem. B*, 2006, **110**, 12500-12511.

71. G. Herzberg, *Spectra and Molecular-Structure I. Spectra of Diatomic-Molecules*, Princeton Univ. Press, Princeton, NJ, 1968.

72. X. H. Li, G. C. Schatz and D. J. Nesbitt, *J. Phys. Chem. B*, 2012, **116**, 3587-3602.

73. G. D. Kubiak, J. E. Hurst, H. G. Rennagel, G. M. McClelland and R. N. Zare, *J. Chem. Phys.*, 1983, **79**, 5163-5178.

74. Y. X. Peng, L. Liu, Z. Cao, S. Li, O. A. Mazyar, W. L. Hase and T. Y. Yan, *J. Phys. Chem. C*, 2008, **112**, 20340-20346.

75. J. C. Tully, *Surf. Sci.*, 1994, **299**, 667-677.

76. K. R. Seddon, *J. Chem. Technol. Biotechnol.*, 1997, **68**, 351-356.

77. N. V. Plechkova and K. R. Seddon, *Chem. Soc. Rev.*, 2008, **37**, 123-150.

78. D. R. MacFarlane, J. Sun, J. Golding, P. Meakin and M. Forsyth, *Electrochim. Acta*, 2000, **45**, 1271-1278.

79. J. G. Huddleston, A. E. Visser, W. M. Reichert, H. D. Willauer, G. A. Broker and R. D. Rogers, *Green Chem.*, 2001, **3**, 156-164.

80. J. M. S. S. Esperanca, J. N. C. Lopes, M. Tariq, L. M. N. B. F. Santos, J. W. Magee and L. P. N. Rebelo, *J. Chem. Eng. Data*, 2010, **55**, 3-12.

81. M. Gorlov and L. Kloo, *Dalton T.*, 2008, 2655-2666.

82. R. Kawano, H. Matsui, C. Matsuyama, A. Sato, M. A. B. H. Susan, N. Tanabe and M. Watanabe, *J. Photoch. Photobio. A*, 2004, **164**, 87-92.

83. R. Y. Lin, P. L. Taberna, S. Fantini, V. Presser, C. R. Perez, F. Malbosc, N. L. Rupesinghe, K. B. K. Teo, Y. Gogotsi and P. Simon, *J. Phys. Chem. Lett.*, 2011, **2**, 2396-2401.

84. A. Lewandowski and A. Swiderska-Mocek, *J. Power Sources*, 2009, **194**, 601-609.

85. W. L. Hough, M. Smiglak, H. Rodriguez, R. P. Swatloski, S. K. Spear, D. T. Daly, J. Pernak, J. E. Grisel, R. D. Carliss, M. D. Soutullo, J. H. Davis and R. D. Rogers, *New J. Chem.*, 2007, **31**, 1429-1436.

86. A. Riisager, R. Fehrmann, M. Haumann and P. Wasserscheid, *Eur. J. Inorg. Chem.*, 2006, 695-706.

87. F. Jutz, J. M. Andanson and A. Baiker, *Chem. Rev.*, 2011, **111**, 322-353.

88. T. Welton, *Chem. Rev.*, 1999, **99**, 2071-2083.

89. J. G. Huddleston, H. D. Willauer, R. P. Swatloski, A. E. Visser and R. D. Rogers, *Chem. Commun.*, 1998, 1765-1766.

90. J. L. Anthony, J. L. Anderson, E. J. Maginn and J. F. Brennecke, *J. Phys. Chem. B*, 2005, **109**, 6366-6374.

91. J. E. Bara, R. D. Noble and D. L. Gin, *Ind. Eng. Chem. Res.*, 2009, **48**, 4607-4610.

92. L. A. Blanchard, D. Hancu, E. J. Beckman and J. F. Brennecke, *Nature*, 1999, **399**, 28-29.

93. L. A. Blanchard, Z. Y. Gu and J. F. Brennecke, *J. Phys. Chem. B*, 2001, **105**, 2437-2444.

94. Y. S. Kim, W. Y. Choi, J. H. Jang, K. P. Yoo and C. S. Lee, *Fluid Phase Equilibr.*, 2005, **228**, 439-445.

95. J. L. Anthony, E. J. Maginn and J. F. Brennecke, *J. Phys. Chem. B*, 2002, **106**, 7315-7320.

96. T. Hammer, M. Reichelt and H. Morgner, *Phys. Chem. Chem. Phys.*, 2010, **12**, 11070-11080.

97. V. Lockett, R. Sedev, S. Harmer, J. Ralston, M. Horne and T. Rodopoulos, *Phys. Chem. Chem. Phys.*, 2010, **12**, 13816-13827.

98. S. Caporali, U. Bardi and A. Lavacchi, *J. Electron Spectrosc.*, 2006, **151**, 4-8.

99. K. Nakajima, A. Ohno, H. Hashimoto, M. Suzuki and K. Kimura, *J. Chem. Phys.*, 2010, **133**.

100. C. S. Santos and S. Baldelli, *J. Phys. Chem. B*, 2009, **113**, 923-933.

101. Y. Huang, A. M. Wodtke, H. Hou, C. T. Rettner and D. J. Auerbach, *Phys. Rev. Lett.*, 2000, **84**, 2985-2988.

102. A. M. Wodtke, D. Matsiev and D. J. Auerbach, *Prog. Surf. Sci.*, 2008, **83**, 167-214.

103. A. M. Wodtke, Y. H. Huang and D. J. Auerbach, *J. Chem. Phys.*, 2003, **118**, 8033-8041.

104. H. Hou, C. T. Rettner, D. J. Auerbach, Y. Huang, S. J. Gulding and A. M. Wodtke, *Faraday Discuss.*, 1999, **113**, 181-200.

105. N. Bartels, K. Golibrzuch, C. Bartels, L. Chen, D. J. Auerbach, A. M. Wodtke and T. Schafer, *P. Natl. Acad. Sci. USA*, 2013, **110**, 17738-17743.

106. N. Shenvi, S. Roy and J. C. Tully, *J. Chem. Phys.*, 2009, **130**, 174107.

107. N. Shenvi, S. Roy and J. C. Tully, *Science*, 2009, **326**, 829-832.

108. W. R. Ronk, D. V. Kowalski, M. Manning and G. M. Nathanson, *J. Chem. Phys.*, 1996, **105**, 4397-4397.

Chapter 2

Experimental Apparatus

2.1 Introduction

The experiment described in this section utilizes quantum state resolved scattering of NO from liquid surfaces to explore energy transfer and collision dynamics at the gas-liquid interface. A supersonically cooled beam of NO($^2\Pi_{1/2}$; J = 0.5) strikes a low vapor pressure liquid in vacuum and the scattered NO molecules are detected via laser induced fluorescence (LIF), yielding full vibrational, rotational and spin-orbit distributions. Fundamental to the success of this experiment are the following components: (i) full characterization of the incident molecular beam, (ii) quantum-state resolved characterization of the scattered flux, (iii) a clean liquid surface and, (iv) confidence that changes in internal states of the molecules are due to collisions with the liquid surface and not from interactions with gas phase molecules. The state-to-state resolved measurements in this experiment enable dynamics and energy transfer at the gas-liquid interface to be investigated by probing changes between the initial and final state distributions of NO. This experiment was built up by Mike Ziemkiewicz, whose thesis delves into a number of details not discussed in this chapter.[1] The first half of this experimental section broadly describes the experimental setup and data analysis routines, with an emphasis on experimental methods and changes made to the apparatus. The latter half of this chapter describes recent experimental

changes made to enable systematic, controlled heating of molten metals up to T_s = 1400 K, which allow molecular beam scattering experiments to be performed from molten gold, among other liquid metals.

2.2 LIF Detection of Nitric Oxide

NO molecules are detected via LIF, which is a quantum state specific and density dependent measurement. A UV laser pulse excites NO molecules in the ground X($^2\Pi$) electronic state to the first A($^2\Sigma^+$) excited electronic state, which then fluoresce back down to the ground state with a ~ 210 ns radiative lifetime[2, 3] and nearly unity quantum yields (Figure 2.1). For radiative lifetimes independent of upper state, the intensity of the fluorescent light will be strictly proportional to the population in a given quantum state. Thus, by tuning the wavelength of the

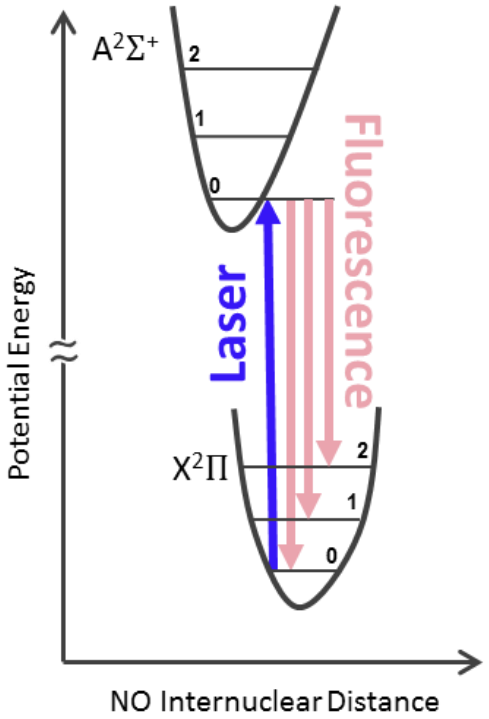

Figure 2.1 LIF detection of NO on the $A^2\Sigma^+$ (v = 0) ⟵ $X^2\Pi$(v = 0) γ band. NO molecules are excited by a ~225 nm pulsed, tunable UV laser. Fluorescence back down to the $X^2\Pi$ state is proportional to the NO population in the $X^2\Pi$ rovibronic state being probed.

laser, NO rovibronic distributions up to N = 50 in both spin-orbit states and vibrational states v = (0, 1) can be observed and quantitatively measured. The energy required to excite the $A^2\Sigma^+ \leftarrow X^2\Pi$ γ band electronic transition is ~ 5.5 eV, which is obtained from a pulsed, tunable UV laser (~225 nm) generated from the tripled output of a Nd:YAG-pumped dye laser. A sample NO $A^2\Sigma^+$ (v = 0) ⟵ $X^2\Pi$(v = 0) spectrum is shown in Figure 2.2 with the P, Q and R branches labeled for all spin-orbit and lambda-doublet electronic states, $^2\Pi^e_{1/2}$ (Q_{21}, P_{11}, R_{11}), $^2\Pi^f_{1/2}$ (Q_{11}, P_{21}, R_{21}), $^2\Pi^e_{3/2}$ (Q_{12}, P_{22}, R_{22}), and $^2\Pi^f_{3/2}$ (Q_{22}, P_{12}, R_{12}). The subscript labels on each of these branches refer to spin-splitting in the upper $A^2\Sigma$ and lower $X^2\Pi$ electronic states, which correspond to the first and second subscripts, respectively.

The ground state of NO has nonzero angular momentum, as the unpaired electron lies in an antibonding π* orbital. The ground $^2\Pi$ electronic state is therefore split into two spin-orbit states, ground ($^2\Pi_{1/2}$) and excited ($^2\Pi_{3/2}$), which in Hund's case (a) are separated by a spin-orbit

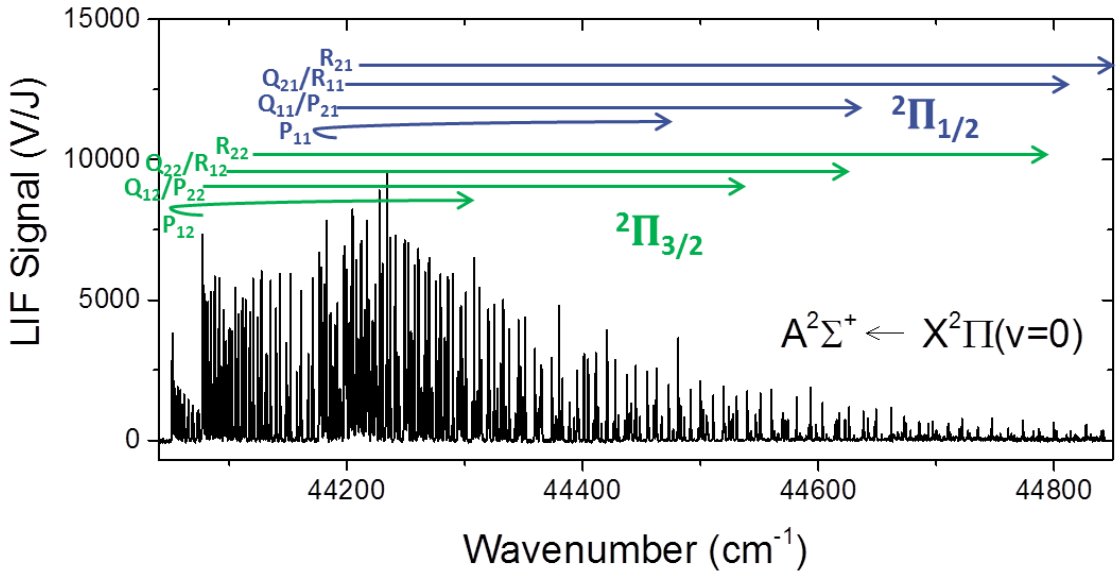

Figure 2.2 Sample LIF spectrum of scattered NO (v = 0) at hyperthermal collision energies (E_{inc} = 20 kcal/mol), where quantum states up to N = 50 in both spin-orbit states ($^2\Pi_{1/2}$ and $^2\Pi_{3/2}$) are populated. The length of the arrows extend up to N = 40 for each branch.

splitting of E_{so} = 123 cm^{-1} at J = 1.5.[4] These spin-orbit states physically correspond to the projections of the spin and orbital angular momenta either aligned ($\Omega = 3/2$) or anti-aligned ($\Omega = 1/2$) with respect to the internuclear axis. NO molecules in low N states, where N represents end-over-end tumbling angular momenta, have energy spacings between rotational states (~$2B_{NO}N$, where B_{NO} =1.72 cm^{-1}) that are small compared to E_{so}. The energy level structures for these molecules are well described by Hund's case (a), where both the orbital and spin angular momenta are strongly coupled to the NO internuclear axis. This case holds up to N ~ 35, where the end-over-end tumbling energy spacing nears the spin-orbit energy splitting and the spin angular momentum decouples from the NO internuclear axis (Hund's case (b)). In the experiments presented, however, nearly all the rotational states of the NO molecules detected fall into the Hund's case (a) scenario where the spin-orbit state label (Ω) remains valid. Each spin-orbit state is also further split into two lambda-doublet states of opposite spectroscopic parity. These spacings are much smaller, at ~0.01 cm^{-1} for the lowest rotational state and physically correspond to the half-filled π^* orbital either parallel (e) or perpendicular (f) to the plane of molecular rotation.[5] Each of these electronic states, as well as the rotational distributions within each state, can be probed independently with LIF detection.

A schematic of pulsed UV light production is shown in Figure 2.3. The primary source of the laser pulse is a Nd:YAG (Continuum PL-8010). The laser medium is a neodymium-doped yttrium aluminum garnet (Nd:YAG) crystal that is optically pumped with flashlamps, which are typically run at an applied voltage of 1.2 kV. The lasing cavity is Q-switched with a Pockels cell that rotates 1064 nm photons a quarter wave of rotation when a voltage is applied, which opens the cavity for optical amplification and outputs a fast, high intensity laser pulse. A digital delay

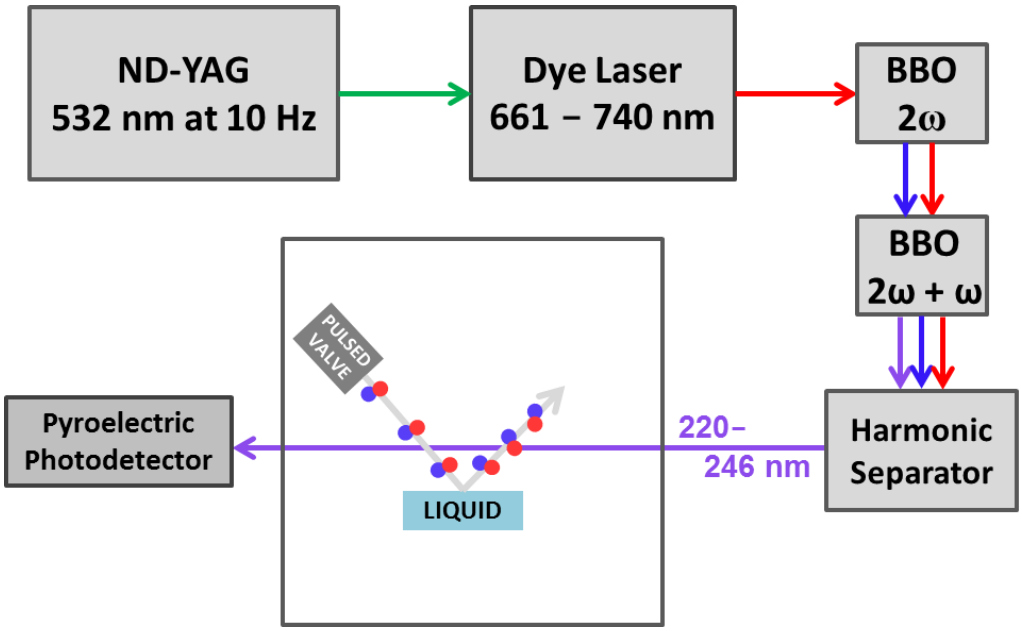

Figure 2.3 Pulsed UV light produced from the tripled output of a Nd:YAG pumped dye laser, which is used to study molecular scattering of NO from liquid surfaces.

generator (DDG, SRS DG535) first triggers the flashlamps to optically excite the Nd:YAG crystal and a second trigger delivers a high voltage pulse to the Pockels cell once an optimum population inversion in the Nd ions is achieved. The 1064 nm light is doubled via second harmonic generation in a beta barium borate (BBO) crystal, which delivers ~ 4 W of 532 nm light in 8 ns pulses, or 400 mJ pulses at 10 Hz.

The doubled Nd:YAG laser pumps a tunable dye laser (Continuum ND-6000) operating with LDS-698 (Pyridine-1) dye, which outputs wavelengths from 661 to 740 nm. Optimal dye concentrations in methanol are 5×10^{-5} M and 2×10^{-4} M for the amplifier and oscillator, respectively, which are circulated through each dye cell window (Continuum DCP 6000 dye circulator). A high resolution diffraction grating within a 'Moya oscillator' allows for laser frequency tuning and good wavelength selectivity. This grating is operated by a sine bar drive, whereby a linear displacement in the translation stage is transformed into a linear change in

wavelength. To ensure smooth wavelength tuning and to avoid mechanical backlash on the sine bar drive, the laser should be scanned from blue to red frequencies. The dye laser is typically scanned at a rate of 0.1 cm^{-1} per second, by a LabView program 'Definitive Scanner'.[1] This dye laser is comprised of one oscillator and two amplifiers, although only one amplifier is needed to obtain sufficient UV laser pulse energies. With the second amplifier blocked, average dye laser output powers of ~100 mW are obtained at 680 nm, or 10 mJ/pulse at 10 Hz repetition rates.

The dye laser output then passes through two nonlinear, BBO crystals that triple the wavelength of the dye laser. The first BBO crystal (phase matching angle $\theta = 34.7^{o}$, Inrad) combines two photons in the incoming laser beam via second harmonic generation and outputs light at twice the frequency of the incident light. The second BBO crystal ($\theta = 53.2^{o}$, Inrad) then adds the fundamental and doubled photons together via sum frequency generation to produce frequency tripled light. These BBO crystals reside in autotrackers (Inrad Autotracker III) that rotate the crystals to maintain optimum frequency mixing production while scanning the frequency of the dye laser with an active feedback servo design. The pulsed laser light output from these autotrackers is a mixture of the fundamental, doubled and tripled light. A series of four prisms in a UV harmonic separator (Inrad, Model 752-104) are used to separate these wavelengths, outputting just the tripled wavelength from the dye laser. This light is vertically polarized with wavelength ranges between 220-246 nm (40500 to 45400 cm^{-1}) and a 0.4 cm^{-1} linewidth, as determined by widths of isolated NO peaks in the LIF spectrum.

The pulsed UV laser enters and exits the vacuum chamber through 2 mm calcium fluoride (CaF_2) Brewster angle windows, which allow the p-polarized laser beam to pass through while minimizing stray light from entering into the chamber. Each of these Brewster windows sit at the end of 24" baffle arms, inside of which a series of aluminum irises are situated with

increasing diameters, ranging from 5 mm to 11 mm, that further help to ensure a zero photon background for LIF detection. The laser beam is aligned through two irises on either side of the chamber. The laser power pulse-to-pulse fluctuations are substantial, with a standard deviation of $\sigma \approx 25\%$. The energy of each laser pulse is measured after passing through the vacuum chamber on a pyroelectric photodetector (Molectron J3-09 Pyroelectric Joulemeter) and its signal is integrated over a 300 ns window with a boxcar integrator (SRS 250). The power measured for each laser pulse is used to normalize the fluorescence measurements described below.

A typical LIF scan of NO (v = 0) on the ($A^2\Sigma^+ \leftarrow X^2\Pi$) γ band spans roughly 800 cm^{-1}, from 44050 to 44850 cm^{-1}, and probes NO rotational states in the ground ($^2\Pi_{1/2}$) and excited ($^2\Pi_{3/2}$) spin-orbit manifolds from J = 0 to J = 50.5. For one of these spectra, it takes ~ 2.5 hours to scan the dye laser at 0.1 cm^{-1} per second. Throughout each scan it is crucial that the LIF signal is linear with laser power. In order to ensure LIF transitions are not saturated, the UV laser powers are kept at ≤ 3 μJ/pulse levels. This lack of saturation is confirmed by a LIF signal curve of growth vs. laser power in Figure 2.4, which shows these 3 μJ pulse energies are safely within the linear regime.

2.3 Incident Molecular Beam

The incident molecular beam is supersonically expanded from an Even-Lavie valve. This expansion yields a narrow distribution of translational velocities and a highly rotationally cold beam. In order to produce a supersonic expansion, where the molecules and atoms in the molecular beam are adiabatically cooled, two conditions must be fulfilled: (i) gas must flow from a high pressure region to a low pressure region, which must differ by *at least* a factor of two in pressure and (ii) the mean free path inside the high pressure region must be much larger than the

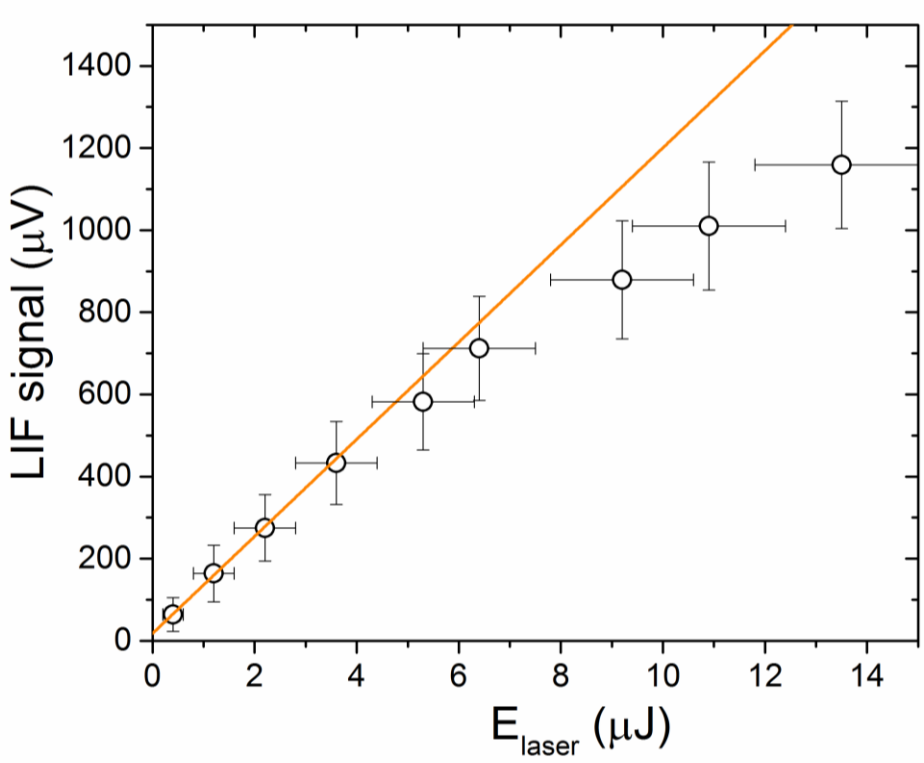

Figure 2.4 LIF signal vs. laser energy curve of growth. These data are taken from the P_{21}(J = 1.5-3.5) bandhead peak at 44198cm^{-1}. Laser pulse energies are typically kept ≤ 3 μJ/pulse to avoid saturation of LIF transitions.

diameter of the pinhole (λ >> d). The Even-Lavie valve (Type E.L.-5-C-2005) produces this supersonic expansion via a solenoid based mechanism coupled with a plunger that presses up against a kapton gasket with a 100 micron diameter pinhole and a stainless steel conical nozzle. These Even-Lavie valves can operate at high pressures (100 bar), high temperatures (400 K), and with short opening times (15 μs), which result in remarkably cold molecular beams.

Rotational cooling in the supersonic molecular beam expansion is very efficient. By way of example, an LIF spectrum of the incident molecular beam of 1% NO in Ne-70 is shown in Figure 2.5. More than 99% of NO is in the lowest J = 0.5 state, which translates into a rotational temperature < 1 K. These rotational temperatures vary slightly depending on the buffer gas mixed with NO. For example, H_2 as a diatomic buffer gas is a less efficient cooler than

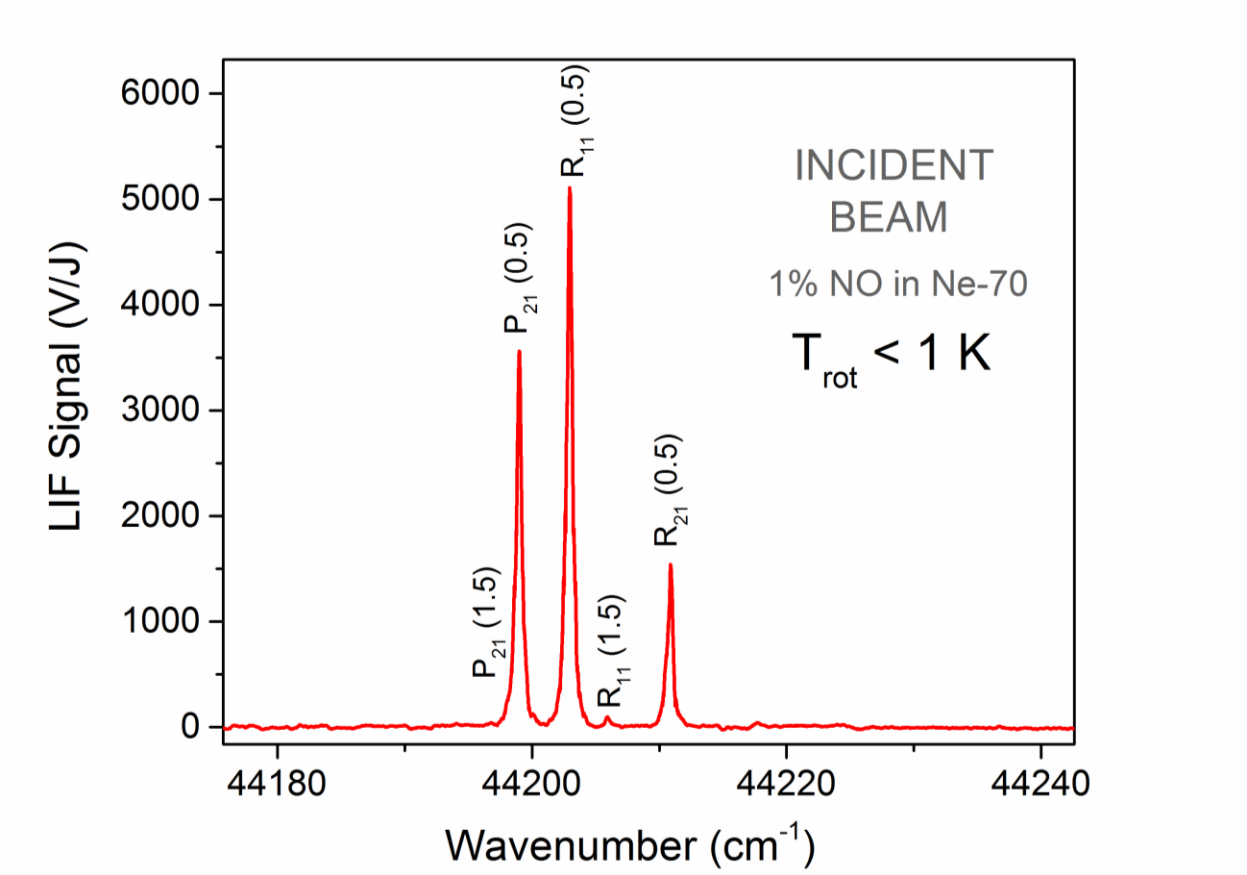

Figure 2.5 LIF spectrum of the supersonically cooled incident molecular beam comprised of 1% NO in Ne-70 (70% Ne, 30% He). The incident beam has a rotational temperature of < 1 K where more than 99% of all NO molecules are in the J = 0.5 state.

monatomic rare gases and yields rotational temperatures just over 2 K. For all expansion conditions, however, all NO molecules in the incident beam are in the ground $^2\Pi_{1/2}$ state with the lambda-doublet states equally populated.

Pulse shapes for the incident beam are shown in Figure 2.6 for varying opening times. The width of these pulses is controlled by the Even-Lavie 'E.L. Driver'. As seen in Figure 2.6, rebound pulses or "bounces" of the plunger appear for longer opening times. To ensure the valve is opening all the way and the molecular beam is fully cooled, pulse widths ≥ 50 μs must be used (Figure 2.6); However, due to corrosion inside the pulsed valve, opening times ≥ 80 μs are now required for complete opening of the valve and maximum cooling. The interior of the valve has

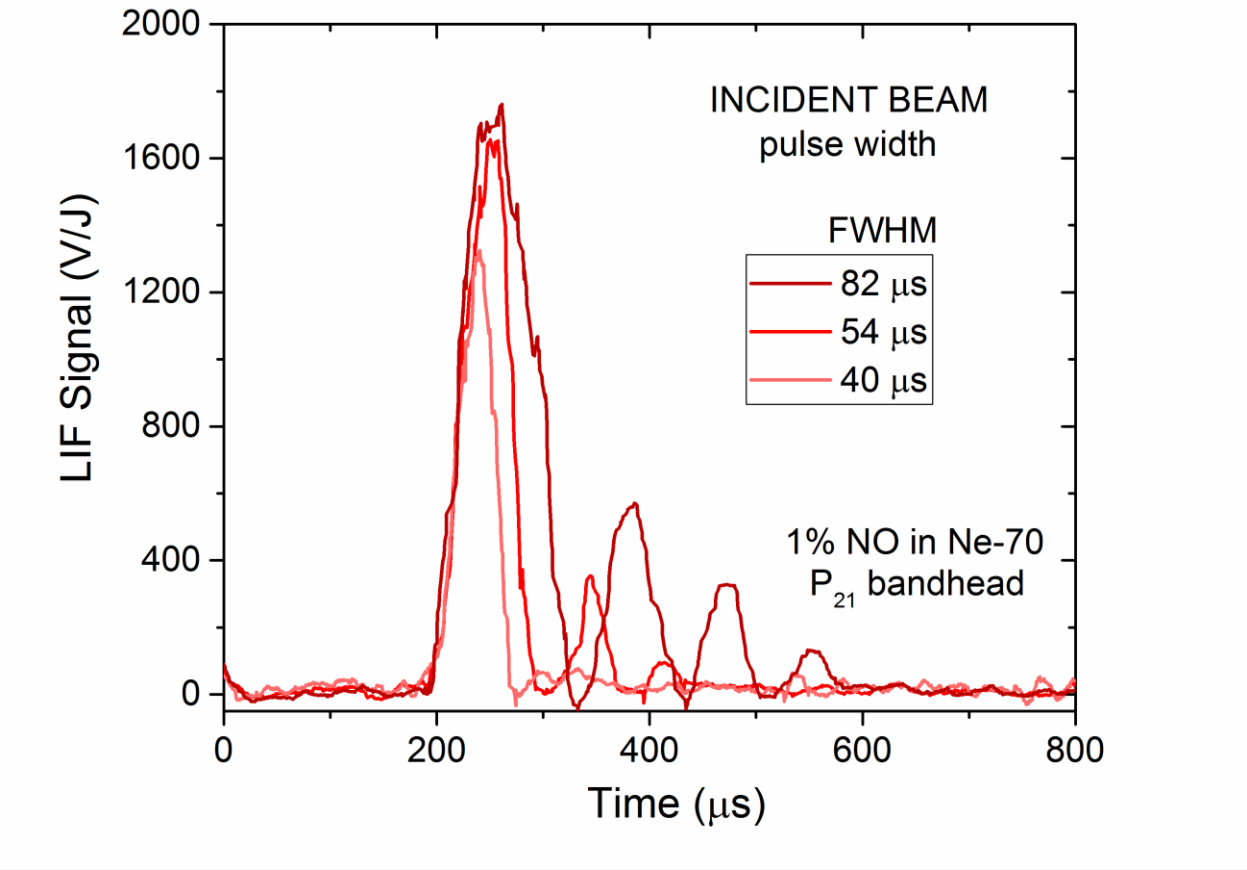

Figure 2.6 Incident molecular beam time profiles from the Even-Lavie pulsed valve at various pulse widths. Rebound pulses are observed for longer opening times.

been cleaned extensively on multiple occasions by scrubbing, scraping and sonicating the plunger, spring, ceramic spacers and high-pressure tube. While this cleaning procedure has improved function, the pulsed valve continues to not open fully at pulse widths < 80 μs.

The gas mixtures are made in 1 L stainless steel cylinders with 1% NO and 99% buffer gas, consisting of either H_2, He, Ne or some mixture of those three. A gas manifold made of welded stainless steel with Swagelok VCO fittings and teflon tubing is used to combine and store these gas mixtures. The manifold connects the mixing cylinders, gas cylinders and Even-Lavie pulsed valve, which allows mixing of a variety of gases and can be evacuated with a small mechanical vacuum pump. Gas mixtures are made by first adding NO and subsequently adding

the buffer gas in bursts to facilitate turbulent mixing. The mixtures are made at a total pressure of 5,000 Torr and are left overnight, or at least 8 hours, to achieve a uniform composition. A 10,000 Torr Baratron is used to measure the partial pressures of each gas, which can be quantitatively confirmed with the relative percent gas mixtures measured by a residual gas analyzer (RGA) in the chamber. A corrosion-resistant, stainless steel Monel regulator stands between these gas mixture cylinders and the pulsed valve, limiting the backing pressure of the valve to ~ 3,000 Torr. Additionally, a metal mesh filter is situated before the valve to remove any particulate matter and keep the interior of the pulsed valve clear of obstructions.

The density of the gas in the supersonic expansion a distance x from the valve opening can be calculated using the following empirical formula, $P_{jet} = C * P_0 * (d/x)^2$, where P_0 is the is the stagnation pressure in the valve, d is the pinhole diameter, and C is a constant related to the heat capacities, which is ~ 0.15 for monatomic gases.[6] The liquid sample sits 13 cm from the pulsed valve, for which the beam conditions translate into a density of 9×10^{12} #/cm^3 at the surface, including both NO and the buffer gas. Under these experimental conditions, an 80 μs gas pulse of molecules moving at 2×10^5 cm/s results in an incident molecular flux of 1.5×10^{14} #/cm^2 at the surface. There are roughly 5×10^{15} sites/cm^2 (calculated based on the size of an incident NO molecule) and, to ensure isolated interactions with the surface, the incident gas pulse flux should be < 0.1 monolayers per pulse. The calculations above confirm this condition is met, with ~ 0.03 monolayers/pulse of incident atoms and molecules striking the surface.

Fractional NO concentrations in the incident beam are chosen to maximize LIF signal while ensuring negligible cluster formation of NO_2 or NO-X (X = diluent gas) in the supersonic expansion, which can occur due to both larger NO partial pressures and high backing pressures in the pulsed valve. To monitor cluster formation in the incident beam, curve of growth

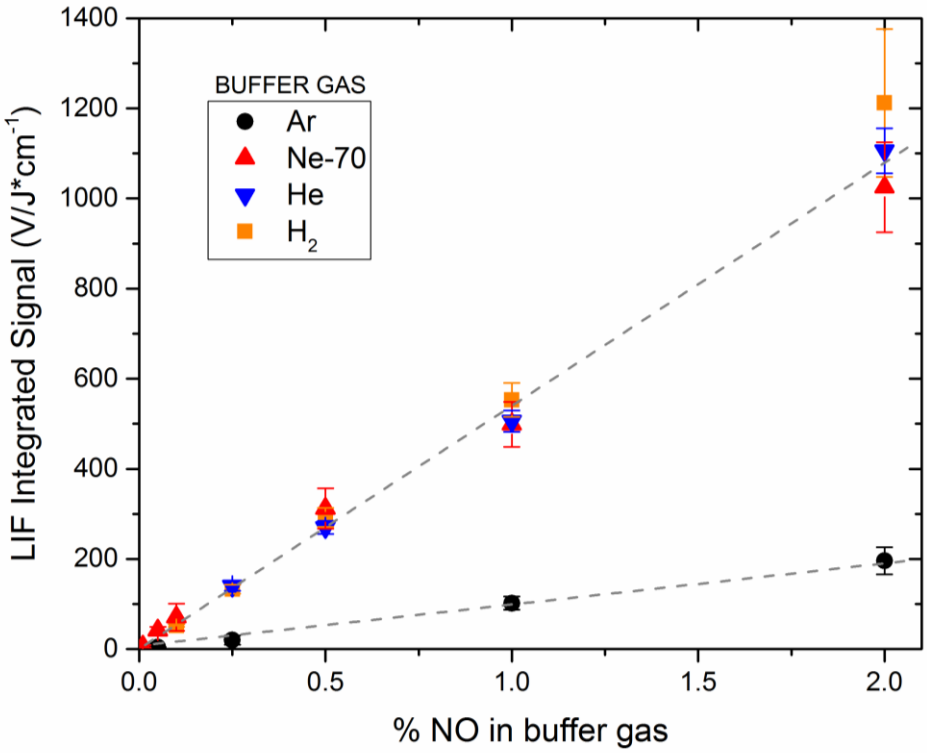

Figure 2.7 LIF signal as a function of fractional NO concentration in the incident molecular beam. Signals are integrated over the $R_{11}(0.5)$ peak and increase linearly with NO partial pressures in the region studied. Gas mixtures with Ar have consistently 4x lower signals, possibly to due freezing of the molecular beam.

measurements have been made with varying fractional NO partial pressures for all buffer gases used. Mixtures of 1% NO in all carrier gases are safely within a linear regime of LIF signal vs. NO fraction (see Figure 2.7), indicative of negligible cluster formation in the incident molecular beam. NO mixtures with Ar consistently yielded 4x lower signal relative to other buffer gases mentioned above (Figure 2.7), even with NO concentrations as low as 0.01%. This could be a result of either cluster formation of NO-Ar van der Waal's complexes or freezing of the molecular beam, therefore Ar was not used in these experiments. The mass of the buffer gas atoms and/or molecules control the speed of NO in the molecular beam. Thus, by changing the buffer gas, the speed of the incident NO molecules is varied. The terminal velocity of the

supersonic expansion can be calculated using the following equation:[7]

$$v_\infty = \sqrt{\frac{2kT}{m}\left(\frac{\gamma}{\gamma-1}\right)} \qquad (2.1)$$

where m is the average molecular weight of the gas mixture, γ is the heat capacity ratio (C_P/C_V), and T is the temperature in the stagnation region. This terminal velocity for supersonic expansions is reached within $x/d \sim 5$, i.e., five times the pinhole diameter away from the valve opening.[7]

These theoretical expectations are compared to experimental measurements with microphone time of flight measurements of gas pulses. A hearing aid microphone is placed on a metal rod in vacuum through an Ultra-Torr feedthrough. This microphone is placed in front of

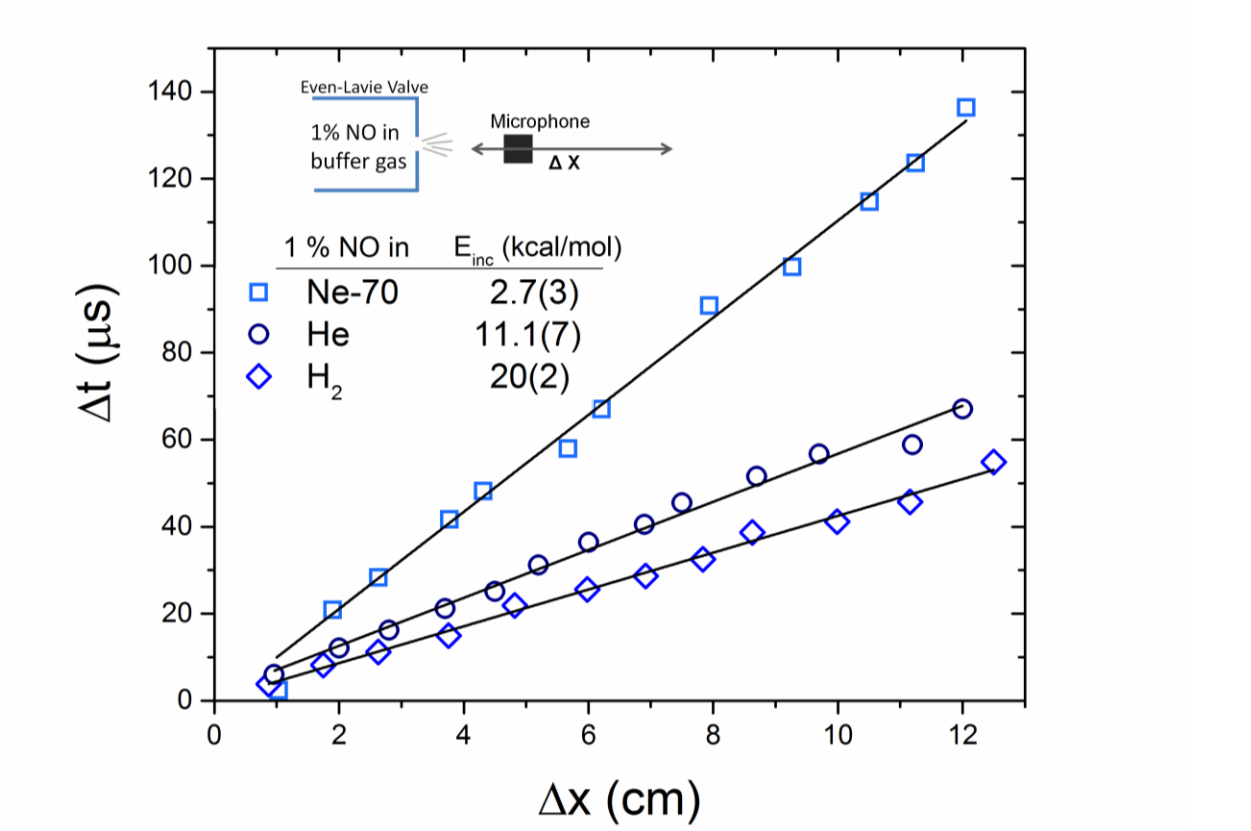

Figure 2.8 Microphone measurements of the incident molecular beam are used to calculate NO velocities and collision energies in various gas mixtures, which correspond to velocities ranging from 8 x 10^4 to 2.5 x 10^5 m/s. Measurements are made by translating a microphone along the axis of the pulsed valve expansion through an Ultra-Torr feedthrough, as illustrated at the top of the figure.

the pulsed valve such that it can be translated along the axis of the supersonic expansion from the pinhole of the valve (see top of Figure 2.8). Molecular speeds are calculated by plotting the displacement of the microphone (Δx) against the difference in peak signal arrival times (Δt), as presented in Figure 2.8 for gas mixtures of 1 % NO in Ne-70 (70% Ne, 30% He), He and H_2. For example, NO speeds of 1.76 x 10^5 cm/s are measured for gas mixtures of 1% NO in He, which correspond to E_{inc} = 11.1(7) kcal/mol, i.e., within experimental uncertainty, but slightly faster than theoretical predictions of 10.5 kcal/mol. This range of buffer gases, from H_2 to Ne, allows creation of tunable incident beam energies from 2.0 to 20 kcal/mol, or velocities from 8 x 10^4 to 2.5 x 10^5 m/s.

2.4 Liquid Surfaces

In these experiments, NO acts as a molecular probe of the gas-liquid interface; therefore, it is crucial that the incident NO molecules, after leaving the pulsed valve, collide only with the liquid surface and do not collide with other gas phase molecules before reaching the LIF detection region. To ensure this condition is met, experiments must take place under vacuum conditions where the mean free path of gas molecules is much larger than the distance an NO molecule travels from the exit of the pulsed valve to the detection region (~15 cm). Furthermore, the vapor pressures of the liquids studied must also correspond to mean free paths (λ) at least an order of magnitude larger than 15 cm. This condition is satisfied by liquids with vapor pressures $\leq 10^{-4}$ Torr, for which $\lambda \geq 500$ cm. In this regime, the state-to-state resolved NO populations observed are truly representative of collision dynamics occurring solely at the gas-liquid interface.

Two liquids that fit this requirement include squalane and perfluoropolyether (PFPE), which both have low vapor pressures at room temperature and have been studied in previous gas-liquid scattering experiments.[8-11] Room temperature ionic liquids (RTILs) are a new class of green solvents that are molten salts with melting temperatures below 100ºC. These ionic liquids are an attractive alternative to many organic solvents due to their low vapor pressures, which also makes them suitable for study in vacuum. A variety of imidazolium based RTILs have been studied with various anion and cation combinations. Experiments have been performed with 1-alkyl-3-methylimidazolium ([$C_n$mim], where n = 2, 4, 8, 12 and 16) cation and three different anions: i) chloride, ii) tetrafluoroborate ($[BF_4]^-$) and (iii) bis(trifluoromethylsulfonyl)imide ($[Tf_2N]^-$). In Figure 2.9, the molecular structures of all liquid surfaces studied are illustrated. Liquid metals have also been studied, the preparation and heating of which will be discussed further in Section 2.9.

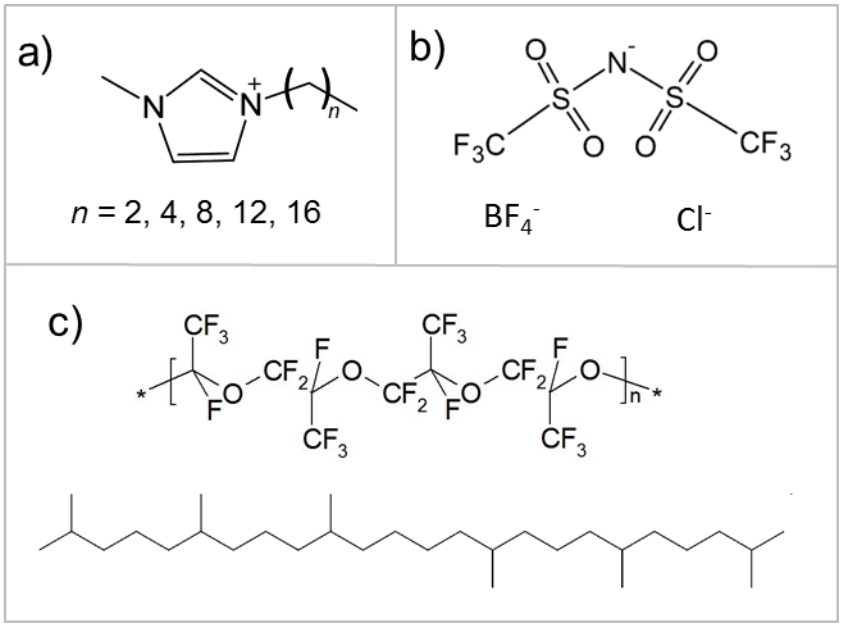

Figure 2.9 Molecular structures of liquids studied. a) RTIL cation, $[C_n\text{-mim}]^+$ (1-alkyl-3-methylimidazolium), with varying hydrocarbon chain lengths, b) RTIL anions: $[Tf_2N]^-$ ($N(CF_3SO_2)_2^-$), $[BF_4]^-$ and Cl^- c) PFPE ($F(CF(CF_3)CF_2O)_{14}CF_2CF_3$) and squalane ($C_{30}H_{62}$)

All RTILs were purchased from Io-li-tec with ≥ 99% purity, while both squalane ($C_{30}H_{62}$, 99% purity) and perfluoropolyether (PFPE, $F(CF(CF_3)CF_2O)_{14}CF_2CF_3$, Krytox 1506) were bought from Sigma-Aldrich. Prior to placement in vacuum, the liquids are heated and stirred for at least 4 hours while being pumped on by a mechanical pump with a liquid nitrogen trap to remove volatile impurities from the liquid samples. In particular, this degassing procedure removes dissolved H_2O, as many of these ionic liquids are quite hygroscopic. The degassed liquids are then poured into a stainless steel crucible in the vacuum chamber with a 2.4 mL reservoir (4 x 2.4 x 0.25 cm^3) and maintained at low pressures ($P_{chamber} < 5 \times 10^{-6}$ Torr) before and during any experimental runs.

One method used by many researchers to ensure that a liquid surface is clean and free of impurities is Ar^+ sputtering, where the surface is bombarded with high energy (i.e. KE = 2 kV) Ar ions. For the aforementioned ionic liquids studied in these experiments, however, this process ablates and vaporizes the liquid through local heating. Unfortunately, these vaporized liquids can in turn coat the imaging lens, resulting in decreased LIF signal. Therefore, to ensure cleanliness of liquid surfaces beyond the degassing procedure, experiments have been performed where the surface is refreshed every five minutes. This is done manually by moving a rod with a wire attached through an Ultra-Torr feedthrough that scrapes the topmost layer of the liquid surface. Scattering results from these refreshed surfaces are in excellent agreement with scattering data for the same experimental parameters where the surface was not scraped. Furthermore, as these liquids remain in vacuum and are bombarded with NO molecules and inert gases, the surfaces do not change over the course of multiple days of running experiments, indicating that the surfaces remain consistent and clean throughout these experiments.

The temperature of the crucible and liquid is measured by a Type K thermocouple that is secured with a set screw in a small hole drilled into the side of the crucible. This stainless steel crucible is heated by two NiCr cartridge heaters that are sandwiched between the crucible and a lower plate. Both of these pieces are machined with grooves to fit the cylindrical heaters and are held together with threaded stainless steel rods and tightened nuts. A variable transformer (Staco, 3PN1010) delivers power to these heaters and is coupled to a solid state relay hooked up to a PID controller (Omega, CNi 3224-C24), which is able to maintain crucible temperatures within ± 1 K. To confirm thermal equilibration, bare thermocouples have also been submerged in the liquid reservoir, which reveal temperatures in agreement with the crucible temperature. This heating system is capable of achieving liquid temperatures up to 600 K, however, the vapor pressure of many of these liquids increases rapidly with surface temperature, thus constraining the experimental upper temperature limit. Higher vapor pressures of liquids can not only interfere with NO molecules, but the evaporating liquids can also coat the imaging lens and decrease the fluorescence signal collection efficiency. For most of the RTILs studied, surface temperatures from 293 – 393 K were investigated, and for both squalane and PFPE only a 293 K surface temperature was studied.

Many of the imidazolium RTILs investigated also have liquid crystal phases. For example, [C_{12}mim][Br] forms a smectic liquid crystal phase between 40ºC and 110ºC.[12] In this crystal formation, the long alkyl chains on the cations align between hydrophilic layers of the charged imidazolium rings and anions, as illustrated in the Figure 2.10 inset. These well-defined layers can slide over one another, giving this phase 'liquid' like characteristics. An image of this liquid crystal formation (Figure 2.10) between two cross-polarized glass slides shows strong birefringence. Each domain corresponds to regions where liquid crystal molecules are well

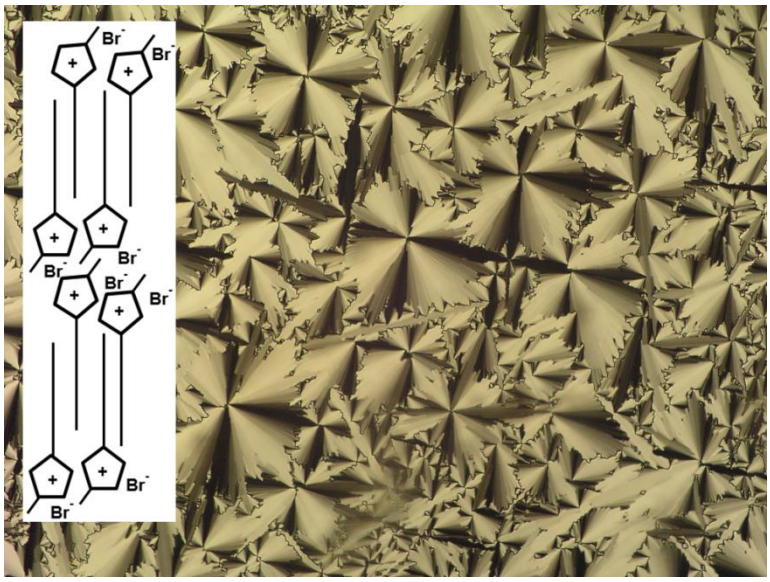

Figure 2.10 Liquid crystal phase of $[C_{12}mim]^+[Br]^-$, as viewed between two cross-polarized glass slides, revealing strong birefringence indicative of smectic ordering. The inset shows the ordering of the cations and anions for the smectic A liquid crystal structure.

ordered, while black shaded regions in between domains indicate isotropic distributions where the direction of alignment is changing from one domain to another.

Scattering experiments of NO from $[C_{12}mim][Br]$ have been carried out in both the liquid crystal and isotropic liquid phases. Differential scanning calorimetry measurements are performed to confirm phase transition temperatures, the results of which found the solid to liquid crystal phase change at 40ºC and the liquid crystal to isotropic liquid at 100ºC, in good agreement with literature values.[12] The sample temperature is varied from 80ºC to 130ºC in the hope of observing differences in scattering dynamics between the rough, fluctuating liquid surfaces and more ordered liquid crystal surfaces. However, no differences were observed in scattering between these two phases, both in terms of overall signal and the extracted rotational/electronic temperatures at both low (2.0 kcal/mol) and high (20 kcal/mol) collision energies. If any differences in scattering from these two different phases exist, they were below

the sensitivity of these experimental measurements, i.e., rotational temperatures of scattered molecules were within 5 K and the integrated signal was within the standard deviation of the average signal. These same studies have also been performed with $[C_{12}mim][BF_4]$, where again no differences in scattering dynamics from its liquid crystal and isotropic phases were observed. This could either indicate that the surface structure presented to incoming gas molecules is not affected by the long-range order present in liquid crystals, or more likely the fact that the molecular beam spot size averages over many different surface domains and the large range of scattering angles detected blurred any major differences.

2.5 Molecular Scattering and Detection Geometry

All molecular scattering takes place within a 90 L vacuum chamber with 1" thick aluminum flanges and a stainless steel frame. The chamber is pumped on by a 1450 L/s turbomolecular pump (Pfeiffer TPH 1801 UP) which is backed by a 25 L/s two stage rotary vane pump (Edwards E2M 80). A stainless steel coaxial metal sieve trap (Nor-Cal) sits between these two pumps to prevent backstreaming of oil from the mechanical pump into the turbopump. This pumping configuration yields base pressures of 2×10^{-8} Torr in the vacuum chamber, as measured with a Bayard-Alpert style ionization gauge. The largest contributor to background pressure is water that leaks out from pores in the metal walls of the chamber, as measured by a residual gas analyzer (SRS RGA200). This RGA is mounted into the vacuum chamber with a mass selection range of 1-200 amu, which is useful for not only monitoring background gas concentrations but also observing and characterizing the evaporation from liquids in the chamber. Additionally, the RGA can serve a leak detector for the vacuum chamber, by externally passing a gas like helium along the flanges and monitoring the m/z = 2 peak.

The molecular scattering geometry and spatial configuration of LIF detection are illustrated in Figure 2.11. The incident molecular beam passes through a 3 mm skimmer (Beam Dynamics) 5.3 cm downstream from the pulsed valve. This collimated beam then travels another 8 cm before striking the liquid surface at a 45º angle, with a 1º half angle divergence. These geometric parameters result in a 1.1 cm x 0.8 cm spot size of incident NO molecules hitting the liquid surface (i.e. well within the 4 cm x 2.4 cm available area). The alignment of the pulsed valve with respect to the liquid surface can be checked by replacing the pulsed valve with a coaxial laser pointer, to ensure the beam passes through the skimmer and lands at the center of the liquid reservoir. The pulsed valve and liquid surface are mounted on an 80/20 structure within the vacuum chamber,[1] with the pulsed valve on a rotatable piece that allows variation of the incident molecular beam angle with respect to the surface. Additionally, this arm can be

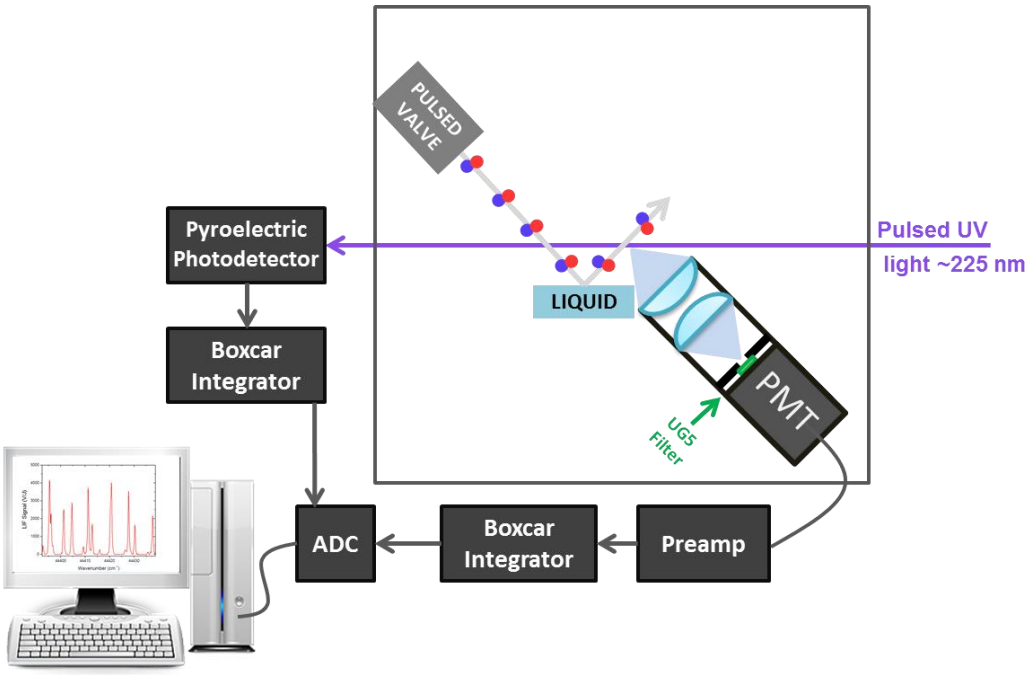

Figure 2.11 Detection of LIF signal, which is measured on a photomultiplier tube and normalized to the laser energy, as measured by a pyroelectric photodetector. Note that the axis of the detection lens and PMT is actually oriented normal to the scattering plane.

rotated so that the pulsed valve is directed toward the LIF detection spot within the chamber, enabling quantum state resolved LIF characterization of the incident beam.

The pulsed UV laser passes 1.6 cm above the surface and in the plane of specular scattering, exciting all NO molecules in its path. Excited NO molecules fluoresce down to the ground state, but only fluorescent photons from NO in a 4 mm section of the laser beam at the center of the chamber are detected and imaged onto a photomultiplier tube (PMT). The PMT sits in an aluminum tube extending into the vacuum chamber, with a viewing axis perpendicular to the plane of specular scattering. Directly in front of the PMT lies a 4 mm pinhole mask and beyond that a 1:1 imaging setup with two plano-convex silica lenses (diameter and focal length = 5 cm) with one lens forming the vacuum seal. This spatial filtering allows only NO in the scattered flux at a specified scattering angle to be detected and prevents NO in the incident beam, which the laser beam also passes through, from contaminating signal of scattered NO. In order to block stray photons in the visible, as well as incident laser light, there is a 4 mm colored glass UV bandpass filter, (240 - 395 nm, UG5 filter, ThorLabs) between the pinhole mask and the PMT. The fluorescent photons are also in the UV and are mostly redder than the initial laser pulse, as illustrated in Figure 2.12. The transmission spectrum of this filter is graphed in Figure 2.12, in addition to the transition probabilities, or Franck-Condon factors, of the fluorescence spectrum from $A^2\Sigma^+$ (v' = 0) to $X^2\Pi$ (v''= 0 – 10).[13] The strongest Franck-Condon factor occurs at $A^2\Sigma^+(v = 0) \rightarrow X^2\Pi$ (v = 1), which is due to the shorter equilibrium N-O bond length in the $A^2\Sigma^+$ state relative to the $X^2\Pi$ state. Plotting these two quantities together reveals that the filter blocks ~90% of the incident laser light and, by summing over the transmission of all vibrational states, transmits ~ 60% of all fluorescent photons.

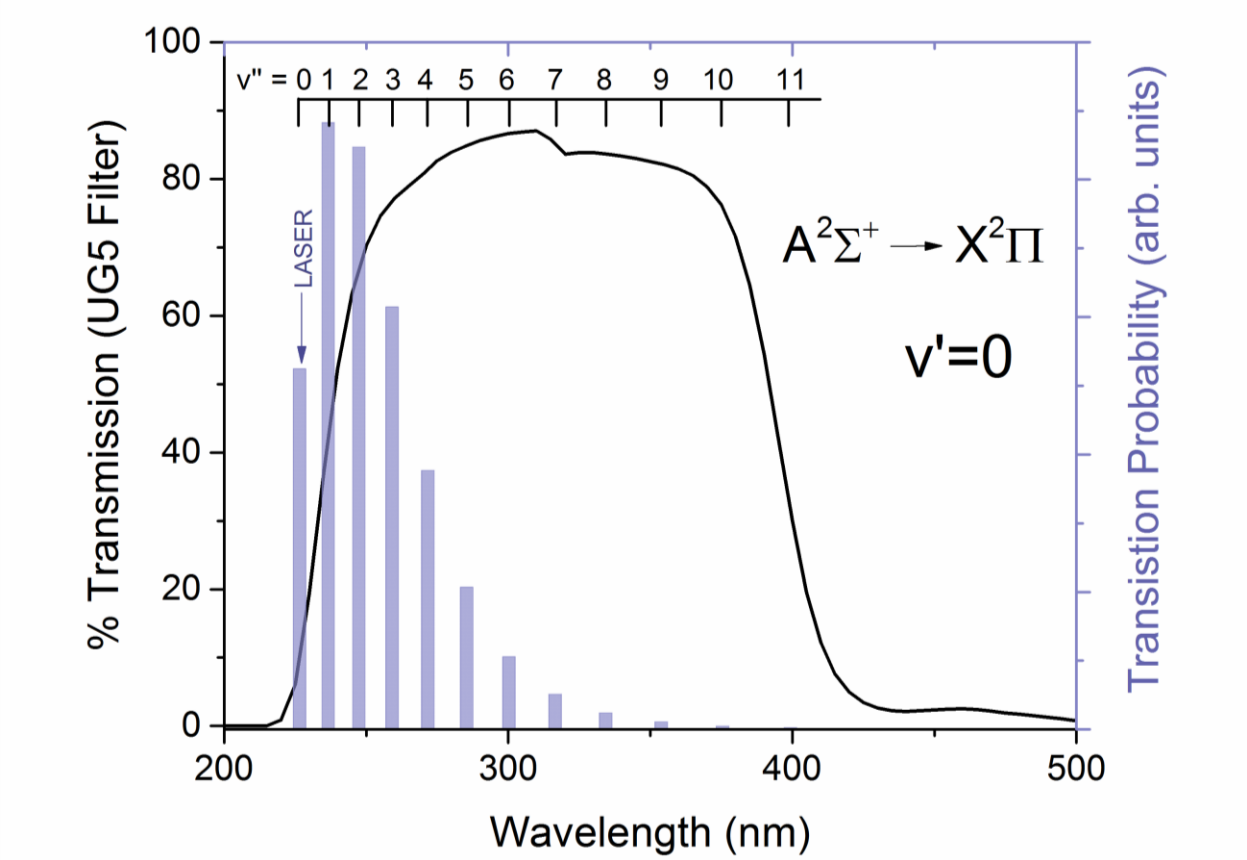

Figure 2.12 Transmission spectrum of the UG5 filter and transition probabilities of fluorescence from $A^2\Sigma^+(v'=0) \rightarrow X^2\Pi(v'')$. The filter transmits 60% of all fluorescence and blocks 90% of the incident laser light (~225 nm). The width of the fluorescence bars for each v" state is representative of the wavelength range for each rovibronic spectrum.

The PMT is set up to image fluorescence from the center point of the vacuum chamber. Therefore, in order to measure different scattering angles, the entire scattering apparatus within the chamber must be moved. The pulsed valve, skimmer and liquid surface within the chamber can be horizontally translated along the axis of the laser to allow detection of a variety of scattering angles. The scattering apparatus can also be translated perpendicular to the plane of specular scattering in order to image off axis scattering, although this degree of freedom has neither been explored in current nor previous thesis work.

Figure 2.13 shows the scattering geometry for studies where the scattered molecules are detected at θ_s = -60º, -30º, 0º, 30º, 45º and 60º. There is a finite range of scattering angles corresponding to each of these experimental conditions due to the detection volume and the spot size of the molecular beam hitting the surface. The geometric limits for scattering angles detected around θ_s = 45º, ranging from a minimum of θ_s = 36º and a maximum of θ_s = 56º, is illustrated in Figure 2.14(a) where all angles are measured with respect to the surface normal. Figure 2.14(b) shows the contribution of all scattering angles for a given experimental configuration. These angular distributions can be estimated by calculating all straight line trajectories from the incident liquid surface to the LIF detection focal volume. The uncertainties in these angles, θ_s = -60(3)º, -30(9)º, 0(12)º, 30(9)º, 45(6)º and 60(3)º, represent 1σ standard deviations based on statistical sampling of all these straight line trajectories. These calculations are purely geometric and do not make any assumptions about the angular distribution of the scattering molecules (e.g. cos(θ_s) or otherwise). Though far from competing with the angular

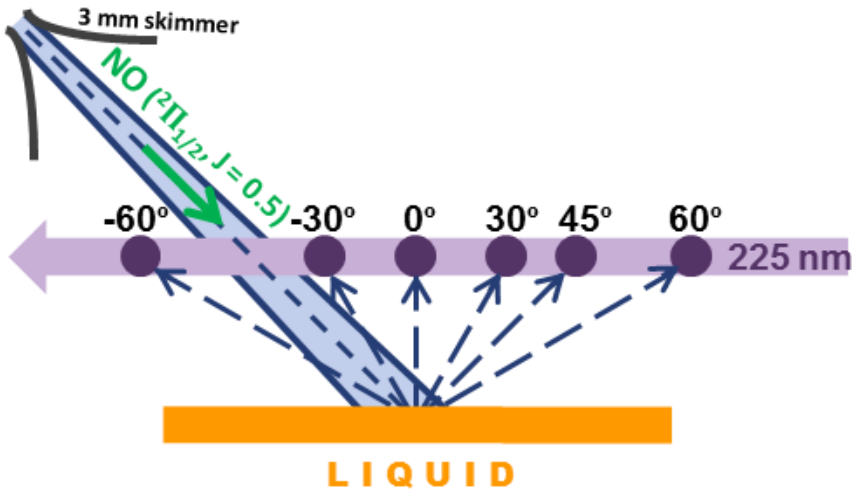

Figure 2.13 Angle resolved molecular scattering of NO at θ_{inc} = 45º and θ_s = -60º, -30º, 0º, 30º, 45º and 60º. The LIF detection setup images a small volume in the center of the vacuum chamber, therefore, in order to image different scattering angles the pulsed valve and liquid surface are translated horizontally along the probe laser axis with respect to the imaging volume.

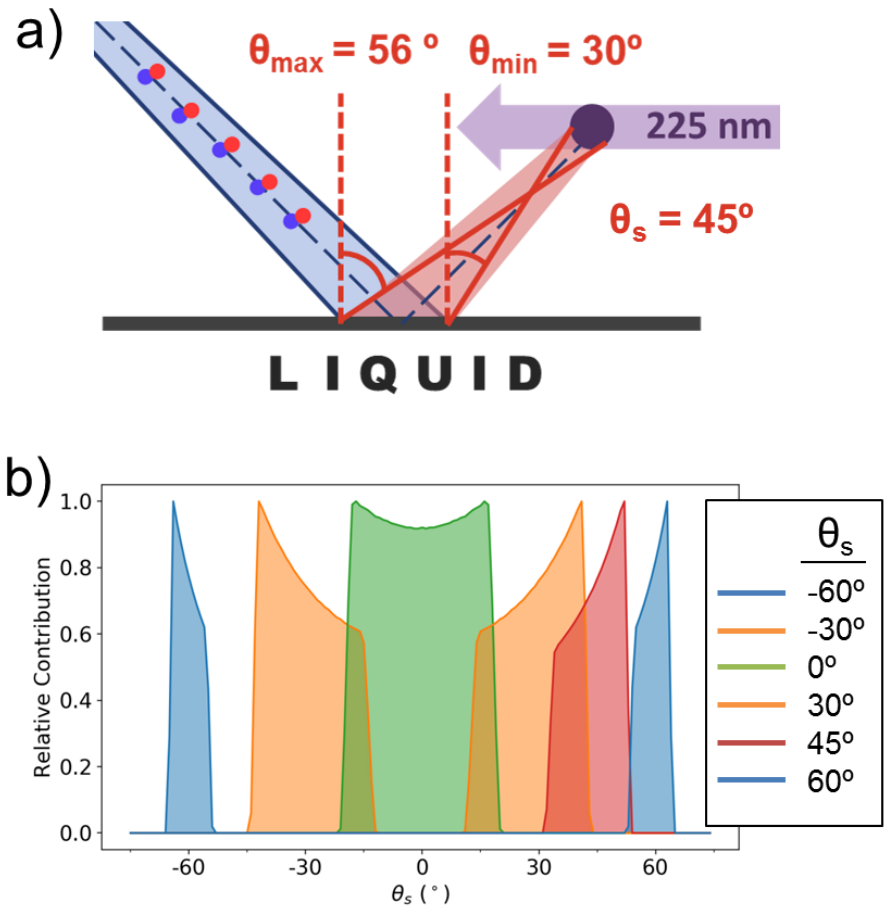

Figure 2.14 a) Range of scattered angles detected at θ_s = 45°, b) Calculated final angle scattering distributions with 1σ standard deviations of θ_s = -60(3)°, -30(9)°, 0(12)°, 30(9)°, 45(6)° and 60(3)° (see text for details).

resolution achievable with flux detection in a rotating molecular beam chamber, this simple spatial filtering scheme nevertheless provides quite useful quantitative angular information on the scattering dynamics (see Chapter 5).

The PMT (Electron Tubes, model 9813QB) has high sensitivity (capable of detecting single photon events), low noise and a fast response (3 ns), making it ideal for fluorescence detection. When a photon strikes the photocathode of the PMT, following the photoelectric effect, it is converted into an electron with 30% efficiency. The bialkali photocathode has a 2" active area diameter and a broad spectral response from 160 to 630 nm. The photoelectrons

generated at the photocathode are accelerated by an electric field toward a series of 14 dynodes set at continuously increasing voltages. At each dynode, a single electron is converted into multiple electrons via secondary electron emission. This avalanche of electrons for a single photon event eventually reaches the anode, where a sharp voltage pulse is produced and measured over a 50 Ω resistor. The electron multiplication from all the dynodes results in a gain of 2.2(0.9) $x10^7$ for a single electron, when the photocathode set is at -2000 V relative to the anode.

The voltage is supplied to the PMT by a high voltage power supply (SRS PS300), with the voltage on the anode that is typically applied for these experiments varying between 1600 and 2000 V relative to the photocathode. Larger voltages yield higher electron gains and thus higher sensitivity, whereas lower voltages are desirable in experiments with strong fluorescence signals to avoid saturating the PMT. Different PMT voltages are often used over the course of a single data scan to maximize the dynamic range of quantum state populations detected. The following conversion factors have been measured and are used to ensure linearity in signal over the course of a scan: 1.0 (V_{PMT} = 2000 V), 3.07 (V_{PMT} = 1800 V), and 12.01 (V_{PMT} = 1600 V). The PMT voltage is then integrated over a 200 ns gate with a boxcar integrator (SRS 250). This module utilizes a gate generator and fast gated integrator to output a voltage that is proportional to the input signal and normalized to the gate width. After the PMT and before the boxcar, both signal and noise are amplified with a 20 dB preamplifier (Mini-Circuits, ZFL-1000LN) to eliminate loss of S/N due to input noise on the boxcar.

All timing of the system is controlled by two digital delay generators, which first trigger the flashlamps and Q-switch of the Nd:YAG laser. The PMT is gated with a boxcar integrator ~ 60 ns after the initial laser pulse to avoid detection of photons from the incident laser. After

passing through the vacuum chamber, the energy of each laser pulse is also gated with another boxcar integrator. An analog to digital converter then delivers these digitized signals to a LabView program ('Definitive Scanner'), with the values saved along with the wavelength for each laser pulse. In addition to scanning the dye laser, this program can also perform scans (at a fixed laser frequency) in the time domain, which is useful for looking at the pulse shape of the incident beam (Figure 2.6) as well as the scattered flux. This function is utilized to choose the optimal time delay setting for the pulse valve, which is selected in order to image fluorescence from the peak signal of scattered NO.

2.6 Data Analysis

The data collection and analysis programs were written by Mike Ziemkiewicz, whose thesis contains more in depth information,[1] the following is a brief overview of these programs and small changes made to them. The 'Definitive Scanner' LabView program outputs data with corresponding laser frequencies, LIF signals (V) and laser energies (J) for each spectral scan. To analyze these data, the LIF background for each spectrum is estimated as a linear correction, based on background measurements from the beginning and end of each scan. The LIF signal is then normalized to the laser power for each data point/laser pulse. If the PMT voltage is varied throughout a scan, the correct conversion factors for each PMT setting must be applied before stitching together the spectrum, which is then smoothed with a Savitzky-Golay smoothing function.[14]

As the dye laser is scanned over the course of an NO spectrum, the frequency reported by the laser can unfortunately vary from the true frequency by up to 0.2 cm^{-1}. Therefore, in order to extract populations from a convoluted NO spectrum with many overlapping peaks, the

frequencies need to be calibrated. This is done with a LabView program 'Frequency Calibration' that uses the known frequencies of NO transitions to perform a linear interpolation/calibration of the laser frequency.[1] This spectrum is then fit to a model with STARPAC nonlinear least squares fitting by a program entitled 'LIFfits'. This program uses the known line positions and absorption coefficients of the NO LIF transitions (from LIFBASE[15]) to fit spectra to a least squares model and extract populations for all rovibronic quantum states populated. This program can be used for analyzing any NO LIF spectrum, notably both $A^2\Sigma^+$ (v = 0) ⟵ $X^2\Pi$(v = 0, v = 1); the only changes required are the wavelength range as well as the input file containing line positions and Einstein B coefficients for all transitions in the region of interest. The 'LIFfits' program outputs populations, up to J = 70.5 (or for however many rotational states are entered into the input file) for all electronic states, $^2\Pi^e_{1/2}$, $^2\Pi^f_{1/2}$, $^2\Pi^e_{3/2}$, and $^2\Pi^f_{3/2}$, within the vibrational state detected, as well as the model fit to the spectrum. An example of the NO $A^2\Sigma^+$ (v = 0) ⟵ $X^2\Pi$(v = 0) spectrum and model fit to the smoothed data is show in Figure 2.15.

The rovibronic populations can be used in two other programs for quick analysis of the rotational and electronic distributions. The program 'Averages' calculates an average rotational temperature for each electronic state and an electronic temperature (where $[^2\Pi_{3/2}]/[^2\Pi_{1/2}] = \exp(-E_{so}/kT_{elec})$ and E_{so} = 123 cm^{-1}). The program 'Double_Exp' fits rotational distributions to a double exponential, or two-temperature Boltzmann fit, which physically represents the TD and IS scattering pathways:

$$P_{TD/IS} = \frac{(2J+1)e^{-E_{rot}/kT_{rot}(TD/IS)}}{Q_{rot}(TD/IS)}$$

$$Pop_J = [\alpha * P_{TD}(J) + (1-\alpha) * P_{IS}(J)] \quad (2.2)$$

Here, $\alpha = P_{TD}/(P_{TD} + P_{IS})$ is the branching ratio into the TD channel, $P_{TD/IS}$ represents the respective fractions of the TD and IS component for a given rotational state, and Q_{rot}(TD/IS) is

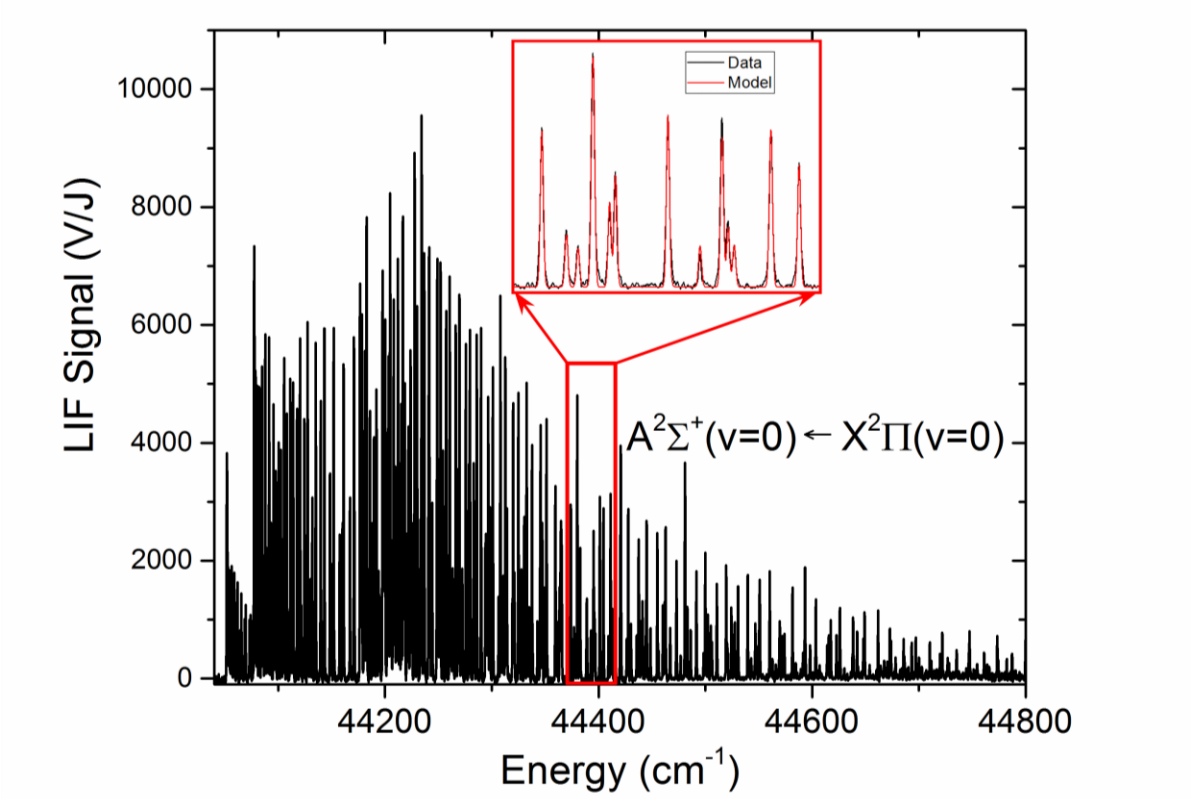

Figure 2.15 Sample LIF spectrum of scattered NO($^2\Pi_{1/2}$, v = 0) and the least squares model fit.

the canonical partition function defined by the rotational temperature. This program allows all parameters (T_{TD}, T_{IS} and α) to be fixed or floated, and the most recent version 'DoubleExp2013', allows different T_{TD} values to be fixed at separate temperatures for the two spin-orbit states, while the lambda-doublet states within each spin-orbit state are kept the same.

In order to evaluate the capability and accuracy of this analysis and LIF detection, a room temperature scan of NO thermalized in the vacuum chamber has been measured. This is done by detecting fluorescence of NO just *before* the pulsed valve fires, so that instead of imaging jet-cooled NO molecules freshly scattered from the liquid surface, NO molecules that have bounced around the vacuum chamber and completely thermalized to room temperature are detected. The Boltzmann rotational distributions of thermalized NO are shown in Figure 2.16, with a global fit

to all four electronic states that yields T_{rot} = 295(4) K. This rotational temperature and the spin-orbit temperature, T_{elec} = 298(10) K, are consistent with NO molecules thermalized with a 293 K chamber and corroborate the validity of the analysis routine.

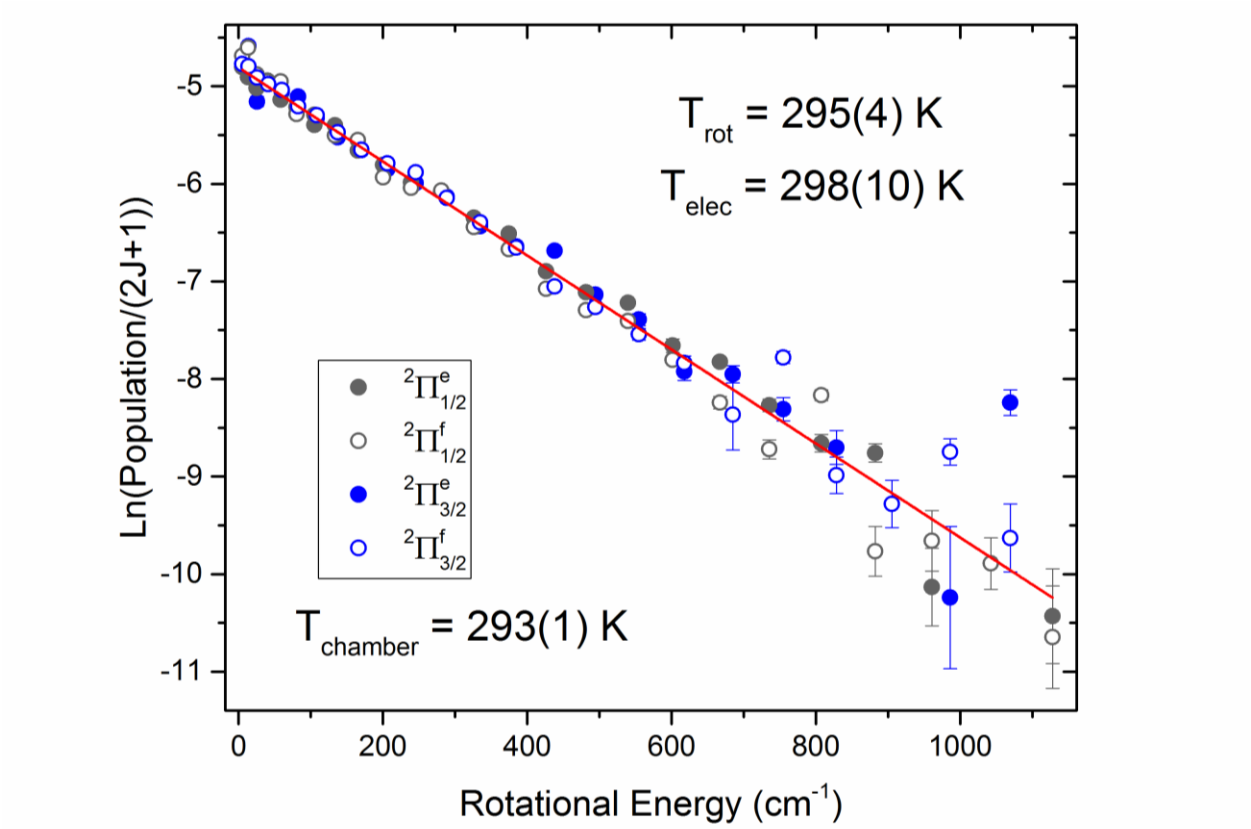

Figure 2.16 Room temperature rotational distributions of NO thermalized with a 293(1) K vacuum chamber. Both the electronic and rotational temperatures are within uncertainties for the chamber temperature, confirming lack of saturation in LIF detection and reliability of the data analysis routine.

2.7 Signal to Noise Estimate

By way of preparation for these experiments, signal to noise calculations are presented for LIF detection of NO scattered from liquid surfaces. In general, there are four numbers needed to calculate the signal of this experiment: (i) number of scattered NO molecules in the detection

volume, (ii) probability of NO being excited by a photon, (iii) fraction of the fluorescence imaged onto the photomultiplier tube, and (iv) the signal of a single photon detected on the PMT. As discussed in Section 2.3, the molecular beam density (NO and buffer gas molecules) at the surface, 13 cm away from the pulsed valve, is 9×10^{12} #/cm^3. Assuming roughly half the molecules scatter specularly, there is a density of 3×10^{12} #/cm^3 15 cm away from the pulsed valve at the detection spot. The detection volume is 0.013 cm^3, which is limited by the width of the laser beam (2 mm) and the 4 mm mask on the PMT. Gas mixtures consist of 1% NO in a buffer gas and approximately 1% of the NO molecules are in a given quantum state, which yields an upper limit of ~ 4×10^6 NO molecules in the detection volume for the rovibronic state being probed.

The probability that an NO molecule absorbs a photon can be calculated with $P_{abs} = 1 - exp(-\sigma * N_{photons}/A_{beam})$. The cross section, σ, is 4.5×10^{-16} cm^2 for a strong line in the spectrum ($P_{21}(1.5 – 3.5)$ bandhead at 44198 cm^{-1}) with an Einstein B coefficient of $B = 6.0 \times 10^8$ m^2/Js and a laser linewidth of 0.4 cm^{-1}. The laser beam operates at ~225 nm and 3 μJ/pulse, with 3.4×10^{12} photons/pulse and an area of ~0.03 cm^2. This yields a ~ 5 % probability that a NO molecule in the detection region absorbs a photon. With fluorescent quantum yields of ~ 1, this means that for 4×10^6 NO molecules, 2×10^5 of these NO molecules in a given quantum state will be excited.

The fluorescence of NO is emitted in 4π steradians, however the position of the imaging lens with respect to the detection volume results in only ~7% of the fluorescence imaged onto the PMT. There are ~5% reflective losses from each surface of the convex lenses, through which 81% of photons are transmitted while only 60% of the fluorescence is transmitted through the UG5 filter (Figure 2.12). Additionally, the 200 ns boxcar gating of the LIF signal, which begins

60 ns after the laser pulse, collects ~47% of the fluorescence based on the 200 ns lifetime of NO. Finally, the photocathode of the PMT has a conversion efficiency of 30%. Totaling all these losses, ≈ 0.5 % of the fluorescent photons are detected by the PMT. For 2 x 10^5 NO molecules excited, we therefore expect ~1 x 10^3 photons on the PMT for one of the highest signal peaks.

A single photon on the PMT results in a ~10 mV signal, which is calculated from $V_{PMT} = geR/\Delta t$, where g is the gain of the PMT, e is the electronic charge, Δt is the 2 ns response time and R is the 50 Ω readout resistor. The signal from the PMT has a width of 3 ns and is detected within a 200 ns gate by the boxcar. Thus, for 1 x10^3 photons detected by the PMT, a 150 mV signal will be measured. While the experiment is running, off peak noise on the PMT is ~300 μV when the anode is set at 1600 V relative to the photocathode. This results in S/N ~ 500 for one of the stronger peaks in the LIF spectrum. On peak noise due to large fluctuations in the gain of the PMT (~40%) is the largest source of noise in these experiments. Rovibronic populations extracted from three data scans are typically averaged together in order to reduce uncertainties for quantum state populations.

2.8 Experimental Changes to Study Hot Metals

In order to study specific metals of interest at hot surface temperatures (T_s > 1000 K), a new heating setup within the chamber was built that is capable of heating the crucible and metal of interest up to 1500 K (and even hotter for metals with low vapor pressures). Additionally, since the vapor pressures of many metals becomes significant near 1000 K, line of sight protection has been installed for the imaging lens and turbopump to prevent evaporating metal atoms from depositing on these surfaces. The melting temperatures and vapor pressures for a number of metals considered for scattering experiments are presented in Figure 2.17.[16, 17] Gold

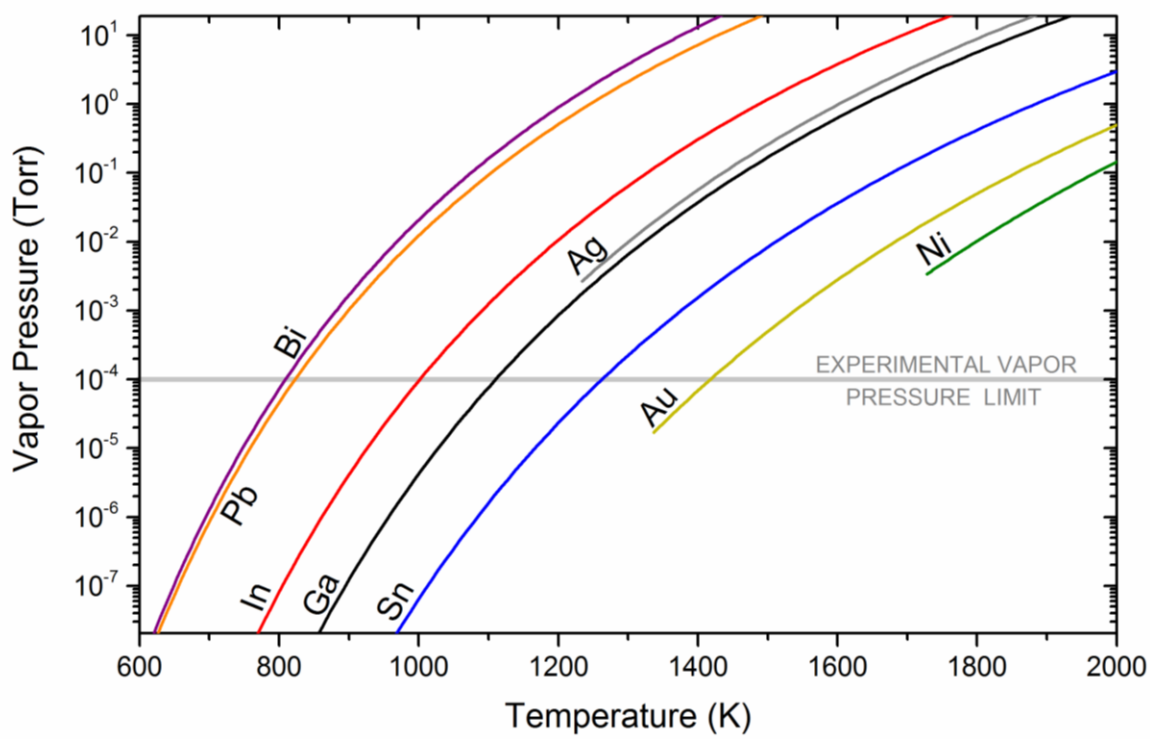

Figure 2.17 Vapor pressures of various molten metals as a function of temperature,[16, 17] where each vapor pressure curve starts at the melting point for a given metal. The experimental vapor pressure limit is set a 10^{-4} Torr to ensure a single collision environment for molecular scattering. Therefore, metals like Ag and Ni are not suitable for molecular scattering experiments in their molten state.

represents one of the more difficult metals to study experimentally, with a melting temperature of 1337 K and a corresponding vapor pressure of 1.5×10^{-5} Torr. Vapor pressures ≤ 10^{-4} Torr, are low enough to allow single-collision conditions for molecular scattering experiments from molten metal surfaces. The following sections discuss the specific experimental changes made to the apparatus to study these hot molten metals.

2.8.1 Resistive Heating Setup

For study of molten metals, the choice of reservoir material is crucially important since many liquid metals like Au and Ga readily amalgamate with other metals at high temperatures. If

a liquid metal were to gradually dissolve atoms of the crucible, this would clearly decrease the purity of the bulk metal and especially the surface of the liquid metal. Tungsten is extremely nonreactive with many metals, including Au and Ga. The Au-Ga equilibrium phase diagram reveals less than 0.128% mixing of tungsten with Au at T_{melt} = 1337 K and the solubility of tungsten in Ga is negligible.[17, 18] In order to prevent metals like gold from wetting, or creeping up and over the crucible walls, an alumina coating is put around the edge of the crucible. Only the sides of the crucible are coated with alumina, which creates a liquid pool with a macroscopically flat liquid surface forming in the reservoir and avoids the formation of metallic droplets/spheres that can form when the bottom of the crucible is also coated. The crucibles used in this experiment are 4" long, ¾" wide, 0.010" thick tungsten pieces with a 1.5" x ½" reservoir that is 1/8" deep and has a 0.005" alumina coating on the edge of the reservoir (S21-AO-W, R.D. Mathis). This ensures a large enough liquid metal surface area with respect to the 1.1 x 0.8 cm^2 spot size of the incident beam hitting the molten metal surface.

The new heating setup heats metal samples via resistive heating, whereby a heating element, in this case a tungsten boat, is heated by passing an electric current through it. The power delivered to the heating element is $P = I^2 * R_{boat}$, therefore all other cables and connections in this circuit are designed to have minimum resistances to ensure maximum power is delivered to the crucible. The tungsten crucible has a 7.2 mΩ resistance, and requires roughly 300 W of power to heat up to 1473 K (as quoted by R.D. Mathis). The power supplied to this circuit comes from a 4 kW, high current, low voltage power supply (LV400, R.D. Mathis), which can output up to 0-5 VAC at 800 A. The power supply is connected by 7.7 awg, 500 A rated cables to two 1" solid Cu feedthroughs (RD Mathis, RDM-FT-400). These feedthroughs are each attached to two 1" x 1/8" Cu bars (oxygen free Copper, alloy 101) which rise 8" above the feedthroughs and

sandwich the tungsten boat, overlapping 1” of the boat on each side, as shown in Figure 2.18. This particular setup is situated to detect specularly scattered molecules at $\theta_s = 45^o$. However, in order to vary the scattered angle observed by the PMT, new copper bars would simply need to be machined to translate the liquid surface with respect to the detection volume (as was done with the previous setup and discussed in Section 2.5).

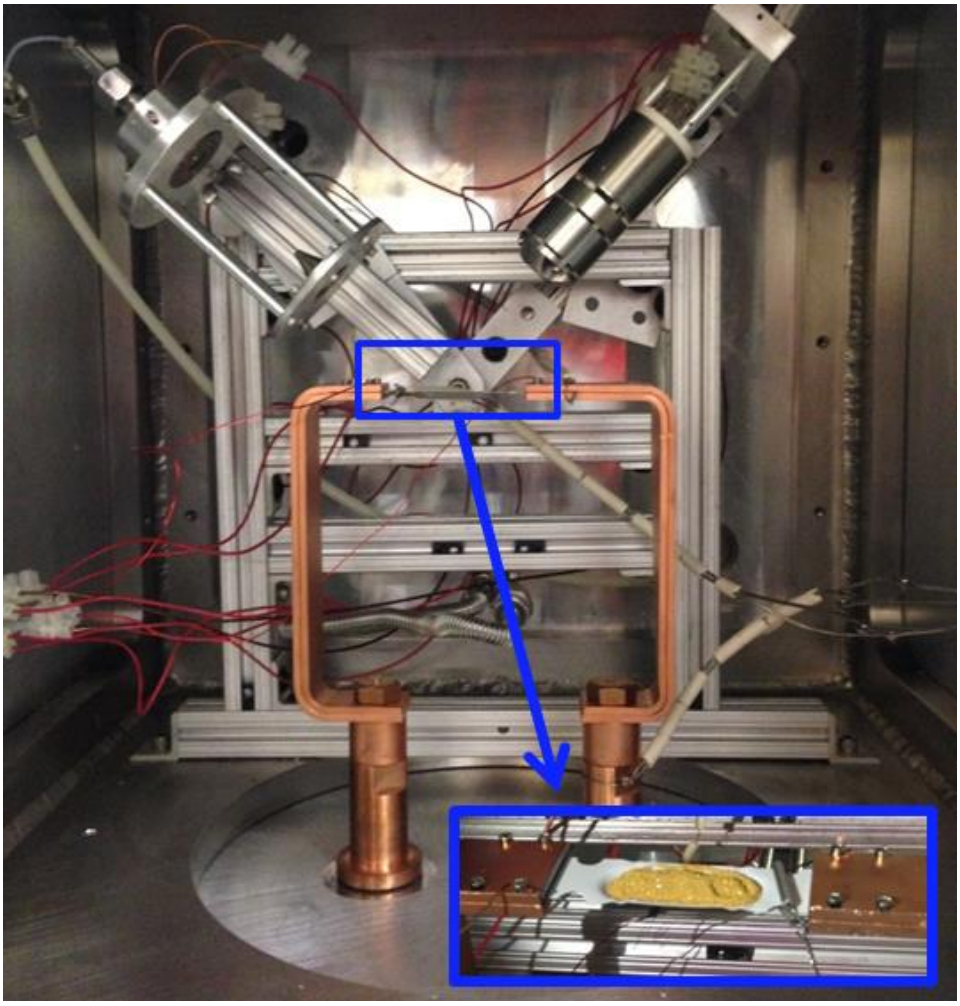

Figure 2.18 Molten metal resistive heating setup. A 4kW, high current, low voltage power supply is connected through the Cu feedthroughs and bars to the boat holding the metal sample (powdered gold pictured). The crucible is made of tungsten with an alumina coating on the edges of the reservoir.

This heating circuit can be modeled as resistors in series, with the resistance of the power supply, feedthroughs, copper bars, evaporation boat and the connections between all of these elements. These resistances total to R_{tot} ~8.2 mΩ, where the power supply impedance is estimated at 1 mΩ, $R_{feedthru} \approx 3$ μΩ, $R_{Cu\ bars} \approx 13$ μΩ, $R_{boat} = 7.2$ mΩ at $T_{boat} = 1473$ K. In order to heat an empty evaporation boat to 1473 K, the company that manufactures these crucibles (R.D. Mathis) states that 313 W need to be delivered to the boat with a voltage drop of 1.7 V across the boat at 212 A. For these numbers, 0.12 W will be delivered to each feedthrough and 0.60 W will be delivered to each set of Cu bars. Based on the mass of these Cu elements, their heat capacity and the amount of power delivered, the Cu feedthroughs (uncooled) of will heat up ~ 2.5 K/hour and the Cu bars will heat up ~ 50 K/hour. However, due to residual gas conductance from the copper bars, black body radiation cooling, and cooling to the vacuum flange, this heating rate is an upper limit.

The resistances of these materials also change with temperature. For example, the resistance of the tungsten evaporation boat at 1473 K is 7.2 mΩ. The resistivity of tungsten (5.6×10^{-8} Ωm) and its temperature coefficient ($\alpha = 0.0045/^{o}C$) can be used to calculate the resistance of the evaporation boat at other temperatures: $R_{W\ boat}(1333\ K) = 4.96$ mΩ, $R_{W\ boat}(1300\ K) = 4.05$ mΩ and $R_{W\ boat}(300\ K) = 1.15$ mΩ. Therefore, as the tungsten boat gets hotter, its resistance increases and a larger fraction of power is delivered to the evaporation boat relative to the other components. The resistivity of the Cu elements will also grow slightly as they warm, but these changes will be negligible with respect to the total resistance of the circuit.

At high temperatures, there will also be significant conductive and radiative heat loss from the system. Conductive heat loss is calculated by, $q_c = -kA\Delta T/\Delta x$, where k is the thermal conductivity, A is the cross sectional area, and ΔT is the change in temperature along the

direction of heat flow of length Δx. The conductive heat loss from the tungsten boat will occur on both sides through each set of Cu bars, which have a cross sectional area of 1.6 cm^2 and are 25 cm long. For a temperature gradient from 1337 K to 300 K, ~60 W will be dissipated on either side of the Cu bars. Additionally, the power dissipated by the alumel and chromel 4 awg wires of the Type K thermocouple is inconsequential at less than 1 W at 1337 K. Thermal radiation represents another source of heat loss and is calculated by, $q_{rad} = \sigma\varepsilon A(T^4)$, where σ is the Boltzmann constant, ε is the emissivity of the surface, A is the surface area, and T is the temperature. For a 25 cm^2 surface area tungsten boat with 0.04 emissivity at 1337 K, 18 W of power is radiated. For Cu heated to ~600 K, with 260 cm^2 surface area and 0.03 emissivity, 5 W of power is radiated. While these radiative heat losses seem small in comparison to conductive power losses, radiative heat loss can rapidly dominate with increasing surface temperature as q_{rad} grows with T^4.

There are wires secured to each Cu feedthrough and on both sides of the evaporation boat that are connected to voltmeters outside the chamber. This enables the measurement of the voltage drop from each Cu feedthrough across the Cu bars to the evaporation boat, where minimal voltage drop is expected and required in order to deliver maximum power to the evaporation boat. Additionally, the voltage drop across the tungsten boat can be measured and monitored. As the potentiometer on the power supply is turned up, the voltage drop across the feedthroughs and Cu bars remains low and relatively constant, between 20 to 30 mV, while the voltage drop across the boat increases significantly. When the tungsten boat is filled with gold and heated to 1400 K, a voltage drop across the boat of V_{boat} = 490 mV is measured with a current of 136 A (67 W). The amount of power required to heat this system to such temperatures is significantly less than what is quoted by the company who manufactures both the evaporation

boats and the power supply, even though their numbers are quoted for a slightly hotter temperature at 1473 K and for an empty boat. This could be due to better base pressures in our vacuum chamber ($P_{chamber}$ ~ 2 x 10^{-8} Torr), where less power is lost via gas conductance.

A final consideration is the thermal expansion of Cu during heating. If the copper bars are heated to 600 K, their thermal expansion in height would be < 1 mm. While this will lead to a slight change the scattered angles of NO detected, these differences are small in comparison to the range of angles detected at $\theta_s = 45(6)^o$.

2.8.2 Temperature Measurement

A number of possible methods have been considered for measuring the temperature of molten metals with temperature ranges from T_S = 293 to 1400 K. Bare type K thermocouples, which have an upper temperature limit of 1523 K, have been submerged in the puddle of molten gallium. Temperature measurements were made up to ~ 1100 K, at which temperature the gallium had fully corroded the thermocouple (Figure 2.19(a)). A Type K thermocouple was also placed in a ceramic thermowell, where the thermocouple was positioned in a close-fitting hole drilled in an alumina block. Alumina does not deteriorate when put in contact with these metals as it is used in the evaporation boats to prevent wetting; however, since alumina repels molten metals like gallium and gold, that also leads to poor, irregular thermal contact between the metal and thermowell (Figure 2.19(b)). These thermowell measurements were calibrated against a bare Type K thermocouple submerged in the metal, which showed the thermowell temperatures to be ~100-200 K colder than the metal itself. Optical pyrometers were also considered, but again presented a few problems, the first being that there are no windows on the vacuum chamber. Only the imaging lens in front of the PMT can be used as a viewport into the chamber when the

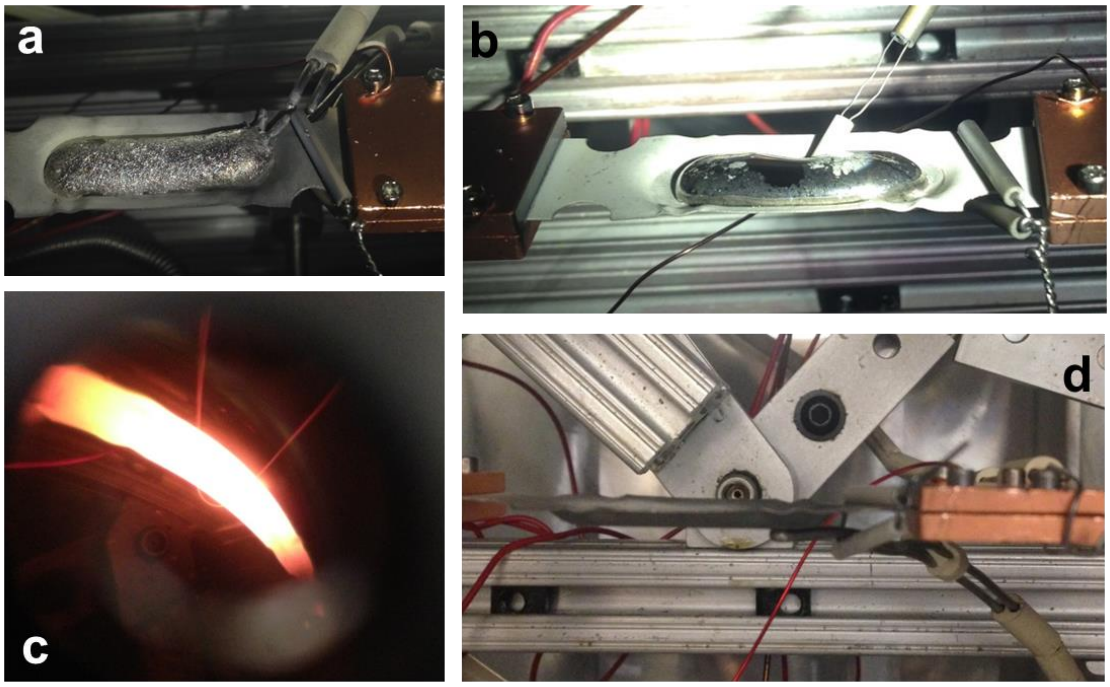

Figure 2.19 Various temperature measurement methods of the evaporation boat: a) Bare type K thermocouple immersed in and corroded by liquid gallium, b) Type K thermocouple in alumina thermowell, which is repelled by the liquid gallium, c) optical pyrometer calibration through the imaging tube and lens, and d) Type K thermocouple pressed against the bottom of evaporation boat.

experiment is not running. Therefore, in order for an optical pyrometer to have visual access to the liquid surface, it would need to be inside the chamber, possibly with a fiber optics bundle. This bundle would need to be directed toward the surface and near the surface, which would mean it would not only get hot and but it would be coated in evaporating metals, thus rendering the instrument unable to measure radiative photons. Furthermore, optical pyrometers only work at temperatures above 1040 K, which would severely limit the ability to study scattering dynamics at lower temperature ranges.

Ultimately, the temperature measurement solution is that a Type K thermocouple has been secured to the bottom of the crucible (Figure 2.19(d)), which can be calibrated against these

other temperature measurements and serves a secondary standard. This thermocouple is in good thermal contact with the boat on one side but exposed to vacuum on its other side, leading to cooler temperatures than the crucible and its molten metal contents. Attempts were made to spot weld a strip of metal over the thermocouple onto the boat to maximize thermal contact, however, tungsten is difficult to spot weld and these attempts were not successful. This thermocouple on the evaporation boat has been calibrated against (i) optical pyrometer measurements of an empty boat through the imaging lens (Figure 2.19(c)) and (ii) a bare Type K thermocouple submerged in the metal. The observed temperatures plotted in Figure 2.20 represent measurements from multiple samples over the course of a week. The thermocouple on the boat has a reliable linear relationship with respect to the true temperature of the hot metal and evaporation boat, which allows a consistent measurement of the liquid metal without interference or contamination. Over the course of a 2 hour scan for a full spectrum, the temperature on the boat thermocouple will vary within ± 5 K. Propagation of uncertainty for these temperature fluctuations combined with standard errors in the linear fit in Figure 2.20 lead to uncertainties of 35 K for a 1083 K surface temperature.

Thermocouples are also placed throughout the chamber to monitor heating of other elements to make sure O-rings and other important experimental components are not overheating. Type K thermocouples have been placed (i) in the imaging tube next to the PMT, (ii) on the copper bars sandwiching the tungsten boat, and (iii) on the copper feedthroughs in vacuum. Additionally, a handheld infrared thermometer has been used to monitor the temperature of the vacuum flanges and the exterior portion of the copper feedthroughs to verify that the O-rings (Viton is rated up to ~ 200ºC) and insulating teflon spacers (T_{melt} = 327ºC) on the copper feedthroughs remain thermally unstressed.

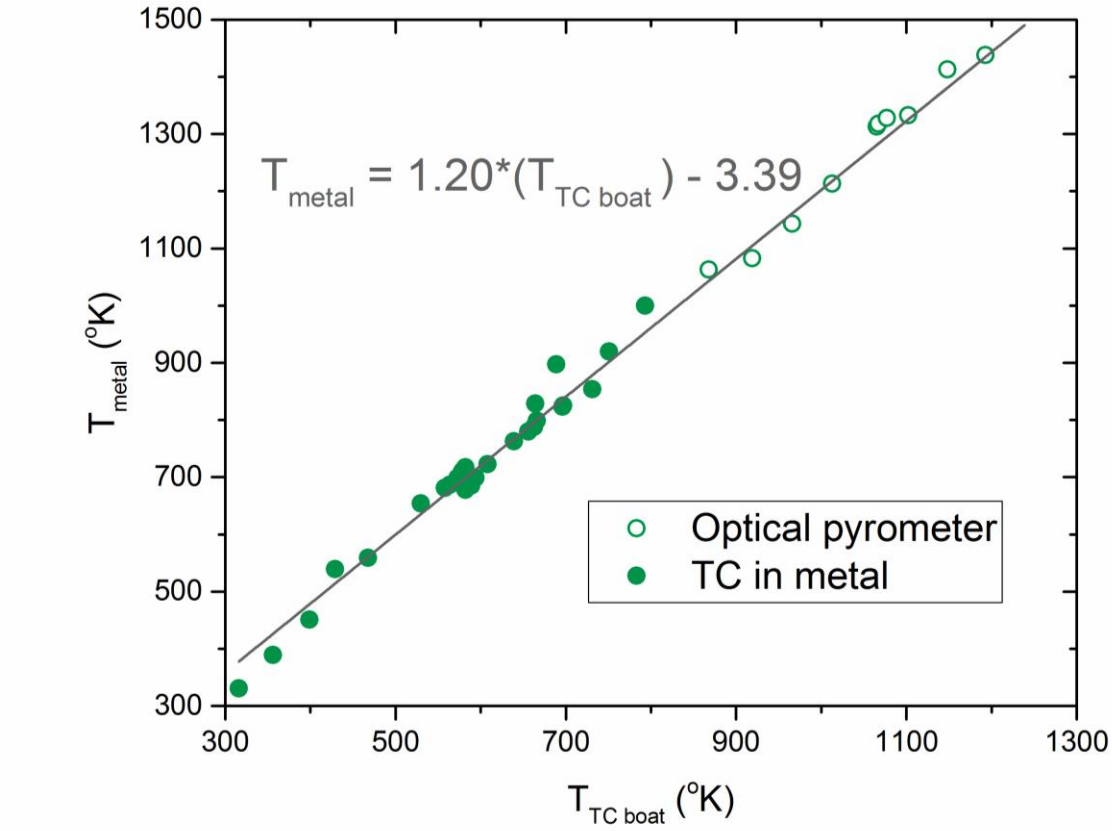

Figure 2.20 Correlation of temperature measurements for molten metals in a tungsten boat. T_{metal} represents the true temperature of the metal and evaporation boat, which is measured either with a bare thermocouple in the molten metal (for T < 1000 K) or with an optical pyrometer for (T > 1100). This is plotted against temperatures from a thermocouple on the bottom of the tungsten boat, called $T_{TC\ boat}$, which serves as a secondary standard to determine the true metal temperature while running experiments.

2.8.3 Metal Evaporation

The vapor pressure of liquids increase with temperature following the expression $exp(-\Delta H_{vap}/kT)$ and hotter molten Au has a vapor pressure of 1.5 x 10^{-5} Torr at its melting temperature. This vapor pressure is low enough that the mean free paths are still sufficiently large ($\lambda \approx 300$ m) with respect to NO distances traveled to detection, but it also means that many metal atoms will be evaporating and coating surfaces throughout the vacuum chamber, as

depicted in Figure 2.21. The one way flux of Au atoms leaving the surface for this vapor pressure is 4.5 x 10^{15} molecules/cm^2/s, which translates to the evaporation of ~30 monolayer/s for liquid gold densities of 17.31 g/cm^3. The gold sample is several millimeters deep and with these evaporation rates it would take ~34 hours for 1 mm of gold to evaporate at 1337 K. If we examine one point on the surface and integrate the solid angle of evaporating atoms (assuming a cosine distribution), approximately 7% of the evaporating atoms are directed toward the imaging lens. If all these Au atoms were to stick, then the imaging lens would be coated with gold atoms at a rate of ~ 125 monolayers/minute. This would make imaging fluorescence through this lens for spectral scans of 2 hours impossible. Additionally, even if this rate were slower and allowed for transmission of light, it would result in a decrease in signal over time and yield systematic errors in relative intensities over the course of a scan.

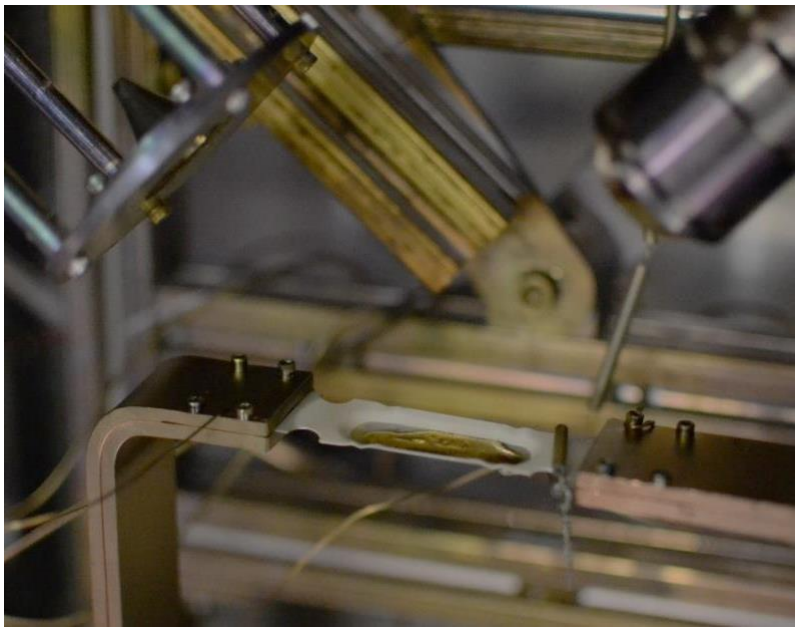

Figure 2.21 Vacuum chamber after molecular scattering experiments from molten gold, which still resides in the tungsten/alumina crucible. High vapor pressures of gold at its melting point result in gold deposition on all line-of-sight surfaces in the vacuum chamber.

As discussed in Section 2.5 and illustrated in Figure 2.11, the fluorescing photons that arrive at the photocathode of the PMT originate from a single spot along the laser beam. A stainless steel cone has been constructed that sits directly in front of the imaging lens (Figure 2.22) and allows all photons of interest, which originate from the detection volume along the laser beam path, to be collected by the PMT. This cone blocks a direct line of sight from the liquid surface to the imaging lens, thus keeping the lens clear for LIF detection when performing scattering experiments from hot metal temperatures with higher vapor pressures.

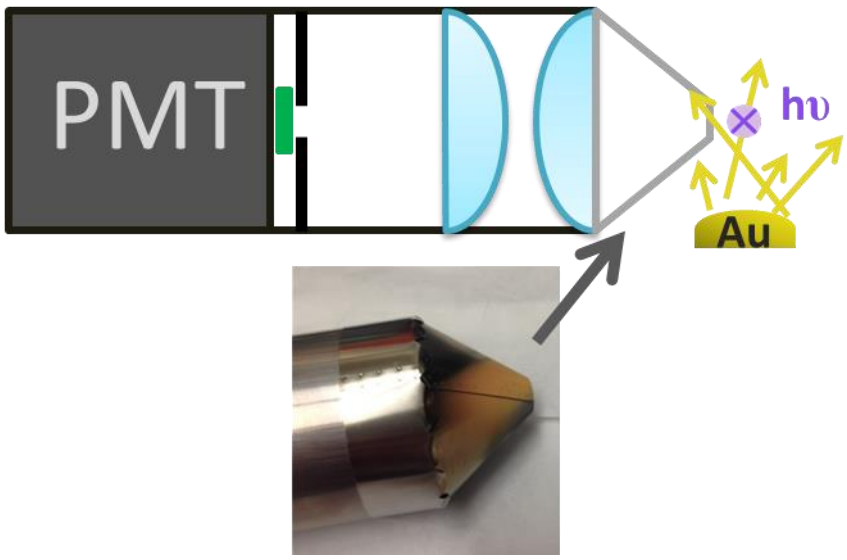

Figure 2.22 A stainless steel cone is placed on the imaging tube to block evaporating metals from coating the imaging lens. As the picture shows, gold has been deposited on the cone, keeping the imaging lens clear for fluorescent detection measurements.

Blackbody radiation from the hot crucible and molten metal grows as T^4, resulting in many stray photons inside the vacuum chamber at high temperatures. Therefore, the cone on the imaging tube not only obstructs metal atom deposition on the lens, but also blocks many of these blackbody photons emitted by the liquid surface and evaporation boat from reaching the PMT. Figure 2.23 displays the transmission of the UG5 filter as well as the spectral distribution of

blackbody radiation at 1400 K. While the peak of the blackbody curve is in the IR (at ~ 2000 nm), there is still a significant amount of radiation in the UV. Figure 2.23 also notes the spectral range of the PMT (from 160 nm to 630 nm), which prevents detection of blackbody photons in the IR, where there is significant transmission in the UG5 Filter, from being converted into signal at the photocathode of the PMT. To estimate the background noise of these photons detected by the PMT that also pass through the transmission filter, we can integrate the blackbody radiation from 240 to 395 nm (where there is ≥ 50% transmission on the UG5 filter)

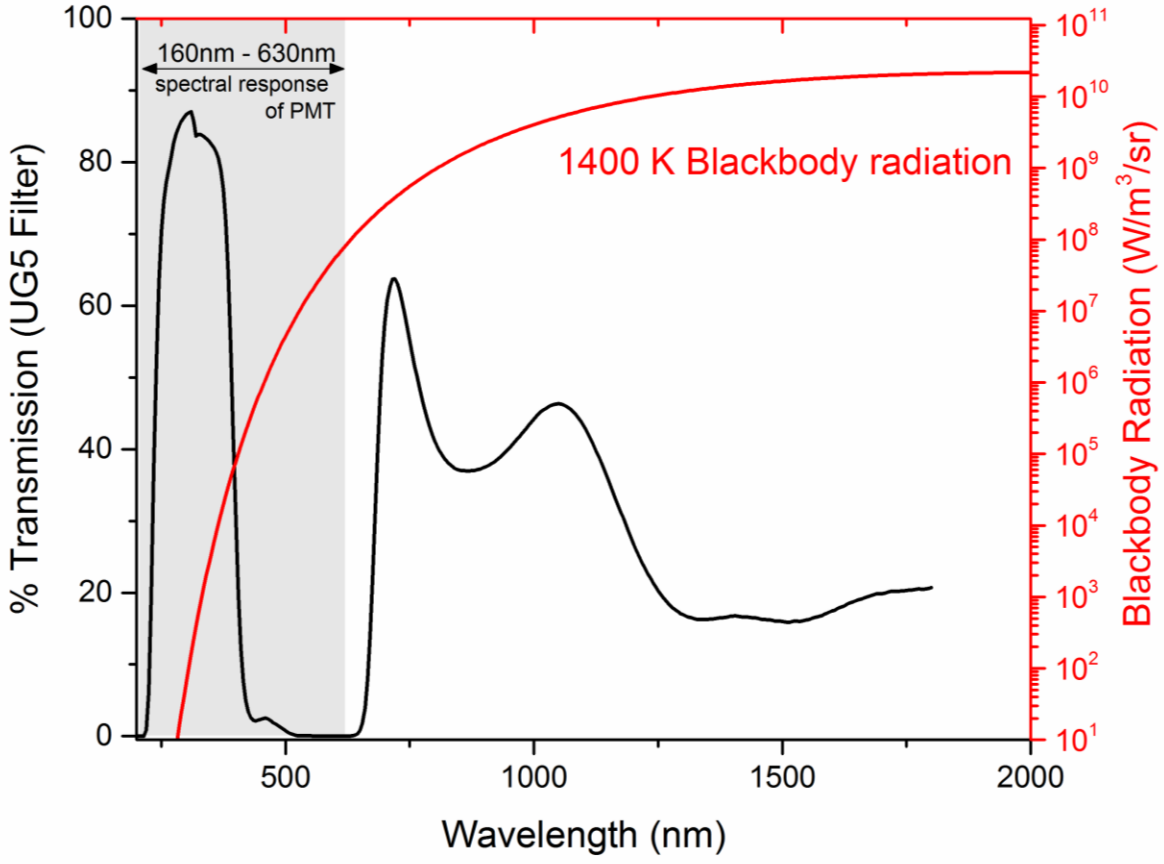

Figure 2.23 A log scale plot of the blackbody radiation spectrum for a 1400 K object (red line) in relation to the transmission spectrum of UG5 filter (black line) and the spectral response range of the PMT (grey shaded region).

for a 200 ns gate, at 1400 K for a 8 cm^2 surface (top surface area of the tungsten boat not covered radiation divided by the power of a single 300 nm photon yields ~ $1.6x10^4$ photons that would by Cu bars), where only ~7% of photons are directed toward the imaging lens. This blackbody reach the photocathode of the PMT for a single laser pulse. These calculations are for a perfect blackbody, whereas emissivities of gold range from 0.05 to 0.47 depending on how polished the surface is. Whether this background is 100 or 10,000 photons, this blackbody radiation represents a significant background for LIF detection that the cone on the imaging lens blocks. While there are still scattered photons present in the chamber, this cone significantly limits those that make it to the PMT.

Within the vacuum chamber, the liquid surface sits directly beneath the turbopump. A metal shield has been placed in the chamber to protect the turbopump blades from getting coated by evaporating metals, which could lead to an imbalance and malfunction of the pump. A circular sheet of aluminum, with the same diameter as the opening of the turbopump (8”), sits ~ 5” beneath the turbopump opening to block a direct line of sight from the liquid surface.

2.8.4 Surface Cleaning

The surface of these metals is cleaned via Ar^+ sputtering (IG2 Model 32-165 RBD Instruments). In this process, the vacuum chamber is filled with 99.995% purity Ar to 4 x 10^{-5} Torr. The Ar ions are generated within a dual filament ionization chamber via electron impact. They are then focused toward the liquid surface target with energies ranging from 0.5 to 2 kV. The Ar^+ beam is produced 5 cm away from the liquid surface and is directed at a 45º angle with respect to surface normal. The Ar ions bombard the surface and impart their momentum to surface atoms, which then have enough energy to escape the surface. This is particularly useful

for cleaning the oxide layer from metal surfaces, notably Ga_2O_3 oxide layers. The metal surfaces are cleaned by operating the Ar^+ sputterer for at least 30 minutes prior to every scan. A decrease in scattered NO signal is observed after the first cleaning for a new metal sample put in vacuum. After this first cleaning NO scattering signals remain constant over time, however, Ar^+ sputtering is continued to ensure NO isn't reacting on the surface by creating an oxide laser over the course of multiple experiments.

2.8.5 Detection of NO(v = 1)

For a thermalized distribution of NO molecules at 1000 K, the following ratios of vibrational states are populated, [v = 1]/[v = 0] = 0.064 and [v = 2]/[v = 0] = 4 x 10^{-3} ($[E_{v=1} - E_{v=0}] = \Delta E_{vib}$ = 1879 cm^{-1}). In order to probe NO(v = 1) with LIF, NO can be excited to either v = 0 or v = 1 of the A electronic state (Figure 2.24). The $A^2\Sigma^+(v = 1) \leftarrow X^2\Pi(v = 1)$ spectrum starts at ~44550 cm^{-1}, which is toward the end of the NO $A^2\Sigma^+(v = 0) \leftarrow X^2\Pi(v = 0)$ spectrum shown in Figure 2.2. Another option for vibrationally excited NO detection is $A^2\Sigma^+(v = 0) \leftarrow X^2\Pi(v = 1)$, which requires an excitation energy of ~ 42200 cm^{-1}. This latter detection scheme is favored since the absorption and emission coefficients are on average 2.7 and 2.3 times larger, respectively, than the former detection scheme. Moreover, not only does this detection of NO(v = 1) have the same emission step as NO(v = 0) detection, making comparisons between vibrational state populations more straightforward, but the $A^2\Sigma^+(v = 0) \leftarrow X^2\Pi(v = 1)$ spectrum also does not overlap with the $A^2\Sigma^+(v = 0) \leftarrow X^2\Pi(v = 0)$ spectrum, which further simplifies the analysis procedure.

A sample NO(v = 1) spectrum, exciting to the $A^2\Sigma^+(v = 0)$ state, is show in Figure 2.25. This spectrum is again fit to a model with the 'LIFfits' program that extracts rovibronic

populations, which then undergo the same analysis as NO(v = 0). The signal to noise on the highest peaks in this spectrum is ~ 30. The NO v = 2 spectrum for $A^2\Sigma^+(v = 0) \leftarrow X^2\Pi(v = 2)$, at ~ 40400 cm^{-1}, has similar transition probabilities as the $A^2\Sigma^+(v = 0) \leftarrow X^2\Pi(v = 1)$ band; however, the v = 2 state is ~ 20 times less populated than the v = 1 state at 1000 K, which puts the largest peaks right at the S/N limit. LIF detection of NO(v = 2) was attempted on the $X^2\Pi(v'' = 2) \leftarrow A^2\Sigma^+(v' = 0)$ transition, however, no peaks were detected in this region. The signal was integrated over wavelength range of expected signal to determine an upper limit for the [v = 2]/[v = 0] population of 1.5×10^{-3}.

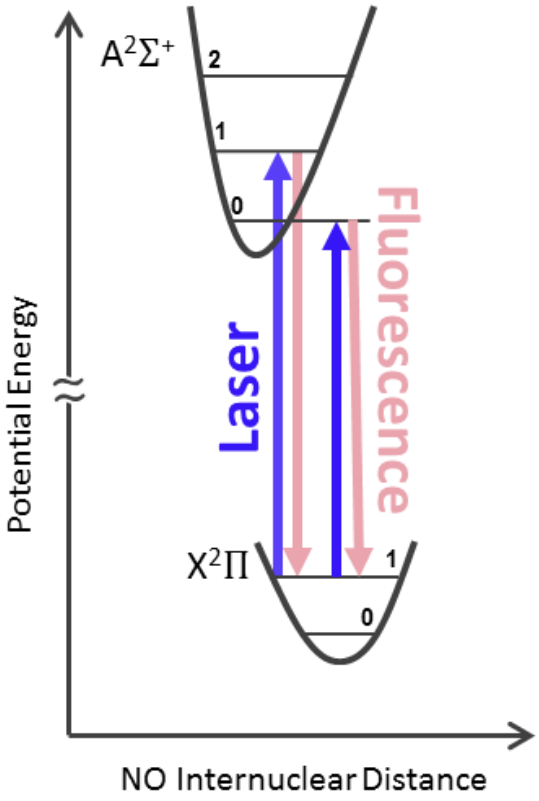

Figure 2.24 LIF detection schemes for NO(v = 1) where a laser beam with energies between 44450 and 45000 cm^{-1} excites $A^2\Sigma^+(v = 1) \leftarrow X^2\Pi(v = 1)$ or energies between 42150 and 42700 cm^{-1} excite $A^2\Sigma^+(v = 0) \leftarrow X^2\Pi(v = 1)$. This latter detection scheme has been used to detect NO(v = 1) since it has stronger transition probabilities as well as an isolated spectrum.

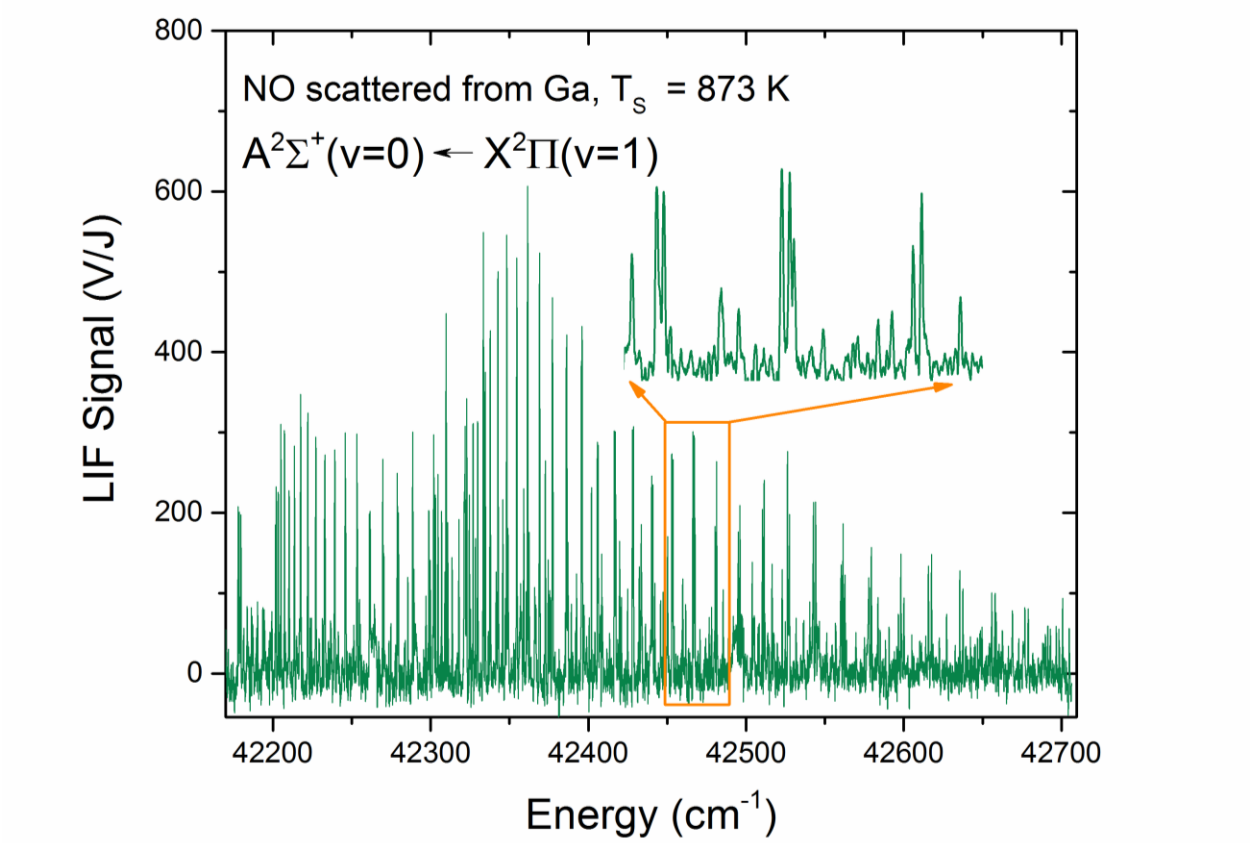

Figure 2.25 NO(v = 1) spectrum with the inset showing representative signal to noise.

A new filter is required in front of the PMT to block incident laser light, which is shifted to lower frequencies for the v = 1 and v = 2 detection. For example, with the current UG5 filter, there is ~40% transmission for $A^2\Sigma^+(v = 0) \leftarrow X^2\Pi(v = 1)$ excitation at 236 nm and ~70% transmission for $A^2\Sigma^+(v = 0) \leftarrow X^2\Pi(v = 2)$ excitation at 247 nm (Figure 2.12). For both of these detection schemes a shortpass filter from Asahi Spectra (XUV0325) is employed. As seen in Figure 2.26, this filter has low transmission for the incident laser light while still collecting 33% of the fluorescence signal.

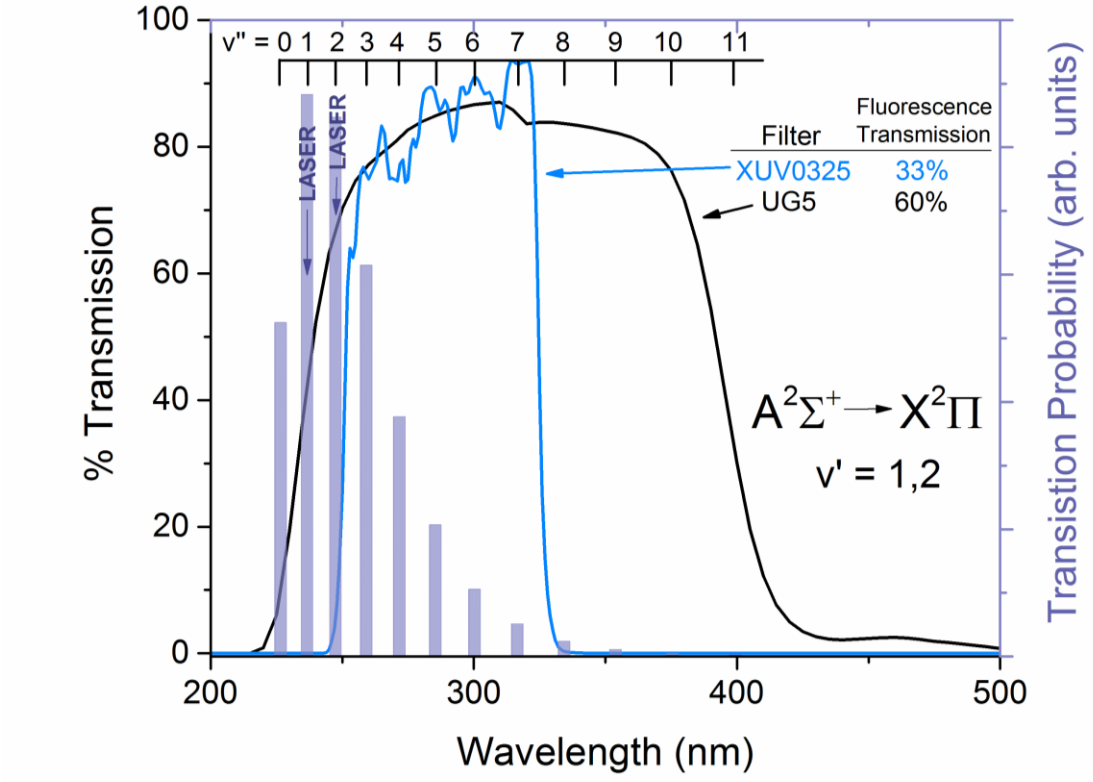

Figure 2.26 Transmission spectrum of the XUV0325 and UG5 filters in addition to transition probabilities of fluorescence from $A^2\Sigma^+(v'=0) \longleftarrow X^2\Pi(v'')$. The XUV0325 is employed for the detection of NO(v = 1) and NO(v = 2), which require incident laser pulses of 236 and 247 nm, respectively, which is blocked by the XUV0325 filter (see text for details). The XUV0325 filter transmits 33% of all fluorescence, roughly half the signal collected from the UG5 filter (the filter used for NO(v = 0) detection).

References for Chapter 2

1. M. P. Ziemkiewicz, *Molecular and Electronic Dynamics in Van der Waals Cluster Spectroscopy, Hydrogen Abstraction Reactions, and Inelastic Collisions at Liquid Surfaces* (Ph.D.). University of Colorado at Boulder, 2012.

2. H. Zacharias, J. B. Halpern and K. H. Welge, *Chem. Phys. Lett.*, 1976, **43**, 41-44.

3. J. Brzozowski, N. Elander and P. Erman, *Phys. Scripta*, 1974, **9**, 99-103.

4. G. Herzberg, *Spectra and Molecular-Structure I. Spectra of Diatomic-Molecules*, Princeton Univ. Press, Princeton, NJ, 1968.

5. M. H. Alexander, P. Andresen, R. Bacis, R. Bersohn, F. J. Comes, P. J. Dagdigian, R. N. Dixon, R. W. Field, G. W. Flynn, K. H. Gericke, E. R. Grant, B. J. Howard, J. R. Huber, D. S. King, J. L. Kinsey, K. Kleinermanns, K. Kuchitsu, A. C. Luntz, A. J. Mccaffery, B. Pouilly, H. Reisler, S. Rosenwaks, E. W. Rothe, M. Shapiro, J. P. Simons, R. Vasudev, J. R. Wiesenfeld, C. Wittig and R. N. Zare, *J. Chem. Phys.*, 1988, **89**, 1749-1753.

6. F. B. Dunning, R. G. Hulet and M. D. Morse, *Atomic, Molecular, and Optical Physics: Atoms and Molecules*, Academic Press, San Diego, 1996.

7. G. Scoles, *Atomic and Molecular Beam Methods*, Oxford University Press, New York, 1988.

8. B. G. Perkins and D. J. Nesbitt, *J. Phys. Chem. B*, 2006, **110**, 17126-17137.

9. A. M. Zolot, P. J. Dagdigian and D. J. Nesbitt, *J. Chem. Phys.*, 2008, **129**, 194705.

10. J. J. Nogueira, S. A. Vazquez, O. A. Mazyar, W. L. Hase, B. G. Perkins, D. J. Nesbitt and E. Martinez-Nunez, *J. Phys. Chem. A*, 2009, **113**, 3850-3865.

11. M. E. King, G. M. Nathanson, M. A. Hanninglee and T. K. Minton, *Phys. Rev. Lett.*, 1993, **70**, 1026-1029.

12. M. Yang, B. Mallick and A. V. Mudring, *Cryst. Growth Des.*, 2013, **13**, 3068-3077.

13. H. Scheingraber and C. R. Vidal, *J. Opt. Soc. Am. B*, 1985, **2**, 343-354.

14. A. Savitzky and M. J. E. Golay, *Anal. Chem.*, 1964, **36**, 1627-&.

15. J. Luque and D. R. Crosley, *LIFBASE: Database and Spectral Simulation (version 1.5)*, Report SRI International Report MP 99-009, 1999.

16. C. B. Alcock, V. P. Itkin and M. K. Horrigan, *Can. Metall. Quart.*, 1984, **23**, 309-313.

17. W. E. Forsythe, *Smithsonian Physical Tables*, Knovel, Norwich, N.Y., 9th rev. edn., 2003.

18. T. B. Massalski and H. Okamoto, *Binary Alloy Phase Diagrams*, ASM International, Materials Park, Ohio, 2nd edn., 1990.

Chapter 3

Non-Adiabatic Spin-Orbit Excitation Dynamics in Quantum State-Resolved NO ($^2\Pi_{1/2}$) Scattering at the Gas-Room Temperature Ionic Liquid Interface*

3.1 Introduction

The surface of a liquid represents an unusually complex and yet intensely relevant nanoscale environment for chemistry, the further elucidation of which is currently one of the major frontier challenges for the chemical physics community. Detailed molecular energy transfer and molecular dynamics at gas-liquid interfaces are crucial to understanding chemical pathways such as i) gas adsorption, accommodation and dissolution into liquids, ii) reactive processing of atmospheric aerosols and iii) heterogeneous gas-liquid catalytic processes.[1-4] Indeed, energy transfer from one molecule to another via inelastic scattering represents a fundamental collisional process that, when coupled with molecular scattering experiments, can yield important insights into both the structure and dynamics of liquid interfaces.[5] The energy transfer between translational, rotational, vibrational and electronic degrees of freedom of a gas projectile and the liquid surface has been probed with the combination of time-of-flight mass spectrometry and universal detection methods. [6-10] Additional information has been obtained at the quantum state level arising from more recent laser-based techniques such as direct IR absorption, multiphoton ionization/velocity map imaging and laser induced fluorescence[11-18]. In

*Published in J Phys. Chem. C, **119**, 8596, (2015)

close conjunction with molecular dynamics simulations[6, 19-22], these experiments have begun to elucidate probabilities for gas molecules sticking, dissociating, desorbing and directly scattering at liquid surfaces. In particular, the synergism between experimental and theoretical efforts has provided substantial evidence for a simple physical picture of *microscopic branching*, whereby incident gas molecules transfer some of their translational energy and can either i) transiently trap on the surface, thermalize and desorb (trapping-desorption, TD), or ii) scatter more or less directly from the surface without complete loss of initial collision conditions (impulsive scattering, IS).[5, 9, 14, 15, 20] Knowledge of such interactions is crucial to developing a better predictive understanding of dynamical processes at gas-liquid interfaces, most notably the kinetics and thermodynamics of adsorption/solvation of gases into the liquid phase.[1, 23, 24]

To both explore and exploit such fundamental understanding, it is particularly useful to have "tunable" solvent systems for study, such as afforded by room temperature ionic liquids (RTILs). As the name implies, RTILs represent a novel class of designer solvents that are liquid at room-temperature and yet exhibit extremely low vapor pressures due to strong cation/anion Coulomb interactions. These molten ionic salts are versatile, green solvents due to their high solubility, low vapor pressures, and chemical and thermal stability. Most importantly, by changing either the cation or anion structure, or even altering a functional group within an ion, the properties of ionic liquids can be tuned to selectively dissolve specific molecules, with an enormous range of potential applications in electrochemistry, biological, analytical, and engineering fields.[25, 26] More specifically, RTILs are being developed for use in fuel cells[27], solar panels[28], electrolytes in batteries[29], drug delivery[30], and a variety of extraction schemes[31, 32]. By way of examples, commercial separation of H_2 from CO in steam gas reformation, or CO_2 sequestration from power plants based on differential solubility in RTIL solvents are actively

being considered,[32-35] for which a detailed understanding of the gas-RTIL interface would obviously be a crucial first step. One parallel direction of keen interest is the investigation of *open shell, radical* systems, which now introduce the role of non-Born Oppenheimer surface hopping between multiple electronic states as well as differential chemical reactivity and even potential prospects for stereochemical dynamics.[36-39]

In order to explore such issues, we have developed novel capabilities for probing internal rovibronic energy distributions of *open shell* NO molecules scattered at the *gas-ionic liquid* interface. Nitric oxide is an open shell radical with nonzero total angular momentum and multiple low-lying electronic states, which allow the electronic degree of freedom in a gas-liquid molecular scattering experiment to be explored. The scattered molecules are probed with laser-induced fluorescence (LIF) in the ground X ($^2\Pi$) electronic state, which is composed of spin-orbit ground ($^2\Pi_{1/2}$) and excited ($^2\Pi_{3/2}$) state manifolds separated by a spin-orbit splitting of $E_{SO} \approx 123$ cm^{-1}.[40] For *low* end-over-end tumbling angular momenta (N), energy differences between NO rotational states ($\approx 2B_{NO}$ N) are small with respect to E_{SO}. Thus, both electron orbital and spin angular momenta are strongly coupled to the NO internuclear bond (i.e., Hund's case (a)), with the total angular momentum projection along the internuclear axis ($\Omega = 1/2, 3/2$) as a good quantum number. Within each spin-orbit state sub-manifold, there are also two weakly split Λ-doublet states of opposite overall parity, which semiclassically correspond to the half-filled orbital either parallel (*e*) or perpendicular (*f*) to the plane of rotation.[41] Most importantly, all four electronic states for each rovibrational NO(v, J) can be independently detected by UV laser induced fluorescence on the A($^2\Sigma$) $\leftarrow$ X ($^2\Pi$) band. This permits exploration of surface hopping between these low lying electronic states arising from collisions at the gas-liquid interface. As will be seen in more detail, this provides an especially interesting molecular probe of electron

dynamics during a collisional event, which can be of particular relevance to liquid systems with high charge densities such as surface anions in ionic conductors like RTILs as well as free electron carrier motion in molten metals.[36, 37]

Recently, a number of experimental and theoretical studies have explored the gas-RTIL interface, with imidazolium-based ionic liquids being of specific interest due to their wide range of applications.[25, 26, 33, 42] One particular focus of such research efforts has been on microscopic surface composition, specifically the relative abundance of anions and cations at the interface, as well as the placement and orientation of functional groups.[16, 17, 22, 43-46] For example, surface tension measurements[43] as a function of bulk composition provided early insights into the synergism between van der Waals, hydrogen bonding and electrostatic interactions at the interface. At a more refined molecular level, the surfaces of these liquids have been probed with nonlinear $\chi^{(2)}$ methods such as sum frequency generation spectroscopy (SFG),[43, 47, 48] which by virtue of phase matching constraints only probes molecules within the first few monolayers of the gas-liquid interface, while rejecting contributions from deeper into the bulk. Similarly, angle-resolved X-ray photoelectron spectroscopy (ARXPS) methods have also been used to explore the composition at the gas-RTIL interface, exploiting angle and kinetic energy resolved escape of electrons into the vacuum from molecules within one electron scattering length from the surface.[44-46, 49]

Inelastic[16, 18] and reactive[6, 12] molecular scattering experiments offer particular advantages in probing only the topmost molecular layer, and which therefore have provided valuable data for molecular interactions at the gas-RTIL interface, as well as help characterize the composition and orientation of molecules present at the surface. For example, hydrogen abstraction scattering methods (e.g., $O(^3P)$ + liquid surface → $OH(^2\Pi)$ or $F(^2P)$ + liquid surface → HF)[6, 12, 50] have

been especially useful in characterizing the presence of alkyl hydrocarbon species at RTIL surfaces, [2, 4, 38] while inelastic scattering experiments can explore interfacial properties via composition dependent energy transfer into internal degrees of freedom of the projectile.[16, 18] In conjunction with theoretical calculations[6, 22], such experiments have shown that alkyl chains on imidazolium cations near the surface act quite hydrophobically and preferentially point into the vacuum. Furthermore, theory predicts a significant thermodynamic propensity for bulky anions to preferentially occupy the topmost layer, which therefore compete with larger alkyl chains for surface sites.[22] This naturally leads to a balance in thermodynamic driving forces between anion size and alkyl chain length for the top surface layer, which in turn can control the degree of hydrophobicity in the gas-liquid interfacial region. Indeed, the relative abundances of anions vs. cations, as well as different functional groups within each of these ions, clearly must influence the energy transfer and collision dynamics for incident gas molecules striking the RTIL surface.

Of particular interest is the potential role of partial electron transfer between interfacial ions and colliding projectiles at the gas-RTIL interface, which could be especially relevant when considering nonadiabatic surface hopping effects in open shell NO + RTIL collision dynamics.[36] RTILs comprise a complex liquid mixture of nevertheless strongly interacting ions, and as a result exhibit interesting surface electronic properties that can be explored using XPS, ultraviolet photoelectron spectroscopy (UPS) and soft X-ray emission spectroscopy (SXES).[51] Because of finite electron scattering lengths, SXES and UPS are both interfacial region-specific techniques that can probe the valence band of liquids with low vapor pressures, which Kanai et al. have exploited to suggest that the HOMO (highest occupied molecular orbital) state in $[bmim]^+[Tf_2N]^-$ is delocalized over *both cation* and *anion* species.[52] Interestingly, this conclusion was found to be anion-dependent over a series of imidazolium-based RTILs. For example, the HOMO and

LUMO (lowest unoccupied molecular orbital) states are thought to be localized primarily on the *cation* for $[bmim]^+[BF_4]^-$ and $[bmim]^+[PF_6]^-$ RTILs, but which contrasts with what has been reported for $[bmim]^+Cl^-$ and $[bmim]^+Br^-$ RTILs, where the HOMO is attributed primarily to the *anion*. Indeed, this would also be consistent with typical *inorganic* ionic liquids like molten NaCl, where the top valence band is localized on the Cl^- anion.[53] However, this also invites comparison with bulky anions such as $[TF_2N]^-$, for which molecular orbital calculations on $[bmim]^+[Tf_2N]^-$ suggest that the HOMO is energetically *higher* than the valence band. This can be rationalized on the basis of the Madelung potential for each ion , e.g., energy level shifts due to electrostatic *destabilization* of the $[bmim]^+$ *cation* molecular orbitals by the surrounding RTIL environment, whereas the molecular orbitals of the *anion* become preferentially stabilized.[52, 54] This is particularly relevant with open shell radical projectiles like NO, for which nonadiabatic effects can play a large role in gas-liquid collision dynamics, with the further intriguing possibility of transient electron transfer amplitude in the interfacial region.

The present work represents a systematic study of quantum state resolved scattering of NO from the gas-$[bmim]^+[Tf_2N]^-$ RTIL interface. The organization of this paper is as follows. In Section 3.2, we provide a brief overview of relevant aspects of the experiment, followed in Section 3.3 by results and analysis on quantum state resolved final rovibronic distributions as a function of (i) incident collision energy and (ii) RTIL surface temperature. As a key observation, we see evidence for strongly nonequilibrium as well nonadiabatic dynamics in the scattered flux, both at low (2.7(9) kcal/mol) and hyperthermal (20(6) kcal/mol) collision energies. This is followed in Section 3.4 by a discussion of possible origins for such nonthermal, surface hopping phenomena. This is aided by preliminary MOLPRO CCSD(T) and multireference calculations of

ab initio equilibrium geometries and well depths for the simple model NO + Cl^- collision system, with summary and conclusions presented in Section 3.5.

3.2 Experimental

A brief description of the experimental setup is described herein, with more thorough descriptions found in previous studies on NO scattering from liquid gallium and imidazolium-based RTILs.[17, 18] A collimated molecular beam of NO is directed at a liquid reservoir and the scattered molecules are detected with rovibrational, electronic spin-orbit and Λ-doublet state resolution. An illustration of the experimental setup is shown in Figure 3.1, where the $[bmim]^+[Tf_2N]^-$ liquid surface displayed is based on quantum mechanics/molecular mechanics (QM/MM) molecular dynamics simulations by Schatz et. al.[22] The incident molecular beam is supersonically expanded from an Even-Lavie pulsed valve (100 μm diameter pinhole, 3000 Torr backing pressure, 80 μs pulse width) and is rotationally and electronically cold; all NO molecules are in the ground spin-orbit state ($^2\Pi_{1/2}$), with equal Λ-doublet populations, and a rotational temperature ≈ 1 K (as shown in previous work[17]), corresponding to ~95% of the NO molecules in the $^2\Pi_{1/2}$, N=0 state. Within the limit of our LIF detection sensitivity (1 part in 10^4), we detect no vibrationally excited NO molecules in the incident beam. The molecular beam is composed of 1% NO/ 99% buffer gas, using H_2 or Ne-70 (70% Ne, 30% He) in order to vary E_{inc} from 2.7(9) up to 20(6) kcal/mol, respectively, with ≤ 1% NO in the buffer gas optimized to eliminate dimer formation. The molecular beam passes through a 3 mm skimmer 5.3 cm downstream from the valve orifice and travels another 8.6 cm to the surface, where the collimated beam strikes the surface at a 45° angle on a 0.8 cm x 1.1 cm area spot size. The gas-liquid molecular scattering

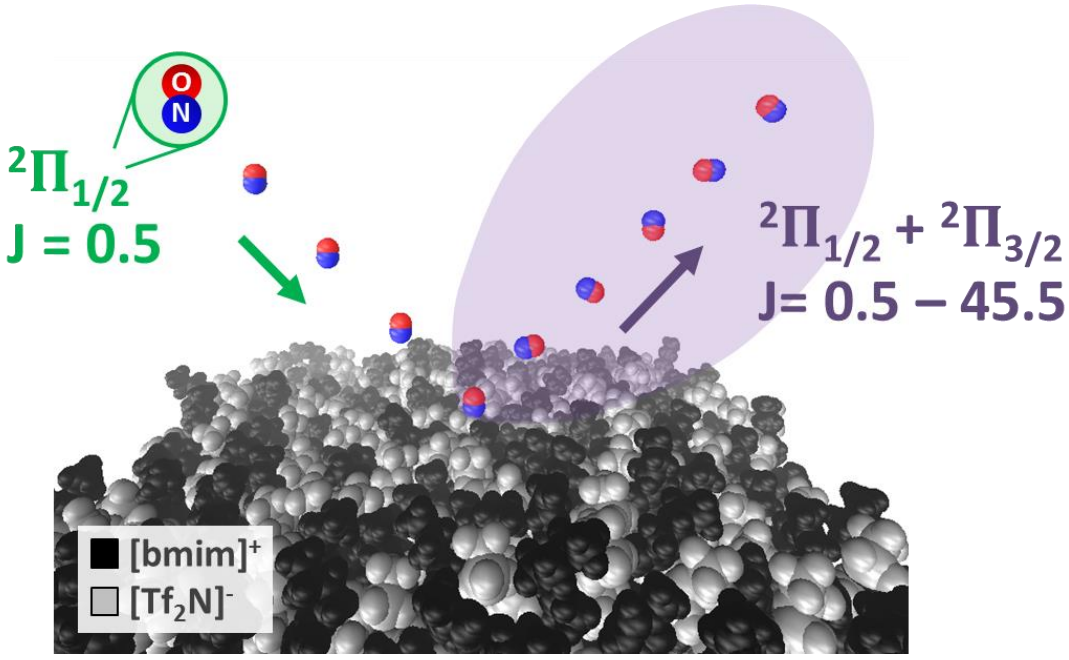

Figure 3.1 Dynamics at the gas-RTIL interface are probed by directing a molecular beam of supersonically cooled NO at RTIL liquid surfaces and detecting scattered molecules with full quantum state resolution. All incident NO molecules are in the ground spin-orbit state ($^2\Pi_{1/2}$) and are rotationally cooled ($T_{rot} \approx 1K$), while rotational levels up to J = 45.5 for both ground and excited spin-orbit states are detected in the scattered molecules after collisions with the surface. The liquid studied is 1-butyl-3-methylimidazolium bis(trifluoromethylsulfonyl)imide (i.e., $[bmim]^+[Tf_2N]^-$), where $[bmim]^+$ and $[Tf_2N]^-$ are shown in black and gray, respectively, in the simulated RTIL interface calculated by Schatz et al.[22]

occurs in a 96 L stainless steel vacuum chamber with a 1500 L/s turbopump, which establishes a base pressure of 2 x 10^{-8} Torr.

Scattered molecules are state-selectively detected using laser induced fluorescence (LIF) by electronically exciting NO molecules via the γ-band ($A(^2\Sigma^+) \leftarrow X(^2\Pi)$) with a UV pulsed laser and imaging the fluorescence back down to the $^2\Pi$ ground state on a photomultiplier tube (PMT). A pulsed UV light source is generated by tripling the output of a YAG-pumped-dye laser, operating at 10 Hz with LDS-698 dye. The resulting light is ~ 225 nm with 0.4 cm^{-1} line width, with pulse energies ≤ 5 μJ/pulse to avoid saturation of LIF transitions. The range of laser intensities is confirmed against studies of NO room temperature distributions and further

checked for clustering effects by curve of growth measurements. The dye laser is scanned over an 800 cm^{-1} range in order to detect all electronic, spin-orbit, Λ-doublet and rovibrational states ($J \leq 45.5$) significantly populated. The fluorescence signal on a PMT is electronically gated in time and normalized to the laser energy for each pulse. The laser beam runs parallel to the surface (1.6 cm above the surface) and in the plane of specular scattering, and is delayed approximately 200 μs (varies with E_{inc}) in time with respect to the gas pulse, which is chosen so that molecules are detected at the peak of the scattered NO signal. A 1:1 confocal lens imaging setup with a 4 mm iris collects the fluorescence for a well-defined volume of scattered molecules (~ 15 mm^3), the size of which is determined by the diameter of the iris and the laser beam width/height. The spot size of the incident gas molecules on the surface, along with the LIF detection volume, results in the range of scattered angles detected at $\theta_s = 45° \pm 10°$, with some preliminary scattering angle studies obtained at normal incidence ($\theta_s = 0° \pm 12°$). It is worth noting that any such fluorescence detection measures the density rather than the flux of scattered molecules, which therefore proportionally underrepresents flux for species with larger velocity components perpendicular to the laser probe direction.

The liquid surface studied herein is $[bmim]^+[Tf_2N]^-$ purchased from Iolitec with 99% purity. The RTIL material was degassed with moderate stirring and heating at ~60ºC for a minimum of 6 hours while being pumped on with a liquid nitrogen cold trap to remove trace amounts of gaseous species. The degassed liquid is placed in a stainless steel crucible with a 4.4 x 2.4 x 0.5 cm^3 reservoir. Resistive heaters can heat the crucible to $T_S \leq$ 900 K, though for $[bmim]^+[Tf_2N]^-$, the accessible range is limited to $T_S \leq 373$ K due to increase in vapor pressure with temperature.[55] Although the bulk of the experiments have been performed for a stationary

liquid surface, the results are consistent with data obtained under conditions where the interface is periodically skimmed *in vacuo* every 5 minutes.

3.3 Results and Analysis

A sample spectrum with typical S/N for NO scattered from $[bmim]^+[Tf_2N]^-$ at E_{inc} = 20(6) kcal/mol is shown in Figure 3.2(a). Each spectrum is modeled with a least-squares fit to Gaussian line shapes and peak populations are determined by integrating over each peak for rotational states up to J = 45.5 for both Λ-doublet states (*e*, *f*) within each of the two spin-orbit states ($^2\Pi_{1/2}$, $^2\Pi_{3/2}$). Since all incident molecules are rotationally cooled into the ground spin-orbit electronic state, the large number of peaks in the spectrum clearly indicates considerable amount of energy transfer taking place with the surface. Sample relative populations as a function of J for each of the electronic states is shown in Figure 3.2(b). Significant differences are observed in the scattered molecules between the two spin-orbit states due to nonadiabatic collision dynamics. By way of contrast, no differences are observed between the two Λ-doublet states within each spin-orbit state, for which we report simple averages unless otherwise stated. Because of possible quantum state dependence in the adsorption behavior, detailed balance considerations yields no *a priori* prediction of the final scattered quantum states. Nevertheless, it is useful for our purposes to construct Boltzmann plots for populations vs. i) rotational state and ii) incident beam energy.

3.3.1 Low E_{inc} Rotational Distributions (E_{inc}= 2.7(9) kcal/mol)

The data at low incident energies (E_{inc} = 2.7(9) kcal/mol) can be quite well described by linear, single temperature Boltzmann plots, consistent with most NO molecules undergoing

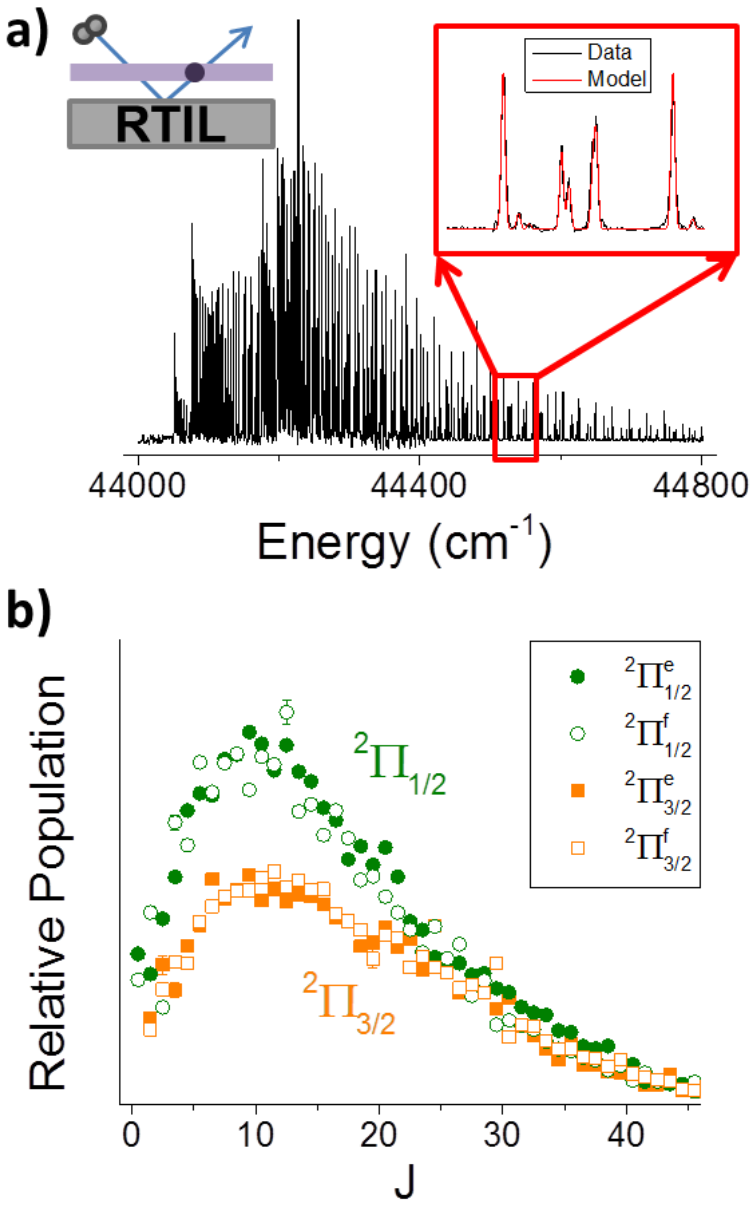

Figure 3.2 (a) Sample LIF spectrum of scattered NO from $[bmim]^+[Tf_2N]^-$. Each spectrum is fit with a least-squares fit (shown in red in the magnified inset), from which quantum-state resolved populations are extracted. This spectrum is taken at high incident collision energy (E_{inc} = 20 kcal/mol), with T_s =333 K. As illustrated in the upper left hand corner, the signal is only measured for a small volume of scattered molecules with $\theta_{scatter} = 45° \pm 10°$. (b) Population distributions corresponding to the above sample spectrum, where the four electronic states ($^2\Pi^e_{1/2}$, $^2\Pi^f_{1/2}$, $^2\Pi^e_{3/2}$, $^2\Pi^f_{3/2}$) are plotted as a function of rotational J state.

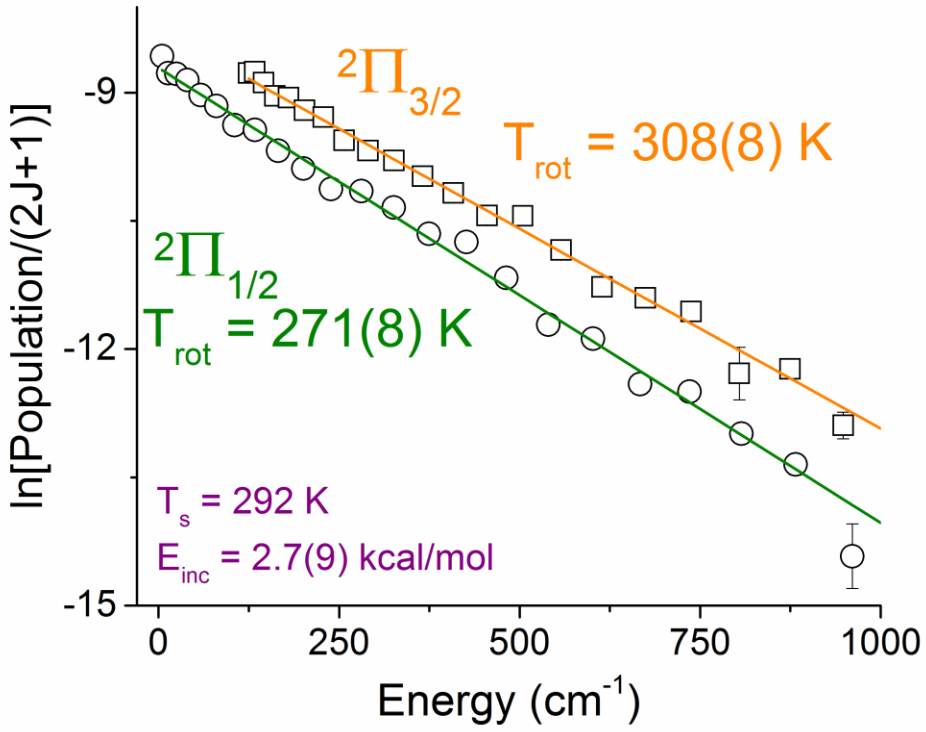

Figure 3.3 Boltzmann plot of scattered rotational populations at low incident translational energy (E_{inc} = 2.7(9) kcal/mol). These distributions display linear fits to a single temperature distribution, with the Λ-doublet states are experimentally equally populated and therefore averaged for each spin-orbit state. Note that T_s = 292 K, and thus that $T_{rot}(^2\Pi_{1/2})$ and $T_{rot}(^2\Pi_{3/2})$ are close to but slightly *cooler* and *hotter* than the liquid interface, respectively.

trapping-desorption events with complete thermal accommodation (i.e., $\alpha \approx 1$). These sample data in Figure 3.3 have been taken at a surface temperature of T_s = 292 K, with the plots representing each spin-orbit state, $^2\Pi_{1/2}$ and $^2\Pi_{3/2}$, averaged over nearly equally populated Λ-doublet states. Interestingly, despite low enough collision energies for complete thermal accommodation at the RTIL surface, the scattered molecules observed in the $^2\Pi_{1/2}$ and $^2\Pi_{3/2}$ manifolds are in fact not in equilibrium with each other and instead exhibit *lower* ($T_{rot}(^2\Pi_{1/2})$ = 271(8) K) and *higher* ($T_{rot}(^2\Pi_{3/2})$ = 308(8) K) rotational temperatures than T_s. These effects can be explored in more detail by varying the surface temperature, as shown in Figure 3.4. The

measured rotational temperatures do increase linearly with surface temperature with a slope of ≈ 0.5 and thus distinctly different from unity. More quantitatively, the slopes for the two spin-orbit states are equal but maintain a constant vertical difference ($\Delta T \approx 30$ K) as the surface temperature is varied from 292 to 373 K. By detailed balance considerations, this necessarily implies deviations from unity sticking behavior at the gas-liquid interface, and suggests a significant angular and/or spin-orbit dependence to the potential surface for adsorption/desorption.[56]

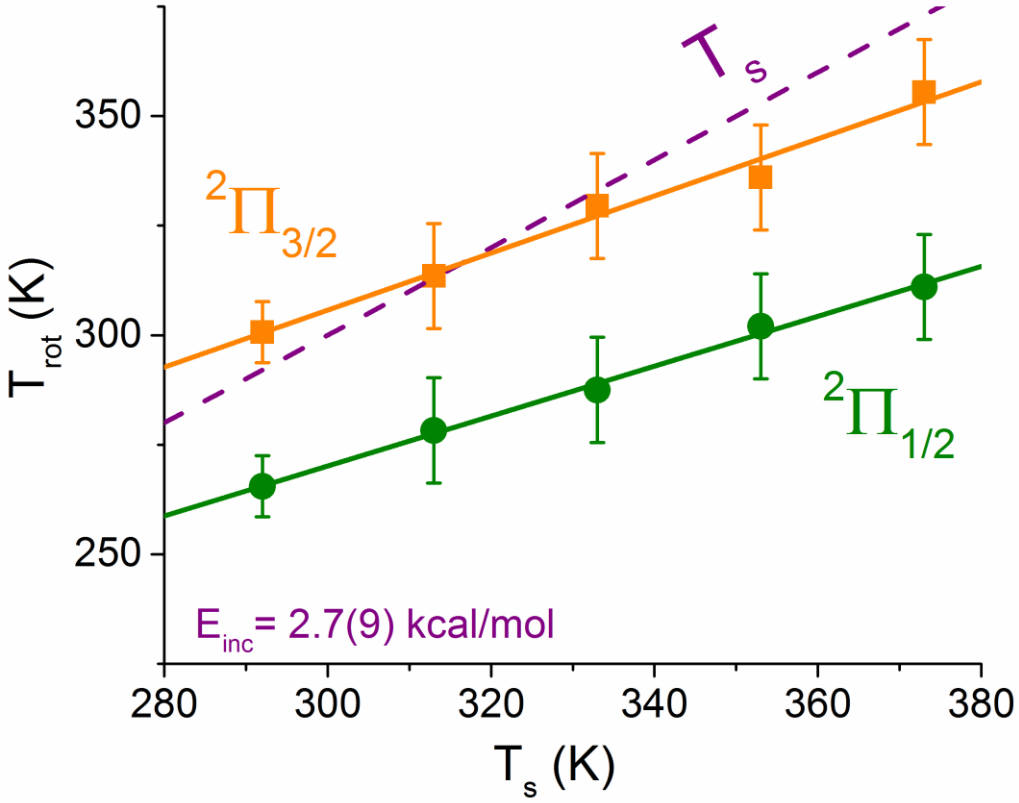

Figure 3.4 Rotational temperature dependence on T_s for low collision energy (E_{inc} = 2.7(9) kcal/mol). The dotted purple line represents a line of "complete accommodation," or what the rotational distributions would look like if fully equilibrated with the surface temperature (T_s) and the sticking coefficient were unity and independent of rotational state. Note that each spin-orbit state manifold exhibits deviations from but still a sensitivity to T_s. Error bars are based on multiple measurements at each surface temperature.

These results are surprising and differ qualitatively from previous studies with CO_2 scattering from PFPE at similarly low incident energies (E_{inc} = 1.6 kcal/mol).[14] Specifically, the CO_2 rotational and even translational Doppler line width temperatures in these prior studies were found to be in close agreement with T_s, consistent with the expectation that low energy incident molecules stick, thermalize and therefore desorb with quantum state distributions in equilibrium with the surface.[14] However, for open shell molecules like NO and OH, there is now growing evidence that gas-surface scattering dynamics clearly differ. [57,58] For example, inelastic scattering experiments with NO scattered at low E_{inc} off molten metals and single crystal surfaces yield rotational temperatures with small differences from T_s near room temperature, but which increase significantly as the surface temperature increases, e.g. as much as $\Delta T \approx 300$ K at T_s = 800 K.[57] From an equivalent perspective, temperature programmed desorption (TPD) experiments have also been conducted on Ru(001) crystals dosed with NO, which from microscopic reversibility samples the quantum state resolved sticking probabilities in the reverse direction.[58] By way of specific example, thermally desorbed NO from Ru(001) is well fit by a single rotational temperature of 235 K, i.e., again significantly *cooler* than the surface temperature of 455 K. Such nonequilibrium dynamics in rotational temperatures between spin-orbit states have also been observed in other $^2\Pi$ projectile scattering experiments. For example, reactive scattering of O(^{3}P) at squalane liquid surfaces revealed small but statistically significant differences (~20K) between rotational temperatures for OH product spin-orbit states, with the excited spin-orbit state appearing slightly hotter.[11] Of particular relevance to the present work, studies by Zare et. al. on NO scatting from metallic Ag(111) at multiple low collision energies found the excited $^2\Pi_{3/2}$ rotational state manifold to be consistently *hotter* than that of the ground $^2\Pi_{1/2}$ state, yet with both not in equilibrium with the surface temperature.[57, 59]

Simple time reversal symmetry and detailed balance ideas[56] can be exploited to provide some insight into the origin of such non-equilibrium dynamics. For a molecular projectile approaching a gas-condensed phase interface in a specific quantum state, incident energy and angle, there will be a probability to trap long enough to thermalize with the surface and eventually desorb. If this sticking probability is unity for all quantum states, energies and angles, then, by detailed balance, all molecules that have thermalized on the surface must desorb into a flux weighted equilibrium distribution representative of the surface temperature. This is simply a consequence of the rigorous kinetic constraint, for conditions of a gas in equilibrium with a surface, that the desorbing flux must *maintain* the system in its equilibrium status. Conversely, the *nonequilibrium* distribution of NO observed in the current low energy scattering experiments necessarily implies that sticking probabilities for the incoming NO molecular beam depend on internal quantum state and/or incident energy.

An even stronger prediction is that detailed balance considerations rigorously require the internal quantum state distributions arising from the surface accommodated fraction (α) for an equilibrium flux of incident molecules at T_s to *exactly* complement those from the non-trapping fraction ($1-\alpha$), and thereby form a composite distribution in *perfect* equilibrium with the surface temperature. It is important to note that even these low incident energy NO beams are cooled predominantly into the *ground* rotational and spin orbit state ($N = 0$, $^2\Pi_{1/2}$) and therefore far from equilibrium with T_s. However, detailed balance requires that the fraction of NO molecules (α) that trap/accommodate with the surface long enough to "forget" this initial condition *must* recapitulate the same distributions (equilibrium or non-equilibrium) as would have been obtained under fully equilibrium incident beam conditions.

Based on the observed NO distributions, these simple but powerful detailed balance ideas make several predictions that stimulate further theoretical exploration. First of all, rotational NO temperatures *lower* than T_s imply that the sticking coefficient (α) must i) depend on J and ii) indeed *decrease* with increasing rotational excitation. There are many possible ways to achieve this behavior, e.g., a strong angular dependence on the gas-liquid surface interaction potential. As a result of such angular anisotropy, incoming jet cooled NO can quantum mechanically mix in excited rotations to form states oriented with respect to the surface and thereby achieve a deeper or shallower adsorption well and thus a higher or lower barrier to surface physisorption. A similar argument applies to the spin-orbit state distributions as well, but now with the hotter than T_s rotational temperatures (at T_s = 292 K) for the excited spin-orbit manifold suggesting a significant shift in the angular anisotropy for the $^2\Pi_{3/2}$ vs. $^2\Pi_{1/2}$ NO –RTIL intermolecular potential. Indeed, we have made preliminary steps toward such an analysis with high level *ab initio* calculations, as will be discussed in more detail later in Section 3.4.

Finally, we note that the formation of excited spin-orbit states from a purely ground electronic state incident beam requires the presence of *nonadiabatic surface hopping* events between the $^2\Pi_{3/2}$ and $^2\Pi_{1/2}$ manifolds. For the low energy collisional studies above, this could in principle arise simply from a high probability for trapping-desorption events and therefore sufficient time to equilibrate the spin-orbit degree of freedom with the surface temperature. For example, summed over all rotational states, the relative population ratio between ground and excited spin-orbit states at 292 K is $[^2\Pi_{3/2}]/ [^2\Pi_{1/2}] = 0.45(2)$, which is close to but lower than the fully equilibrated T_s predictions of 0.54 (Figure 3.5). At the highest RTIL temperatures sampled ($T \approx 373$ K), this spin-orbit population ratio rises to $[^2\Pi_{3/2}]/ [^2\Pi_{1/2}] = 0.50(3)$, which is again close to, though still systematically below, the equilibrium value of 0.62. Indeed, much larger

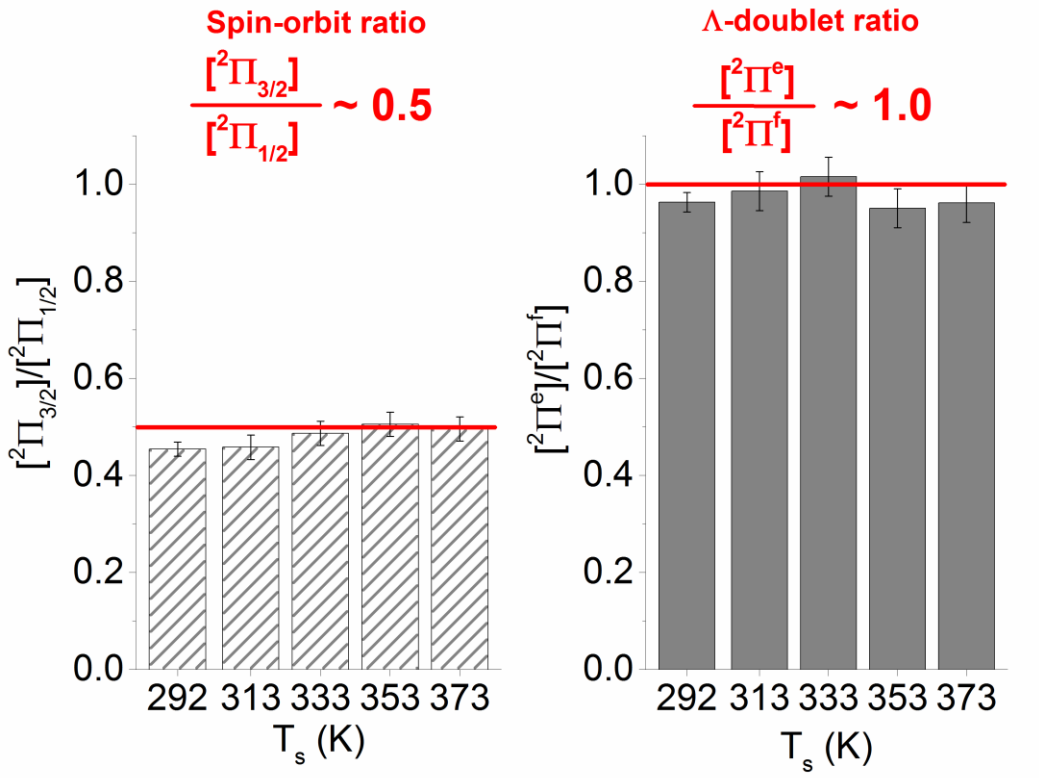

Figure 3.5 Comparison of electronic state populations relative to each other as the surface temperature is varied for E_{inc} = 2.7(9) kcal/mol. (a) Spin-orbit state ratios, where each spin-orbit state population is summed over all J states and both Λ-doublet states. The spin-orbit ratio $[^2\Pi_{3/2}]/[^2\Pi_{1/2}]$ ~ 0.45-0.52 and varies little with T_s. The energy difference between the two spin-orbit state manifolds is 123 cm^{-1}. (b) Λ-doublet electronic ratios are shown on the right, where each Λ-doublet state is summed over all J states and both spin-orbit states. The Λ-doublet states ($\Delta\nu \approx 0.01$ cm^{-1}) are nearly equally populated independent of surface temperature.

deviations from near equilibrium behavior in the spin-orbit distributions are observed at high incident collision energies, as discussed below.

3.3.2 High Incident Energy Rotational Distributions (E_{inc} = 20 kcal/mol)

With increasing E_{inc}, deviations from this pure trapping desorption behavior due to impulsive scattering events become apparent. In particular, at superthermal collision energies, E_{inc} = 20(6) kcal/mol, there is no longer a linear Boltzmann plot characterized by a single

temperature, but instead strong curvature that unambiguously signals the presence of additional *nonequilibuium* rotational dynamics in the scattered flux. As shown in previous work,[8, 15, 19, 23] such distributions can be well fit to a two-temperature model described by Eq. (3.1):

$$P_{TD/IS} = \frac{(2J+1)e^{-E_{rot}/kT_{rot}(TD/IS)}}{Q_{rot}(TD/IS)}$$

$$Pop_J = [\alpha * P_{TD}(J) + (1-\alpha) * P_{IS}(J)] \qquad (3.1)$$

where $\alpha = P_{TD}/(P_{TD} + P_{IS})$ is the branching ratio into the TD channel (with $\alpha = 1$ signaling all molecules undergoing TD scattering) and P_{TD} and P_{IS} represent the respective fractions in the TD and IS component for a given rotational state. Although there must clearly be a continuum of such IS scattering channels, the resulting rotational quantum state distributions are surprisingly well characterized by a "temperature" over 2 orders of magnitude in dynamic range. Such dual temperature behavior has now been verified in many quantum state resolved studies and for many different gas-liquid molecular scatterers, as well as confirmed theoretically with detailed trajectory studies.[5, 8, 12, 14, 57]

The fundamental source of this rather remarkable simplicity is not yet theoretically well understood; however, we offer the following observations. First of all, there is no *a priori* reason for the nonthermally accommodating IS dynamics to be described by a superthermal Boltzmann distribution; indeed, one would expect deviations from such simple behavior to become evident with sufficient experimental sensitivity. Second, we have recently initiated studies as a function of scattering angle, exploring quantum state resolved NO distributions at both specular ($\theta_s = 45^o$) and normal incidence ($\theta_s = 0^o$). Even for microscopically rough gas-RTIL interfaces, the preliminary results for normal vs. specular scattering angles are consistent with the angular trends anticipated for TD vs. IS pathways, for example, (i) significant *increase* (20-30%) in

fractional trapping-desorption probability α, (ii) significant growth in TD signals with little change in rotational distributions at low E_{inc}, and (iii) significantly *colder* spin-orbit temperatures (T_{elec}). Lastly, such dual temperature Boltzmann behavior necessarily predicts overlapping TD and IS contributions at low final state energies, as clearly verified in the extensive molecular dynamics simulations of Hase and coworkers. [19, 20] In any event, such a dual temperature description in Eq. (3.1) empirically provides a physically motivated, few parameter characterization of scattered populations over a wide experimental dynamic range (Figure 3.6).

Rotational populations at high collision energies for each spin-orbit state have been fit to Eq. (1) with α and T_{IS} floated. Consistent with detailed balance considerations, T_{TD} has been fixed at T_{rot} values obtained from the low E_{inc} scattering results for the corresponding surface temperature and spin-orbit state. Figure 3.6 shows a sample Boltzmann plot for the ground spin-orbit ($^2\Pi_{1/2}$) manifold at E_{inc} = 20(6) kcal/mol; the fitted α and T_{IS} values plotted in Figure 3.7 as a function of i) surface temperature and ii) electronic state, which reveal two significant trends. First of all, the IS temperatures are nearly 3-4-fold hotter than T_s, which indicates the presence of highly rotationally inelastic collisions at superthermal incident energies. Second, the IS temperature component is relatively insensitive to increasing T_s, with the $^2\Pi_{3/2}$ distributions consistently hotter than the $^2\Pi_{1/2}$ state, a pattern also noted above at low E_{inc}. Bimodal rotational distributions have also been observed in orientation dependent scattering of NO from Ag(111), which have found *hotter* rotational distributions for O-end scattering than for N-end scattering.[60] These effects are most pronounced at more glancing scattering angles (i.e., $\theta_s = 70^o$) and more modest at specular scattering angles. More recent work has been done by Wodtke et. al. looking at these orientation effects in scattering vibrationally excited NO from Au (111) and with similar qualitative results.[38, 39]

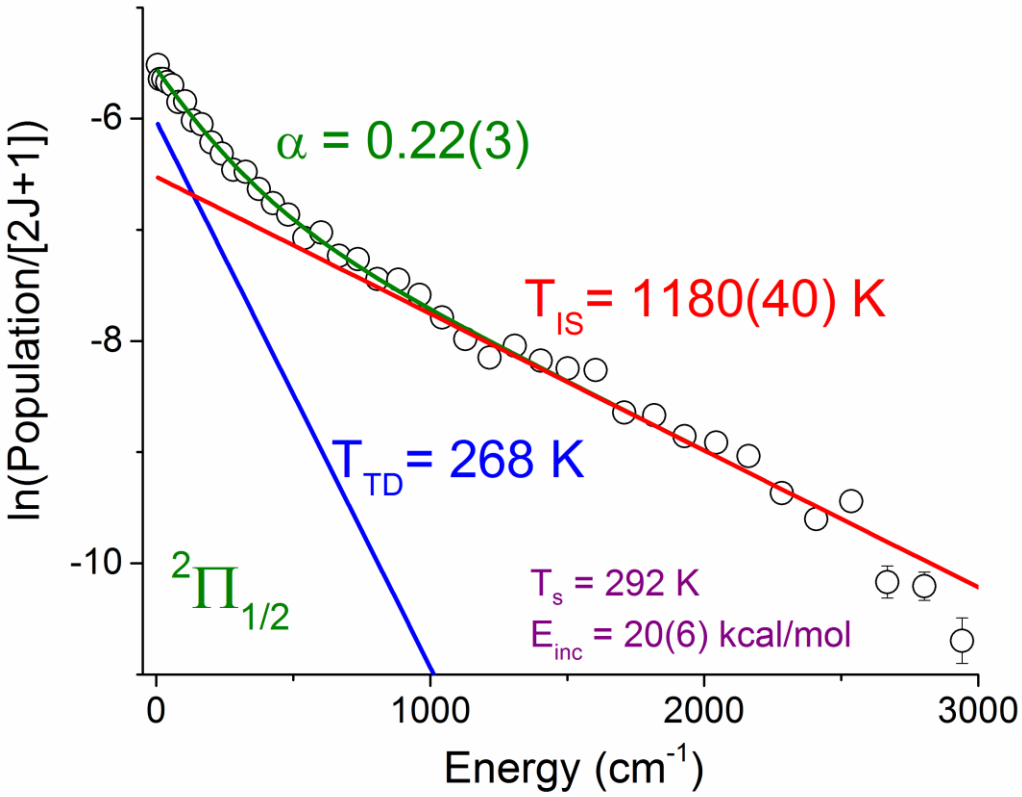

Figure 3.6 Sample high incident energy (E_{inc} = 20(6) kcal/mol) rotational distributions for the $^2\Pi_{1/2}$ Boltzmann plot. Unlike the *linear trends* exhibited at low E_{inc} (Figure 3.3), at higher collision energies, distinct *curvature* is observed in the rotational Boltzmann populations. This dynamic range (over 150-fold) is well fit by a dual-temperature distribution, where the lower temperature (T_{TD}) is fixed at values from the low E_{inc} fits, with the hotter temperature (T_{IS}) and branching ratio (α) between to the TD/IS scattering pathways floated.

It is also worth noting that the branching ratios between the TD and IS channels (α = 0.15-0.30) are surprisingly small at high collision energy, much smaller, for example, than the corresponding values (α =0.65-0.72) observed for hyperthermal scattering of CO_2 from RTILs.[16] This implies that distributions at these higher incident energies are dominated by non-equilibrium gas-liquid scattering dynamics and indeed, by detailed balance considerations, are consistent with significant deviations from unity sticking behavior also noted in the thermally accommodated flux. There is again a clear spin-orbit state dependence to the accommodation

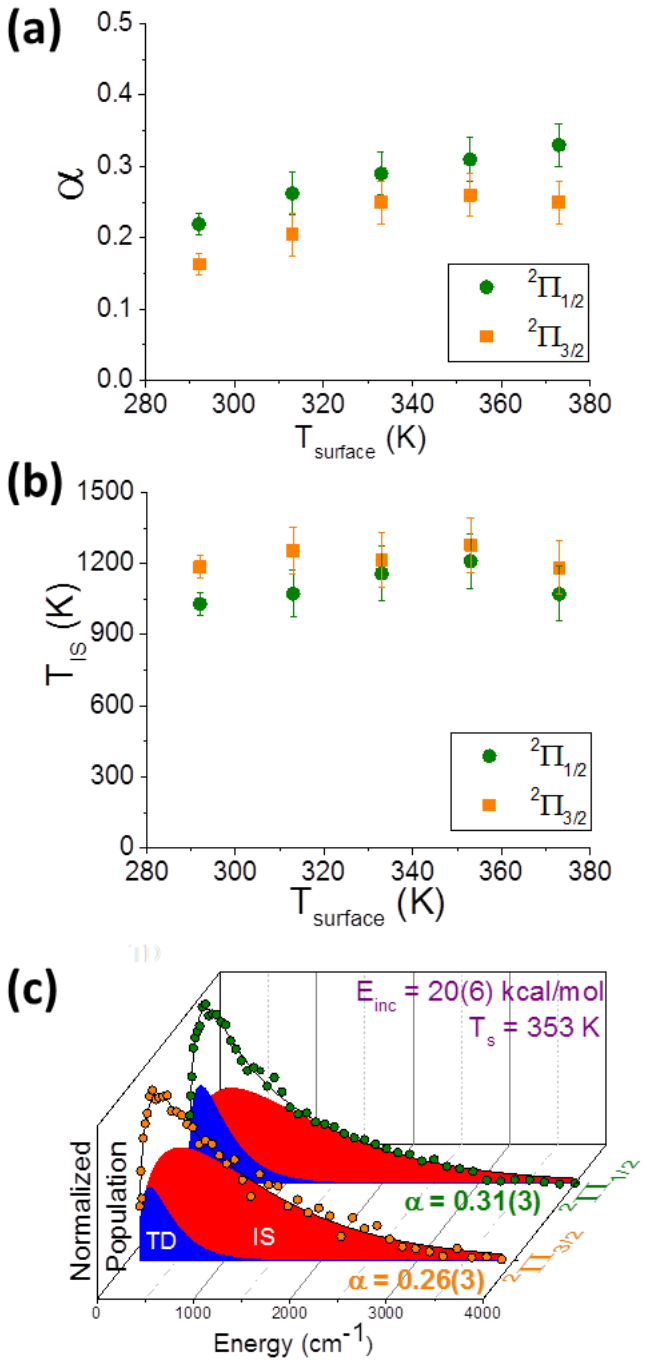

Figure 3.7 Dependence of T_{IS} and α as a function of surface temperature at E_{inc} = 20(6) kcal/mol. (a) Branching ratios (α) increase systematically with surface temperature, consistent with greater thermal roughening of the RTIL interface. (b) Conversely, T_{IS} is relatively insensitive to surface temperature, with hotter temperatures for $^2\Pi_{3/2}$ vs. $^2\Pi_{1/2}$ state manifolds (c) Sample fits to a two temperature distribution for $^2\Pi_{1/2}$ and $^2\Pi_{3/2}$, with total populations normalized to unity. The rotationally cold TD component (blue) represents a significantly larger fraction for $^2\Pi_{1/2}$ vs. $^2\Pi_{3/2}$ states, consistent with strong T_s dependent coupling between rotational and spin-orbit degrees of freedom.

dynamics, with a consistently higher fraction of the spin-orbit conserving collisions ($^2\Pi_{1/2} \rightarrow {}^2\Pi_{1/2}$) proceeding through the TD channel than for the spin-orbit changing events ($^2\Pi_{1/2} \rightarrow {}^2\Pi_{3/2}$). These differences can also be seen directly in the rotational energy distributions in Figure 3.7(c), which reveal a visibly larger fraction of TD collision dynamics in fits for the $^2\Pi_{1/2}$ vs. $^2\Pi_{3/2}$ states. The ground electronic state has a higher trapping-desorption component, by roughly 10%, than the excited spin-orbit state. Since all of the incident NO molecules are in the ground spin-orbit state, spin-orbit conserving collisions ($^2\Pi_{1/2} \rightarrow {}^2\Pi_{1/2}$) at 292 K result in thermal accommodation ~ 25% of the time, whereas significantly fewer (~15%) molecules undergoing spin-orbit changing collisions ($^2\Pi_{1/2} \rightarrow {}^2\Pi_{3/2}$) thermalize with the surface. Alternatively stated, the more highly *rotationally inelastic* impulsive scattering (IS) channel appears to be accompanied by a greater propensity for *electronically inelastic* spin-orbit changing collisions. This suggests a strong coupling between rotational and electronic degrees of freedom in the gas-RTIL collision event and offers interesting new challenges to dynamical theory.

It is also worth noting that the fraction of collisions proceeding via the TD pathway increases monotonically with surface temperature. This has been noted previously in other gas-liquid studies[7, 8, 14], and is consistent with increased inelastic energy loss contributions due to thermally induced surface roughening at higher T_s, thus resulting in a larger fraction of molecules accommodating on the surface. Interestingly, thermal roughening with increased surface temperature does not appear to exert any collateral influence on energy transferred into rotation via the IS channel. Furthermore, despite such strong temperature dependent effects on the branching ratio α, the corresponding spin-orbit differences are clearly maintained. All of these observations reflect nonunity sticking coefficients and the presence of angular/electronic

features in the NO-RTIL potential surface, which translate into a strong sticking dependence on both the incident rotational and spin-orbit state.

3.4. Discussion

3.4.1 Nonadiabatic Electronic Effects

Scattering an open shell radical species such as NO provides the ability to probe the probability of electronically nonadiabatic events at the gas-liquid interface. In order to explore such surface hopping dynamics in more detail, the rotational populations are summed over all rotational states and are plotted in Figure 3.5 (E_{inc} = 2.7 kcal/mol) and Figure 3.8 (E_{inc} = 20 kcal/mol) as a function of (i) spin-orbit state, (ii) Λ-doublet state (only at low E_{inc}), and (iii) RTIL surface temperature. One message from these plots is unambiguous; since the initial jet cooled beam has a spin-orbit ratio indistinguishable from zero $[^2\Pi_{3/2}]/[^2\Pi_{1/2}] \approx 0.0$, the observation of strong spin-orbit excited populations under both low and high incident collision energy conditions implies the presence of surface hopping effects in the gas-surface collision dynamics. More specifically, Figure 3.5(a) reveals that low collision energies achieve spin-orbit population ratios of $[^2\Pi_{3/2}]/[^2\Pi_{1/2}] \approx 0.4 - 0.5$, with a relatively weak dependence on surface temperature. As noted previously, these values are close to but *consistently lower* than predictions based on complete equilibration with the surface in the desorbing flux, with equivalent electronic spin-orbit temperatures varying between T_{elec} = 215 and 252 K over T_s = 292 – 373 K. By way of contrast, relative populations for NO molecules scattering into *e* and *f* parity Λ-doublet states are compared in Figure 3.5(b). As also demonstrated in Figure 3.2, there are no significant differences in the scattered molecules' rotational distributions between the Λ-

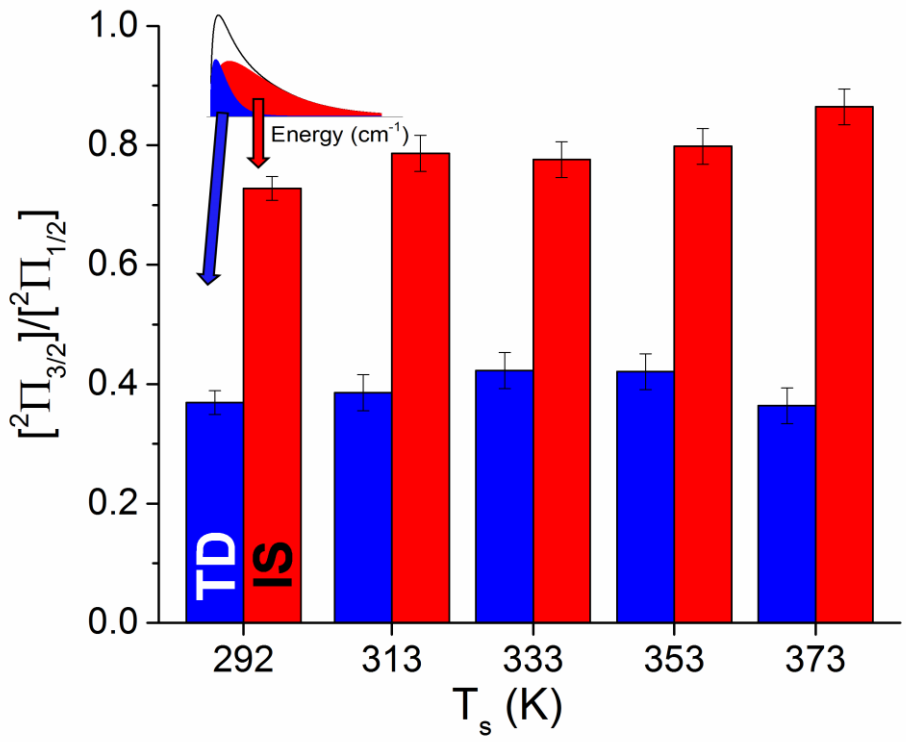

Figure 3.8 Spin-orbit ratios for the TD and IS scattering channels summed over all rotational and Λ-doublet states for E_{inc} = 20(6) kcal/mol. The ratio of spin-orbit populations within the TD component (blue) is $[^2\Pi_{3/2}]$: $[^2\Pi_{1/2}] \approx 0.40$, corresponding to an electronic temperature of ~ 200 K and relatively insensitive to surface temperature. By way of comparison, the equivalent ratios for the impulsively scattered fraction (red) are $[^2\Pi_{3/2}]$: $[^2\Pi_{1/2}] \approx 0.70$-$0.85$ corresponding to a ~ 500 – 1000 K range of electronic temperatures and a gradual increase with T_s.

doublet states within each spin-orbit state and the ratio of these Λ-doublet states is largely insensitive to changes in the surface temperature.

The non-adiabatic dynamics in the scattered flux are further explored further at high collision energies in Figure 3.8, where the TD and IS contributions are now treated separately, with the spin-orbit ratio within each scattering pathway considered by itself. The TD fraction exhibits a spin-orbit ratio of $[^2\Pi_{3/2}]/[^2\Pi_{1/2}] \sim 0.35$ - 0.40, with no appreciable dependence on T_s. As expected, these results are quite similar to those previously discussed at low E_{inc}, despite

nearly 8-fold higher collision energy. This is consistent with what our fits identify as the TD component, correctly reflecting the fraction of fully thermally accommodated NO trajectories, which from detailed balance considerations must yield the same spin-orbit and Λ-doublet ratios (and indeed rotational distributions) independent of the incident collision energy. By way of contrast, however, this spin-orbit fraction jumps precipitously for the impulsively scattered component, for which there are nearly as many excited as ground spin-orbit state molecules ($[^2\Pi_{3/2}]/[^2\Pi_{1/2}] \sim$ 0.71 - 0.85). Expressed in terms of an equivalent electronic "temperature", this would correspond to a range of T_{elec} from 500 to1000 K. It is worth noting that this is more consistent with the window of temperatures experimentally observed in the impulsively scattered rotational distributions, which might suggest a simple dynamical picture of coupling/partial equilibration between electronic and rotational degrees of freedom on the time scale of an IS collisional event. Furthermore, there is a clear surface temperature dependence to the nonadiabatic excitation effects in these collisions, with the fraction of excited $^2\Pi_{3/2}$ molecules in the IS channel *increasing* with increasing T_s and ostensibly correlated with microscopic roughening of the RTIL surface. Finally, this trend again highlights the connection between i) rotationally inelastic and ii) spin-orbit changing ($^2\Pi_{1/2} \rightarrow {}^2\Pi_{3/2}$) collision dynamics in the impulsive scattering pathway, i.e., that *rotational and electronic* degrees of freedom must be strongly correlated.

3.4.1 Theoretical Considerations

Though a complete treatment is well beyond the scope of the present work, it is worth briefly exploring the fundamental source of such open shell nonadiabatic dynamics in NO + RTIL scattering at the gas-liquid interface. To make things simple, we replace the surface by a

single scattering center, NO + M, which allows us to borrow directly from the pioneering work of Alexander and co-workers.[61, 62] From such studies for NO + rare gas dynamics, this yields A' and A" potential surfaces in C_s symmetry, on which the energy transfer collisions occur. As elegantly shown by Alexander and coworkers, *spin-orbit conserving* interactions are governed by the *sum* potential, $V_{sum} = (A' + A'')/2$, while *spin-orbit changing* interactions depend upon the *difference* potential, $V_{diff} = (A'' - A')/2$. V_{diff} provides a description of the electronic anisotropy of the NO molecule as a 2D function of Jacobi coordinates i) M-N-O bond angle (θ) and ii) center of mass NO –M separation (R) with respect to the scattering center.[62, 63]Far from the scattering center at collinear C_{inv} (M-N-O or M-O-N) geometries, these two adiabatic surfaces are exactly degenerate. However, this degeneracy is broken during approach, the magnitude and geometrical differences of which control the propensity for spin-orbit state changing dynamics.

It is worth stressing that comparably high levels of spin-orbit excitation have been observed in other gas-surface scattering systems, in particular NO + molten gallium[17] and NO + Ag (111).[57] By way of contrast, spin-orbit excitation/deexcitation for crossed molecular beam studies[64] of NO + Ar is diminished by roughly an order of magnitude. This clearly speaks to a significant increase in the V_{diff} potential surface for conducting liquid/single crystal metals and RTILs. As first suggested in vibrational relaxation studies for NO(v) + Au (111) by Tully[37], Wodtke and coworkers[65], and later proposed by Alexander et. al. for NO + Ag(111)[66], one intriguing reason for such large V_{diff} potential surfaces for conducting liquids and solids could be due to *partial charge transfer* to/from the NO molecule during the collisional process. As discussed previously for imidazolium-based RTILs[52, 54], this could in principle come from either the anion or cation species at the gas-liquid interface, although charge donation from the anion

would tend to be more energetically favorable, the simplest of which would be atomic halide anions.

In order to explore the magnitude of such nonadiabatic effects, we have therefore performed preliminary *ab initio* geometry optimizations for the simple model system, NO + Cl^-, using both high level single reference (CCSD(T)) and multireference (CASSCF+MRCI) methods on a MOLPRO software platform. The CCSD(T) calculations have been performed with explicitly correlated F12 electron methods and specially optimized correlation consistent f12 basis sets of Peterson et al. (denoted VnZ-f12, n = 2,3) [67] and extrapolated to the complete basis set limit (CBS). Each of the equilibrium geometries for A', A" symmetry Cl^-–NO structures at the CCSD(T) level are summarized in the left hand column of Table 3.1. Note that the A' surface exhibits two such weakly bound minima, one for collinear approach with the O end pointing inward toward the Cl^- anion ($\theta = 180.0^o$, R = 4.098 Å, r_{NO} = 1.1500 Å, D_e = 1.12 kcal/mol), and a second for a more bent structure ($\theta = 101.1^o$, R = 3.620 Å, r_{NO} = 1.1502 Å, D_e = 1.18 kcal/mol), with a very shallow trench and transition state connecting the two equilibrium geometries. Of particular importance, however, there is also a much more strongly bound equilibrium geometry of A" symmetry, which is bent with the N end pointing preferentially toward the Cl^- anion and far more deeply bound ($\theta = 67.4^o$, R = 3.157 Å, r_{NO} = 1.1565 Å, D_e = 3.97 kcal/mol) than either of the two A' symmetry equilibrium states. This implies a surprisingly large magnitude of the *difference* potential (i.e., V_{diff}) both in well depth and geometry, which from the scattering calculations of Alexander et. al. begins to rationalize the high propensity for *spin-orbit state changing* dynamics observed experimentally.

With open shell radical molecular systems such as NO, it is appropriate to be concerned that single reference *ab initio* quantum calculations, even at the CCSD(T)-f12 level, might prove

insufficient for predicting accurate equilibrium geometries and well depths. We therefore have repeated these A', A" Cl^- – NO geometry optimizations with multireference MOLPRO methods. Specifically, we start from state-averaged CASSCF (MULTI) calculations with explicitly correlated VnZ-f12 basis sets (n=2,3), balanced average over the lowest two A', A" states (2A', 2A"), with (15,4) and (9,1) occupied and closed orbitals, respectively. A subsequent

		CCSD(T)				MULTI (2A'+2A") MRCI occ, 15, 4 + Q closed, 9, 1			
basis VnZ-f12	symmetry C_{2V}	$R_{X\text{-}NO}$	$q_{X\text{-}NO}$	r_{NO}	D_e (kcal)	$R_{X\text{-}NO}$	$q_{X\text{-}NO}$	r_{NO}	D_e(kcal)
n=2	A'	4.089	180.0	1.1509	1.22	4.122	180.0	1.1520	1.34
	A'	3.618	101.3	1.1510	1.24	3.690	104.2	1.1520	1.29
	A"	3.165	67.4	1.1571	4.03	3.300	74.3	1.1549	3.56
n=3	A'	4.098	180.0	1.1499	1.15	4.125	180.0	1.1512	1.25
	A'	3.619	101.2	1.1503	1.21	3.691	104.2	1.1512	1.26
	A"	3.163	67.5	1.1563	4.00	3.301	74.1	1.1541	3.52
CBS	A'	4.098	180.0	1.1500	1.12	4.124	180.0	1.1512	1.22
	A'	3.620	101.1	1.1502	1.18	3.691	104.2	1.1512	1.19
	A"	3.157	67.4	1.1565	3.97	3.302	73.8	1.1542	3.49

Table 3.1 *Ab initio* equilibrium geometries for X^- + NO, with X^- = Cl^- as a simple atomic RTIL anion. Left side: MOLPRO calculations at the CCSD(T)/VnZ-f12 level for n = 2, 3 and extrapolated to the complete basis set (CBS) limit. Right side: multireference MOLPRO calculations (MULTI/MRCI(+Q)) for an explicitly correlated VnZ-f12 basis set (n = 2, 3, and CBS limit). $R_{X\text{-}NO}$ and r_{NO} in angstroms, $\theta_{X\text{-}NO}$ in degrees, D_e in kcal/mol. Note the dramatic difference in equilibrium geometries and well depths for the A' and A" potential surfaces, which provides a physical mechanism for the non-adiabatic surface hopping dynamics observed experimentally. See text for details.

multireference calculation with the Davidson correction (MRCI-f12 + Q) is then performed for each of the lowest A' and A" symmetry states, with additional reference symmetries specified to ensure balanced configuration spaces for both calculations. When extrapolated to the CBS limit and optimized with respect to all three Jacobi coordinates, the multireference results again reveal the presence of two weakly bound A' equilibrium structures, one collinear ($\theta = 180.0^o$, R = 4.124 Å, r_{NO} = 1.1512 Å, D_e = 1.22 kcal/mol) and one bent structure ($\theta = 104.2^o$, R = 3.691 Å, r_{NO} =

1.1512 Å, D_e = 1.19 kcal/mol), with a relatively flat trench connecting the two local minima. Likewise, the mutireference calculations yield a much more strongly bound A" geometry (θ = 73.8^o, R = 3.302 Å, r_{NO} = 1.1542 Å, D_e = 3.49 kcal/mol), in nearly quantitative agreement with CCSD(T) predictions (see Table 3.1). Once again, it is worth stressing the large shifts in equilibrium geometry and well depth between the A' and A" surfaces, which yield both a large difference potential (V_{diff}) and thus provide a clear quantum mechanical mechanism for the strong spin-orbit changing collision dynamics observed experimentally.

As a final comment, it is worth pointing out that the NO bond lengths for both the CCSD(T) and multireference A" equilibrium geometries are systematically larger (+ 0.003-0.005 Å) than for either of the corresponding A' minima. This would suggest a simple physical picture of partial charge donation from the Cl^- anion into the antibonding π^* NO molecular orbitals, as can be confirmed by direct inspection of the wave function composition. Such partial charge transfer mechanisms have been previously invoked to interpret vibrational relaxation and excitation for NO scattering from metals vs. insulating systems.[36, 68, 69] For example, when vibrationally excited NO (v =12) is scattered from *metallic surfaces* with low work functions, the NO molecules readily lose significant amounts of vibrational energy. Electron emission ("chemicurrents") has also been detected from metallic surfaces following collisions with highly vibrationally excited molecules.[69] However, when these same highly vibrationally excited molecules were scattered from *insulating surfaces*, there was only quite modest vibrational relaxation.[68] Such nonadiabatic electronic effects clearly indicate a breakdown of the Born-Oppenheimer approximation, which assumes the electrons can adjust instantaneously to nuclear motion while staying on the same electronic adiabatic potential energy surface. As one simple model of the dynamics, electron-hole pair excitation in metallic surfaces could result in partial

electron donation to the incident molecule to form a transient NO^- species, which then flows back into the metallic Fermi sea as the NO scatters away from the surface.

It is therefore of interest whether such a charge transfer picture could also offer a novel mechanism for nonadiabatic NO collision dynamics at the gas-RTIL interface. In particular, charge donation from anions at the gas-liquid interface both into and out of the two π^* antibonding molecular orbitals of NO could facilitate particularly efficient spin-orbit excitation, simply by interchanging the $\Lambda = \pm 1$ projections of the orbital angular momentum and thus achieving the desired change in spin-orbit state ($\Omega = \Lambda + \Sigma$) without any requisite flip of the electron spin projection (Σ). However, additional experimental and theoretical work will be needed to confirm or refute the importance of such a partial charge transfer mechanism in controlling nonadiabatic collision dynamics at the gas-RTIL interface, toward which we hope the present study has provided some stimulation and useful first insights.

3.5 Summary and Conclusions

The gas-RTIL interface has been explored via quantum state resolved scattering of supersonically cooled NO molecules from $[bmim]^+[Tf_2N]^-$, where collision dynamics are monitored by observing rovibronic scattered populations as a function of collision energy and surface temperature. By exploiting open shell NO molecules cooled into the lowest spin-orbit state, "surface hopping" between its multiple low-lying electronic states has been probed, with the presence of strong nonadiabatic collisional processes confirmed via spin-orbit excited molecules in the scattered flux.

At low collision energies (E_{inc} = 2.7(9) kcal/mol), the distribution of scattered NO is well described by a single rotational temperature, however, one that is not in equilibrium with the

surface temperature. Furthermore, there is evidence for nonequilibrium *electronic* effects as well; for *spin-orbit changing* collisions ($^2\Pi_{1/2} \rightarrow {}^2\Pi_{3/2}$), T_{rot} is roughly 30K hotter than for *spin-orbit conserving* collisions with the surface ($^2\Pi_{1/2} \rightarrow {}^2\Pi_{1/2}$). While these collision energies are low enough to facilitate complete accommodation of molecules at the surface, these results clearly indicate i) a nonunity sticking coefficient as well as ii) rotational and electronic state dependent sticking probabilities to adsorption/desorption. At higher collision energies (E_{inc} = 20(6) kcal/mol), highly nonequilibrium rotational distributions are observed that can be well fit to a two-temperature distribution which can be associated with fully accommodated (TD) and all non-accommodated (IS) scattering pathways. The branching ratio into the TD channel, α, increases with surface temperature, consistent with roughening of the gas-liquid interface. Differences in these branching ratios are also observed between the two spin-orbit state manifolds, which reveal that spin-orbit conserving interactions are correlated more strongly with trapping desorption behavior than the spin-orbit changing collisions. The consistency between such data at both high and low incident collision energies further reinforces the notion that there exist dynamical barriers to adsorption/desorption that are dependent both on spin-orbit electronic state and angular orientation for incident NO molecules striking the RTIL surface.

The propensity for electronic excitation, or nonadiabatic surface hopping, is quantified by summing over all rotational states within each of the electronic states. Negligible differences of the scattered NO molecules are observed between Λ-doublet states, while large differences are seen between the two spin-orbit manifolds. Specifically, at lower collision energies, where the full accommodation pathway is likely to predominate, $[^2\Pi_{3/2}]:[^2\Pi_{1/2}] \sim 0.4$ and is close to thermal equilibrium with the surface temperature. At higher collision energies, conversely, this ratio becomes closer to $[^2\Pi_{3/2}]:[^2\Pi_{1/2}] \sim 0.8$, i.e., substantially higher than predicted from a full

equilibration picture. If we consider the TD and IS channels separately, the relative population of the excited spin-orbit state is found to be significantly higher for the IS component, with that pathway therefore being more favorable for electronically inelastic, *spin-orbit changing* collisions.

To explore these nonadiabatic effects further, preliminary *ab initio* calculations for Cl^- + NO, where Cl^- represents a simple RTIL anion, have been performed on a MOLPRO software platform using both single reference CCSD(T) and multireference (CASSCF+MRCI) methods. The results predict large differences, both in well depths and equilibrium geometries, between the A' and A'' potential energy surfaces, which from the work of Alexander and co-workers begins to explain the high propensity for spin-orbit excitation observed experimentally. Additionally the equilibrium bond lengths for the A'' state are found to be systematically longer than the A' state, consistent with transient partial charge donation from the Cl^- anion into the NO π^* orbital, and which raises the possibility of a novel electron exchange mechanism that changes in the spin-orbit state. Though there is clearly more work needed to confirm the role of such nonadiabatic pathways, we hope such calculations will serve as motivation for further theoretical efforts exploring the detailed mechanism for spin-orbit excitation at the gas-RTIL interface.

Chapter 3 References

1. P. Davidovits, C. E. Kolb, L. R. Williams, J. T. Jayne and D. R. Worsnop, *Chem. Rev.*, 2006, **106**, 1323-1354.

2. B. J. Gertner and J. T. Hynes, *Science*, 1996, **271**, 1563-1566.

3. J. P. D. Abbatt, *Chem. Rev.*, 2003, **103**, 4783-4800.

4. G. B. Ellison, A. F. Tuck and V. Vaida, *J. Geophys. Res.-Atmos.*, 1999, **104**, 11633-11641.

5. M. E. Saecker, S. T. Govoni, D. V. Kowalski, M. E. King and G. M. Nathanson, *Science*, 1991, **252**, 1421-1424.

6. B. H. Wu, J. M. Zhang, T. K. Minton, K. G. McKendrick, J. M. Slattery, S. Yockel and G. C. Schatz, *J. Phys. Chem. C*, 2010, **114**, 4015-4027.

7. M. E. King, K. M. Fiehrer, G. M. Nathanson and T. K. Minton, *J. Phys. Chem. A*, 1997, **101**, 6556-6561.

8. M. E. King, M. E. Saecker and G. M. Nathanson, *J. Chem. Phys.*, 1994, **101**, 2539-2547.

9. G. M. Nathanson, *Annu. Rev. Phys. Chem.*, 2004, **55**, 231-255.

10. J. P. Wiens, G. M. Nathanson, W. A. Alexander, T. K. Minton, S. Lakshmi and G. C. Schatz, *J. Am. Chem. Soc.*, 2014, **136**, 3065-3074.

11. S. P. K. Kohler, M. Allan, H. Kelso, D. A. Henderson and K. G. McKendrick, *J. Chem. Phys.*, 2005, **122**, 24712.

12. C. Waring, P. A. J. Bagot, J. M. Slattery, M. L. Costen and K. G. McKendrick, *J. Phys. Chem. A*, 2010, **114**, 4896-4904.

13. M. A. Tesa-Serrate, K. L. King, G. Paterson, M. L. Costen and K. G. McKendrick, *Phys. Chem. Chem. Phys.*, 2014, **16**, 173-183.

14. B. G. Perkins and D. J. Nesbitt, *J. Phys. Chem. B*, 2008, **112**, 507-519.

15. B. G. Perkins and D. J. Nesbitt, *J. Phys. Chem. B*, 2006, **110**, 17126-17137.

16. J. R. Roscioli and D. J. Nesbitt, *J. Phys. Chem. A*, 2011, **115**, 9764-9773.

17. M. P. Ziemkiewicz, J. R. Roscioli and D. J. Nesbitt, *J. Chem. Phys.*, 2011, **134**, 234703.

18. M. P. Ziemkiewicz, A. Zutz and D. J. Nesbitt, *J. Phys. Chem. C*, 2012, **116**, 14284-14294.

19. E. Martinez-Nunez, A. Rahaman and W. L. Hase, *J. Phys. Chem. C*, 2007, **111**, 354-364.

20. J. J. Nogueira, S. A. Vazquez, O. A. Mazyar, W. L. Hase, B. G. Perkins, D. J. Nesbitt and E. Martinez-Nunez, *J. Phys. Chem. A*, 2009, **113**, 3850-3865.

21. T. Y. Yan, W. L. Hase and J. R. Barker, *Chem. Phys. Lett.*, 2000, **329**, 84-91.

22. X. H. Li, G. C. Schatz and D. J. Nesbitt, *J. Phys. Chem. B*, 2012, **116**, 3587-3602.

23. G. M. Nathanson, P. Davidovits, D. R. Worsnop and C. E. Kolb, *J. Phys. Chem.*, 1996, **100**, 13007-13020.

24. M. A. Wilson and A. Pohorille, *J. Phys. Chem. B*, 1997, **101**, 3130-3135.

25. N. V. Plechkova and K. R. Seddon, *Chem. Soc. Rev.*, 2008, **37**, 123-150.

26. M. Armand, F. Endres, D. R. MacFarlane, H. Ohno and B. Scrosati, *Nat. Mater.*, 2009, **8**, 621-629.

27. B. Winther-Jensen, O. Winther-Jensen, M. Forsyth and D. R. MacFarlane, *Science*, 2008, **321**, 671-674.

28. Y. Bai, Y. M. Cao, J. Zhang, M. Wang, R. Z. Li, P. Wang, S. M. Zakeeruddin and M. Gratzel, *Nat. Mater.*, 2008, **7**, 626-630.

29. H. Matsumoto, H. Sakaebe and K. Tatsumi, *J. Power Sources*, 2005, **146**, 45-50.

30. W. L. Hough, M. Smiglak, H. Rodriguez, R. P. Swatloski, S. K. Spear, D. T. Daly, J. Pernak, J. E. Grisel, R. D. Carliss, M. D. Soutullo, J. H. Davis and R. D. Rogers, *New J. Chem.*, 2007, **31**, 1429-1436.

31. J. G. Huddleston, H. D. Willauer, R. P. Swatloski, A. E. Visser and R. D. Rogers, *Chem. Commun.*, 1998, 1765-1766.

32. L. A. Blanchard, Z. Y. Gu and J. F. Brennecke, *J. Phys. Chem. B*, 2001, **105**, 2437-2444.

33. L. A. Blanchard, D. Hancu, E. J. Beckman and J. F. Brennecke, *Nature*, 1999, **399**, 28-29.

34. Y. S. Kim, W. Y. Choi, J. H. Jang, K. P. Yoo and C. S. Lee, *Fluid Phase Equilibr.*, 2005, **228**, 439-445.

35. J. L. Anthony, E. J. Maginn and J. F. Brennecke, *J. Phys. Chem. B*, 2002, **106**, 7315-7320.

36. N. Shenvi, S. Roy and J. C. Tully, *J. Chem. Phys.*, 2009, **130**, 174107.

37. N. Shenvi, S. Roy and J. C. Tully, *Science*, 2009, **326**, 829-832.

38. N. Bartels, K. Golibrzuch, C. Bartels, L. Chen, D. J. Auerbach, A. M. Wodtke and T. Schafer, *J. Chem. Phys.*, 2014, **140**, 54710.

39. N. Bartels, K. Golibrzuch, C. Bartels, L. Chen, D. J. Auerbach, A. M. Wodtke and T. Schafer, *P. Natl. Acad. Sci. USA*, 2013, **110**, 17738-17743.

40. G. Herzberg, *Spectra and Molecular-Structure I. Spectra of Diatomic-Molecules*, Princeton Univ. Press, Princeton, NJ, 1968.

41. M. H. Alexander, P. Andresen, R. Bacis, R. Bersohn, F. J. Comes, P. J. Dagdigian, R. N. Dixon, R. W. Field, G. W. Flynn, K. H. Gericke, E. R. Grant, B. J. Howard, J. R. Huber, D. S. King, J. L. Kinsey, K. Kleinermanns, K. Kuchitsu, A. C. Luntz, A. J. Mccaffery, B. Pouilly, H. Reisler, S. Rosenwaks, E. W. Rothe, M. Shapiro, J. P. Simons, R. Vasudev, J. R. Wiesenfeld, C. Wittig and R. N. Zare, *J. Chem. Phys.*, 1988, **89**, 1749-1753.

42. T. Welton, *Chem. Rev.*, 1999, **99**, 2071-2083.

43. I. S. Martinez and S. Baldelli, *J. Phys. Chem. C*, 2010, **114**, 11564-11575.

44. C. Kolbeck, T. Cremer, K. R. J. Lovelock, N. Paape, P. S. Schulz, P. Wasserscheid, F. Maier and H. P. Steinruck, *J. Phys. Chem. B*, 2009, **113**, 8682-8688.

45. K. R. J. Lovelock, C. Kolbeck, T. Cremer, N. Paape, P. S. Schulz, P. Wasserscheid, F. Maier and H. P. Steinruck, *J. Phys. Chem. B*, 2009, **113**, 2854-2864.

46. T. Hammer, M. Reichelt and H. Morgner, *Phys. Chem. Chem. Phys.*, 2010, **12**, 11070-11080.

47. S. Rivera-Rubero and S. Baldelli, *J. Phys. Chem. B*, 2006, **110**, 4756-4765.

48. T. Iimori, T. Iwahashi, K. Kanai, K. Seki, J. H. Sung, D. Kim, H. O. Hamaguchi and Y. Ouchi, *J. Phys. Chem. B*, 2007, **111**, 4860-4866.

49. V. Lockett, R. Sedev, C. Bassell and J. Ralston, *Phys. Chem. Chem. Phys.*, 2008, **10**, 1330-1335.

50. A. M. Zolot, P. J. Dagdigian and D. J. Nesbitt, *J. Chem. Phys.*, 2008, **129**, 194705.

51. K. R. J. Lovelock, I. J. Villar-Garcia, F. Maier, H. P. Steinruck and P. Licence, *Chem. Rev.*, 2010, **110**, 5158-5190.

52. K. Kanai, T. Nishi, T. Iwahashi, Y. Ouchi, K. Seki, Y. Harada and S. Shin, *J. Electron Spectrosc.*, 2009, **174**, 110-115.

53. R. T. Poole, J. G. Jenkin, J. Liesegang and R. C. G. Leckey, *Phys. Rev. B*, 1975, **11**, 5179-5189.

54. D. Yoshimura, T. Yokoyama, T. Nishi, H. Ishii, R. Ozawa, H. Hamaguchi and K. Seki, *J. Electron Spectrosc.*, 2005, **144**, 319-322.

55. D. H. Zaitsau, G. J. Kabo, A. A. Strechan, Y. U. Paulechka, A. Tschersich, S. P. Verevkin and A. Heintz, *J. Phys. Chem. A*, 2006, **110**, 7303-7306.

56. J. C. Tully, *Surf. Sci.*, 1994, **299**, 667-677.

57. G. D. Kubiak, J. E. Hurst, H. G. Rennagel, G. M. McClelland and R. N. Zare, *J. Chem. Phys.*, 1983, **79**, 5163-5178.

58. R. R. Cavanagh and D. S. King, *Phys. Rev. Lett.*, 1981, **47**, 1829-1832.

59. G. M. Mcclelland, G. D. Kubiak, H. G. Rennagel and R. N. Zare, *Phys. Rev. Lett.*, 1981, **46**, 831-834.

60. F. H. Geuzebroek, A. E. Wiskerke, M. G. Tenner, A. W. Kleyn, S. Stolte and A. Namiki, *J. Phys. Chem.*, 1991, **95**, 8409-8421.

61. M. H. Alexander, *J. Chem. Phys.*, 1999, **111**, 7426-7434.

62. M. H. Alexander, *J. Chem. Phys.*, 1993, **99**, 7725-7738.

63. J. E. Smedley, G. C. Corey and M. H. Alexander, *J. Chem. Phys.*, 1987, **87**, 3218-3231.

64. C. J. Eyles, M. Brouard, C. H. Yang, J. Klos, F. J. Aoiz, A. Gijsbertsen, A. E. Wiskerke and S. Stolte, *Nat. Chem.*, 2011, **3**, 597-602.

65. Y. Huang, A. M. Wodtke, H. Hou, C. T. Rettner and D. J. Auerbach, *Phys. Rev. Lett.*, 2000, **84**, 2985-2988.

66. S. Gregurick, M. H. Alexander and A. E. Depristo, *J. Chem. Phys.*, 1994, **100**, 610-621.

67. J. S. Vieceli and D. J. Tobias, *Abstr. Pap. Am. Chem. S.*, 2004, **227**, U1003-U1003.

68. A. M. Wodtke, D. Matsiev and D. J. Auerbach, *Prog. Surf. Sci.*, 2008, **83**, 167-214.

69. J. D. White, J. Chen, D. Matsiev, D. J. Auerbach and A. M. Wodtke, *Nature*, 2005, **433**, 503-505.

Chapter 4

Quantum state-resolved molecular scattering of NO ($^2\Pi_{1/2}$) at the gas-[$C_n$mim][Tf_2N] room temperature ionic liquid interface: Dependence on alkyl chain length, collision energy, and temperature*

4.1 Introduction

Room temperature ionic liquids (RTILs) are molten salts with melting temperatures < 100 ºC which represent a novel class of green solvents with high electrical/thermal conductivity,[1] low vapor pressures,[2] and high thermal stability.[3] These novel liquids consist purely of ions and have many valuable applications in catalytic reactions,[4-6] Li-ion batteries,[7, 8] fuel cells,[9, 10] CO_2 capture,[11-14] and solar cells.[15, 16] Of particular practical importance is that interfacial and bulk properties of RTILs can be targeted for specific applications by either changing the anion/cation combination,[17, 18] or even simply varying functional groups within the ions. This results in enormous flexibility in the "design" of such RTILs, with well over 10^6 liquids feasible by combinatorial substitution.[19] These effects are important not only in controlling bulk equilibrium properties (e.g., Henry's Law solubilities) as well as non-equilibrium dynamical processes, such as molecular solvation kinetics at the gas-liquid interface. An outstanding challenge to the chemical physics community has been to provide a more fundamental and predictive understanding of how cation/anion composition (e.g., cation hydrophobicity) might be used to "tune" the interfacial properties of these novel liquids.

*Published in AIP Advances, **6**, 105207 (2016)

Due to utility in several of the above mentioned applications, many RTIL studies to date have focused on imidazolium based cations with an aliphatic C_n side chain and bis(trifluoromethylsulfonyl)imide anions (denoted [$C_n$mim][Tf_2N]). For such [$C_n$mim][Tf_2N] RTILs, the charge of the cation is delocalized over the imidazolium ring with a nonpolar alkyl side chain, while the [Tf_2N] anion has its charge centered on the central $N(SO_2)_2$ group with two outer nonpolar CF_3 groups (Figure 4.1). The C_n hydrocarbon chain length plays a crucial role in moderating intermolecular interactions, including hydrogen bonding, dispersion forces, π-stacking, and Coulomb attraction between the cation and anion. For example, dispersion forces between alkyl chains increase for longer hydrocarbons, affecting how the ions arrange and thus overall liquid properties. In particular, theoretical and experimental studies have reported on the formation of bilayers in the bulk for $n > 4$, where the long alkyl chains align, separating charged layers of anions and imidazolium cation rings.[3, 20-22] Specifically for [$C_n$mim][Tf_2N] RTILs, an increase in *n* is accompanied by an increase in bulk viscosity[23, 24] and yet a decrease in both density[23-25] and ionic conductivity.[23] It is important to stress that bulk composition can in principle differ fundamentally from the gas-liquid interface. For example, the extreme "hydrophobicity" of the vacuum likely plays a dominant role in structure and chemical composition of the interfacial region, which clearly motivates further study of the top most interfacial layer itself.

The gas-liquid interface is particularly crucial for applications such as CO_2 sequestration and supported ionic liquid phase (SILP) catalysis[4], where the adsorption of gas molecules on the liquid surface is a critical first step for dissolving in the liquid. Many experimental techniques have been exploited to investigate the RTIL liquid surface, including surface tension measurements,[24-26] sum frequency generation (SFG),[27-31] neutral impact collision ion scattering

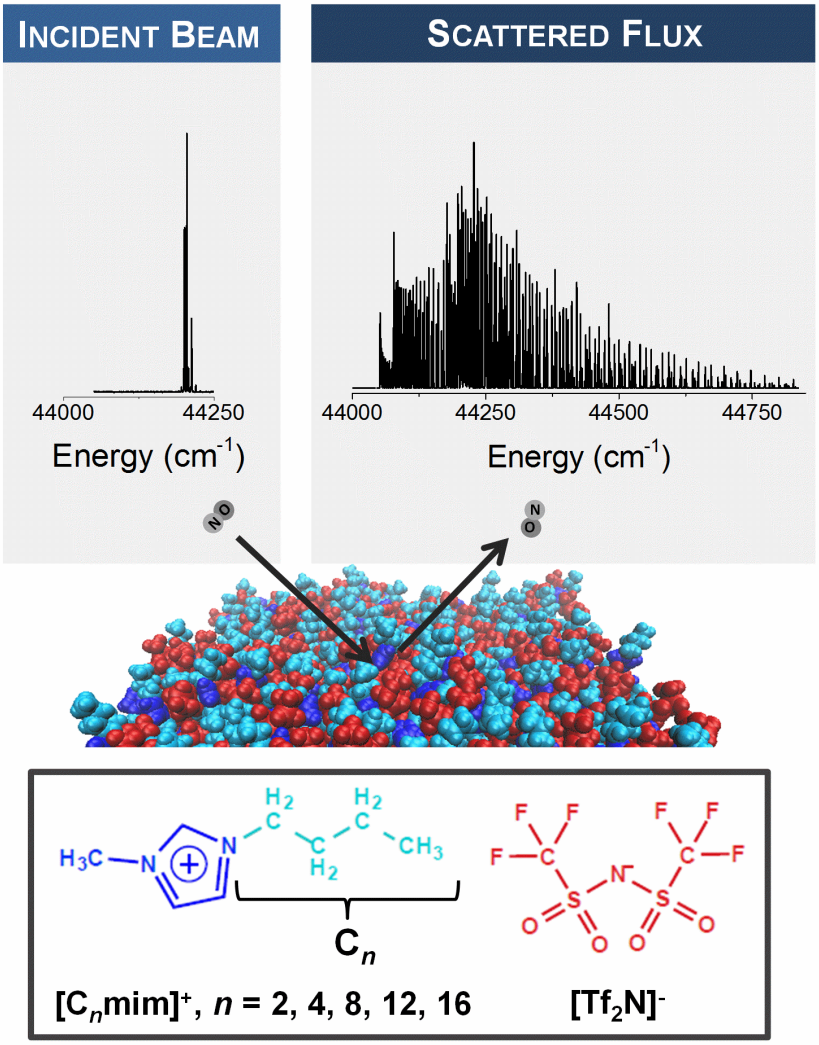

Figure 4.1 Experimental cartoon for studies of supersonically cooled NO scattered at θ_{inc} = 45º from [$C_n$mim][Tf_2N] RTILs and detected via laser induced fluorescence (LIF) at near specular angles (θ_s = 45º). Sample LIF spectra are shown in the top panels, with only the $^2\Pi_{1/2}$ state populated and T_{rot} ~ 1 K in the incident beam (top left), whereas the scattered NO flux (top right) shows significant electronic and rotational excitation with both spin-orbit states and rotational states up to J = 45.5 observed. The [C_4mim][Tf_2N] surface snapshot was constructed by molecular dynamics simulations by Schatz et. al.,[32] where the Tf_2N anion is shown in red, the cation imidazolium ring is dark blue and the cation alkyl chain is light blue. The relevant chemical structures of the ions are shown at the bottom of the figure. In the present work, we investigate a series of RTIL cations where the alkyl chain, C_n, is varied over *n* = [2, 4, 8, 12, 16].

spectroscopy (NICISS),[21, 33] angle-resolved X-ray photoelectron spectroscopy (ARXPS),[33-38] X-ray diffraction,[31, 39] neutron reflectivity,[40] low-energy ion scattering (LEIS),[41] metastable atom electron spectroscopy (MAES),[42] and molecular beam scattering,[43-48] as well as molecular dynamics simulations.[32, 44, 49] Each of these studies has varying levels of explicit surface vs. subsurface sensitivity and are therefore capable of extracting different information relevant to the interface, such as density and atomic composition (ARXPS, NICISS, LEIS) or molecular orientation (SFG, MAES). The combination of experimental and theoretical efforts have begun to build up a more complete picture of these liquid surfaces, and specifically have identified for $[C_n\text{mim}][Tf_2N]$ RTILs the presence of both anions and cations at the interface.[32, 33, 37, 38, 41, 42, 44, 50] In particular, the studies suggest a preference for nonpolar alkyl chains at the surface pointing into the vacuum with the charged imidazolium rings directly below in the liquid.[33, 42, 49] Similarly, the bulky nonpolar CF_3 moieties of the Tf_2N anions point out from the surface,[32, 37, 38, 42, 49] resulting in aggregation of both ionophobic (alkyl chains and CF_3 groups) and ionophilic (anion centers and cation imidazolium rings) groups.

While experiment and theory agree that both anions and cations are present at the gas-liquid interface, the fractional population of anions is found to decrease as *n* increases.[25, 41-44] LEIS atomic composition studies of the liquid surface report that, as the alkyl chain is lengthened from $n = 2$ to 12, the anion signals diminish by 4x but do not disappear entirely.[41] Elegant reactive scattering experiments of hyperthermal $O(^3P)$ with RTILs producing OH radical products have also demonstrated an increased propensity for alkyl chains at the surface for larger *n*,[44, 45] as well as sensitivity to fractional methylenic (CH_2) vs. methyl (CH_3) hydrocarbon presence at the interface. Of special interest, a change in the orientation of molecules at the gas-liquid interface has been observed as alkyl chains are lengthened in $[C_n\text{mim}][Tf_2N]$ RTILs. For

short alkyl chain lengths ($n \leq 4$), both experiment[29, 31] and simulation[32, 44, 49] suggest that the alkyl chains point parallel to the surface normal, while for longer hydrocarbons ($n \geq 5$), these appear to "flop over" and lie more or less parallel to the surface plane.[33, 44]

The present study significantly extends our previous efforts[47, 48] to elucidate equilibrium/non-equilibrium collision dynamics of radicals at the gas-RTIL interface, and how these dynamics are affected by conformation changes at the surface. This is done specifically via quantum state-resolved molecular beam scattering as a function of (i) incident collision energy (E_{inc}), (ii) surface temperature (T_S) and (iii) alkyl chain length of the imidazolium cation (n). Full quantum state-to-state resolution of the scattering dynamics is made possible with a supersonically cooled (1K) beam of NO, with the scattered molecules sensitively detected with laser induced fluorescence (LIF). The presence of multiple low-lying electronic states in NO allows *nonadiabatic* surface hopping dynamics to be observed, in addition to inelastic *rovibrational* excitation within the four spin-orbit and Λ-doublet electronic manifolds. In particular, the results provide additional confirmation of fractional population and orientation of alkyl chains at the RTIL surface, as well as insight into how such conformational changes affect state-resolved collision dynamics at the gas-liquid interface.

4.2 Experimental

The apparatus has been described in detail previously; we present only a brief overview of conditions relevant to the present study.[47, 48] Quantum state-resolved molecular beam experiments at the gas-liquid interface have been carried out for jet cooled NO($^2\Pi^{1/2}$ (N=0)) projectiles[48, 51] scattering from 1-alkyl-3-methylimidazolium bis(trifluoromethylsulfonyl)imide, or [$C_n$mim][Tf_2N], as a function of i) alkyl chain length (n = 2, 4, 8, 12, and 16), ii) collision

energy (E_{inc} = 2.7 and 20 kcal/mol) and iii) surface temperature (T_S = 293 – 373 K). The center panel in Figure 4.1 displays a sample theoretical snap shot at the $[C_4mim][Tf_2N]$ gas-liquid interface, obtained from quantum mechanics/ molecular mechanics (QM/MM) simulations by Schatz et. al.[32] The different molecular components are colored (anions in red, cation imidazolium rings in dark blue and cation alkyl chains in light blue), which highlight the abundance of different functional groups populating the liquid surface. All ionic liquids are purchased from Iolitec with ≥ 98% purity, with samples stirred, heated and degassed for a minimum of 6 hours while pumped on with a liquid nitrogen trap, before being placed in a 4.4 × 2.4 × 0.5 cm^3 crucible in a stainless steel vacuum chamber with base pressures of 2×10^{-8} Torr. For each scattering study, the liquid temperatures are varied from 293 K (or 315 K for the highest melting point RTIL $[C_{16}mim][Tf_2N]$[20]) to a maximum of 373 K, where the upper limit to our operating temperature range reflects the increase in vapor pressure with temperature.[52] Scattering experiments are performed on a stationary liquid surface, with indistinguishable results obtained for sample data skimming of the liquid surface every five minutes. The molecular beam is produced from an Even-Lavie pulsed valve with a 100 μm diameter pinhole and 3000 Torr backing pressure, yielding rotationally cold ($T_{rot} \approx 1$ K) NO molecules in the ground spin-orbit state ($^2\Pi_{1/2}$). The molecular beam is comprised of 1% NO doped into either H_2 or Ne-70 (70% Ne and 30% He), which yields beam-surface collision energies of E_{inc} = 20(2) and 2.7(9) kcal/mol, respectively. A 3 mm diameter skimmer results in a collimated beam striking the liquid surface at $\theta_{inc} = 45^o$ with a 1.5º half angle divergence.

Molecular scattering in the specular direction ($\theta_s \approx 45^o$) is detected with quantum state resolution via LIF, yielding density measurements of rovibrational and electronic state populations. A pulsed UV light source (225 nm) is generated by tripling the output of a YAG-

pumped dye laser operating with LDS-698 dye at 10 Hz. Final state distributions of NO 1.6 cm above the liquid surface are probed on the ($A^2\Sigma^+ \leftarrow X^2\Pi$) γ band, with the laser scanned over 800 cm^{-1} to access $J \leq 45.5$ for each electronic manifold, spin-orbit and Λ-doublet state ($^2\Pi^e_{1/2,}$ $^2\Pi^f_{1/2,}$ $^2\Pi^e_{3/2,}$ $^2\Pi^f_{3/2}$). The fluorescence signals (normalized to laser pulse energy and < 5 μJ/pulse to ensure operation in the linear regime) are imaged on a photo-multiplier tube (PMT) with spatial filtering to limit the probe volume to 15 mm^3. Data are primarily taken near $\theta_s = 45(6)^o$, with additional tests of angle resolved scattering at $\theta_s = -60(3)^o$, $0(12)^o$, and $60(3)^o$. The PMT is electronically gated at the peak of the arrival time distribution, which, for an 80 μs gas pulse duration, reflects both thermally desorbing (TD) and hyperthermally scattering (IS) pathways. LIF spectral scans are analyzed with homemade software and STARPAC least squares subroutines[51, 53] to fit overlapping peaks and extract populations for each quantum state. The quantitative accuracy of the procedure is confirmed by Boltzmann analysis of room temperature NO thermally equilibrated (298 K) with the vacuum chamber.

4.3 Results

Sample LIF spectra (E_{inc} = 20(2) kcal/mol) for both i) incident and ii) scattered NO molecules are found in the top panel of Figure 4.1, which highlight the extreme differences between incident (1K) and outgoing (collisionally excited) quantum state distributions. Scattered NO (v=0) molecules are detected with up to J = 45.5 for both e/f parities within each spin-orbit manifold, $^2\Pi_{1/2}^{(e,f)}$ and $^2\Pi_{3/2}^{(e,f)}$. Since all incident NO molecules have been cooled into the ground $^2\Pi_{1/2}$ state, electronic spin-orbit excitation at the gas-liquid interface represents a significant pathway, with clear differences between *spin-orbit conserving* collisions than *spin-orbit changing* collisions. By way of contrast, no statistically significant differences are observed

between the two Λ-doublet states within each spin-orbit manifold, for which we report only populations averaged over e/f parity channels for the remainder of this paper.

The rotational populations within each spin-orbit manifold can be further analyzed in logarithmic Boltzmann plots of population scaled by rotational degeneracy vs. total internal energy, as displayed in Figure 4.2. At low incident collision energies (E_{inc} = 2.7(9) kcal/mol), where all molecules accommodate with the liquid surface, the data are well fit to a single straight line reflecting a single temperature Boltzmann distribution. Note that this rotational temperature is close to but distinctly cooler (≈ 30 K) than the surface temperature (T_S = 293 K). This *non-equilibrium* behavior is consistent with our previous NO gas-liquid studies,[48] but in clear contrast to closed shell gas molecules such as CO_2 and HCl, which at similarly low E_{inc} desorb with rotational/translational distributions in *equilibrium* with the surface temperature.[54, 55] From detailed balance considerations, the CO_2 and HCl data imply unity sticking coefficients in the reverse (i.e., incident) direction, independent of quantum state, translational energy, and angle impinging on the surface. The dynamics for NO colliding with RTILs at low incident energies is clearly more complicated, as indeed confirmed by observation of similarly sub-thermal distributions in scattering experiments on other single crystal, liquid and molten metal surfaces.[48, 51, 56-58] At the very least, detailed balance arguments imply a rotational state dependence to the sticking coefficients for NO in the reverse direction, with the *higher* NO rotational states being less likely to trap, accommodate and eventually desorb.

It is worth considering whether all NO molecules at these low collision energies trap on the surface, or whether there might still be some residual energy dependence to the sticking coefficient. Towards this end, we have initiated *angle-resolved* studies and obtained preliminary data on final angular dependent scattering at these low collision energies, probing at θ_s = - 60°,

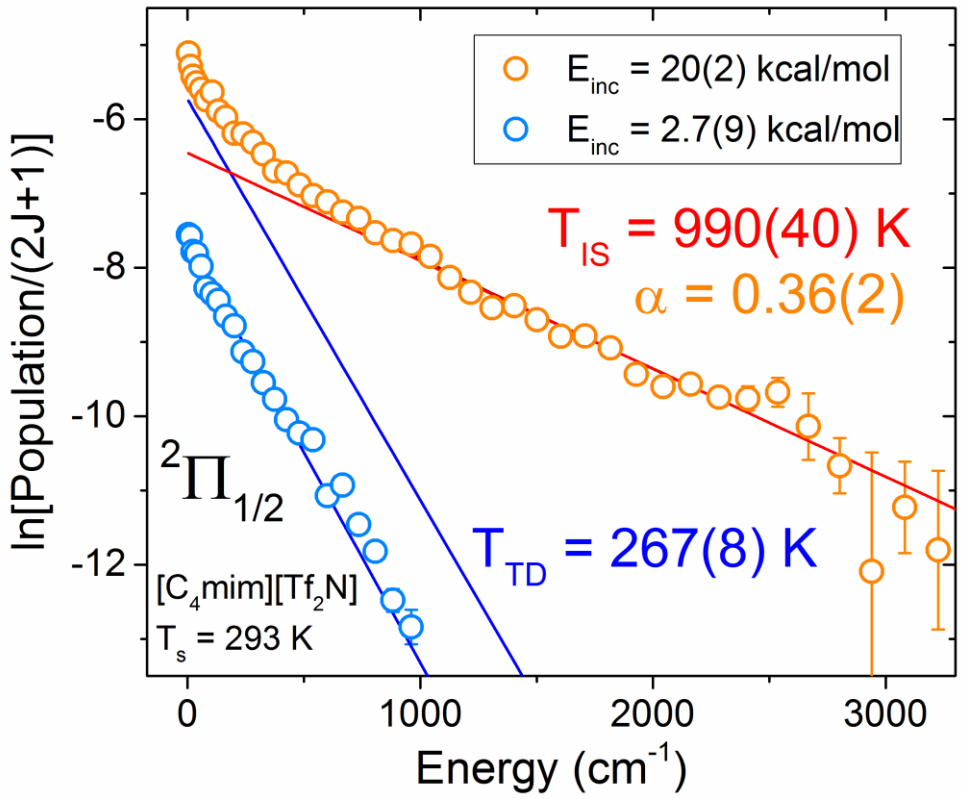

Figure 4.2 Boltzmann plots of scattered NO rotational populations for E_{inc} = 2.7(9) and 20(2) kcal/mol. At low E_{inc}, rotational populations fit well to a line, describing molecules thermally desorbing from the surface that are characterized by a single rotational Boltzmann temperature. At higher E_{inc}, significant curvature is observed, which can be well fit to a simple two-temperature model physically representing the TD and IS scattering pathways. The colder component is fixed at T_{rot} from the data at low E_{inc}, while the hotter component, T_{IS}, and the branching ratio into the TD channel, α, are floated.

0°, 45° and 60°. The results consistently support that rotational temperatures for the desorbing NO flux are i) independent of the final scattering angle and yet ii) weakly *sub-thermal* (≈ 30 K) with respect to the RTIL temperature. Thus, although a sub-thermal nature of the desorbing population signals a clear rotational state dependence to the adsorption event, the observed independence with respect to outgoing scattering angle implies an efficiency of trapping-desorption events independent of incident angle (as discussed in greater detail in previous work[48]). Specifically, if accommodation of NO on RTILs has no dependence on incident beam

angle, then, via detailed balance considerations, there can be no difference in the quantum state distributions probed as a function of scattering angle, as observed experimentally.

At high E_{inc}, distinct curvature is observed in these Boltzmann plots (Figure 4.2), with significant contributions from molecules impulsively scattering (IS) from the surface and yielding excess population in high J states. These distributions can be fit to a two-temperature model[47, 48] where the total distribution reflects a sum of hot and cold components representing the IS and TD scattering pathways, and α reflects the microscopic branching between the TD and IS channel, summed over all final J states. To be consistent with this model, the (cooler) TD temperatures are fixed from the corresponding quantity observed at low E_{inc}, while the (hotter) component, T_{IS}, and branching fraction, α, are determined by least squares fit to the data. As seen in Figure 4.3, the rotational temperatures obtained under such low E_{inc} = 2.7(9) kcal/mol scattering conditions appear to be independent of RTIL chain length, within 1σ error bars based on repeated measurements. However, the rotational temperatures for both spin-orbit states are again systematically *below* the actual liquid temperature (solid line) for all RTILs probed, with a weak but clear additional sensitivity to the outgoing spin-orbit state. By detailed balance, these observations imply the presence of dynamical barriers to adsorption that depend on both rotational and spin-orbit state, but insensitive to length of the alkyl chain.

It is worth stressing that a simple description of the quantum state resolved scattering populations microscopically bifurcating into thermal (TD) and hyperthermal (IS) components *must fail* at sufficient level of scrutiny. Indeed, a quite plausible anticipation would be to observe a *continuum* of possible IS scattering pathways, as suggested in trajectory simulations[59-63] with different molecular interaction potentials. In spite of such expectations, it is therefore remarkable that such a simple, dual-temperature model empirically fits the data over two orders of

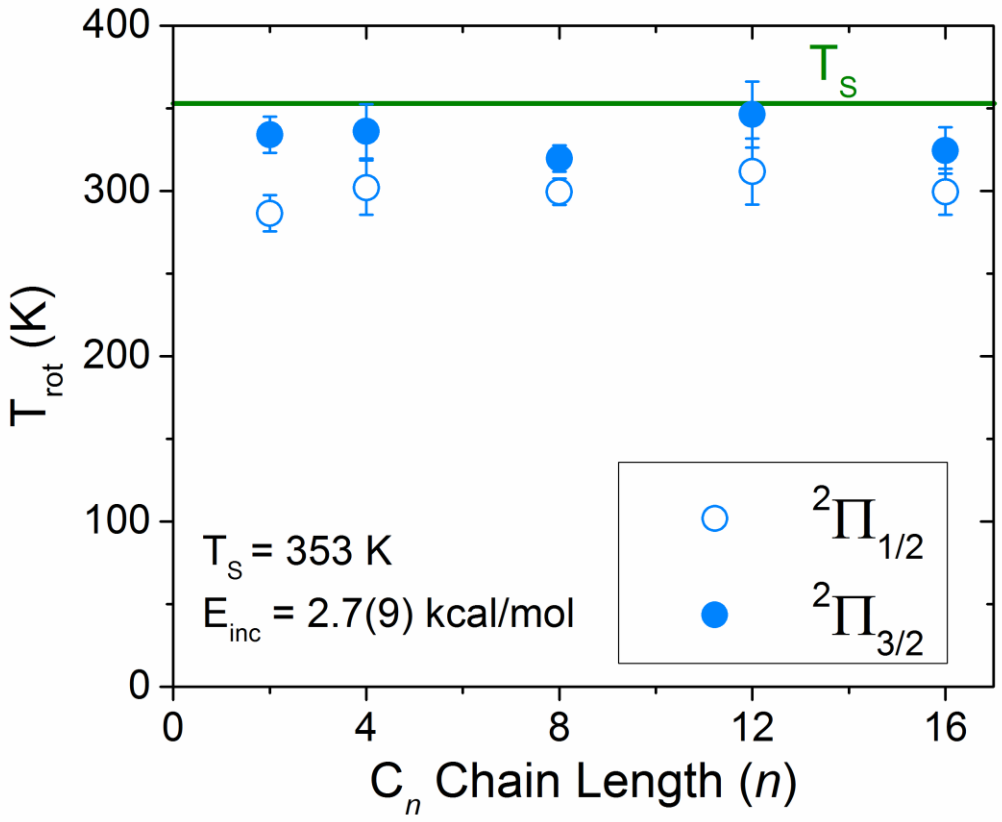

Figure 4.3 Rotational temperatures for NO scattered from [$C_n$mim][Tf_2N] at low E_{inc} = 2.7(9) kcal/mol. These temperatures have been extracted from linear Boltzmann fits (e.g., see Figure 4.3) for each spin-orbit state. Note that T_{rot} is systematically *lower* than T_S, while $T_{rot}(^2\Pi_{3/2})$ is consistently *hotter* (by ~30 K) than $T_{rot}(^2\Pi_{1/2})$. This signals the influence of non-equilibrium dynamics in the desorbing channel and, by detailed balance considerations, a rotational and spin-orbit dependence to the sticking coefficients in the adsorption event. Furthermore, increasing the cation chain length (n) for the RTIL does not appear to affect rotational temperatures at low E_{inc}.

magnitude in dynamic range and, in particular, up to internal rotational energies more than 10-fold higher than kT_S (see Figure 4.2). Although it is reasonable to exploit such behavior for a simplest empirical characterization of the data, our intention is for such quantum state resolved data to provide the requisite stimulus for development and testing of more sophisticated theoretical models that go beyond the canonical assumption of a microscopic bifurcation into TD/IS components.

With open shell species such as NO, we also probe collisional energy transfer at the gas-RTIL interface into low lying electronic degrees of freedom, with information on nonadiabatic scattering dynamics obtained from relative populations of the final spin-orbit states. As the incident NO molecules are cooled into the ground $^2\Pi_{1/2}$ state, the presence of NO($^2\Pi_{3/2}$) in the scattered flux necessarily represents nonadiabatic, surface hopping collisional events.[64] As the range of J states sampled is quite large ($J \approx 45.5$) one should confirm that NO is adequately described as a Hund's case (a) molecule, i.e., with spin and orbital angular momenta strongly coupled to the internuclear axis. This requires differences in NO end-over-end tumbling energies ($\Delta E \approx 2B_{NO}N$) to be comparable to or less than the spin-orbit energy splitting (E_{SO}), a condition satisfied up to all but the highest few NO rotational states detected. The spin-orbit distributions obtained as a function of surface temperature and alkyl chain length are summarized in Table 4.1 and will be discussed below in Sec IV.

4.4 Discussion

4.4.1 Alkyl Chain Length Dependence

We first begin by considering the effects of alkyl chain length on the low E_{inc} scattering dynamics. Sample results are shown in Figure 4.3 for a single liquid temperature (T_S = 353 K), with all error bars representing standard deviations of the mean obtained from multiple measurements. Although at these energies essentially all NO molecules trap and thermally desorb from the surface, this does not necessarily mean that the desorbing flux remains in equilibrium with the liquid temperature. Indeed, both ground and spin-orbit excited states are distinctly *cooler* rotationally than the surface temperature for all RTILs probed, which signals the presence of angular anisotropy and/or dynamical barriers for the desorption event as well as,

α at E_{inc} = 20(2) kcal/mol						
	T_s	*n* = 2	4	8	12	16
$^2\Pi_{1/2}$	293	0.34(3)	0.22(2)	0.38(2)	0.32(2)	
	313	0.33(2)	0.26(3)	0.39(3)	0.29(3)	
	333	0.32(3)	0.29(3)	0.42(3)	0.37(3)	0.42(2)
	353	0.37(3)	0.31(3)	0.40(3)	0.40(3)	0.42(3)
	373	0.39(3)	0.33(3)	0.43(3)	0.41(3)	0.41(2)
$^2\Pi_{3/2}$	293	0.22(3)	0.16(1)	0.28(2)	0.28(2)	
	313	0.23(2)	0.21(3)	0.32(3)	0.28(3)	
	333	0.26(3)	0.25(3)	0.34(3)	0.33(3)	0.38(2)
	353	0.29(3)	0.26(3)	0.36(3)	0.37(3)	0.44(3)
	373	0.29(3)	0.25(3)	0.36(3)	0.40(3)	0.37(3)
T_{IS} (K) at E_{inc} = 20(2) kcal/mol						
	T_s	*n* = 2	4	8	12	16
$^2\Pi_{1/2}$	293	1060(70)	1030(40)	920(40)	980(50)	
	313	1030(40)	1070(90)	930(70)	940(80)	
	333	1070(70)	1160(90)	970(70)	990(80)	880(30)
	353	1120(70)	1210(90)	930(70)	1030(80)	900(30)
	373	1140(70)	1070(90)	1050(70)	1180(80)	890(50)
$^2\Pi_{3/2}$	293	1160(70)	1190(40)	1010(40)	1090(50)	
	313	1190(40)	1260(90)	1050(70)	1110(80)	
	333	1190(70)	1210(90)	1020(70)	1070(80)	1050(30)
	353	1140(70)	1280(90)	1050(70)	1080(80)	1100(30)
	373	1140(70)	1180(90)	1130(70)	1140(80)	1000(50)

Table 4.1 Summary of least squares analysis fit parameters for NO scattered from $[C_n mim][Tf_2N]$ at E_{inc} = 20(2) kcal/mol as a function of T_S and C_n, for both ground ($^2\Pi_{1/2}$) and excited ($^2\Pi_{3/2}$) spin-orbit states.

from detailed balance considerations, rotational quantum state dependence in sticking coefficients for the incoming flux[48]. Furthermore, the spin-orbit excited ($^2\Pi_{3/2}$) state NO

rotational distributions are consistently ~30 K hotter than the ground ($^2\Pi_{1/2}$) state, indicating sensitivity in these dynamical barriers and sticking probabilities at the gas-liquid interface to spin-orbit electronic excitation. As mentioned earlier, this behavior is reminiscent of NO dynamics scattering/desorption from single crystal metals (e.g. Ag(111) and Ru(001)), for which a similar propensity toward colder rotational distributions was reported.[56, 58]

Although the results in Figure 4.3 reflect a single surface temperature (T_S = 353 K), the same qualitative trends are observed over a wide range of T_S, with desorbing NO rotational temperatures from low incidence energy scattering systematically *lower* than the liquid reservoir. Interestingly, Figure 4.3 indicates both i) T_{rot} and ii) sub-T_S cooling trend in T_{rot} to be relatively *insensitive* to alkyl chain length. Based on a nearly unity trapping probability for jet cooled low J states of NO, such an independence on chain length is not surprising. The persistent cooling trend in T_{rot} implies that as RTILs are varied by lengthening the hydrocarbon chain, any dynamical barriers to adsorption/desorption do not change significantly.

While sticking probabilities governing the trapping-desorption channel at low energies appear to be independent of *n*, significant differences as a function of chain length are indeed observed in scattering dynamics at higher collision energies. At E_{inc} = 20(2) kcal/mol, the TD/IS two-temperature fits to rotational populations are summarized in Figure 4.4, with normalized populations for the $^2\Pi_{1/2}$ state plotted vs. rotational energy and alkyl chain length (*n*). For each rotational distribution, the IS component (red) represents the majority species, while the TD component (blue) comprises the remainder of the scattered flux. As the alkyl chain is lengthened, the relative intensity of the TD component systematically *increases* from low *n* = [2, 4] to high *n*

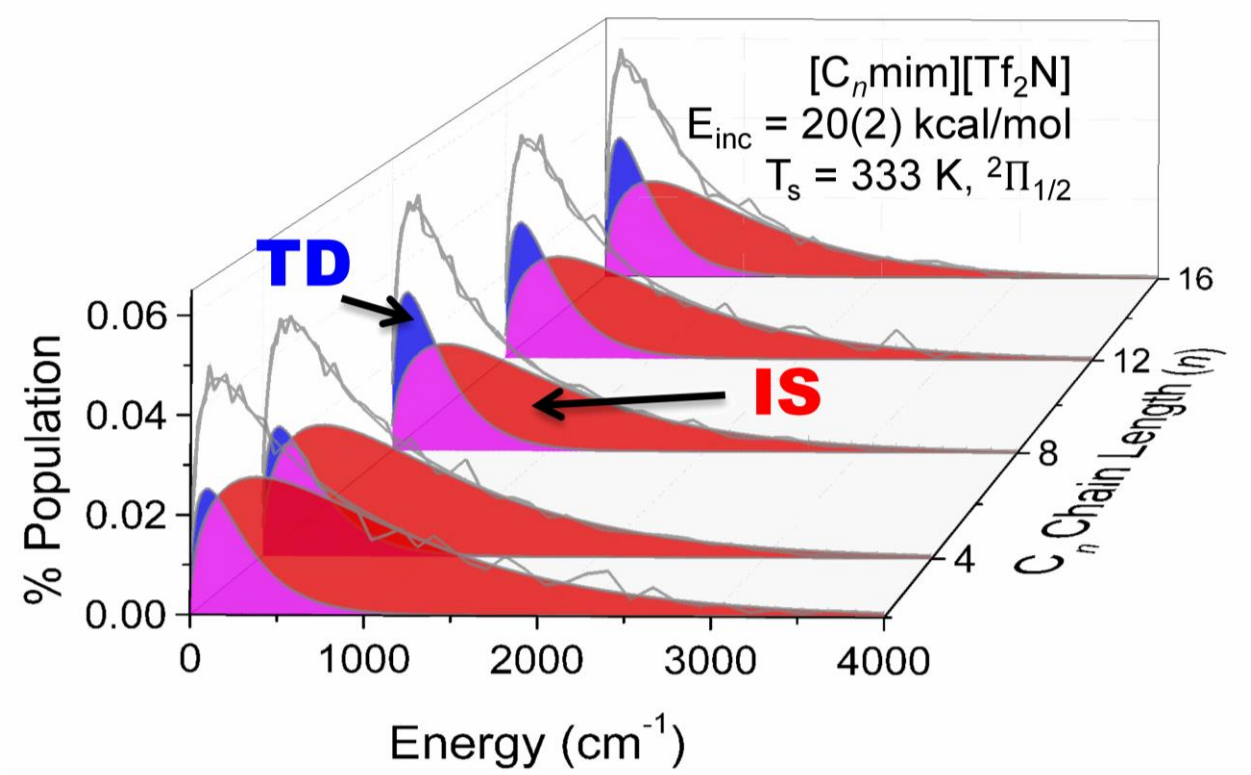

Figure 4.4 Two-temperature fits to rotational populations for NO scattered at E_{inc} = 20(2) kcal/mol from [$C_n$mim][Tf_2N]. As the alkyl chain is lengthened, the relative magnitude of the TD component *increases*, consistent with a larger fraction of the incident NO molecules thermally trapping on the liquid surface. The above data represent surface temperatures of T_S = 333 K and only the ground $^2\Pi_{1/2}$ spin-orbit state, though similar trends are observed for the $^2\Pi_{3/2}$ spin-orbit excited state and over multiple liquid temperatures (see text for details).

= [8, 12, 16], representing a comparable *increase* in the fraction of NO molecules trapping at the surface. Two-temperature fit parameters to these data, in addition to those for the $^2\Pi_{3/2}$ state, as a function of alkyl chain length are plotted in Figure 4.5 at T_S = 333 K, with the complete data set at all liquid temperatures summarized in Table 4.1.

As immediately evident in Figure 4.4 and 4.5(a), the TD branching fraction α for these RTILs is strikingly low (α = 0.25 - 0.40) for all chain lengths, with nearly 60 - 75% of the molecules experiencing impulsive scattering (IS) events at the gas-RTIL interface. This contrasts with the nearly *200% larger* values (α ≈ 0.70) observed in previous scattering studies

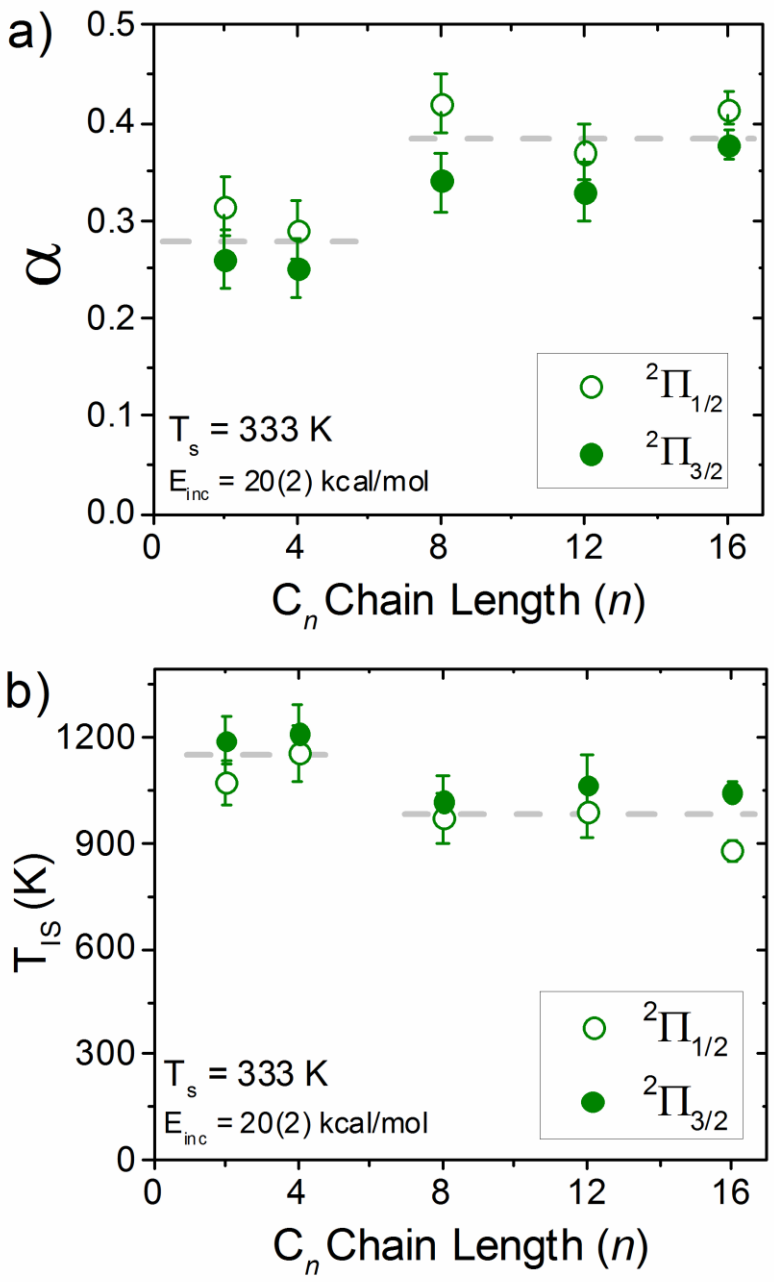

Figure 4.5 Two-temperature Boltzmann fit parameters for E_{inc} = 20(2) kcal/mol as a function of alkyl chain length. As *n* increases, α, the branching ratio into the TD channel, also increases and then plateaus at longer alkyl chain lengths. Spin-orbit changing collisions ($^2\Pi_{1/2} \rightarrow {}^2\Pi_{3/2}$) have a higher propensity to impulsively scatter (i.e., lower α) than spin-orbit conserving collisions. Additionally, the degree of rotational excitation into the IS channel decreases with alkyl chain length. As indicated by the dashed lines, both accommodation and IS rotational temperature plots suggest a discontinuous shift between short ($n \leq 4$) and long ($n \geq 8$) chain lengths, which would be consistent with molecular dynamics predictions of surface reorganization of the alkyl groups over a similar range in *n* (see text for details).

of CO_2 from [$C_n$mim][Tf_2N] at E_{inc} = 15 kcal/mol.[46] This significant difference in accommodation is not explained solely by slight discrepancies in the incident energies and, in the limit of thermal accommodation as the rate limiting step, implies proportionately *slower kinetics for NO vs CO_2 solvation* into the bulk RTIL liquid. The fundamental reasons must reflect differences in chemical/physical interactions at the interface. As a simple physical picture, this could be rationalized to arise from the 4-5 fold larger NO vs. CO_2 rotational constants, and thus the 4-5 fold larger gap between final rotational levels impeding energy transfer from incident translation into rotation at the gas-liquid interface. This would be interesting to explore systematically by probing gas-liquid collisional energy transfer into rotation for different isotopomeric molecular rotors with larger rotational constants such as DCl ($B \approx 5.39$ cm^{-1}) and HCl ($B \approx 10.4$ cm^{-1}).

Secondly, Figure 4.5(a) indicates a systematic spin-orbit state dependence for the trapping desorption fraction, i.e., $\alpha(^2\Pi_{1/2}) > \alpha(^2\Pi_{3/2})$, which based on the incident beam population in $^2\Pi_{1/2}$ implies that electronically adiabatic *spin-orbit conserving* collisions ($^2\Pi_{1/2} \rightarrow {}^2\Pi_{1/2}$) undergo trapping-desorption more readily than non-adiabatic *spin-orbit changing* collisions ($^2\Pi_{1/2} \rightarrow {}^2\Pi_{3/2}$). This has been noted in earlier studies with NO scattering from RTILs, and provides additional evidence for the presence of *non-adiabatic surface hopping* dynamics taking place at the gas-liquid interface.[47, 48] An intriguing parallel observation is the fact that fully accommodated TD collisions desorb from the surface *with colder ground* ($^2\Pi_{1/2}$) vs. *excited* ($^2\Pi_{3/2}$) spin-orbit state rotational temperatures, which by detailed balance considerations would suggest i) decreased trapping efficiency for higher J states and ii) lower trapping efficiency for ground vs. excited spin-orbit states for a given high J state. This latter prediction would at first seem to contradict the *larger* sticking coefficients for the *lower* spin-orbit state noted above.

There is no paradox, however, as these scattering experiments sample very *low J* states in the incident beam, whereas the detailed balance arguments are based on depletion of *high J* state populations in the outgoing NO flux. In any event, the data clearly indicate an unusually rich coupling between i) rotational and ii) spin-orbit state collision dynamics of NO at the gas-RTIL interface, which offer many challenges for non-adiabatic theoretical study.

Thirdly, the TD branching fraction α shows a clear sensitivity to alkyl chain length (*n*), with systematically more trapping/desorption with increasing hydrocarbon tail. These trends are in agreement with molecular beam experiments of both CO_2 and $O(^3P)$ inelastically scattering from $[C_n mim][Tf_2N]$ RTILs, which have also shown an increase in the TD fraction for longer alkyl chains.[44, 46] Such behavior is certainly consistent with a propensity for buildup of the soft and longer hydrophobic hydrocarbon chains at the interface, as also supported by theoretical molecular dynamics simulations.[44, 49] Of particular interest, however, is that Figure 4.5(a) and 4.5(b) suggest that these shifts do not appear to occur uniformly, but rather with a more nearly *discontinuous* upward shift between *short* (*n* = 2 - 4) and *long* (*n* = 8 - 16) alkyl chains. We will return to this below, but simply note again that this is the same region of hydrocarbon length over which a *discontinuous* shift in gas-RTIL interfacial alkyl chain orientation (extended outward vs. folded over) is also predicted from MD simulations.[33, 44]

Figure 4.5(b) displays the measured IS rotational temperatures as a function of *n* and spin-orbit state. It is worth noting that these rotational temperatures range from 900 to 1200 K, i.e., considerably hotter than the 333 K surface and indicating significant energy transfer from hyperthermal translational energy of the beam into the rotational degree of freedom. Secondly, these IS rotational temperatures cool slightly as *n* increases and again suggest a break from short (*n* = 2 - 4) to long (*n* = 8 - 16) alkyl chains, as similarly noted in Figure 4.5(a) for the sticking

coefficient α. On closer inspection, the excited spin-orbit state is rotationally hotter than the ground electronic state, which was also previously observed at low E_{inc}. These results are in good qualitative agreement with both experimental and theoretical work, which suggest that the interfacial landscape changes significantly for alkyl chain lengths between $n = 4$ and 8. Specifically, for larger *n*, theoretical studies suggest i) alkyl chains preferentially populating the surface more at the expense of anion representation, ii) alkyl chains reorienting and lying flat on the surface, as opposed to pointing perpendicular to the surface (as seen for small *n*) and iii) a more loosely packed, less dense interfacial region with lower surface tension.

Such compositional changes at the surface have been confirmed with LEIS[41] and XPS[25, 33] experiments, which are able to extract atomic densities at the gas-liquid interface. These studies have found more hydrocarbons and fewer anions present at the surface for larger *n*, with a distinct change in the orientation of alkyl chains at the surface observed around $n = 4$. Based on combinations of various photoelectron spectroscopy and atom scattering techniques, the hydrocarbon tails for $n \leq 4$ [$C_n$mim][Tf_2N] RTILs are found to stick outward into the vacuum, while the longer hydrocarbons ($n \geq 8$) tend to flop over on top of the surface.[33, 42] Moreover, as a function of hydrocarbon length, Kolbeck and coworkers[25] found the surface tension to decrease from $n = 1$ to 4, with the surface tension then remaining constant out to larger *n*. These results support significant topological changes in hydrocarbon/anion surface structure up to $n \leq 4$, beyond which the alkyl chains have established a dominant compositional presence at the [$C_n$mim][Tf_2N] surface.

Elegant molecular beam scattering studies from RTILs have been performed by Minton, McKendrick and coworkers, who scattered hyperthermal O(^{3}P) from [C_2mim][Tf_2N] and [C_{12}mim][Tf_2N] and detected inelastically scattered O atoms as well as reactively scattered OH

and H_2O from hydrogen abstraction at the liquid surface, which provide a probe of fractional hydrocarbon presence at the surface.[44] Given the stoichiometric difference in the number of CH_2 groups in each RTILs, (where H-abstraction reactions are expected to occur), they found a higher than stoichiometric reactivity for n = 12 compared to n = 2, thus inferring an increase in alkyl chain presence at the surface for $[C_{12}mim][Tf_2N]$ RTIL.[44] Further efforts by McKendrick et al. reactively scattered $O(^3P)$ from $[C_nmim][Tf_2N]$ RTILs, with n = 2, 4, 5, 8, and 12, and detected OH, the yield of which was found to increase with n.[43, 45] These results again support increasing alkyl coverage at the surface with hydrocarbon length, in good agreement with the current results, but where the OH yield increases continuously and does not saturate, thus suggesting alkyl chain coverage may still be evolving at n = 12. This may suggest a differential sensitivity to RTIL surface features between $O(^3P)$ and $NO(^2\Pi)$, for which lengthening of alkyl chains between n = 8 to 16 does not appear to affect the scattering dynamics. However, given the quite different reactive vs. inelastic scattering methods of probing the surface, the qualitative trends between these molecular beam studies are clearly in excellent agreement.

A greater propensity for alkyl groups present at the surface coupled with a more flexible interface with increasing n is also in very good agreement with inelastic scattering results presented in Figures 4.4 and 4.5. As a simple physical picture, smaller chain lengths result in a rougher surface, where incident translational energy is more efficiently transferred into the rotational degree of freedom. For small n, this would predict hotter IS rotational temperatures, with slightly cooler temperatures for larger n where the alkyl chains are lying flat on the surface. The branching ratio, α, increases even more dramatically ($\approx$ 40%) over this same range of chain lengths, consistent with a softer, more flexible surface at higher n that can more readily absorb molecular incident energy. Simply stated, larger n leads to a looser arrangement of alkyl chains

with a lower effective surface mass, whereby molecules can more readily rearrange and become trapped transiently on the surface. Our data reveal that such a longer, looser arrangement of alkyl chains on the surface leads to increased trapping of NO gas molecules on the surface, which is a necessary prerequisite for solvation into the bulk.

4.4.2 Spin-Orbit Distribution: Dependence on C_n

We next explore the nonadiabatic interactions occurring at the surface by considering the electronic spin-orbit ratios of the scattered NO, $[^2\Pi_{3/2}]/[^2\Pi_{1/2}]$, as a function of alkyl chain length (*n*) and collision energy (see Figure 4.6). At low E_{inc} = 2.7(9) kcal/mol and T_S = 353 K, spin-orbit ratios of $[^2\Pi_{3/2}]/[^2\Pi_{1/2}] \approx 0.5$ are observed (Figure 4.6), which implies only roughly one-third of the incident NO molecules are electronically excited ($^2\Pi_{1/2} \rightarrow {}^2\Pi_{3/2}$) in the collisional process. A simple estimate of an "electronic temperature" can be extracted from the Boltzmann expression $[^2\Pi_{3/2}]/[^2\Pi_{1/2}] = \exp(-E_{SO}/kT)$, with the energy difference between the two spin-orbit states (Eso) equal to 123 cm^{-1}.[65] At low E_{inc} , these spin-orbit ratios correspond to ~ 250 K, i.e., significantly hotter than the ~ 1 K rotational/electronic temperatures in the incident beam and yet still significantly colder than the 353 K liquid interface itself. Interestingly, the magnitude of this spin-orbit excitation appears to be *insensitive* to the alkyl chain length, recapitulating the trends observed for T_{rot}. This is not surprising, as both rotational and electronic populations resulting from fully accommodated species could be additionally sensitive to dynamical barriers along the desorption pathway. At high collision energies (E_{inc} = 20 kcal/mol) which facilitate both TD and IS scattering pathways, a greater spin-orbit ratio of $[^2\Pi_{3/2}]/[^2\Pi_{1/2}] \approx 0.66$ is observed (see Figure 4.6), corresponding to electronic temperatures now in excess of T_S. Since spin-orbit excitation out of the incident $^2\Pi_{1/2}$ ground state reflects a non-adiabatic event, a surface hopping sensitivity

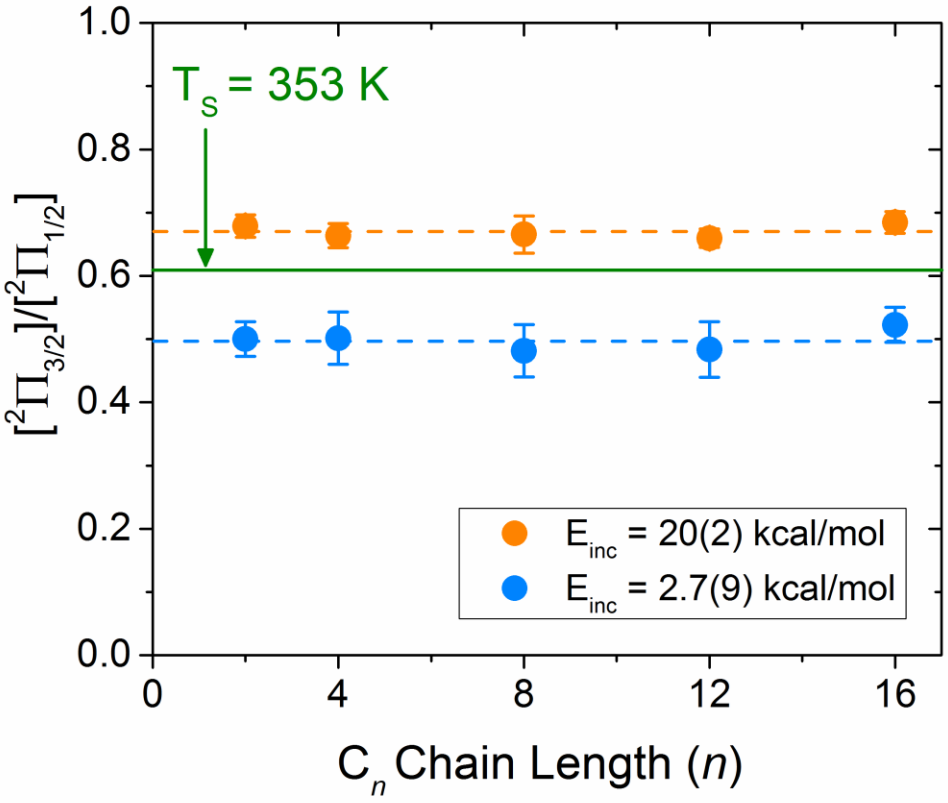

Figure 4.6 Spin-orbit ratio of scattered NO at both low/high E_{inc} and as a function of alkyl chain length. The horizontal green line represents the "spin-orbit temperature" corresponding to the surface temperature where $[^2\Pi_{3/2}]/[^2\Pi_{1/2}] = e^{-E_{SO}/kT}$ and E_{SO} = 123 cm^{-1}. Error bars represent 2σ standard deviations.

to incident translational energy would be at least qualitatively consistent with simple 1D Landau-Zener models for curve-crossing dynamics.[66, 67]

4.4.3 Dependence on Surface Temperature

Scattering dynamics of NO from this series of $[C_n mim][Tf_2N]$ RTILs have also been investigated as a function of surface temperature, with the resulting two-temperature fit parameters at high E_{inc} plotted vs. T_S in Figure 4.7. For visual clarity, only data for NO scattering

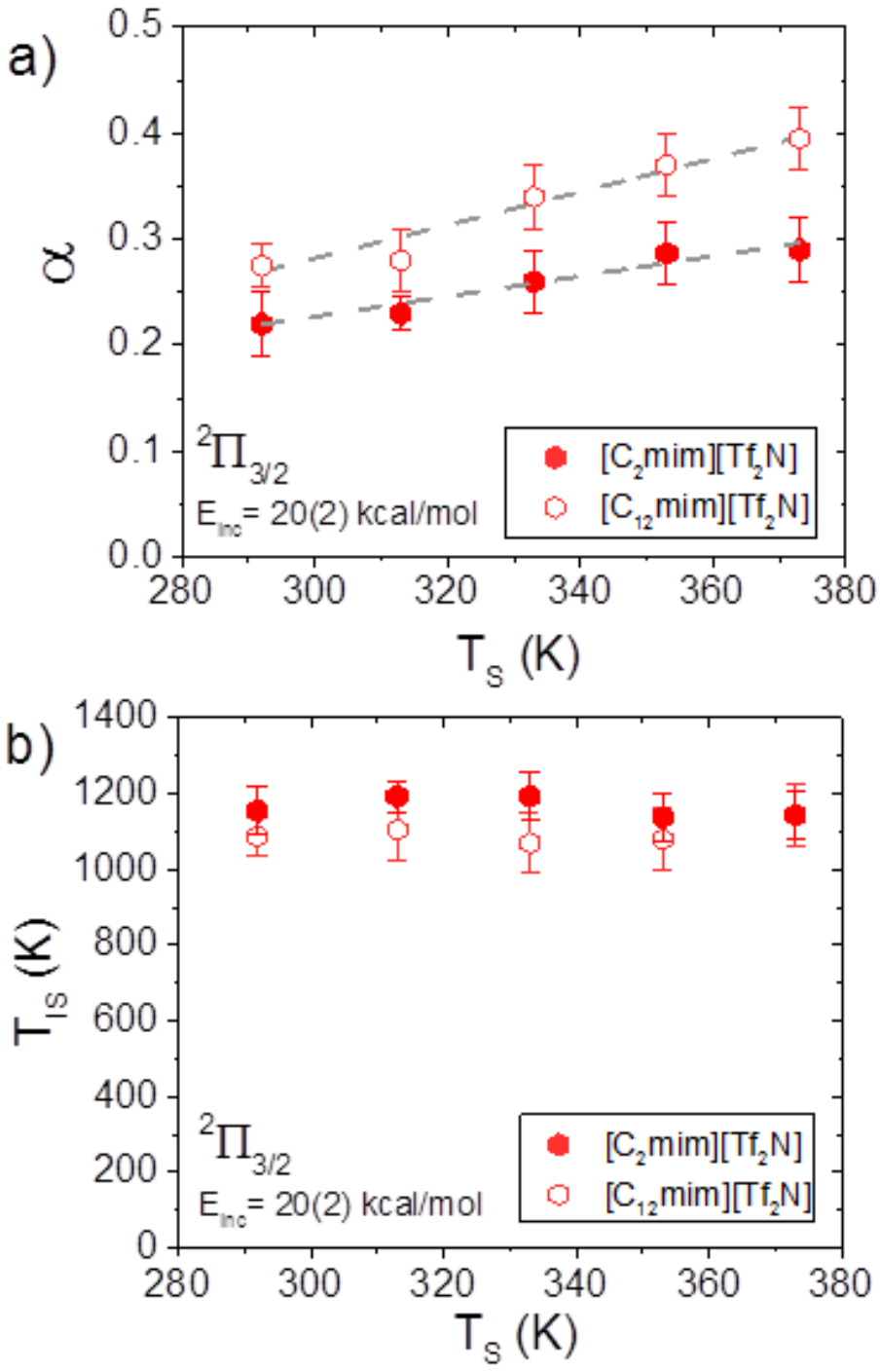

Figure 4.7 Two-temperature fit parameters to rotational distributions at E_{inc} = 20(2) kcal/mol as the surface temperature is varied for two alkyl chain length RTILs, *n* = 2 and 12. As the liquid temperature increases and the surface roughens, the branching into the TD channel increases linearly whereas the IS rotational temperatures remain essentially flat.

from $[C_2mim][Tf_2N]$ and $[C_{12}mim][Tf_2N]$ into the excited spin-orbit states are plotted, with the complete set of data for all RTILs and both spin-orbit states summarized in Table 4.1 as a function of surface temperature. Trends in alkyl chain length discussed earlier are apparent here as well, with longer alkyl chains resulting in a larger fraction of molecules trapping on the surface (i.e., higher α) and lower rotational excitation in the impulsively scattered channel (i.e., colder T_{IS}). As seen in Figure 4.7(a), the trapping-desorption fraction increases very nearly linearly with T_S, as observed in other gas-liquid scattering experiments[54, 68, 69] and can be ascribed to an increase in microscopic surface roughness with surface temperature. The slope is approximately 0.0015(19)/K for $[C_{12}mim][Tf_2N]$, i.e., 15(2)% more NO trap and desorb from the surface per 100 K increase in T_S, and 0.0010(12)/K for $[C_2mim][Tf_2N]$. As evident from Table 4.1, similar slopes (e.g., 6(4) – 16(3)% per 100 K) are observed for all RTILs studied and for both spin-orbit states. By way of comparison, CO_2 scattering (at E_{inc} = 15 kcal/mol) from perfluoropolyether (PFPE) and fluorinated self-assembled monolayer surfaces (F-SAMs) has also been studied over T_S = 232 – 323 K.[54] An equivalent analysis of the temperature dependence of α yields slopes of 17(3)% and 11(6)% per 100 K for the PFPE and F-SAM surfaces, respectively, i.e., reflecting a comparable range of NO + RTILs values as reported herein.

The impulsively scattered rotational temperatures are plotted in Figure 4.7(b), again focusing on the $^2\Pi_{3/2}$ state of n = 2 and 12 $[C_n mim][Tf_2N]$ RTILs. As noted earlier, the $T_{IS}(n = 2)$ values are slightly hotter than the $T_{IS}(n = 12)$ values. Furthermore, each of these T_{IS} rotational temperatures is significantly hotter than T_S, though with remarkably little sensitivity to the actual surface temperature. Thus, while the branching ratio α into the TD channel is clearly strongly influenced by T_S, the temperature of the liquid surface appears to have little influence over the

impulsively scattered IS temperatures observed experimentally. One simple physical picture for such behavior would be that interaction times with the surface for IS events are too short to be significantly influenced by liquid temperature, though the fraction of trajectories that proceed via IS vs. TD channels remains sensitive to thermally induced surface roughness.[68]

4.5 Conclusions

We report molecular beam scattering results of supersonically cooled NO from $[C_n\text{mim}][Tf_2N]$ RTILs with state-to-state resolution. The energy transfer between the surface and incident NO molecules is explored as a function of the incident collision energy, surface temperature and the cation alkyl chain length, which is varied over n = [2, 4, 8, 12, 16]. At low collision energies, all molecules accommodate and thermally desorb from the surface in a single Boltzmann temperature. However, even in this simplest of dynamical scenarios, we observe rotational and spin-orbit temperatures that are systematically *cooler* than the surface temperature. Furthermore, the rotational and spin-orbit temperatures are unaffected by the alkyl chain length. Thus, while physiochemical changes are occurring on the surface as n is varied in these $[C_n\text{mim}][Tf_2N]$ RTILs, the sticking probabilities that govern the TD channel for both the rotational and electronic degree of freedom are not influenced.

At high incident collision energies (E_{inc} = 20 kcal/mol), rotational populations of scattered molecules are well described by a two temperature TD/IS model. As these alkyl chains are lengthened, the landscape of the RTIL surface is changed such that more incident gas molecules trap on the surface and those that do impulsively scatter leave the surface with less rotational energy. These results are in agreement with a simple physical picture building on other theoretical and experimental work,[33, 44-48] whereby longer hydrocarbon RTILs have an enhanced

presence of alkyl chains at the surface that result in a more flexible, loosely packed surface more able to promote energy transfer into the liquid. Additionally, the surface temperature dependence of these RTILs on scattering dynamics has been explored, revealing for all RTILs studied that, as T_S increases, more molecules trap on the surface and yet the rotational component of the IS channel remains unaffected. In summary, these studies provide quantitative data into the rich quantum-state resolved dynamics for both inelastic and non-adiabatic scattering of open-shell species with the surfaces of room temperature ionic liquids, and how qualitative conformational changes occuring at the gas-liquid interface affect these dynamics. Detailed theoretical modeling will clearly be invaluable in interpreting the T_S and alkyl chain length dependence of these interfacial collision dynamics with more molecular level of detail, and toward which we hope these studies help provide the requisite stimulus.

References for Chapter 4

1. D. R. MacFarlane, J. Sun, J. Golding, P. Meakin and M. Forsyth, *Electrochim. Acta*, 2000, **45**, 1271-1278.

2. J. M. S. S. Esperanca, J. N. C. Lopes, M. Tariq, L. M. N. B. F. Santos, J. W. Magee and L. P. N. Rebelo, *J. Chem. Eng. Data*, 2010, **55**, 3-12.

3. J. G. Huddleston, A. E. Visser, W. M. Reichert, H. D. Willauer, G. A. Broker and R. D. Rogers, *Green Chem.*, 2001, **3**, 156-164.

4. A. Riisager, R. Fehrmann, M. Haumann and P. Wasserscheid, *Eur. J. Inorg. Chem.*, 2006, 695-706.

5. R. Sheldon, *Chem. Commun.*, 2001, 2399-2407.

6. F. Jutz, J. M. Andanson and A. Baiker, *Chem. Rev.*, 2011, **111**, 322-353.

7. R. Y. Lin, P. L. Taberna, S. Fantini, V. Presser, C. R. Perez, F. Malbosc, N. L. Rupesinghe, K. B. K. Teo, Y. Gogotsi and P. Simon, *J. Phys. Chem. Lett.*, 2011, **2**, 2396-2401.

8. A. Lewandowski and A. Swiderska-Mocek, *J. Power Sources*, 2009, **194**, 601-609.

9. S. Y. Lee, A. Ogawa, M. Kanno, H. Nakamoto, T. Yasuda and M. Watanabe, *J. Am. Chem. Soc.*, 2010, **132**, 9764-9773.

10. R. F. de Souza, J. C. Padilha, R. S. Goncalves and J. Dupont, *Electrochem. Commun.*, 2003, **5**, 728-731.

11. J. L. Anthony, J. L. Anderson, E. J. Maginn and J. F. Brennecke, *J. Phys. Chem. B*, 2005, **109**, 6366-6374.

12. J. E. Bara, R. D. Noble and D. L. Gin, *Ind. Eng. Chem. Res.*, 2009, **48**, 4607-4610.

13. L. A. Blanchard, Z. Y. Gu and J. F. Brennecke, *J. Phys. Chem. B*, 2001, **105**, 2437-2444.

14. L. A. Blanchard, D. Hancu, E. J. Beckman and J. F. Brennecke, *Nature*, 1999, **399**, 28-29.

15. M. Gorlov and L. Kloo, *Dalton T.*, 2008, 2655-2666.

16. R. Kawano, H. Matsui, C. Matsuyama, A. Sato, M. A. B. H. Susan, N. Tanabe and M. Watanabe, *J. Photoch. Photobio. A*, 2004, **164**, 87-92.

17. C. H. Hoffman and D. J. Nesbitt, *J. Phys. Chem. C*, 2016, **120**, 16687–16698.

18. L. S. Brown and S. J. Sibener, *J. Chem. Phys.*, 1988, **89**, 1163-1169.

19. N. V. Plechkova and K. R. Seddon, *Chem. Soc. Rev.*, 2008, **37**, 123-150.

20. A. E. Bradley, C. Hardacre, J. D. Holbrey, S. Johnston, S. E. J. McMath and M. Nieuwenhuyzen, *Chem. Mater.*, 2002, **14**, 629-635.

21. C. Ridings, V. Lockett and G. Andersson, *Phys. Chem. Chem. Phys.*, 2011, **13**, 17177-17184.

22. A. Triolo, O. Russina, H. J. Bleif and E. Di Cola, *J. Phys. Chem. B*, 2007, **111**, 4641-4644.

23. H. Tokuda, K. Hayamizu, K. Ishii, M. A. B. H. Susan and M. Watanabe, *J. Phys. Chem. B*, 2005, **109**, 6103-6110.

24. S. V. Dzyuba and R. A. Bartsch, *Chemphyschem*, 2002, **3**, 161-166.

25. C. Kolbeck, J. Lehmann, K. R. J. Lovelock, T. Cremer, N. Paape, P. Wasserscheid, A. P. Froba, F. Maier and H. P. Steinruck, *J. Phys. Chem. B*, 2010, **114**, 17025-17036.

26. P. J. Carvalho, M. G. Freire, I. M. Marrucho, A. J. Queimada and J. A. P. Coutinho, *J. Chem. Eng. Data*, 2008, **53**, 1346-1350.

27. C. Aliaga, G. A. Baker and S. Baldelli, *J. Phys. Chem. B*, 2008, **112**, 1676-1684.

28. I. S. Martinez and S. Baldelli, *J. Phys. Chem. C*, 2010, **114**, 11564-11575.

29. S. Rivera-Rubero and S. Baldelli, *J. Phys. Chem. B*, 2006, **110**, 4756-4765.

30. T. Iimori, T. Iwahashi, K. Kanai, K. Seki, J. H. Sung, D. Kim, H. O. Hamaguchi and Y. Ouchi, *J. Phys. Chem. B*, 2007, **111**, 4860-4866.

31. Y. Jeon, J. Sung, W. Bu, D. Vaknin, Y. Ouchi and D. Kim, *J. Phys. Chem. C*, 2008, **112**, 19649-19654.

32. X. H. Li, G. C. Schatz and D. J. Nesbitt, *J. Phys. Chem. B*, 2012, **116**, 3587-3602.

33. T. Hammer, M. Reichelt and H. Morgner, *Phys. Chem. Chem. Phys.*, 2010, **12**, 11070-11080.

34. K. R. J. Lovelock, C. Kolbeck, T. Cremer, N. Paape, P. S. Schulz, P. Wasserscheid, F. Maier and H. P. Steinruck, *J. Phys. Chem. B*, 2009, **113**, 2854-2864.

35. C. Kolbeck, T. Cremer, K. R. J. Lovelock, N. Paape, P. S. Schulz, P. Wasserscheid, F. Maier and H. P. Steinruck, *J. Phys. Chem. B*, 2009, **113**, 8682-8688.

36. V. Lockett, R. Sedev, C. Bassell and J. Ralston, *Phys. Chem. Chem. Phys.*, 2008, **10**, 1330-1335.

37. V. Lockett, R. Sedev, S. Harmer, J. Ralston, M. Horne and T. Rodopoulos, *Phys. Chem. Chem. Phys.*, 2010, **12**, 13816-13827.

38. S. Caporali, U. Bardi and A. Lavacchi, *J. Electron Spectrosc.*, 2006, **151**, 4-8.

39. E. Bodo, L. Gontrani, R. Caminiti, N. V. Plechkova, K. R. Seddon and A. Triolo, *J. Phys. Chem. B*, 2010, **114**, 16398.

40. J. Bowers, M. C. Vergara-Gutierrez and J. R. P. Webster, *Langmuir*, 2004, **20**, 309-312.

41. I. J. Villar-Garcia, S. Fearn, G. F. De Gregorio, N. L. Ismail, F. J. V. Gschwend, A. J. S. McIntosh and K. R. J. Lovelock, *Chem. Sci.*, 2014, **5**, 4404-4418.

42. T. Iwahashi, T. Nishi, H. Yamane, T. Miyamae, K. Kanai, K. Seki, D. Kim and Y. Ouchi, *J. Phys. Chem. C*, 2009, **113**, 19237.

43. C. Waring, P. A. J. Bagot, J. M. Slattery, M. L. Costen and K. G. McKendrick, *J. Phys. Chem. A*, 2010, **114**, 4896-4904.

44. B. H. Wu, J. M. Zhang, T. K. Minton, K. G. McKendrick, J. M. Slattery, S. Yockel and G. C. Schatz, *J. Phys. Chem. C*, 2010, **114**, 4015-4027.

45. M. A. Tesa-Serrate, B. C. Marshall, E. J. Smoll, S. M. Purcell, M. L. Costen, J. M. Slattery, T. K. Minton and K. G. McKendrick, *J. Phys. Chem. C*, 2015, **119**, 5491-5505.

46. J. R. Roscioli and D. J. Nesbitt, *J. Phys. Chem. A*, 2011, **115**, 9764-9773.

47. M. P. Ziemkiewicz, A. Zutz and D. J. Nesbitt, *J. Phys. Chem. C*, 2012, **116**, 14284-14294.

48. A. Zutz and D. J. Nesbitt, *J. Phys. Chem. C*, 2015, **119**, 8596-8607.

49. A. S. Pensado, P. Malfreyt and A. A. H. Padua, *J. Phys. Chem. B*, 2009, **113**, 14708-14718.

50. K. Nakajima, A. Ohno, H. Hashimoto, M. Suzuki and K. Kimura, *J. Chem. Phys.*, 2010, **133**.

51. M. P. Ziemkiewicz, J. R. Roscioli and D. J. Nesbitt, *J. Chem. Phys.*, 2011, **134**, 234703.

52. D. H. Zaitsau, G. J. Kabo, A. A. Strechan, Y. U. Paulechka, A. Tschersich, S. P. Verevkin and A. Heintz, *J. Phys. Chem. A*, 2006, **110**, 7303-7306.

53. M. Ziemkiewicz, M. Wojcik and D. J. Nesbitt, *J. Chem. Phys.*, 2005, **123**, 224307.

54. B. G. Perkins and D. J. Nesbitt, *J. Phys. Chem. B*, 2008, **112**, 507-519.

55. J. R. Roscioli and D. J. Nesbitt, *Faraday Discuss.*, 2011, **150**, 471-479.

56. G. D. Kubiak, J. E. Hurst, H. G. Rennagel, G. M. McClelland and R. N. Zare, *J. Chem. Phys.*, 1983, **79**, 5163-5178.

57. G. M. Mcclelland, G. D. Kubiak, H. G. Rennagel and R. N. Zare, *Phys. Rev. Lett.*, 1981, **46**, 831-834.

58. R. R. Cavanagh and D. S. King, *Phys. Rev. Lett.*, 1981, **47**, 1829-1832.

59. J. J. Nogueira, S. A. Vazquez, O. A. Mazyar, W. L. Hase, B. G. Perkins, D. J. Nesbitt and E. Martinez-Nunez, *J. Phys. Chem. A*, 2009, **113**, 3850-3865.

60. D. Kim and G. C. Schatz, *J. Phys. Chem. A*, 2007, **111**, 5019-5031.

61. Y. X. Peng, L. Liu, Z. Cao, S. Li, O. A. Mazyar, W. L. Hase and T. Y. Yan, *J. Phys. Chem. C*, 2008, **112**, 20340-20346.

62. E. Martinez-Nunez, A. Rahaman and W. L. Hase, *J. Phys. Chem. C*, 2007, **111**, 354-364.

63. T. Y. Yan, W. L. Hase and J. R. Barker, *Chem. Phys. Lett.*, 2000, **329**, 84-91.

64. N. Shenvi, S. Roy and J. C. Tully, *J. Chem. Phys.*, 2009, **130**, 174107.

65. G. Herzberg, *Spectra and Molecular-Structure I. Spectra of Diatomic-Molecules*, Princeton Univ. Press, Princeton, NJ, 1968.

66. C. Zener, *Proceedings of the Royal Society of London Series a*, 1932, **137**, 696-702.

67. *Nitrogen Oxides (NOx), Why and How they are Controlled*, Report US EPA Technical Bulletin No. EPA-456/F-99-006R, 1999.

68. M. E. King, K. M. Fiehrer, G. M. Nathanson and T. K. Minton, *J. Phys. Chem. A*, 1997, **101**, 6556-6561.

69. M. E. King, M. E. Saecker and G. M. Nathanson, *J. Chem. Phys.*, 1994, **101**, 2539-2547.

Chapter 5

Angle-Resolved Molecular Beam Scattering of NO at the Gas- Liquid Interface*

5.1 Introduction

Nitric oxide and nitrogen oxides (NO_x = NO + NO_2) are major pollutants in the atmosphere and play a crucial role in the formation of acid rain and photochemical smog.[1-4] While there are natural sources of atmospheric NO_x such as lightening, soil emissions and forest fires, its considerable presence in the atmosphere is largely anthropogenic, with leading emission sources from power plants and fossil fuel emissions.[5, 6] One way to curb the introduction of excess NO_x into the atmosphere is by the use of wet scrubbers, which when placed in smokestacks can remove NO_x from flue gas emissions.[4, 7, 8] As a result, NO collisions at gas-liquid interfaces have important implications in pollution chemistry. NO also plays an important role in the chemistry of atmospheric aerosols,[5, 9-12] where thermal adsorption/desorption at the gas-liquid interface significantly influences the subsequent chemical oxidation processes. For these and many other atmospheric pollution chemistry applications in environmental chemistry, a first principles understanding of how small molecules such as NO transfer energy to and/or equilibrate with a gas-liquid interface becomes crucially relevant.

As one of several questions of fundamental interest, we ask what are the energy transfer dynamics of NO colliding with complex liquid surfaces? In particular, what properties of the

*To be submitted to J. Chem. Phys.

interface govern whether a gas molecule sticks, thermally accommodates, and dissolves into the liquid, or simply interacts with the liquid surface transiently to achieve full thermal accommodation with respect to internal rovibronic quantum states? Molecular scattering studies have provided critically important insights into the nature of such gas-liquid dynamics and how a number of liquid properties might be engineered to "tune" these interfacial interactions systematically. Specifically, multiple experiments have investigated the behavior of gas molecules striking liquid surfaces, probing how surface temperature,[13-15] presence (or absence) of solvated ions,[16, 17] and different functional groups[18, 19] at the interface can influence the resulting collision dynamics. Time of flight mass spectrometry[17, 19-22] and quantum state resolved[15, 19, 23-26] detection techniques have also proven to be extremely powerful and complementary tools for examining elastic, inelastic, and reactive molecular scattering at liquid surfaces. In these studies, a diverse range of molecules and atoms (e.g., CO_2, HCl, OH, O, noble gases, etc.), have been scattered from a variety of low vapor pressure liquids, the results of which have helped formulate a more predictive framework for energy transfer dynamics of atomic, diatomic and polyatomic colliders at the gas-liquid interface.

In the limit where molecules have become fully thermally accommodated with and eventually desorb from a liquid interface, the outgoing distributions are often presumed to be well described by rotational, vibrational, translational and electronic temperatures characteristic of the surface temperature (T_S). From microscopic reversibility/detailed balance considerations,[27, 28] this behavior would imply unity sticking coefficients for the corresponding reverse collisional event, independent of internal quantum state, incident angle, and range of speeds appreciably sampled in a gas at T_S. Indeed, such simple, intuitive behavior of complete thermal equilibration in the desorbing flux has been verified experimentally for scattering of CO_2

from perfluoropolyether (PFPE)[13] and HCl from alkanethiol self-assembled monolayers (SAMs)[29] over a wide range of surface temperatures.

In the case of NO, however, the rotational and electronic temperatures of the desorbing molecules are *often not* in equilibrium with the liquid interface. Instead, the molecules are better characterized by distinctly *subthermal* temperatures (i.e., $T_{rot} < T_s$) for NO desorbing from condensed phase interfaces.[14, 30-35] A variety of low incident energy molecular scattering experiments have revealed these results from (i) crystalline, (ii) organic self-assembled monolayer, (iii) low vapor pressure liquid and even (iv) molten metal surfaces, all with varying degrees of rotational cooling observed.[14, 18, 34-36] Indeed, arguably the most dramatic example of this can be found in temperature programmed desorption (TPD) studies, where absorbed NO molecules have residence times of minutes to hours and thus certainly have achieved complete thermal equilibrium with the surface. Nevertheless, cold rotational temperatures on the order of 235(35) K have been noted for NO desorbing from Ru(001)[30] at T_s = 455 K, with correspondingly sub-thermal values (T_{rot} = 600(4) K) for NO desorption from even hotter (T_S = 1100 K) Pd(111) surfaces.[31]

Previous work exploiting quantum state-resolved laser induced fluorescence (LIF) detection of jet-cooled NO molecular beams scattered from the gas-liquid interface has provided modest but clearly supporting evidence for such non-equilibrium desorption behavior. Rotational temperatures have been observed some 30 K *cooler* than T_s for NO scattering from both imidazolium-based room temperature ionic liquids (RTILs) and molten gallium. Due to geometrical limitations in the LIF collection optics, however, these studies were only able to detect NO molecules emerging into a single, near-specular scattering angle. Apparatus modifications implemented in the present work have successfully eliminated such optical

constraints and now permit quantum state-resolved detection of the scattered NO flux as a function of solid angle in the 2π upper half plane, most importantly even *backscattering* into solid angles more glancing than the incident molecular beam. This new capability makes possible i) angle- ii) collision energy, and ii) quantum state-resolved investigation of NO scattering dynamics at a series of gas-liquid interfaces, with which we can help further probe and elucidate the observed non-equilibrium behavior.

Specific questions of interest at low E_{inc} are as follows. Do NO molecules in all quantum states fully accommodate on the liquid surface, which, for example, would imply scattering with forward/backward symmetry? Does the thermally accommodated NO flux reemerge into a $\cos(\theta_s)$ distribution for all internal quantum states, which would be consistent with unity sticking coefficients in the reverse direction for all incident angles? What are the NO rotational/electronic distributions as a function of final scattering angle and what does this suggest with respect to "surface-hopping" dynamics between $^2\Pi_{1/2}$ and $^2\Pi_{3/2}$ electronic surfaces? Could orientation and/or quantum state dependent adsorption dynamics for NO at a liquid interface be responsible for the non-equilibrium behavior evidenced in subthermal rotational and spin-orbit temperatures? Finally, how are these experimental trends all consistent with detailed balance and microscopic reversibility considerations?

It is worth clarifying at the outset that our ability to independently probe angular and internal quantum state distributions samples two different aspects of the scattering dynamics. For example, detailed balance considerations and observation of a $\cos(\theta_s)$ distribution for any one NO quantum state permit rigorous prediction of the angular independence of *sticking coefficients* for that specific quantum state. However, the existence of such $\cos(\theta_s)$ angular distributions does not impose any corresponding constraint on the actual rotational and/or spin-orbit internal

quantum state distributions of the desorbing NO. Thus, as we shall see, it is entirely possible to have $\cos(\theta_s)$ angular distributions mimicking perfect angle independent thermal accommodation of the incident flux, but with *non-equilibrium* internal state distributions in the outgoing flux. Indeed, by detailed balance considerations, such observations directly imply quantum state dependent sticking coefficients and signal the presence of dynamical barriers to adsorption and desorption processes.

In this work, we explore angle- and quantum-state resolved collision dynamics at the gas-liquid interface via molecular beam scattering of NO from low vapor pressure [bmim][Tf_2N] RTIL, squalane and perfluoropolyether (PFPE) liquids. Specifically, we first exploit tunable beam collision energies at low E_{inc} to investigate the angular dependence of thermally accommodated NO desorption dynamics in isolation. Next, angle-resolved IS scattering dynamics are explored at high E_{inc} to probe the scattering angle dependence of microscopic branching between TD vs. IS pathways. Finally, we take advantage of our quantum state-resolved LIF detection capabilities at high E_{inc} to examine the explicit angular dependence for rotational and spin-orbit distributions in the scattered NO.

5.2 Experimental

For the present studies, supersonically cooled NO has been scattered at $\theta_{inc} = 45(1)^o$ from 1-butyl-3-methyl-trifluorosulfonylimide ([bmim][Tf_2N]), perfluoropolyether (PFPE), and squalane gas-liquid interfaces, followed by with quantum state and angle-resolved ($\theta_s = -60^o$ to 60^o) LIF detection of the subsequently scattered NO molecules. The scattering takes place in a 90 L vacuum chamber, evacuated with a 1500 L/s turbomolecular pump that achieves base pressures of 2 $x10^{-8}$ Torr. The jet-cooled molecular beam of NO is produced from an Even-Lavie

pulsed valve with an 80 μs pulse width, resulting in rotationally and electronically cold NO with T_{rot} ~ 1 K and only the ground spin-orbit state significantly populated ($^2\Pi_{1/2}$; J=0.5). Stagnation gas mixtures consist of 1% NO in either Ne-70 (70:30 mixture of Ne:He) or H_2 diluent, which permits tuning the incident energies from E_{inc} = 2.7(9) to 20(2) kcal/mol, respectively. After passing through a 3 mm skimmer 5.4 cm downstream of the nozzle, the collimated beam strikes the liquid surface at θ_{inc} = 45° in a 4.4 cm x 2.4 cm x 0.5 cm stainless steel reservoir, resulting in a 1.1 cm x 0.8 cm locus for NO scattering on the gas-liquid interface.

The [bmim][Tf_2N] species (IoLiTec, 99% purity) is degassed by stirring/heating for at least six hours prior to placement in the chamber, with similar degassing protocol for liquid squalane ($C_{30}H_{62}$, Sigma-Aldrich, 99% purity) and PFPE ($F(CF(CF_3)CF_2O)_{14}CF_2CF_3$, Krytox 1506, Sigma-Aldrich). All liquid temperatures are held constant at T_s = 293(1) K, with scattered

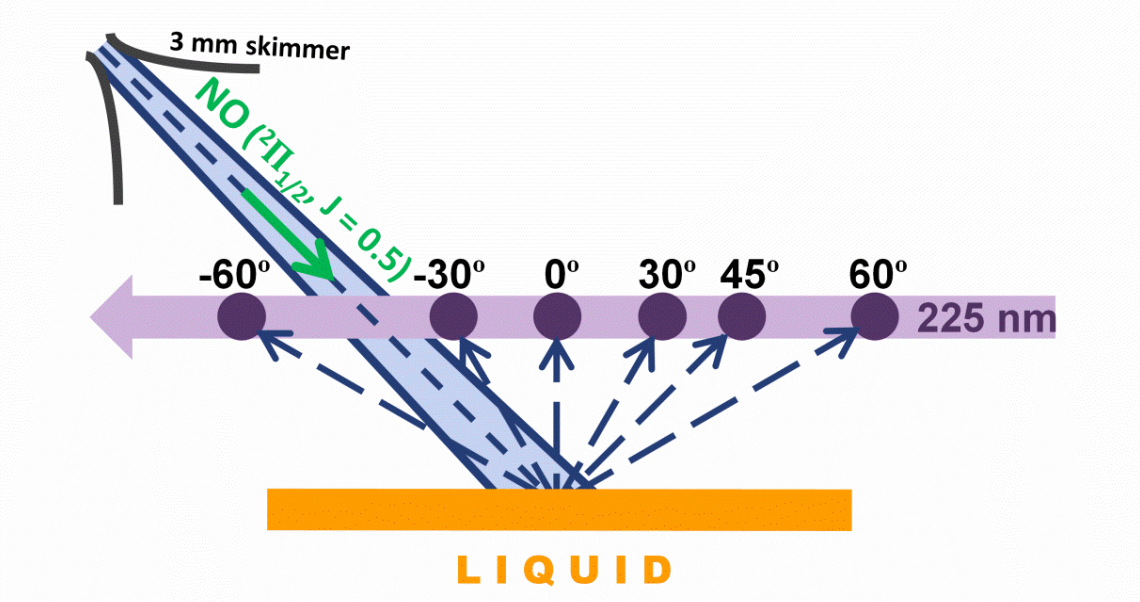

Figure 5.1 An incident beam of supersonically cooled NO ($^2\Pi_{1/2}$(N=0), T_{rot} ~ 1 K) strikes the liquid surface at 45(1)° and E_{inc} = 2.7(9) or 20(2) kcal/mol. Scattered NO molecules are detected with quantum-state resolution via LIF in a 13 mm^3 probe volume, which is scanned along the 225 nm excitation laser path to achieve angular detection windows at θ_s = -60(3)°, -30(9)°, 0(12)°, 30(9)°, 45(6)° and 60(3)°.

NO molecules detected using laser induced fluorescence (LIF) on the γ band ($A^2\Sigma^+ \leftarrow X^2\Pi$). The requisite UV pulses (~ 225 nm) are generated via the tripled output of a YAG-pumped dye laser, which enters the chamber through baffle arms and passes 1.6 cm above the gas-liquid interface and in parallel to the scattering plane (see Fig. 5.1). Fluorescence from the scattered NO is focused onto a photomultiplier tube (PMT) through a 4 mm diameter pinhole mask in a 1:1 confocal imaging geometry. This spatial filtering permits fluorescence detection from only a restricted focal region (13 mm^3), which, by translating the PMT with respect to the scattering plane, allows systematic variation of the detection angle into which the NO has been scattered. Specifically, the measured scattering angle windows are θ_s = -60(3)º, -30(9)º, 0(12)º, 30(9)º, 45(6)º and 60(3)º, where the uncertainties represent 1σ standard deviations based on statistical sampling of all collision free (i.e., straight line) trajectories from the liquid surface to the LIF detection focal volume.

The pulsed valve duration (≈ 80 μs) is much longer than time scales for the gas-liquid collision event (≈ 1-10 ps) and thus the data reflect scattering under steady state conditions. A boxcar integrator captures the fluorescence signal at the peak of the time domain signal, therefore NO molecules are probed that arise from both i) full thermal accommodation/desorption (TD) as well as ii) direct, impulsive scattering (IS) from the gas-liquid interface. The LIF data is least squares fit using STARPAC software to a LIFBASE model of the NO spectrum,[35, 37, 38] from which quantum state populations and uncertainties are extracted. The reliability of such fitting routines is systematically tested on ≈ 10^{-6} Torr samples of NO introduced into the vacuum chamber, the quantitative spectral analysis of which correctly recapitulates room temperature rotational and electronic distributions within experimental uncertainty. At least 3 spectral scans are obtained and least squares fit for each i) collision energy, ii) liquid, and iii) scattering angle,

with the results averaged to yield improved standard deviations of the mean as well as a more realistic assessment of statistical errors.

5.3 Results

By way of initial overview, sample LIF spectra for forward [θ_s = 30(9)°] and backward [θ_s = -30(9)°] scattered NO are displayed in Figure 5.2, under hyperthermal incident beam conditions of E_{inc} = 20(2) kcal/mol and an incident angle of θ_{inc} = 45°. In contrast to the incident NO beam, which has nearly all population supersonically cooled into ($^2\Pi_{1/2}$; J = 0.5), the scattered spectra reveal extensive rotational population up to J ≈ 45.5 in both ground ($^2\Pi_{1/2}$) and

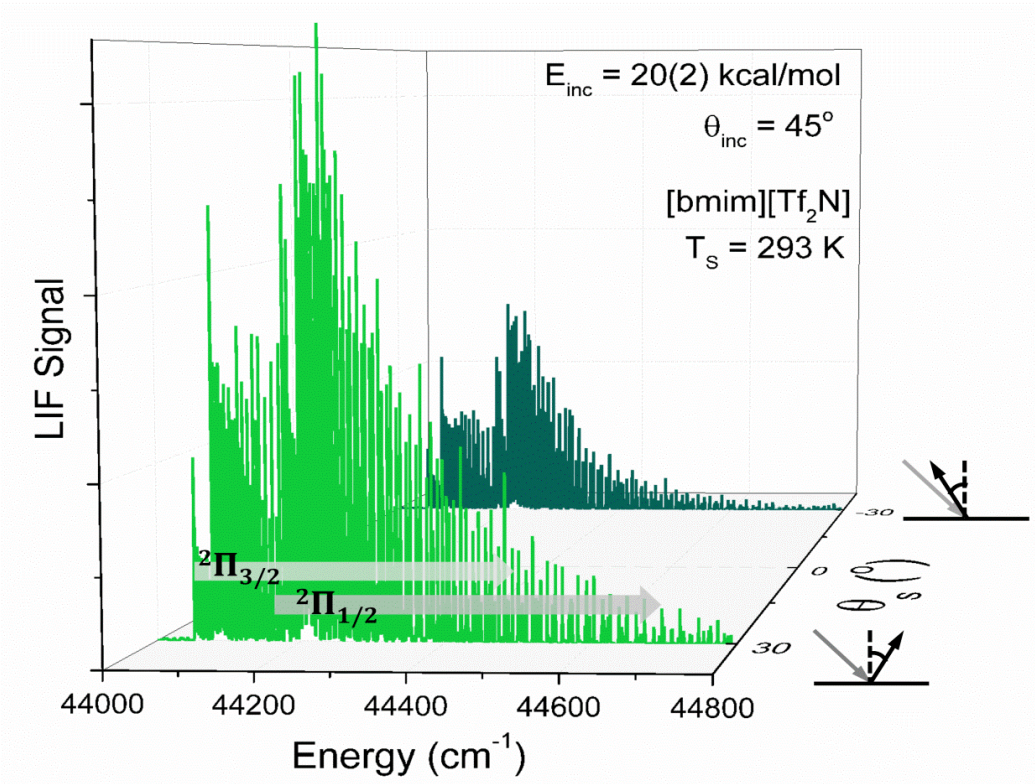

Figure 5.2 Sample LIF spectra for θ_s = -30(9)° and 30(9)° scattering of jet-cooled NO ($^2\Pi_{1/2}$ (N=0)) at E_{inc} = 20(2) kcal/mol from [bmim][Tf_2N], which reveal significant inelastic energy transfer into highly excited rotational (up to J ≈ 45.5) and spin-orbit electronic ($^2\Pi_{1/2}$ and $^2\Pi_{3/2}$) states. The 3-fold more intense signals observed in the forward vs. backward direction indicate a strong propensity for forward scattering at high collision energies.

excited ($^2\Pi_{1/2}$) spin-orbit manifolds. This indicates substantial inelastic rotational energy transfer as well as significant nonadiabatic spin-orbit "surface-hopping" dynamics at the gas-liquid interface, for both backward- and forward-scattered NO species. As physically expected under hyperthermal conditions and $\theta_{inc} = 45^o$, there is a marked predominance for *forward* scattering in the near-specular direction, with roughly 3x more signal at $\theta_s = 30^o$ than at $\theta_s = -30^o$. Equally noteworthy is the still quite significant fraction of NO recoiling *in the backward direction*, even at $\theta_{inc} = 45^o$ and high incident collision energies. Since collisions from a nominally "flat" liquid surface potential would conserve parallel momentum and thereby predict specular scattering in the forward direction, this speaks to the high degree of surface *corrugation* on the nanometer scale that such gas-liquid interfaces must present to the incoming NO projectile.

5.3.1 Low Energy Collisions: Cos(θ_s) Angular Distributions and Thermal Desorption Dynamics

To simplify our scattering conditions, we first consider data at low collision energies (E_{inc} = 2.7(9) kcal/mol), where from previous gas-liquid scattering studies, one expects all incident molecules to stick, have sufficient opportunity to fully thermally accommodate, and eventually desorb from the liquid surface. By way of sample data, NO rotational distributions for the ground ($^2\Pi_{1/2}$) spin-orbit state are plotted in Figure 5.3 as a function of final scattering angle (θ_s), where in anticipation of a "temperature-like" Maxwell-Boltzmann behavior, the data have been reported as semilogarithmic plots of degeneracy scaled rotational populations vs. internal rotational energy. The rotational distributions at all θ_s are indeed well described by a common temperature, T_{rot} ~ 257(10) K, i.e., considerably cooler than the 293 K surface temperature and, most notably, *independent* of the final scattering angle. Data for all four spin-orbit/lambda-doublet states are extracted from at least 3 spectral scans at each final angle, with temperature

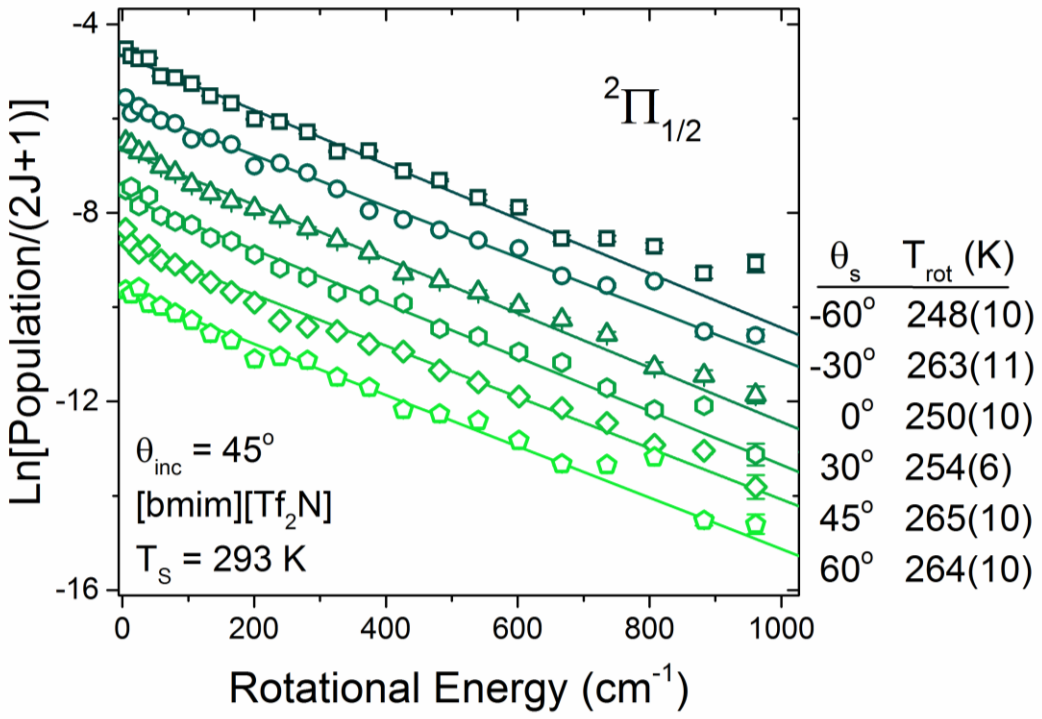

Figure 5.3 Sample rotational Boltzmann plots for ground spin-orbit scattered NO($^2\Pi_{1/2}$) at E_{inc} = 2.7(9) kcal/mol as a function of scattering angle θ_s. Note that T_{rot} is i) independent of θ_s and yet ii) systematically *cooler* ($\Delta T \approx -35$ K) than the liquid surface temperature. By detailed balance considerations, these observations are consistent with i) *angle-independent* and yet ii) internal *quantum-state dependent* sticking coefficients for incoming NO at low incident collision energies.

uncertainties estimated from the standard deviation of values obtained for the individual Boltzmann least squares fits. Since statistically significant differences in the Λ-doublet data are not evident, the reported populations are therefore simply summed over the final (e/f) parity states. Similar cooling and angle independent trends are also confirmed for Boltzmann plots for the excited spin-orbit ($^2\Pi_{3/2}$) state, though with a much smaller magnitude cooler from T_S. Specifically, the Maxwell-Boltzmann plots are again quite linear with no dependence of the scattered rotational temperatures on final scattering angle θ_s. Thus, evidence for "rotational cooling" below the surface temperature is observed for both spin-orbit-conserving and spin-orbit changing trajectories, with $T_{rot}(^2\Pi_{1/2}) \approx 257(10)$ K< $T_{rot}(^2\Pi_{3/2}) \approx 254(10)$ K (where numbers in

parentheses represent one standard devotion of the mean from multiple measurements) and value less than the actual surface temperature of $T_s \approx 293(1)$ K.

Rotational temperatures for both ground and spin-orbit excited states of NO averaged over multiple scans are displayed vs. θ_s in a polar plot (Fig. 5.4(a)). The data clearly illustrate two important points: T_{rot} is i) *independent* of scattered angle and yet ii) statistically different for the two spin-orbit states, with excited and ground spin-orbit T_{rot} values cooler by ~ 10 K and ~ 35 K than the surface temperature. We note that such behavior (i.e., $T_{rot} < T_s$ for scattering at low E_{inc}) is distinctly different from molecules such as HCl and CO_2,[13, 29] which have been found to thermally desorb from a variety of liquid surfaces with $T_{trans} \approx T_{rot} \approx T_s$. As previously hypothesized[14] and as detailed balance arguments insist,[27] this necessitates the presence of quantum state-dependent sticking dynamics that favor an excess of *rotationally colder* species in the thermally desorbing NO flux. Specifically, this means that *higher* energy rotational states colliding with the interface under equilibrium conditions ($T_{rot} \approx T_S$) must have *smaller* sticking probabilities, and vice versa. Since the reverse *desorption* rates of thermally accommodated NO must reflect this behavior precisely by detailed balance, the outgoing NO flux is thereby systematically depleted in higher J states and thus "colder" than T_S, as observed experimentally. One simple physical mechanism for achieving such behavior would be the presence of NO orientation dependent potential wells for molecular adsorption at the liquid surface, which could dynamically allow more slowly rotating J states in the incoming flux to better align and thereby stick with higher efficiency than more rapidly rotating molecules in higher J states. By way of contrast, we see do not see corresponding evidence for any dependence in the desorbing NO distributions on scattering angle. Again by detailed balance considerations, such an independence (at low E_{inc}) of quantum state rotational distributions (T_{rot}) with θ_s is consistent

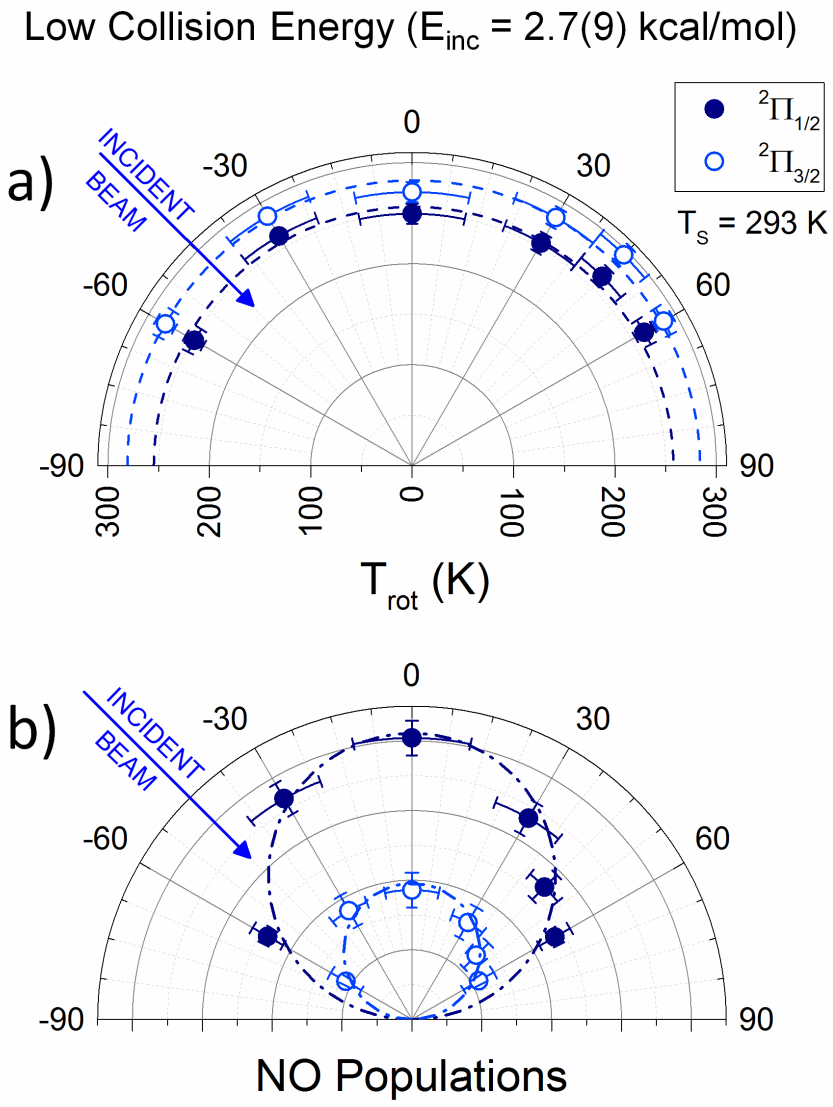

Figure 5.4 Polar plots for NO scattering at E_{inc} = 2.7(9) kcal/mol. a) NO rotational temperatures for each spin-orbit state as a function of final scattering angle θ_s. Note the rotational cooling effects, with $T_{rot}(^2\Pi_{1/2})$ and $T_{rot}(^2\Pi_{3/2})$ some $\Delta T \approx$ -35 K and $\Delta T \approx$ -10 K cooler than T_s, respectively. (b) NO populations for each spin-orbit state as a function of θ_s, corrected for distance to angular detection region (see text). Note that the fits to $\cos(\theta_s)$ distributions (dashed circles) are consistent with complete thermal accommodation at the surface and unity sticking coefficients for all angles (θ_s) at low collision energies. Error bars represent standard deviations of the mean (σ_{mean}) from multiple ($\geq$ 3) frequency scans.

with *angle-independent* sticking/adsorption probabilities for incident NO striking the gas-liquid interface in a specific rovibronic state.

We can rigorously test these detailed balance predictions by examining actual quantum state-resolved density distributions of the scattered NO. For a probe laser beam parallel to the gas-liquid interface, the NO densities must first be corrected for variation in distance from the surface (see Figure 5.1), which we can model by averaging over the $1/r^2$ density drop off from the liquid surface to all points in the detection volume. This procedure yields corrected quantum state-resolved NO densities corresponding along some arc at fixed radial distance from the gas-liquid collision center. These NO densities are plotted as a function of scattered angle in Figure 5.4(b), where for simplicity we have further summed over all rotational states within each spin-orbit state manifold. The data fit very well to a $\cos(\theta_s)$ angular distribution, which is again consistent with the simple physical picture of NO molecules *at all incident angles* sticking to and thermally accommodating with the surface. By detailed balance arguments, such data, along with the experimentally-observed angle-independence of the rotational temperatures, strongly supports a simple physical picture of NO scattering from the liquid at low E_{inc} arising from all trajectories *fully thermally accommodating* and eventually *desorbing* from the gas-liquid interface.

Two final comments in this sub-section are worth noting. First of all, the presence of such uniform $\cos(\theta_s)$ angular distributions does not require sticking coefficients to be independent of *internal quantum state*. Indeed, this is already clearly demonstrated in the rotational Boltzmann distributions for the desorbing NO, which are distinctly out of equilibrium with the surface temperature T_S. Furthermore, significant deviations from equilibrium behavior are also observed in electronic degrees of freedom. For example, as is clear in Fig. 5.4(b), NO signals out of the

excited spin-orbit manifold are only ≈ 2 times smaller than that of the ground state manifold. This would correspond to a spin-orbit temperature of $T_{elec} \approx 220$ K, i.e., again very much out of equilibrium with and substantially colder than T_S.

Secondly, we note that these LIF-based measurements yield densities rather than fluxes of the probed NO species. If the desorbing speed distributions of NO are the same at all scattering angles, then the density-to-flux conversion factor would be the same for each θ_s measurement and a cosine density distribution would also be a cosine flux distribution. By detailed balance arguments,[27] this would stipulate the sticking coefficients for NO collisions at low E_{inc} to be independent of incident θ_{inc} and speed (that is, for a range of thermal speeds sampled by thermally desorbing molecules, which breaks down at hyperthermal energies). In turn, this would require all outgoing distributions (speed, J, spin-orbit, vibration, etc.) from thermally accommodated NO to be independent of θ_s. It is worth stressing that sticking coefficients being independent of angle and speed is *not* equivalent to sticking coefficients being *unity* for all NO internal quantum states. Indeed, by detailed balance, a perfectly unity sticking coefficient would result in the much stronger requirement that $T_{rot} \approx T_{elec} \approx T_S$, which is in fact *not* observed experimentally. Our LIF detection of NO in this experiment does not directly measure velocities of the scattered molecules. However, the results presented above are certainly *consistent* with the simplest Occam's razor physical picture of both angle and speed independent sticking coefficients, at least for the range of incident energies commensurate with T_S.

5.3.2 High Energy Collisions: Angle-Dependent Rotational Distributions

We next consider how such angular independence in the scattering data may be influenced by magnitude of the incident collision energy. At higher incident speeds, the

Boltzmann plots become significantly non-linear, which has been interpreted in numerous gas-liquid scattering systems in terms of a linear combination of thermal desorption (TD) and impulsive scattering (IS) pathways. With the present experimental capability for final angle/quantum-state resolved detection, we can now actually isolate and probe the dynamics of these two separate scattering pathways as a function of θ_s. In Figure 5.5, the TD and IS rotational populations obtained from LIF spectral fits at E_{inc} = 20(2) kcal/mol and θ_{inc} = 45º are shown for the ground $^2\Pi_{1/2}$ spin-orbit state in a waterfall plot vs. scattering angle and rotational energy, with the distributions at each angle normalized to unity. Significant rotational excitation up to ≈ 4000 cm^{-1} (J = 45.5) is observed and, quite differently than behavior described previously at low E_{inc}, the rotational distributions now clearly evolve toward *hotter* temperatures with *increasing*

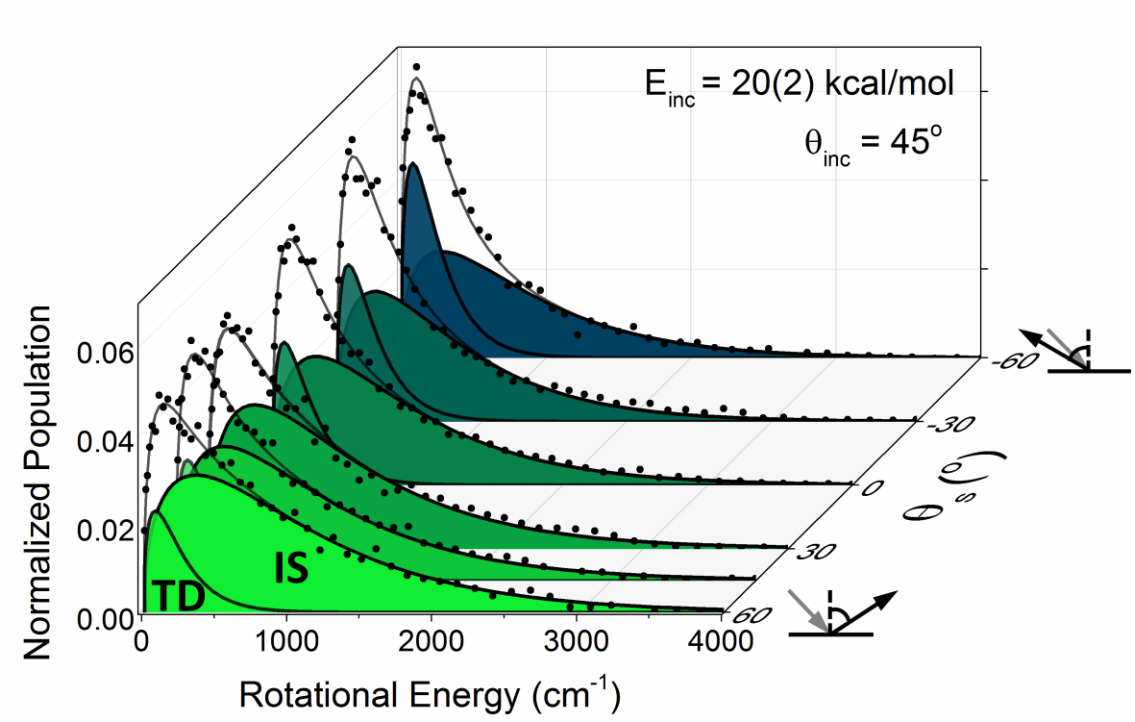

Figure 5.5 Rotational distributions for hyperthermal NO scattering (E_{inc} = 20(2) kcal/mol) as a function of final angle θ_s. Least squares fits into trapping desorption (TD) and impulsive scattering (IS) components are shown (see text for details). Note the strong dependence of IS vs. TD signals with final θ_s, which are dominated by IS and TD components for forward and backward scattering, respectively.

scattering angle. Stated alternatively, the lower J state populations are preferentially enhanced at backward scattering angles ($\theta_s < 0^o$), whereas higher J rotational energy states are preferentially scattered in the forward direction ($\theta_s > 0^o$).

More quantitatively, the data can be fit to a two-temperature Boltzmann model consisting of cold and hot scattering components that correspond to TD and IS channels, respectively. Specifically, $Pop(J) = [\alpha * P_{TD}(J) + (1- \alpha) * P_{IS}(J)]$ where $P_{TD}(J)$ and $P_{IS}(J)$ can be used to represent the normalized probabilities for scattering into a specific rotational J state via either the TD or IS scattering channel. The corresponding Boltzmann probabilities are represented by $P_{TD/IS}(J) = (2J+1) * \exp(-E_{rot}/(kT_{rot}(TD/IS))/Q_{rot}(TD/IS))$. It is worth noting that such a "microscopic branching" description of these populations is not an obvious choice; indeed, one might physically expect more of a continuum of IS scattering pathways to be taking place.[39-43] Nevertheless, there is an impressive amount of experimental support for such a two- temperature model, with, for example, recent REMPI studies of HCl scattered from self-assembled monolayers with both quantum state and 3D velocity map imaging resolution.[29] The current experimental results on NO scattering from [bmim][Tf_2N] provide yet another independent confirmation for the presence of a Boltzmann-like IS component in the rotational distributions.[29] From a purely empirical perspective, such a two-temperature model fits the data remarkably well over two orders of magnitude in dynamic range and therefore permits one to extract useful parameters with which to more quantitatively characterize and interpret angle and/or collision energy dependent changes in the rotational/spin-orbit state distributions.

In such two temperature analyses (see Fig. 5.5), the thermally accommodated rotational temperatures (T_{TD}) are held fixed at values determined from low collision energy scattering at E_{inc} = 2.7(9) kcal/mol, with the trapping-desorption fraction (α) and IS temperature (T_{IS}) floated

in a least squares process. The use of the low E_{inc} rotational temperatures for the TD component is supported by the angular independence of the desorbing flux presented above, which confirm that these low E_{inc} results arise from fully thermally accommodated TD scattering events. The fit parameters to the two-temperature model at high E_{inc} are graphed in Figure 5.6 as a function of scattering angle and spin-orbit state (E_{inc} = 20(2) kcal/mol and θ_{inc} = 45º). With more molecules scattering impulsively at higher incident speeds, a simple physical intuition leads to an expectation for a relatively larger fraction of molecules undergoing IS scattering at near specular scattered angles ($\theta_s \approx 45º$) and correspondingly fewer at back scattered angles. This is indeed observed (see Fig. 5.6a) where α, the branching ratio into the TD channel *decreases* from 0.52 to 0.28 with the scattering angle *increasing* from θ_s = 60º to -60º. Thus, the fraction of TD molecules detected nearly doubles from forward to backward scattering angles, in agreement with expectations for a larger fractional IS contribution in the forward scattering direction.

It is remarkable, however, that even at strongly backscattered angles (θ_s = -60º), nearly half of the NO molecules still arise from the rotationally hot IS channel. In previous experiments of CO_2 scattered from PFPE,[44] similar results were also observed, with α = 0.6 at backward scattering angles for θ_{inc} = 45º and E_{inc} = 10.6(8) kcal/mol. While there are obviously differences in the molecular systems studied, these results and the magnitude of the changes are in agreement what those in Figure 5.6(a). This is in contrast to observations of NO scattering from single crystal surfaces, where a significantly smaller fraction of molecules are found for NO backscattered angles from graphite[32] and Pt(111)[32]. This again speaks to the substantial differences in the microtopography for gas-liquid vs. gas-crystalline interfaces. In contrast to atomically flat crystalline surfaces, liquid surfaces are microscopically rough with thermally excited capillary wave activity. At the atomic level, functional groups extending out from the

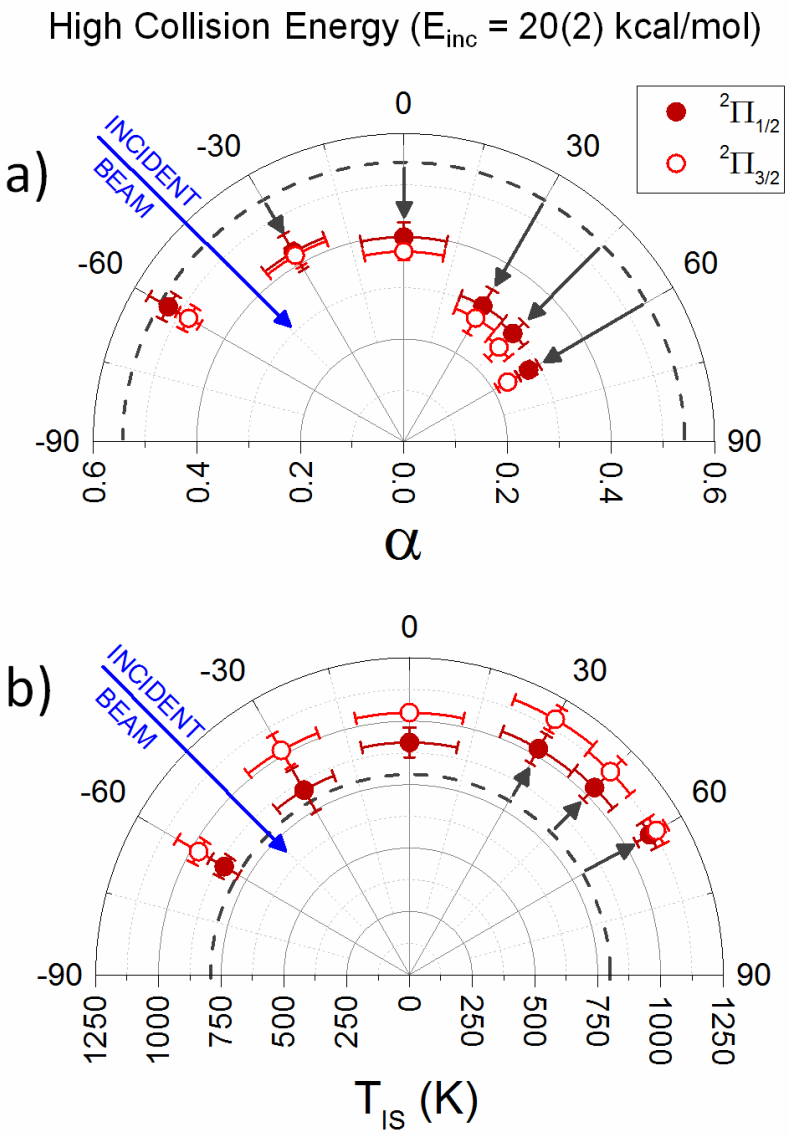

Figure 5.6 Polar plots of two-temperature (IS/TD) Boltzmann fits at hyperthermal collision energies (E_{inc} = 20 kcal/mol) to rotational/spin-orbit distributions as a function of final scattering angle θ_s. (a) Branching ratios (α) into the thermal accommodation TD channel, which decrease dramatically in the forward direction. (b) IS rotational temperatures, which systematically increase with scattering angle ($T_{IS} \approx$ 800-1200 K) and are 3-4-fold hotter than the liquid (T_s = 293(3) K). Note that spin-orbit *conserving* ($^2\Pi_{1/2} \rightarrow {}^2\Pi_{1/2}$) vs. spin orbit *changing* ($^2\Pi_{1/2} \rightarrow {}^2\Pi_{3/2}$) collisions are both i) systematically hotter and ii) less prone to thermal accommodation (i.e. result in smaller α values).

gas-liquid interface into the vacuum can promote significant backward scattering into the IS channel as well as facilitate significant hyperthermal rotational energy transfer.

NO rotational distributions in the IS scattering channel are probed further in Figure 5.6(b), where the fitted rotational temperature (T_{IS}) is explored as a function of θ_s for both ground and excited spin-orbit states. Substantially hyperthermal temperatures from T_{IS} = 800 - 1200 K are detected, indicative of significant impulsive translational-to-rotational energy transfer occurring at the gas-liquid interface. Interestingly, the hotter temperatures are now clearly observed in the *forward* scattered direction, which implies the degree of rotational excitation must increase with scattering angle. These results are consistent with a simple physical picture of forward scattering, hyperthermal collisions from a microscopically rough liquid surface. When a diatomic molecule strikes a liquid surface, the torques tend to arise from contact with functional groups protruding out into the vacuum, resulting in strong rotational excitation of the projectile coupled with recoil from the surface in a predominantly forward scattered direction. Indeed, molecular dynamics simulations have confirmed this expectation theoretically.[45, 46] Further confirmation of these trends has been provided by infrared quantum state resolved studies of gas-liquid scattering experiments, which reveal the IS component to be preferentially peaked in the forward direction and well fit to a lobular $\cos^n(\theta_s-\theta')$ distribution with *n* greater than unity.[47-50]

5.3.3 Angle-Dependent Spin-Orbit Distributions at Low and High Collision Energies

NO molecules in the incident beam are strongly supersonically cooled in the ground [$^2\Pi_{1/2}$] spin-orbit state; however, collision dynamics at the gas-liquid interface clearly lead to significant fractional population of spin-orbit excited NO molecules in the scattered flux. It is worth noting that such spin-orbit conversion dynamics require “surface hopping” between two

electronic potential energy surfaces.[51] Thus, by detailed balance considerations, angle-dependent NO electronic state distributions in the scattered flux offer first glimpses into spin-orbit state dependent sticking coefficients in an intrinsically non-adiabatic process. For simplicity of language, we simply express this spin-orbit ratio as an electronic "temperature," where T_{elec} is calculated from with $[^2\Pi_{3/2}]/[^2\Pi_{1/2}] = \exp(E_{so}/kT_{elec})$ and $E_{so} = 123\ cm^{-1}$.[52]

This electronic temperature T_{elec} is plotted in Figure 5.7 as a function of scattering angle, θ_s at both low (2.7(9) kcal/mol) and hyperthermal (20(2) kcal/mol) collision energies. First of all, the spin-orbit temperatures) at low E_{inc} ($T_{elec} \approx 227(15)$ K, $[^2\Pi_{3/2}]/[^2\Pi_{1/2}] \sim 0.45$) are robustly independent of final scattering angle. This is completely consistent with the observed angular insensitivity in the NO rotational distributions noted above and is again consistent with angle-independent NO sticking coefficients in the corresponding gas-to-liquid interfacial collision events. Secondly, and perhaps more surprisingly, these electronic temperatures are now significantly colder than the surface liquid temperature ($\Delta T \approx 66$ K), which predicts there to be a substantial sensitivity in sticking probabilities with spin-orbit quantum state. As there are only vanishingly small concentrations of spin-orbit excited NO in the incident beam, the observation of $[^2\Pi_{3/2}]$ NO population in the scattered flux unambiguously signals the presence of nonadiabatic "surface-hopping" dynamics in NO collisions at the gas-liquid interface.

With increased collision energies (E_{inc} = 20(2) kcal/mol) and summing over all rotational states and scattering channels, we observe increased opportunities for non-adiabatic excitation into the spin-orbit excited state ($T_{elec} \approx 325$ - 425 K). Of particular dynamic interest, T_{elec} increases by as much as $\Delta T \approx 100$ K between backward and forward scattering direction, equivalent to spin-orbit ratios of $[^2\Pi_{3/2}]/[^2\Pi_{1/2}] \sim 0.58$-0.66. Simply stated, ~ 15% more scattering trajectories arise from spin-orbit changing interactions into forward scattering relative to

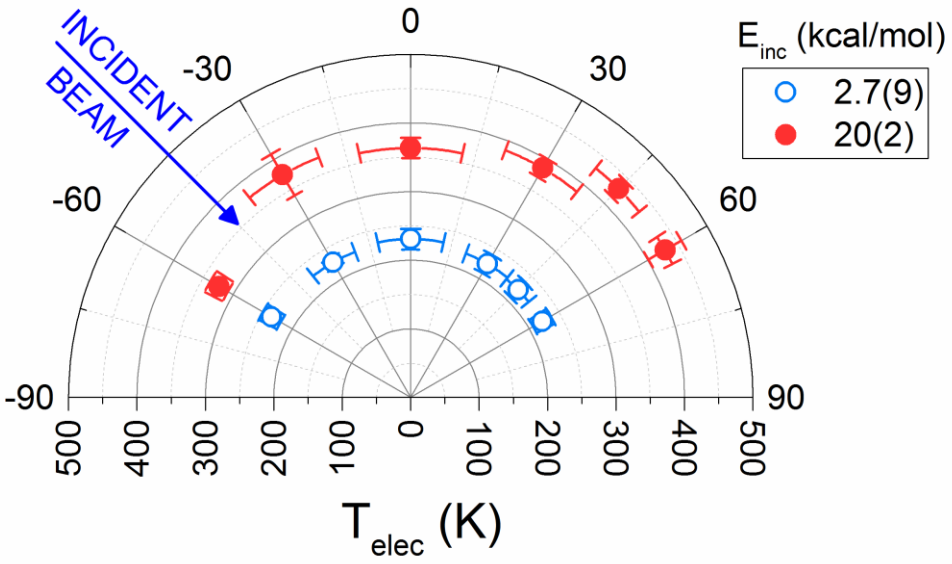

Figure 5.7 Spin-orbit temperatures (estimated via $[^2\Pi_{3/2}]/[^2\Pi_{1/2}] \approx \exp(-E_{so}/kT_{elec})$, E_{so} = 123 cm^{-1}) as a function of scattering angle θ_s at E_{inc} = 2.7 and 20 kcal/mol. Note that at low collision energies, the spin-orbit temperature ($T_{elec} \approx 227(15)$ K) is i) independent of θ_s and ii) considerably *colder* than the gas-liquid interface (T_s = 293(1) K). At hyperthermal collision energies, the spin-orbit temperatures increase significantly for forward vs. backward scattering, consistent with greater inelastic spin-orbit excitation in the predominantly forward scattered IS channel.

backward scattering angles. As noted previously,[14] there is a higher propensity for spin-orbit excitation in the impulsive scattering (IS) channel rather than the thermal desorption (TD) scattering pathway, which is of course consistent with an increase in spin-orbit excitation for flux in the forward scattering half plane.

5.3.4 NO Scattering from Squalane and PFPE

The data thus far have all focused on NO scattering from a single room-temperature ionic liquid, [bmim][Tf_2N]. In order to establish a broader context for these results, we now explore

similar angle-resolved trends in gas-liquid scattering dynamics with squalane ($C_{30}H_{62}$) and perfluoropolyether (PFPE) fluids, which in conjunction with the RTIL studies span a dramatic range of surface compositions. The rotational and spin-orbit temperatures obtained at low E_{inc} as a function of liquid and θ_s are presented in Table 5.1. All data have been obtained at T_s = 293 K and θ_{inc} = 45°, with scattered molecules probed in the backward (θ_s = -60°), normal (θ_s = 0°), and forward (θ_s = 45°) scattered directions. Despite the wide range of liquid surface properties, the observed T_{rot} and T_{elec} values for NO + squalane and NO + PFPE at low E_{inc} are in surprising agreement with NO + [bmim][Tf_2N], indeed, essentially indistinguishable at all scattering angles within experimental uncertainty. Of particular dynamical interest, the $^2\Pi_{1/2}$ rotational distributions from all three liquids (see Table 5.1) are each distinctly colder (T_{rot} = 259(9)K) than

		θ_s = -60°	0°	45°
$T_{rot}(^2\Pi_{1/2})$ (K)	[bmim][Tf_2N]	248(7)	250(10)	265(7)
	PFPE	262(9)	256(6)	275(8)
	Squalane	257(10)	253(6)	261(8)
T_{elec} (K)	[bmim][Tf_2N]	234(10)	227(10)	222(10)
	PFPE	216(6)	216(5)	209(7)
	Squalane	212(8)	202(6)	217(13)

Table 5.1 Angle-dependent rotational ($^2\Pi_{1/2}$) and spin-orbit electronic temperatures from jet-cooled NO (E_{inc} = 2.7(9) kcal/mol) desorbing from three different gas-liquid interfaces. Note the much colder rotational ($T_{rot} \approx 259(9)$ K) and electronic ($T_{elec} \approx 217(10)$ K) vs. liquid surface ($T_S \approx 293(1)$ K) temperatures, which unambiguously signal the presence of non-equilibrium, exit channel dynamics in the desorption process. Note also the relative insensitivity of these results to θ_s, which, by detailed balance considerations, is consistent with a constant sticking coefficient as a function of incident angle. Data for the excited spin-orbit state ($^2\Pi_{3/2}$) reveal a similar insensitivity to scattering angle, though with warmer values ($T_{rot} \approx 284(9)$ K) approaching the T_s = 293(1) K surface temperature.

the actual liquid temperature (T_S = 293(1)K), with an even cooler temperature for the spin-orbit degree of freedom (T_{elec} = 217(10)K)). This also is in agreement with previous studies[18] of low collision energy NO scattering from [$C_n$mim][Tf_2N] RTILs, for which T_{rot} at low E_{inc} was found to be surprisingly independent of the C_n alkyl chain length (n = 2, 4, 8, 12, and 16). As the rotational and electronic distributions are consistent within experimental error over the three liquids and range of scattering angles studied, the data constitute exceptionally strong support for a physical picture at low E_{inc} of i) complete thermal accommodation and ii) subsequent desorption from an *equilibrium* distribution of states at the gas-liquid interface.

As one obvious corollary, this implies that the *out-of-equilibrium* rotational and electronic distributions in the asymptotic NO flux must arise from exit channel dynamics occurring in the desorption process, which, by detailed balance considerations, predict a rotational and spin-orbit dependence to sticking coefficients for the reverse adsorption event. In the interest of completeness, we have also extended scattering studies on these liquids to high incident collision energies (E_{inc} = 20(2)), with spin-orbit T_{elec}, impulsive scattering T_{IS} and sticking coefficient α summarized in Figure 5.8 as a function of scattering angle (θ_s = -60°, 0°, 45°) for squalane, PFPE and [bmim][Tf_2N]. Once again, each of the three liquids exhibit very much the same trends, specifically with T_{elec} and T_{IS} gently *increasing* and α strongly *decreasing* as a function of increasing scattering angle.

5.4 Discussion

5.4.1 Rotational State Dependence on θ_s

A key feature of the present experiment is the ability to obtain complete rovibronic distributions at the gas-liquid interface as a function of θ_s and E_{inc}. We exploit this further by

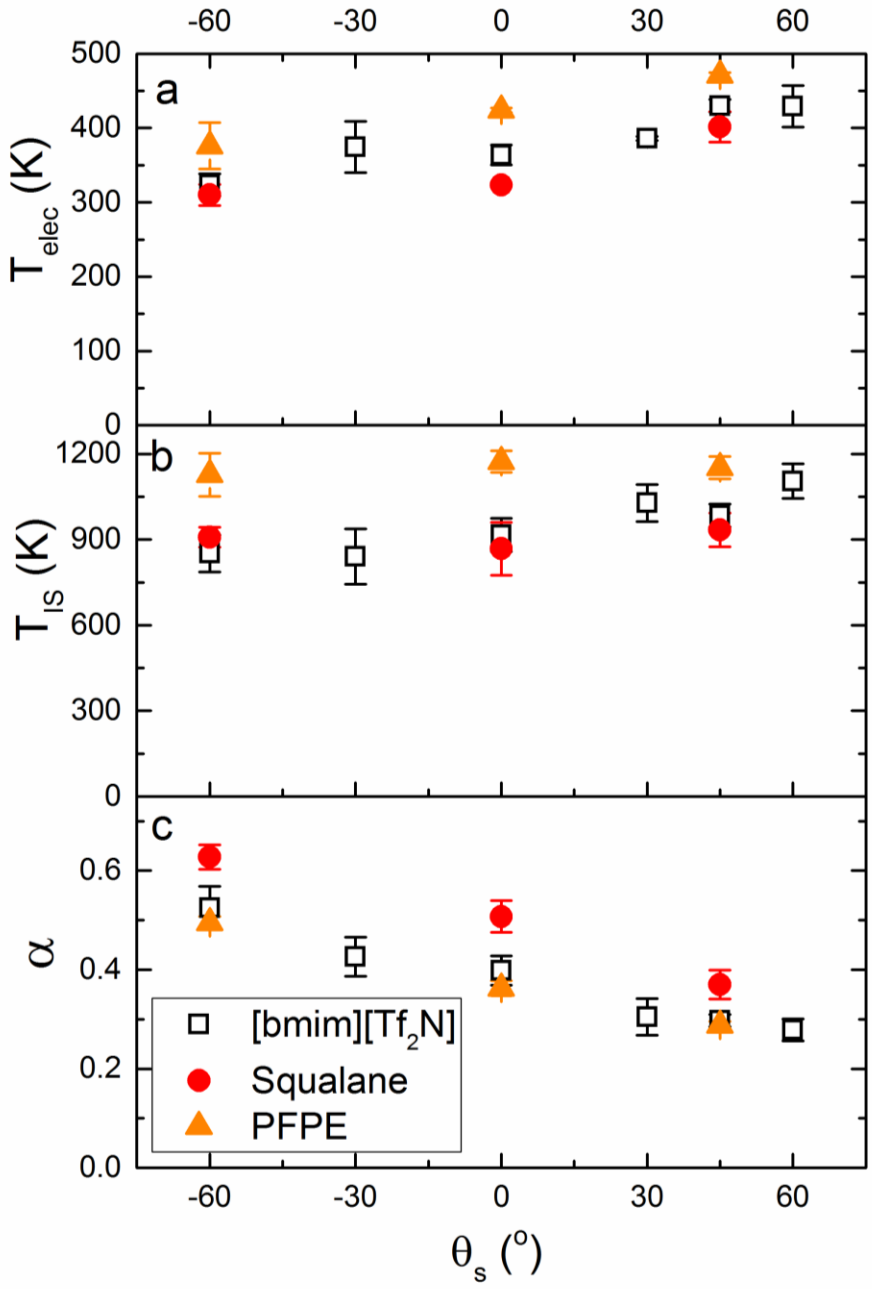

Figure 5.8 Comparison of (a) spin-orbit temperature (T_{elec}), (b) impulsive scattering rotational temperature (T_{IS}) and c) thermal accommodation coefficient (α) for hyperthermal NO scattering (E_{inc} = 20(2) kcal/mol) from a range of low vapor pressure liquids: [bmim][Tf_2N], perfluoropolyether (PFPE) and squalane ($C_{30}H_{62}$). Note the overall agreement in trends for all three liquids, despite substantial differences in chemical composition. There is also a systematic decrease in α with θ_s for all three liquids, with ≈ 2-fold differences between forward (θ_s = 60°) and backward (θ_s = -60°) scattering of the NO.

probing the dependence of individual J state populations with scattering angle in Figure 5.9. Here, the relative population of specific J states is extracted from normalized rotational distributions at each θ_s. Under low E_{inc} conditions (Figure 5.9(a)), which isolate the full thermal accommodation (TD) channel, the rotational distributions are essentially *flat* with respect to final scattering angle. This is not surprising and indeed reflects a similar message equivalent to the sequence of parallel Boltzmann plots shown in Figure 5.3. At higher E_{inc} (Figure 5.9(b)), however, the net rotational distributions do vary significantly with scattering angle. This echoes the data presented in Fig. 5.6(b), but requires no additional simplifying assumptions of a two temperature Boltzmann model. For hyperthermal scattering into low J states, (J =1.5 – 19.5), the relative rotational state populations are again very nearly flat with respect to θ_s. This is consistent with NO signals from these lower J states being dominated by trapping-desorption (TD) events, which should reflect a fully thermally accommodated rotational distribution. As final NO rotation increases ($J \geq 24.5$), however, the populations become increasingly peaked in the forward direction. The data specifically confirm that maximally efficient translational to rotational (T-R) energy transfer events at the gas-liquid interface result in *forward scattering* collisions, in agreement with physical intuition. The effects are quite significant: high J states are as much as ~2-3 times more likely to be detected under forward ($\theta_s = 60^o$) vs. backscattering ($\theta_s = -60^o$) conditions. Fig. 5.9(b) only contains data for the manifold of spin-orbit changing collisions ($[^2\Pi_{1/2}] \rightarrow [^2\Pi_{3/2}]$), though equivalent trends are observed for the spin-orbit conserving ($[^2\Pi_{1/2}] \rightarrow [^2\Pi_{1/2}]$) collisions as well.

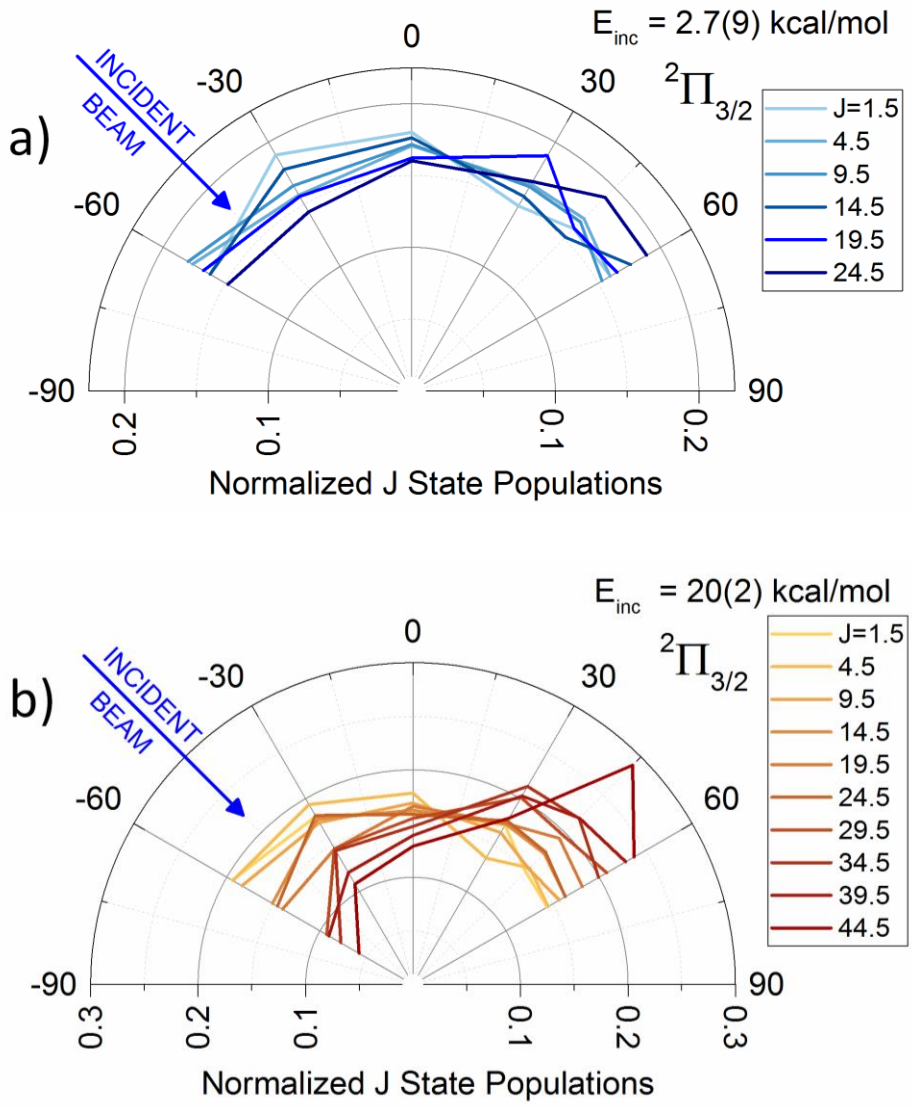

Figure 5.9 Polar plots of NO($^2\Pi_{3/2}$) rotational distributions as a function of final scattering angle θ_s. (a) At low E_{inc} conditions with NO thermally desorbing from the surface, the NO rotational distributions are relatively insensitive to θ_s. (b) At high E_{inc}, however, the rotational distributions evolve considerably with increasing θ_s, with a greater propensity for high J state populations scattered in the forward direction.

5.4.2 Spin-orbit Dependence on θ_s

The spin-orbit ratio as a function of both scattered angle and total angular momentum, N, are considered in Figure 5.10. Previously (see Figure 5.7), the spin-orbit temperature has been plotted vs. θ_s at high E_{inc}, summing over all rotational states. Here we focus on how the spin-orbit state populations evolve explicitly with N, which represents the angular momentum quantum number exclusive of electronic spin (N = (J+1/2) for $^2\Pi_{1/2}$ and N = (J-1/2) for $^2\Pi_{3/2}$). In such a plot, the spin-orbit ratio, $[^2\Pi_{3/2}(N)]/[^2\Pi_{1/2}(N)]$ has been appropriately multiplied by N/(N+1) to correctly account for the respective 2J+1 degeneracies associated with each spin-

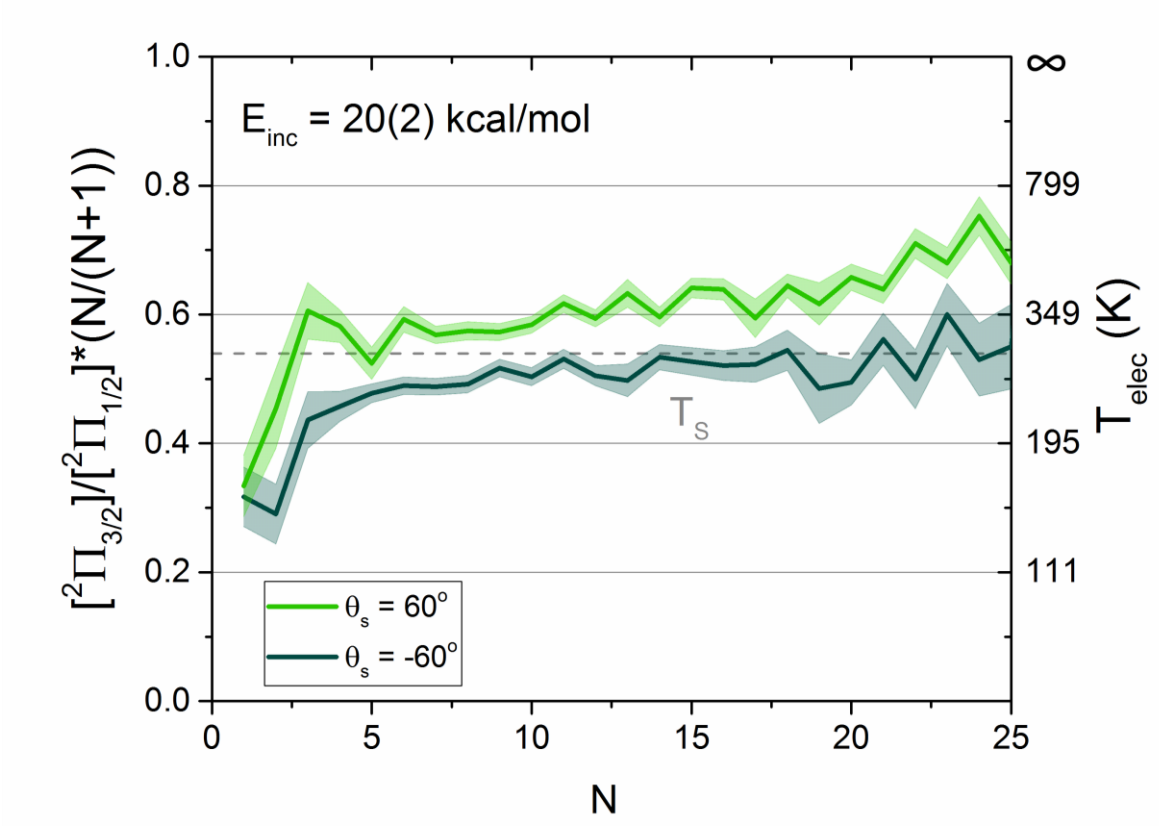

Figure 5.10 Spin-orbit ratios as a function of NO rotational quantum number and final scattering angle under hyperthermal incident conditions. Note the strong dependence on rotational quantum state, with a 2-fold increase in spin-orbit changing ($^2\Pi_{1/2} \rightarrow {}^2\Pi_{3/2}$) vs. spin-orbit conserving ($^2\Pi_{1/2} \rightarrow {}^2\Pi_{1/2}$) collisions over the N ≈ 0-5 range. A smaller but still quite significant increase (≈ 20%) in spin-orbit ratio for forward vs. backscattered NO species is also observed.

orbit state for the same N value. At high E_{inc} and $\theta_s = 60^o$, the spin-orbit ratio increases with angular momentum (N) by more than two-fold , with $[^2\Pi_{3/2}]/[^2\Pi_{1/2}] \approx 0.30$ at $N \approx 1$ and $[^2\Pi_{3/2}]/[^2\Pi_{1/2}] \approx 0.70$ by $N \approx 25$. By way of comparison, equilibration with the liquid (293 K) would correspond to a spin orbit ratio of $[^2\Pi_{3/2}]/[^2\Pi_{1/2}] = 0.54$. Thus, the lowest angular momentum states ($N < 10$) leave the surface with sub-thermal electronic temperatures, while the higher rotational states ($N > 10$) scatter with hyperthermal spin-orbit temperatures. Again, these lower rotational states are dominated by the TD channel, notably $N \cong 1 - 2$, while the higher rotational states predominately reflect the IS events. The ground spin-orbit state population gets to be low enough at $N > 25$, that the error on the ratio measurement makes comparisons difficult. However, the $N < 25$ data show a clear increase in spin-orbit excitation with N. At backscattering angles, $\theta_s = -60^o$, these same trends are observed but with consistently smaller spin-orbit ratios. These data also confirm spin-orbit excitation is more favored for forward vs. backward scattering, which is to say there is an increased degree of electronic nonadiabaticity in the forward direction.

Even in these high N states, the two spin-orbit state populations do not fully equilibrate. Studies by the McKendrick group found similar trends for OH formed by reactively scattered $O(^3P)$ from hydrocarbon liquids,[53] whereby the ground spin-orbit state was also found to be preferred in the scattered flux ($^2\Pi_{3/2}$ state is the ground state for OH). Furthermore, the ratio of the excited spin-orbit state grew with N, but the two spin-orbit populations did not equilibrate at large N, as we also observe in in Figure 5.10. This is in contrast to experiments of NO scattering from Ag(111) at $E_{inc} = 19.8$ kcal/mol,[54] where an increase in the spin-orbit ratio with N was observed, however the spin-orbit ratio centered around unity at high N states ($N > 20$). These differences in the spin-orbit ratio plateau at high J are likely a result of the silver crystalline

surface facilitating spin-orbit excitation of NO via electron transfer mechanisms.[51] Experimental and theoretical work by Wodtke, Tully and coworkers on the NO + Au(111) system have provided strong evidence for nonadiabatic surface hopping dynamics via electron transfer at the NO-metal interface.[51, 55-58] The relative stability of NO^- near a metallic vs. ionic liquid surface leads to the differences in these spin-orbit excitation comparisons, though more theory is clearly needed on this subject to help elucidate the nonadiabatic dynamics occurring in these systems.

5.4.3 Strong Correlation Between $<\theta_s>$ and Angular Momentum N

As a final topic, we take a more quantitative look at angular distributions in the scattered NO flux under hyperthermal scattering conditions (E_{inc} = 20 kcal/mol). As these angular distributions are relatively broad, it offers more physical insight to express the data in terms of an average scattering angle, $<\theta_s>$, as an explicit function of N (see Fig. 5.11). Note that such a parsing of the angular data by N is rigorous and does not require any model dependent assumptions concerning branching between TD vs. IS pathways. Furthermore, since all incident projectiles are initially in the ground ($N \approx 0$) rotational state, the final angular momentum N also serves as a metric of the net torque delivered to the projectile by collision with the gas-liquid interface. At low N values, the average scattering angle in Figure 5.11 approaches zero within experimental uncertainty. Though no such assumptions are necessary for this analysis, the vanishing of $<\theta_s>$ at low N would be completely consistent with full thermal accommodation and subsequent desorption of NO, yielding a perfectly forward/backward symmetric, indeed, $\cos(\theta_s)$ distribution centered around $\theta_s \sim 0^o$. Most intriguingly, however, the data in Figure 5.11 reveal a striking correlation between i) average scattering angle and ii) net torque experienced by the NO, with equally good agreement for both spin-orbit conserving and spin-orbit changing

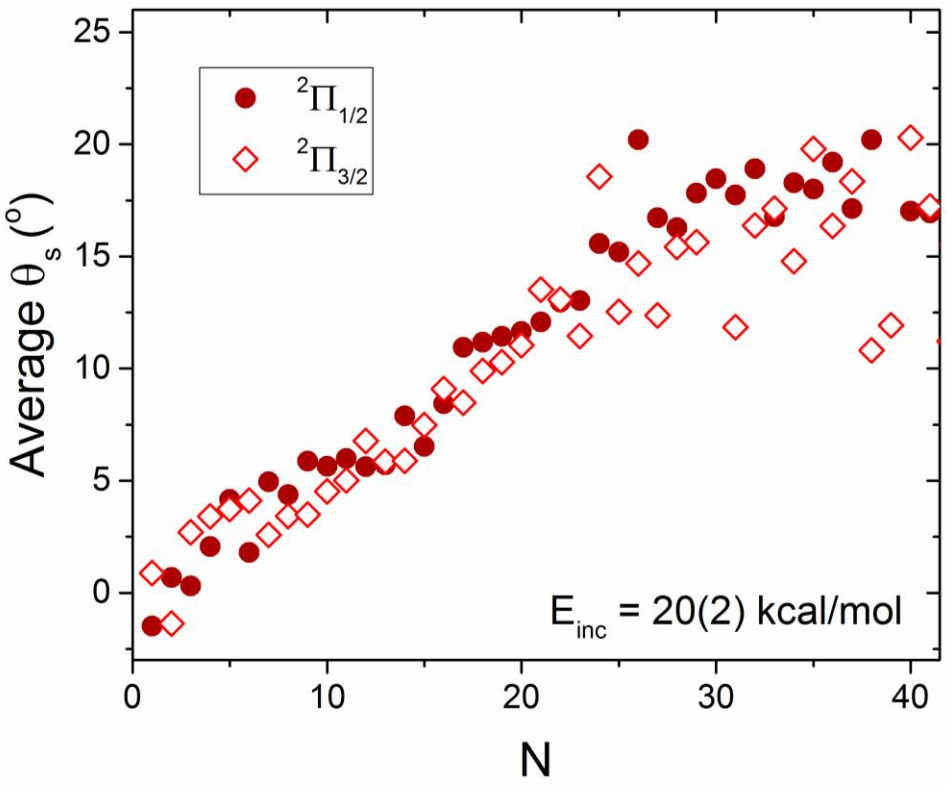

Figure 5.11 Average NO scattering angle $<\theta_s>$ as a function of angular momentum quantum number excluding electron spin (N) for both ground ($^2\Pi_{1/2,}$ N = J+1/2) and excited ($^2\Pi_{3/2,}$ N = J-1/2) spin-orbit states. Scattering into low N states is dominated by thermal accommodation (TD), for which $<\theta_s> \approx 0^o$ is in excellent agreement with a $\cos(\theta_s)$ distribution. For scattering into high N states, the IS channel is favored and the distribution tends toward specular scattering. Note the remarkably strong linear correlation between i) average angle $<\theta_s>$ and ii) amount of torque ($\Delta N \approx N$) delivered to the NO molecule, with a slope of $m \approx 0.5$ degree per N. See text for a simple physical interpretation of the dynamics.

manifolds. More quantitatively, $<\theta_s>$ increases remarkably linearly with N up to $N \approx 20$, with an approximate slope of ≈ 0.5 degree per ħ transferred in the gas-liquid collision. Furthermore, there appear to be some indications of saturation ($<\theta_s>_{max} \approx 15^o$ - 20^o) in this average angle above $N \approx 25$.

Though a detailed analysis of such a correlation is beyond the scope of the present work, we note that this represents an ideal target for further exploration with gas-liquid molecular

dynamics simulations, toward which we defer more quantitative attention in a later venue. However, we can offer the following preliminary observations. To start, all qualitative trends observed in the data are completely consistent with the microscopic branching, two-temperature model presented above. For example, the NO flux desorbing into low angular momentum states will tend to be dominated (though not completely) by TD scattering dynamics,[48] for which we would expect perfectly forward/backward symmetric scattering with an average value of $\langle\theta_s\rangle \approx 0$, as observed experimentally. Furthermore, for this two-temperature model, the NO flux into intermediate N values and rotational energies will accumulate progressively more from the IS scattering channel, which will tend to tilt the average scattering angle in the forward scattering direction and therefore predict a systematic increase in $\langle\theta_s\rangle$. Indeed, in the limit of high N and rotational energy, the two-temperature model contribution from IS scattering must rigorously become predominant. Since IS behavior is anticipated to be strongly forward scattered into the near specular direction, this would even predict the onset of saturation effects in average angle as a function of N, toward which the present data already offer strikingly good qualitative agreement with experiment.

As a parting comment, we take this one step further with a very simplified physical model for collisional torques acting at the gas-liquid interface. Specifically, the microscopically rough liquid surface provides a source of friction for exerting unbalanced torques on the incoming NO projectile over some small duration of collisional time Δt_{coll}. The net angular momentum accrued by the NO molecule is directly reflected in the final N value, which in a semiclassical picture would translate into an asymptotic rotational frequency of $\omega \approx 2B_{NO}N$. As a zeroth-order picture, one might crudely estimate the net forward rotation ($\Delta\theta > 0$) of the molecule-fixed NO frame during the gas-liquid collision event by $\Delta\theta \approx \omega\, \Delta t_{coll} \approx 2B_{NO}N\, \Delta t_{coll}$,

where the collision duration (Δt_{coll}) is the net time for application of any surface torques. Though more theoretical consideration will be necessary to explore this connection further, it is worth noting that even such a simple heuristic model does correctly predict a linear scaling of the average scattering angle with the final angular momentum quantum number N, as indeed experimentally observed.

5.5 Conclusion

The dynamics of NO colliding at liquid surfaces has been investigated as a function of final scattering angle and with quantum state-to-state and final scattering angle resolution. Specifically, rovibronic populations of scattered NO have been explored as a function of i) scattering angle (θ_s = -60(3)º, -30(9)º, 0(12)º, 30(9)º, 45(6)º and 60(3)º), ii) incident collision energy (E_{inc} = 2.7(9) and 20(2) kcal/mol), and iii) liquid composition ([bmim][Tf_2N], squalane, and PFPE). The extensive data set firmly supports the conclusion that at low collision energies (E_{inc} = 2.7(9) kcal/mol), all incident NO molecules trap, thermalize and desorb from the surface for all three liquids. Furthermore, the angular studies indicate that the NO molecules desorb from the surface in a cos(θ_s) distribution and with rotational temperatures independent of θ_s. These results are in agreement with detailed balance expectations based on uniform (but not necessarily unity) sticking coefficients for a given internal NO quantum state as a function of incident angle and speed. However, this simple dynamical behavior in the angular coordinate is clearly not the case for internal rotational and electronic quantum states, which reveal rotational distributions in the asymptotic NO flux systematically colder (T_{rot} ($^2\Pi_{1/2}$) ≈ 257(10), T_{rot} ($^2\Pi_{3/2}$) ≈ 284(10)) than the liquid surface temperature (T_s = 293 K) and colder still (T_{elec} ≈ 227(15)) in the corresponding spin-orbit electronic temperatures. These trends have been quantitatively confirmed for NO

scattering from a variety of liquid systems ranging from completely ionic liquids (RTIL) to liquids with strongly polar bonds (PFPE) to fully non-polar saturated hydrocarbons (squalane), which yield the same rotational and electronic temperatures for the three liquids within experimental uncertainty. By detailed balance, this novel behavior, i.e., the desorbing NO angular distributions are purely $\cos(\theta_s)$ whereas the internal quantum state distributions are significantly *out of equilibrium* with the surface temperature, rigorously implies clearly *non-unity* sticking coefficients for NO and thus the presence of dynamical barriers to adsorption as a function of rotational and/or spin-orbit quantum state. As changes in the internal spin-orbit state reflect non-adiabatic surface hopping events between two electronic surfaces, the adsorption/desorption dynamical barriers of such NO collisional events at the gas-liquid interface are richly complex and deserve further detailed theoretical attention. These results provide insight into the fundamental interactions between NO and liquid surfaces, for example, slowly vs. rapidly rotating NO molecules are more likely to trap on liquid surfaces, which helps build toward a more predictive kinetic understanding of collision and solvation dynamics at gas-liquid interfaces relevant for environmental applications.

By way of comparison, we have also explored angle dependent rotational/spin-orbit scattering dynamics as a function of incident beam energy. Whereas the rovibronic quantum state distributions are clearly quite insensitive to θ_s at low E_{inc}, at higher collision energies, the molecules are far more likely to scatter in the forward direction at more nearly specular angles and into correspondingly higher rotational states. A two-temperature trapping desorption (TD)/impulsive scattering (IS) Boltzmann fit to the rotational distributions at high E_{inc} is quite consistent with this picture, which accounts for more molecules impulsively scattering into forward angles and with ≈ 3-4 fold hotter rotational temperatures in the IS vs. TD channels.

Conversely, the fractional branching coefficient (α) between trapping desorption and impulsive scattering pathways clearly depends quite significantly on the choice of scattering angle, varying by nearly two-fold between forward and backward scattering directions. The spin-orbit ratios of the hyperthermal scattered NO are also found to depend sensitively on final rotational state (two-fold increase between N = 0-25) with a clear propensity for higher spin-orbit excitation in the IS channel and for forward ($\theta_s = 60^o$) vs. backward ($\theta_s = -60^o$) scattering. As such data highlight the effects of hyperthermal collision energy on electronic surface hopping events, this provides particular incentive for further theoretical exploration of such non-adiabatic, state-to-state collision dynamics at the gas-liquid interface.

References for Chapter 5

1. B. Dimitriades, *Environ. Sci. Technol.*, 1972, **6**, 253.

2. *Nitrogen Oxides (NOx), Why and How they are Controlled*, Report US EPA Technical Bulletin No. EPA-456/F-99-006R, 1999.

3. G. E. Likens, R. F. Wright, J. N. Galloway and T. J. Butler, *Sci. Am.*, 1979, **241**, 43-51.

4. *Nitric and Adipic Acid Manufacturing Plants*, Report EPA-450/3-91-026, 1991.

5. P. J. Crutzen, *Annu. Rev. Earth Planet. Sci.*, 1979, **7**, 443-472.

6. M. O. Andreae and P. Merlet, *Global Biogeochem. Cycles*, 2001, **15**, 955-966.

7. N. D. Hutson, R. Krzyzynska and R. K. Srivastava, *Ind. Eng. Chem. Res.*, 2008, **47**, 5825-5831.

8. D. S. Jin, B. R. Deshwal, Y. S. Park and H. K. Lee, *J. Hazard. Mater.*, 2006, **135**, 412-417.

9. L. R. Martin, D. E. Damschen and H. S. Judeikis, *Atmos. Environ.*, 1981, **15**, 191-195.

10. F. J. Dentener and P. J. Crutzen, *J. Geophys. Res.*, 1993, **98**, 7149-7163.

11. V. H. Grassian, *J. Phys. Chem. A*, 2002, **106**, 860-877.

12. V. H. Grassian, *Int. Rev. Phys. Chem.*, 2001, **20**, 467-548.

13. B. G. Perkins and D. J. Nesbitt, *J. Phys. Chem. B*, 2008, **112**, 507-519.

14. A. Zutz and D. J. Nesbitt, *J. Phys. Chem. C*, 2015, **119**, 8596-8607.

15. S. P. K. Kohler, M. Allan, H. Kelso, D. A. Henderson and K. G. McKendrick, *J. Chem. Phys.*, 2005, **122**, 24712.

16. A. W. Gisler and D. J. Nesbitt, *Faraday Discuss.*, 2012, **157**, 297-305.

17. J. A. Faust, T. B. Sobyra and G. M. Nathanson, *J. Phys. Chem. Lett.*, 2016, **7**, 730-735.

18. A. Zutz and D. J. Nesbitt, *AIP Adv.*, 2016, **6**, 105207.

19. M. A. Tesa-Serrate, B. C. Marshall, E. J. Smoll, S. M. Purcell, M. L. Costen, J. M. Slattery, T. K. Minton and K. G. McKendrick, *J. Phys. Chem. C*, 2015, **119**, 5491-5505.

20. D. K. Lancaster, A. M. Johnson, D. K. Burden, J. P. Wiens and G. M. Nathanson, *J. Phys. Chem. Lett.*, 2013, **4**, 3045-3049.

21. M. E. King, K. M. Fiehrer, G. M. Nathanson and T. K. Minton, *J. Phys. Chem. A*, 1997, **101**, 6556-6561.

22. I. Chorny, I. Benjamin and G. M. Nathanson, *J. Phys. Chem. B*, 2004, **108**, 995-1002.

23. C. Waring, P. A. J. Bagot, J. M. Slattery, M. L. Costen and K. G. McKendrick, *J. Phys. Chem. A*, 2010, **114**, 4896-4904.

24. J. R. Roscioli and D. J. Nesbitt, *J. Phys. Chem. A*, 2011, **115**, 9764-9773.

25. J. R. Roscioli and D. J. Nesbitt, *Faraday Discuss.*, 2011, **150**, 471-479.

26. M. A. Tesa-Serrate, E. J. Smoll, L. D'Andrea, S. M. Purcell, M. L. Costen, D. W. Bruce, J. M. Slattery, T. K. Minton and K. G. McKendrick, *J. Phys. Chem. C*, 2016, **120**, 27369-27379.

27. J. C. Tully, *Surf. Sci.*, 1994, **299**, 667-677.

28. E. P. Wenaas, *J. Chem. Phys.*, 1971, **54**, 376.

29. C. H. Hoffman and D. J. Nesbitt, *J. Phys. Chem. C*, 2016, **120**, 16687–16698.

30. R. R. Cavanagh and D. S. King, *Phys. Rev. Lett.*, 1981, **47**, 1829-1832.

31. J. A. Prybyla, T. F. Heinz, J. A. Misewich and M. M. T. Loy, *Surf. Sci.*, 1990, **230**, L173-L179.

32. F. Frenkel, J. Hager, W. Krieger, H. Walther, G. Ertl, J. Segner and W. Vielhaber, *Chem. Phys. Lett.*, 1982, **90**, 225-229.

33. M. Asscher, W. L. Guthrie, T. H. Lin and G. A. Somorjai, *J. Chem. Phys.*, 1983, **78**, 6992-7004.

34. G. D. Kubiak, J. E. Hurst, H. G. Rennagel, G. M. McClelland and R. N. Zare, *J. Chem. Phys.*, 1983, **79**, 5163-5178.

35. M. P. Ziemkiewicz, J. R. Roscioli and D. J. Nesbitt, *J. Chem. Phys.*, 2011, **134**, 234703.

36. G. M. Mcclelland, G. D. Kubiak, H. G. Rennagel and R. N. Zare, *Phys. Rev. Lett.*, 1981, **46**, 831-834.

37. M. Ziemkiewicz, M. Wojcik and D. J. Nesbitt, *J. Chem. Phys.*, 2005, **123**, 224307.

38. J. Luque and D. R. Crosley, *LIFBASE: Database and Spectral Simulation (version 1.5)*, Report SRI International Report MP 99-009, 1999.

39. J. J. Nogueira, S. A. Vazquez, O. A. Mazyar, W. L. Hase, B. G. Perkins, D. J. Nesbitt and E. Martinez-Nunez, *J. Phys. Chem. A*, 2009, **113**, 3850-3865.

40. D. Kim and G. C. Schatz, *J. Phys. Chem. A*, 2007, **111**, 5019-5031.

41. Y. X. Peng, L. Liu, Z. Cao, S. Li, O. A. Mazyar, W. L. Hase and T. Y. Yan, *J. Phys. Chem. C*, 2008, **112**, 20340-20346.

42. E. Martinez-Nunez, A. Rahaman and W. L. Hase, *J. Phys. Chem. C*, 2007, **111**, 354-364.

43. T. Y. Yan, W. L. Hase and J. R. Barker, *Chem. Phys. Lett.*, 2000, **329**, 84-91.

44. B. G. Perkins and D. J. Nesbitt, *J. Phys. Chem. A*, 2008, **112**, 9324-9335.

45. X. H. Li, G. C. Schatz and D. J. Nesbitt, *J. Phys. Chem. B*, 2012, **116**, 3587-3602.

46. U. S. Tasic, T. Y. Yan and W. L. Hase, *J. Phys. Chem. B*, 2006, **110**, 11863-11877.

47. L. S. Brown and S. J. Sibener, *J. Chem. Phys.*, 1988, **89**, 1163-1169.

48. B. G. Perkins and D. J. Nesbitt, *J. Phys. Chem. A*, 2009, **113**, 4613-4625.

49. D. J. Garton, T. K. Minton, M. Alagia, N. Balucani, P. Casavecchia and G. G. Volpi, *Journal of Chemical Physics*, 2000, **112**, 5975-5984.

50. J. A. Serri, M. J. Cardillo and G. E. Becker, *J. Chem. Phys.*, 1982, **77**, 2175-2189.

51. N. Shenvi, S. Roy and J. C. Tully, *J. Chem. Phys.*, 2009, **130**, 174107.

52. G. Herzberg, *Spectra and Molecular-Structure I. Spectra of Diatomic-Molecules*, Princeton Univ. Press, Princeton, NJ, 1968.

53. G. M. Sweeney, A. Watson and K. G. McKendrick, *J. Chem. Phys.*, 1997, **106**, 9172-9181.

54. A. C. Luntz, A. W. Kleyn and D. J. Auerbach, *J. Chem. Phys.*, 1982, **76**, 737-738.

55. N. Shenvi, S. Roy and J. C. Tully, *Science*, 2009, **326**, 829-832.

56. Y. Huang, A. M. Wodtke, H. Hou, C. T. Rettner and D. J. Auerbach, *Phys. Rev. Lett.*, 2000, **84**, 2985-2988.

57. Y. H. Huang, C. T. Rettner, D. J. Auerbach and A. M. Wodtke, *Science*, 2000, **290**, 111-114.

58. A. M. Wodtke, Y. H. Huang and D. J. Auerbach, *J. Chem. Phys.*, 2003, **118**, 8033-8041.

Chapter 6

Incident Collision Energy Dependence of NO Scattering Dynamics at the Gas-RTIL Interface

6.1 Introduction

In this chapter unpublished results are presented for incident collision energy dependence on NO scattered from the gas-[bmim][Tf_2N] interface. Previous molecular and atomic scattering experiments from a variety of low vapor pressure liquids,[1-4] in addition to nitric oxide scattered from crystalline surfaces,[5-7] have explored atomic/molecular collisional energy dependence. These experimental results have provided evidence for thermal desorption (TD) and impulsive scattering (IS) pathways; at low collision energies all incident molecules trap on the surface, in contrast to increasing collisional speeds where more molecules inelastically scatter. Stated more broadly, a decrease in sticking coefficients is observed at higher incident collision energies.

The molecular scattering experiments presented in this chapter, which examine the collision energy dependence of NO at liquid surfaces, are largely motivated by the prediction of rotational and spin-orbit dependent sticking probabilities, as discussed in Chapters 3.3.1 and 5.3.1. These results suggest the possibility of translational energy dependent NO sticking coefficients on liquid surfaces. In order to investigate this theory, experiments have been performed with a series of molecular beams at low incident collision energies (E_{inc} = 2.0 – 4.0 kcal/mol) where the thermal desorption channel is isolated. Scattering experiments are also

performed for a series of increasingly higher collision energies (E_{inc} = 4.9 – 20 kcal/mol) to explore how the microscopic branching ratio between the TD and IS scattering pathways are impacted, as well as the degree of excitation into molecular rotational and spin-orbit degrees of freedom.

6.2 Experimental

A complete description of the experimental apparatus can be found in Chapter 2. The speed of the incident molecular beam is varied by changing the identity/mass of the buffer gas in which NO is seeded. Gas mixtures of 1% NO are seeded in Ne, He, and H_2, which generate collision energies of 2.0(2), 11.1(7) and 20(2) kcal/mol, respectively. These kinetic energies correspond to molecular speeds ranging from 7.5 x 10^4 to 2.4 x 10^5 m/s. Buffer gases are also mixed in specific concentrations to create intermediate incident beam energies. In principle, heavier buffer gases, such as Ar and Kr, could be used to achieve even slower molecular beam speeds, however, these mixtures result in low LIF signal levels, likely due to cluster formation in the molecular beam. All molecular scattering in this chapter is from a 293 K [bmim][Tf_2N] RTIL surface. Incident supersonically cooled NO($^2\Pi_{1/2}$, J = 0.5) molecules approach at θ_{inc} = 45º and scattered molecules are detected via LIF at specular scattering angles, θ_s = 45(6)º.

6.3 Results and Analysis

LIF spectra of scattered NO (v=0) molecules are shown in Figure 6.1 for incident collision energies E_{inc} = 2.7 and 20 kcal/mol. Significant spin-orbit and rotational excitation are observed at both collision energies, although Figure 6.1 reveals that the LIF spectra arising from scattering at faster incident speeds extend to higher wavenumbers (~44800 cm^{-1}), which

correspond to larger populations in higher rotational states (up to J = 50.5). This understandably indicates that more energy is transferred from the translational to rotational degree of freedom at higher collision energies when there is more translational energy available to the system. The LIF signal at lower frequencies (44050 to 44300 cm^{-1}), and correspondingly lower J states, is also stronger for faster incident speeds (ranging from 10 - 50% more for E_{inc} = 20 vs. 2.7 kcal/mol) due to the specular scattering detection geometry of the experiment. Specifically, at lower collision energies all molecules are expected to thermalize on the surface and desorb in near cos(θ_s) distributions; consequently a small fraction of these molecules are directed toward

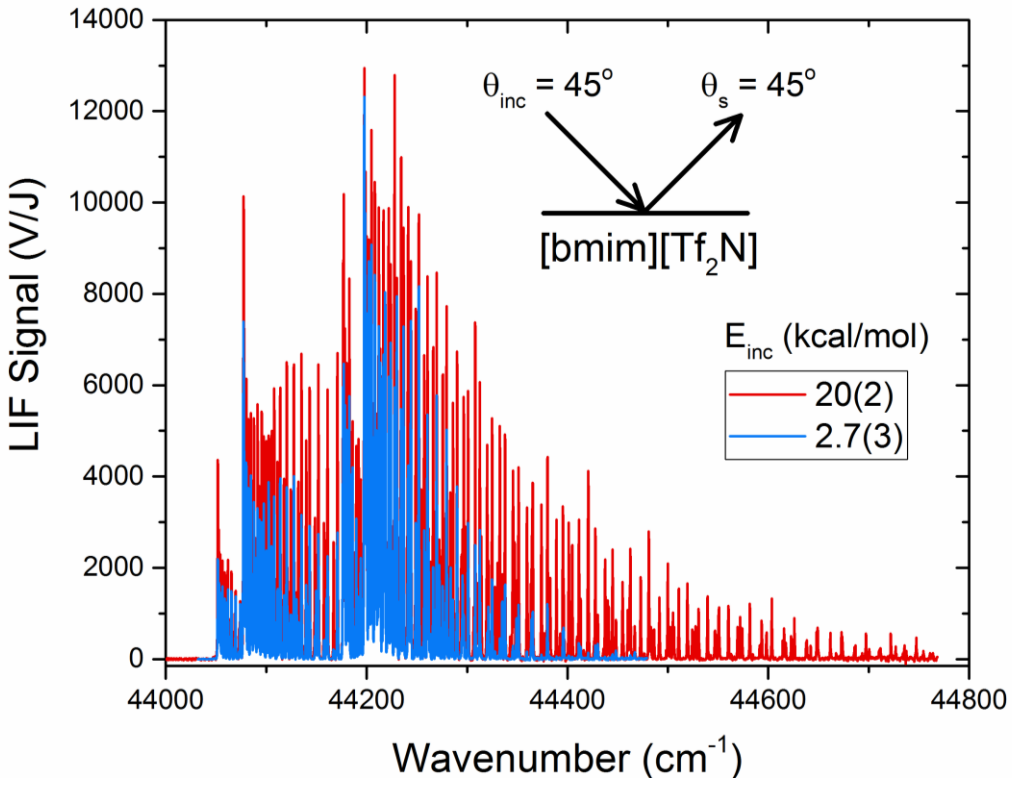

Figure 6.1 LIF spectra of NO scattered from a T_s = 293 K [bmim][Tf_2N] surface at incident collision energies E_{inc} = 2.7 and 20 kcal/mol. Decreased rotational excitation coupled with a smaller LIF signal is observed at lower collision energies, where all molecules are thermally desorbing from the surface in a cos(θ_s) distribution with colder rotational temperatures. At higher incident speeds, however, more molecules impulsively scatter into near specular angles (i.e., toward the detection region) with hyperthermal rotational excitation.

the LIF detection volume at θ_s = 45(6)º. At faster incident speeds, however, increasingly more molecules impulsively scatter into near specular angles, i.e., toward the LIF detection region, which results in larger LIF signals at θ_s = 45(6)º relative to the low E_{inc} case where all molecules are thermally desorbing from the surface in a cos(θ_s) distribution.

The corresponding rotational distributions derived from the LIF spectra in Figure 6.1 are displayed in Figure 6.2 for the ground $^2\Pi_{1/2}$ spin-orbit state, as well as those for two intermediate incident energies (E_{inc} = 11 and 15 kcal/mol). The population distributions at each collision energy are normalized to unity so that the relative distribution of J states populated can be compared between different incident molecular beam conditions. As also predicted from the LIF

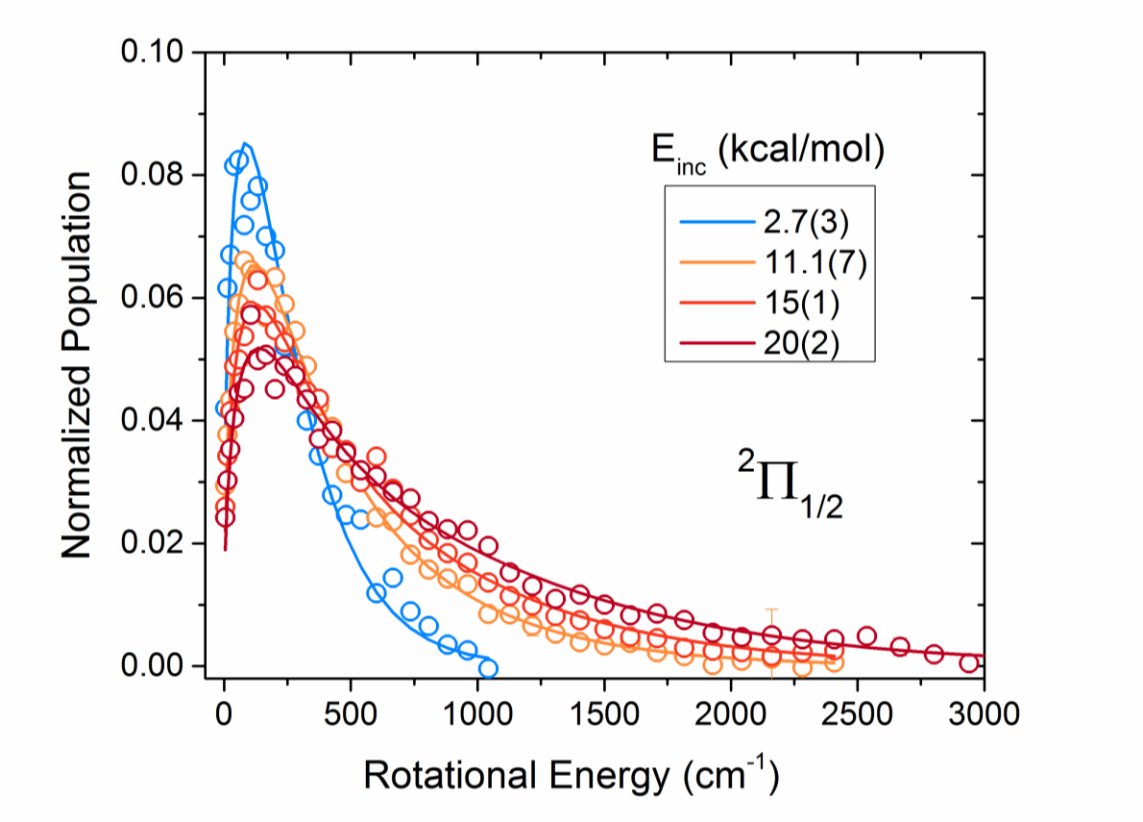

Figure 6.2 Scattered NO rotational distributions for varied E_{inc}, where each population distribution is normalized to unity and from the ground ($^2\Pi_{1/2}$) spin-orbit state. At faster incident speeds molecules scatter into relatively higher J states, revealing significantly more translational-to-rotational energy transfer than at lower E_{inc}.

spectra in Figure 6.1, these data reveal that lower collision energies result in fractionally more molecules scattered into low rotational states, whereas higher collision speeds result in preferential population of high rotational states. The spin-orbit excitation of NO as a function of collision energy is considered in Figure 6.3. All incident NO molecules are prepared in the ground $^2\Pi_{1/2}$ spin-orbit state, thus scattered NO molecules detected in the $^2\Pi_{3/2}$ state represent *spin-orbit changing* collisions. As seen below in Figure 6.3, spin-orbit excitation of NO scattered from a RTIL liquid surface grows with increasing collision energy. As discussed in Chapter 5, spin-orbit excitation is more favored in the IS channel relative to the TD scattering pathway. Therefore, as more molecules impulsively scatter as E_{inc} increases, spin-orbit excitation in the scattered flux also increases.

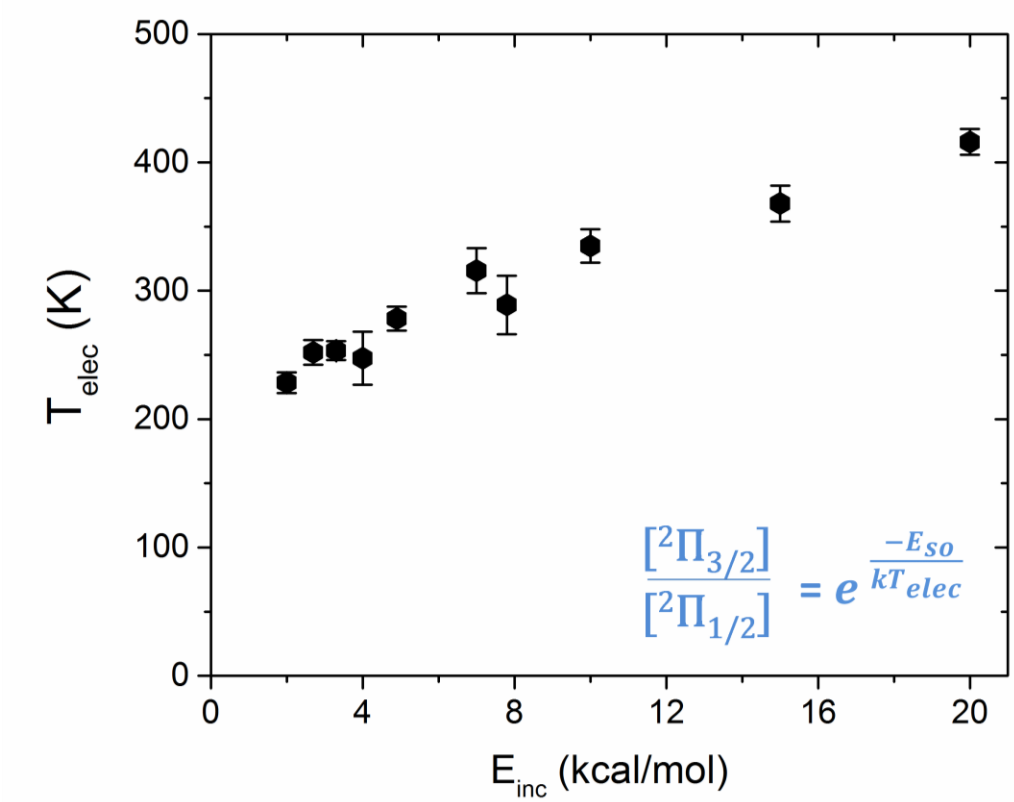

Figure 6.3 Spin-orbit excitation of NO as a function of incident collision energy. Note the increase in spin-orbit changing collisions ($^2\Pi_{1/2} \rightarrow {}^2\Pi_{3/2}$) as E_{inc} increases, with electronic temperatures colder than the T_s = 293 K liquid at low E_{inc} and above T_s at high E_{inc}.

6.3.1 Isolating Thermal Desorption at Low Collision Energies

Rotational distributions from low incident energy scattering are displayed in a Boltzmann plot in Figure 6.4, where the populations of each rotational state are normalized to their respective 2J+1 degeneracy and plotted on a log scale. At low collision energies (E_{inc} = 2.0 – 4.0 kcal/mol) there is no clear evidence for dual temperature scattering behavior (i.e., microscopic branching) and thus the rotational distributions are fit to single temperatures, which are characteristic of 100% sticking coefficients. These rotational temperatures, particularly for the $^2\Pi_{1/2}$ state, are considerably cooler than the liquid surface (T_s = 293 K) and largely independent of E_{inc}.

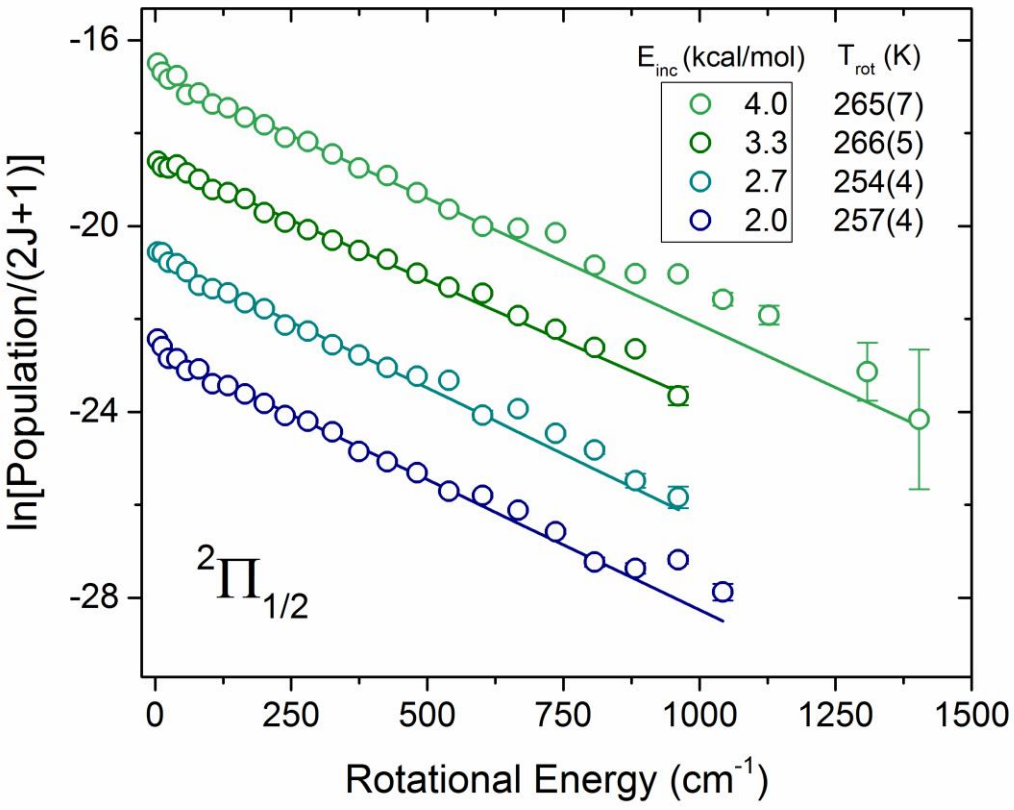

Figure 6.4 Boltzmann rotational distributions for scattered NO at E_{inc} = 2.0 – 4.0 kcal/mol, with corresponding single temperature fits representative of complete thermal accommodation at the surface. All scattering takes place from a 293 K [bmim][Tf_2N] surface at θ_{inc} = 45º and θ_s = 45(6)º.

In Figure 6.5, the single temperature rotational Boltzmann fits are plotted for both spin-orbit states at E_{inc} = 2.0, 2.7, 3.3, and 4.0 kcal/mol. The $^2\Pi_{1/2}$ rotational temperatures are consistently ~30-40 K cooler than the 293 K surface temperature, while $T_{rot}(^2\Pi_{3/2})$ is closer to and often within experimental uncertainty of the surface temperature. The rotational temperatures for each spin-orbit state are largely insensitive to collision energy in this range, consistent with there being no translational energy dependence to the sticking probability at the surface for the range of low collision energies sampled. These results combined with the angle-resolved data presented in Chapter 5.3.1 indicate that (i) at low incident energies (E_{inc} = 2.0 –

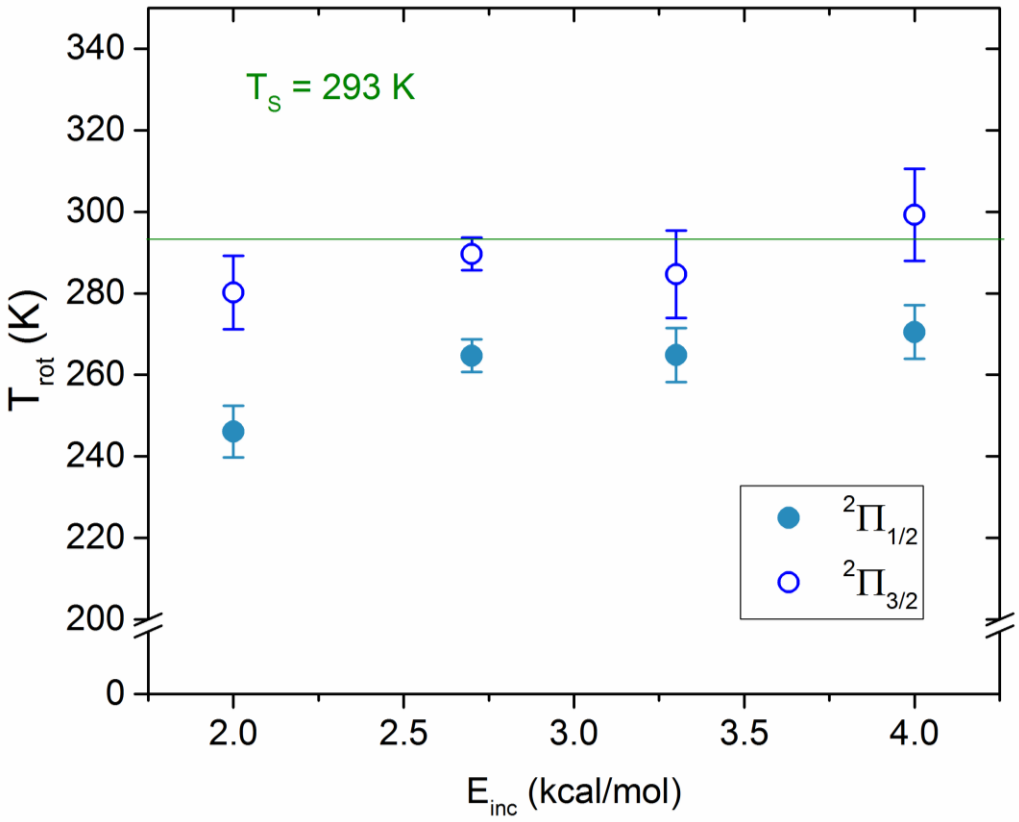

Figure 6.5 Single temperature Boltzmann fits for NO scattered at low collision energies (E_{inc} = 2.0 – 4.0 kcal/mol), where all molecules thermalized and subsequently desorbed from the liquid surface. The rotational temperatures are largely unchanged as E_{inc} is varied, consistent with no translational energy dependence to the sticking coefficient at low E_{inc}.

4.0 kcal/mol), all scattered NO molecules follow a thermal desorption scattering pathway, (ii) there exist rotational and spin-orbit state dependent sticking coefficients that yield rotational/electronic cooling of the desorbing flux, and (iii) the surface sticking probabilities do not depend on incident translational energy at low E_{inc}. These conclusions are consistent with adsorption/desorption dynamical barriers that are dependent on angular orientation and give rise to quantum state dependent sticking coefficients.

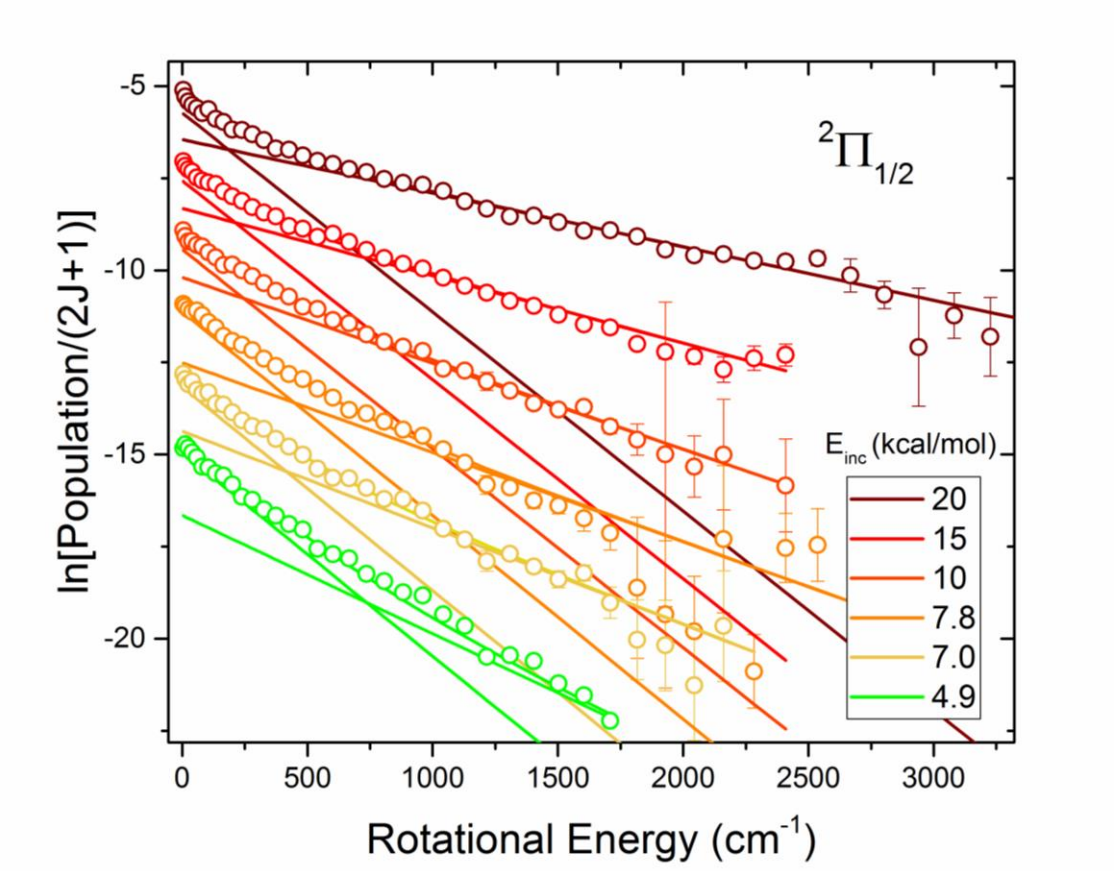

Figure 6.6 Boltzmann rotational distributions for scattered NO at hyperthermal collision energies from E_{inc} = 4.9 to 20 kcal/mol. Two-temperature fits to the data are also plotted, which represent rotational excitation into the TD and IS scattering pathways as well as the branching between those two channels. Here the colder component (T_{TD}) is fixed at $T_{rot}(^2\Pi_{1/2})$ from low E_{inc} scattering results where the TD channel is isolated.

6.3.2 Branching into Multiple Scattering Pathways at High Collision Energies

The rotational distribution of scattered NO at higher collision energies (E_{inc} = 4.9 - 20 kcal/mol) are analyzed in a Boltzmann plot in Figure 6.6. Unlike at low E_{inc}, these rotational distributions exhibit significant curvature, which can be well fit to a double exponential. This two-temperature model physically corresponds to the trapping-desorption (TD) and impulsive scattering (IS) pathways, as discussed in more detail in Chapter 3.3, 4.3 and 5.3. These rotational Boltzmann fits displayed in Figure 6.6 consist of three parameters: (i) the colder temperature, T_{TD}, corresponds to the thermally desorption scattering pathway, (ii) the hotter temperature component, T_{IS}, describes the impulsive scattering pathway, and (iii) α represents the branching ratio into the TD channel. Both T_{IS} and α are floated, while T_{TD} is fixed at the value of T_{rot} for each spin-orbit state from low collision energy scattering ($T_{rot}(^2\Pi_{1/2}) \approx 260$ K and $T_{rot}(^2\Pi_{3/2}) \approx 285$ K , Figure 6.4) where the TD component is isolated.

The branching ratio (α) from these two-temperature fits is plotted as a function of incident collision energy in Figure 6.7. At each of the low collision energies (2.0 to 4.0 kcal/mol), α is fixed at unity (corresponding to single temperature fits in Figure 6.4). However, as collision speeds are increased beyond 4 kcal/mol, α decreases monotonically. This decrease in α with E_{inc} is consistent with NO preferentially impulsively scattering from the surface at higher incident speeds, as observed in previous studies.[1-4, 6, 8] Furthermore, there appears to be some minimum translational energy required (i.e. ≈ 4.0 kcal/mol) to scatter inelastically instead of 100% trapping-desorption on the surface. For NO to trap on the liquid surface, we can imagine a scenario where an approaching NO molecule must transfer some fraction of incident translational energy to the liquid. Thus for larger E_{inc}, NO colliding with the surface has increasingly more energy to dispose and with which to escape the liquid surface before thermalizing. The results

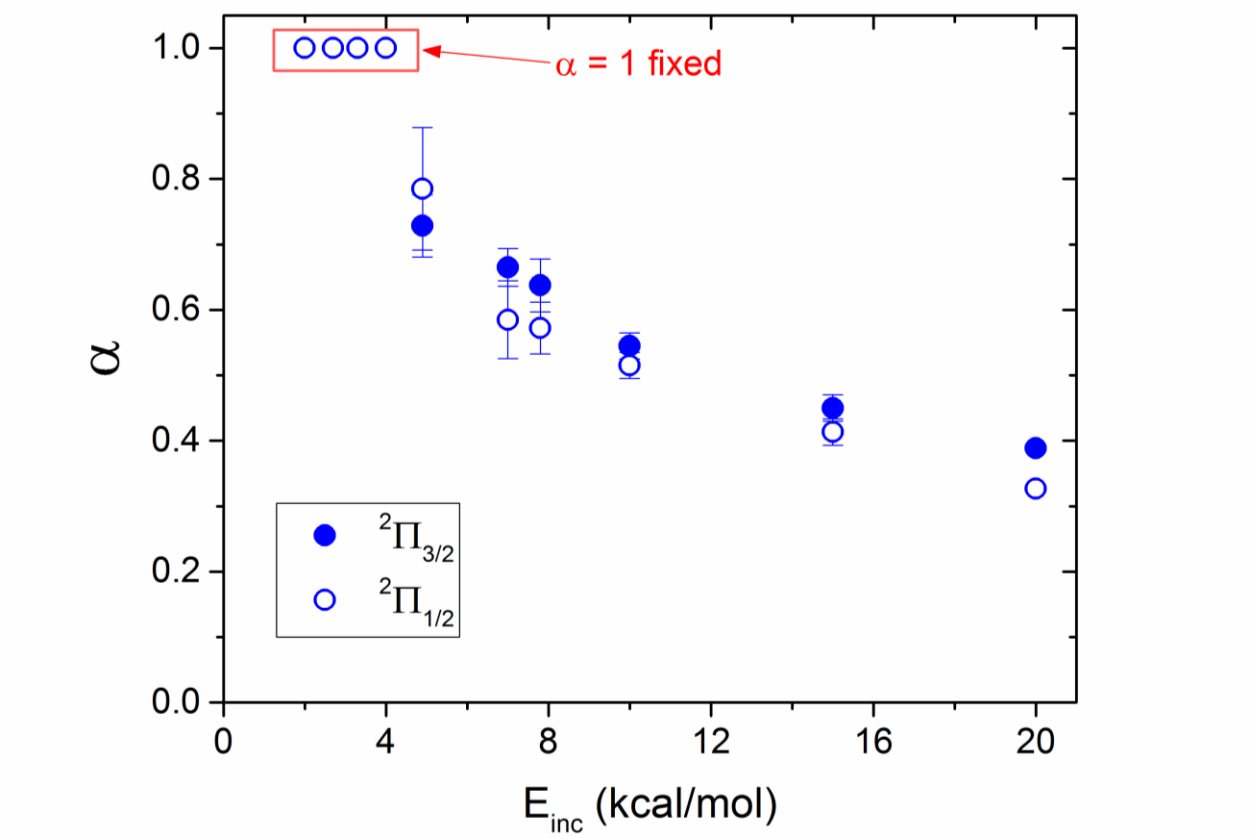

Figure 6.7 Thermal accommodation coefficient, α, as a function of collision energy. At the lowest collision energies (E_{inc} = 2.0 - 4.0 kcal/mol) α is fixed at unity, whereas all other branching ratios are from two-temperature Boltzmann fits to rotational distributions of scattered NO. These data reveal a decrease in α with E_{inc}, i.e. more molecules impulsively scatter at higher incident speeds.

presented in this chapter suggest that this threshold would be just above E_{inc} = 4 kcal/mol for the NO + RTIL system studied.

The impulsively scattered rotational temperatures are summarized in Figure 6.8 and exhibit a nearly linear increase with collision energy. These rotational temperatures are displayed for both spin-orbit states of NO scattered from [bmim][Tf_2N], in addition to previous results from the Nesbitt group of CO_2 scattered from perfluoropolyether (PFPE).[4] Despite the differences in these molecular systems, the two data sets reveal similar efficiencies of translational-to-rotational (T-R) energy transfer at each gas-liquid interface studied.

Hyperthermal rotational temperatures over a range of ~ 500 – 1200 K are observed in the IS channel, which correspond to ~1.0 – 2.5 kcal/mol (where $E_{rot}(IS) = 2/2\ kT_{IS}$). At E_{inc} = 4.9 kcal/mol, just under 25% of the incident collision energy is converted into rotational excitation in the IS channel. This fraction decreases with increasing incident speeds down to ~11% of translation-to-IS rotation energy conversion occurring at the largest incident energy studied (E_{inc} = 20 kcal/mol). These results are consistent with numerous other molecular scattering experiments from liquid, crystalline and self-assembled-monolayer surfaces, which also reveal an increase in T-R energy transfer (and a decrease in factional energy transfer) with increasing collision energy.[4-10]

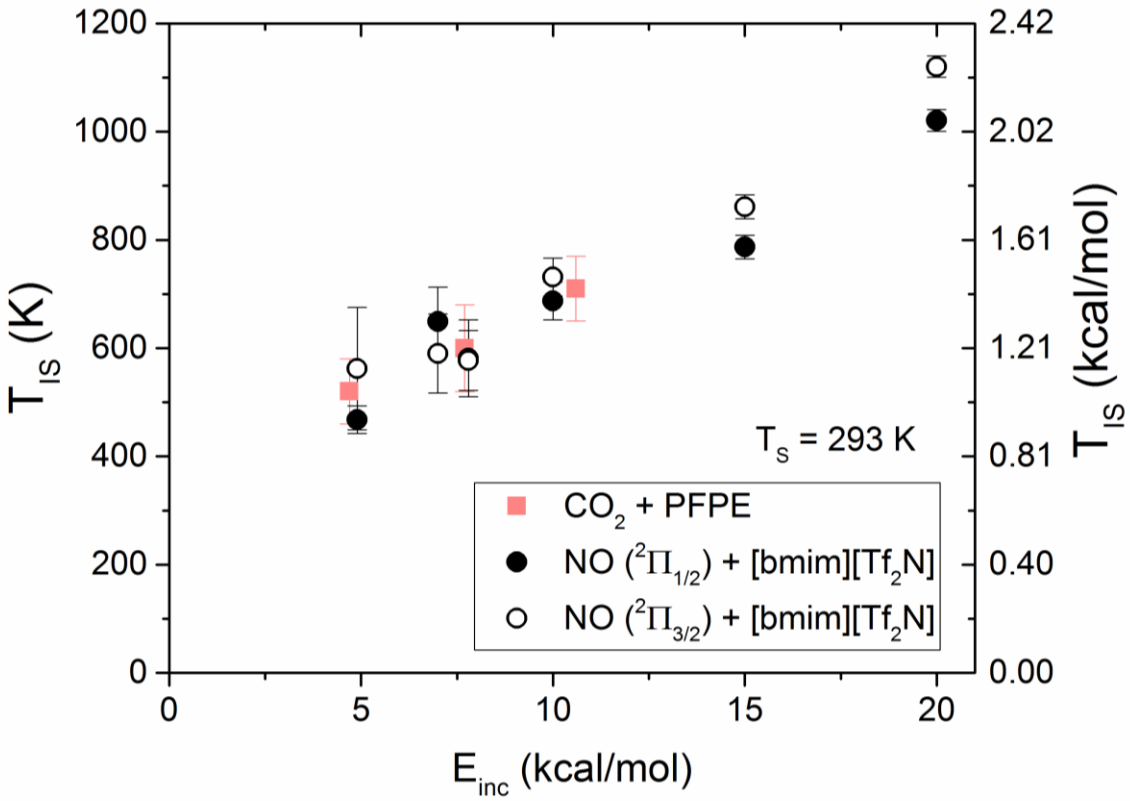

Figure 6.8 Incident collision energy dependence on IS rotational temperature. Data are shown for both spin-orbit states of NO scattered from [bmim][Tf_2N], as well as CO_2 scattered from PFPE,[4] which reveal similar efficiencies and trends of translational to rotational energy transfer.

References for Chapter 6

1. M. E. Saecker, S. T. Govoni, D. V. Kowalski, M. E. King and G. M. Nathanson, *Science*, 1991, **252**, 1421-1424.

2. M. E. Saecker and G. M. Nathanson, *J. Chem. Phys.*, 1993, **99**, 7056-7075.

3. M. E. King, M. E. Saecker and G. M. Nathanson, *J. Chem. Phys.*, 1994, **101**, 2539-2547.

4. B. G. Perkins and D. J. Nesbitt, *J. Phys. Chem. B*, 2006, **110**, 17126-17137.

5. A. W. Kleyn, A. C. Luntz and D. J. Auerbach, *Phys. Rev. Lett.*, 1981, **47**, 1169-1172.

6. G. D. Kubiak, J. E. Hurst, H. G. Rennagel, G. M. McClelland and R. N. Zare, *J. Chem. Phys.*, 1983, **79**, 5163-5178.

7. J. Kimman, C. T. Rettner, D. J. Auerbach, J. A. Barker and J. C. Tully, *Phys. Rev. Lett.*, 1986, **57**, 2053-2056.

8. C. H. Hoffman and D. J. Nesbitt, *J. Phys. Chem. C*, 2016, **120**, 16687–16698.

9. M. P. Ziemkiewicz, J. R. Roscioli and D. J. Nesbitt, *J. Chem. Phys.*, 2011, **134**, 234703.

10. K. R. Lykke and B. D. Kay, *J. Chem. Phys.*, 1990, **92**, 2614-2623.

Chapter 7

State-to-State Resolved Scattering of NO from Molten Gold and Gallium

7.1 Introduction

Electronically nonadiabatic interactions have been investigated extensively in molecular collisions with solid metallic surfaces,[1-10] yet there has been little study of these molecular details of energy transfer between gas phase molecules at *molten* metal surfaces. The conduction band of a metal consists of a continuum of infinitesimally spaced electronic states, from which an electron hole pair can be formed when an electron is excited above the Fermi level, then creating a hole in the conduction band. Because of the continuum of electronic states present, these electron hole pairs can be resonant with any rovibronic excitation of an incident molecule on a metallic surface, thereby presenting a potential avenue for efficient energy transfer between the metal and gas molecule. This electron hole pair mediated rovibronic excitation of incident gas molecules is an intrinsically nonadiabatic electronic process, whereby electronic degrees of freedom in the metal couple to vibrational degrees of freedom in the adsorbate.

A number of experiments have studied how nitric oxide transfers energy from a variety of solid crystalline surfaces, which have provided evidence for electron hole pair mediated vibrational and electronic energy transfer between NO and metal surfaces. For example, vibrationally excited NO(v = 15) has been scattered from Au(111) with relaxation of ~ 8

vibrational quanta observed in the scattered flux.[9] Conversely, when NO(v = 12) was scattered from an insulting LiF surface,[7] vibrational relaxation was almost entirely absent, possibly due to the lack of resonant electron hole pair states with the incoming NO molecule. These results provide strong evidence that the metal surface is responsible for multiquanta vibrational relaxation. Additional experiments investigated electron emission from surfaces of Au(111) covered in Cs, which lowered the work function of the surface down to 1.6 eV.[10] NO molecules were directed at the surface with tunable incident vibrational states, which yielded detection of electron emission only when the incident NO vibrational energy was greater than the work function of surface. These results provide strong evidence for coupling of molecular vibrational energy to surface electrons in the metal, which represents a fundamental breakdown of the Born-Oppenheimer approximation.

Numerous experiments dating back to the mid-1980's have observed vibrational excitation of NO scattered from solid crystalline surfaces.[1, 11-16] These experiments have demonstrated Arrhenius behavior of vibrational excitation probabilities with surface temperature,[1, 11, 12, 16] where the activation energy is equal to the vibrational energy spacing of NO. This behavior has been shown to be characteristic of strong coupling between NO and the metallic surface where electron hole pair formation in the metal couples to vibrational excitation of scattered NO molecules. This behavior has become well observed and established for scattering from solid crystalline surfaces, however, in all previous scattering experiments from molten metal surfaces,[17-21] vibrational excitation collision dynamics have not been reported.

The experiments in this chapter not only represent first quantum state resolved scattering from liquid gold, but also first reported vibrational excitation of scattered molecules from a molten metal surface. We investigate NO scattering dynamics from liquid metals as a function of

(i) metal (Ga and Au), (ii) collision energy (E_{inc} = 2 and 20 kcal/mol) and (iii) surface temperature (Ga, T_s = 600 – 1000 K). These studies further explore electronically nonadiabatic dynamics at the gas-metal interface with surface temperatures up to T_s = 1400 K for Au and T_s = 1000 K for Ga, which is hotter than has previously been studied for these systems.[17, 18, 20] These experiments show first results of vibrationally excited NO from collisions with molten Ga and Au surfaces, as well as evidence suggestive of energy transfer between electron hole pairs in the liquid metal with the NO vibrational degree of freedom. This electronically nonadiabatic behavior has been well studied for NO + crystalline surfaces, but has not previously been observed from liquid metal surfaces.

7.2 Experimental

The gas-liquid scattering apparatus has been described in detail previously.[20, 22] Here we provide a brief description of the setup while highlighting experimental changes made to the heating system that enable study of molten metals up to temperatures T_s = 1400 K. In summary, supersonically cooled NO($^2\Pi_{1/2}$, N = 0) is scattered from molten Ga and Au metal surfaces with quantum state resolved detection. A molecular beam of rotationally and electronically cooled NO is produced from an Even-Lavie valve, with all molecules cooled to the ground $^2\Pi_{1/2}$ spin-orbit state and T_{rot} ~ 1 K. The NO is seeded in a buffer gas of either Ne or H_2 (1:99 ratio), which yield incident collision energies of 2 and 20 kcal/mol (0.09 and 0.87 eV), respectively. The molecular beam passes through a 3 mm skimmer, creating a collimated beam that strikes the liquid surface at an angle of 45º with 1º half angle divergence. The molten metal and scattering apparatus reside in a 90 L stainless steel vacuum chamber that is pumped on by a 1500 L/s turbomolecular pump (base pressure ~ 2 x 10^{-8} Torr).

The liquid metal sits in a tungsten crucible with an alumina coating along the edge to prevent wetting (S21-AO-W, R.D. Mathis). This boat is resistively heated by a 4kW power supply (LV400, R.D. Mathis), which is connected by a series of cables, feedthroughs and copper bars with low resistivities to minimize heat loss and maximize power delivered to the tungsten boat (~ 300 W required to heat a 7 mΩ crucible to 1400 K). More specifically, the power supply is connected to two 1" solid Cu feedthroughs (R.D. Mathis, RDM-FT-400) that are each attached to two 1" x 1/8" Cu bars (oxygen free Copper, alloy 101) that rise 8" above the feedthroughs and sandwich the tungsten boat, overlapping 1" of the boat on each side.

The scattering apparatus and heating system are pictured in Figure 7.1. The reservoir is 3.8 cm x 1.3 cm, i.e. sufficiently larger than the 0.8 cm x 1.1 cm spot size of the incident beam

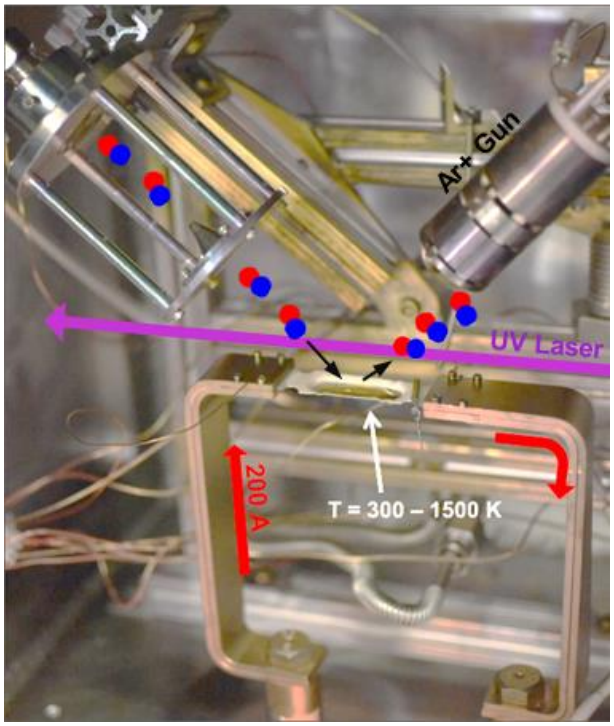

Figure 7.1 Molecular scattering apparatus. Supersonically cooled NO ($^2\Pi_{1/2}$, N=0) is scattered from molten Au (pictured) and Ga, which sit in a resistively heated tungsten crucible and can be heated up to T_s = 1500 K. Scattered NO molecules are detected with quantum state resolution via LIF.

hitting the surface. Both Ga (99.9999%, Acros Organics) and Au (99.95%, Goodfellow) are studied in the present work. Metal surfaces are cleaned by 30 minutes of Ar^+ sputtering at 2kV while heating the surface prior to each data scan. The temperature is measured by a Type K thermocouple on the bottom of the tungsten boat, which has been calibrated against measurements from (i) an optical pyrometer and (ii) a thermocouple submerged in the liquid metal. The experimental upper temperature limit of these metals is constrained by their vapor pressures at high temperatures. Gallium (T_{melt} = 295 K) is studied from T_s = 600 –1000 K while gold (T_{melt} = 1337 K) is studied at a single liquid temperature 1400(40) K, i.e. above experimental uncertainty such that the sample is fully melted, but cool enough to maintain low vapor pressures above the liquid surface to ensure a single collision environment for NO scattering.

Scattered NO molecules are detected with quantum state resolution via laser induced fluorescence (LIF) on the γ band, $A^2\Sigma^+(v = 0) \leftarrow X^2\Pi(v = 0, 1, 2)$. A pulsed UV light source (223-246 nm) is produced from the tripled output of a Nd:YAG pumped dye laser laser operating with LDS698 dye. The laser beam passes 1.6 cm above the liquid surface and in the plane of specular scattering with the laser polarization parallel to surface normal. The fluorescence of scattered molecules is imaged onto a photomultiplier tube (PMT), but only for a 13 mm^3 volume along the laser path due a 1:1 confocal lens imaging setup with a 4 mm pinhole mask in front of the PMT. This results in detection of specularly scattered molecules at $\theta_s = 45(6)^o$. For these experiments, a cone is placed in front of the imaging lens to block direct line of sight from the liquid surface to the imaging lens, thus keeping the lens clear of metal deposition for LIF detection; moreover, this cone still allows all photons of interest that originate from the detection volume along the laser beam path to be collected by the PMT. A UV bandpass filter sits in front

of the PMT to block incident laser light while maximizing fluorescence gathered. Each vibrational band is detected at a different wavelength range, therefore different UV filters were necessary to block the wavelength of each incident laser beam: UG5, Thorlabs for NO(v = 0); XUV0325, Asahi Spectra for NO(v = 1); UG11, Thorlabs for NO(v = 2). All comparisons between vibrational states correct for the varying fluorescence transmission spectra of these filters. The PMT signal is integrated for 200 ns at the peak of scattered NO signal in time and normalized to the laser power for each pulse.

7.3 Results

Sample LIF spectra for scattered NO(v = 0) and NO(v = 1) are displayed in Figure 7.2, where fluorescence is gathered from the $X^2\Pi(v'' = 0, 1) \leftarrow A^2\Sigma^+(v' = 0)$ transition. The spectra are fit to a least squares model from which rovibronic populations are collected.[20, 23] This data analysis has been confirmed with room temperature rotational and spin-orbit distributions of

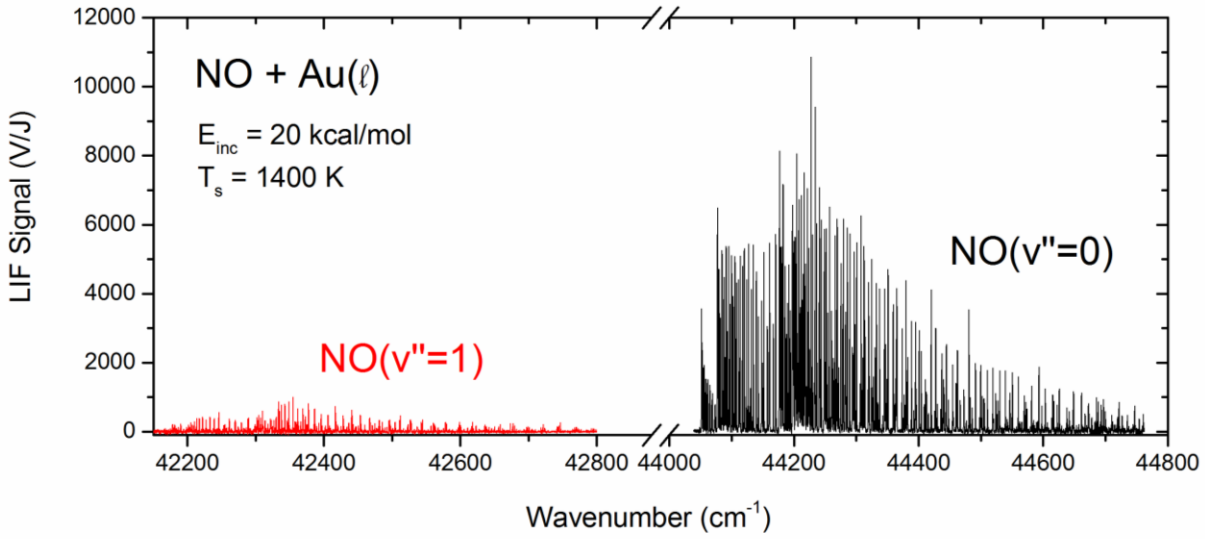

Figure 7.2 LIF spectra of scattered NO(v'' = 0, 1) scattered from Au(l) (T_s = 1400 K) with fluorescence from the $X^2\Pi(v'') \leftarrow A^2\Sigma^+(v' = 0)$ transition.

thermalized NO in the vacuum chamber. The data in Figure 7.2 represent scattering of NO (E_{inc} = 20 kcal/mol) from a T_s = 1400(40) K liquid gold surface. Only specularly scattered molecules are detected, where $\theta_{inc} = \theta_s = 45^o$. All incident NO molecules directed at the molten metal surface are cooled into the ground vibrational state, thus all NO(v = 1) detected result from vibrationally exciting collisions at the gas-metal interface. Significant rotational and spin-orbit excitation of NO by the metal surface is also observed by the large number of peaks within each vibrational state. The substantial energy transfer into spin-orbit and vibrational degrees of freedom indicate nonadiabatic, surface hopping collision dynamics occurring at the NO-Au(l) interface.

7.3.1 NO scattered from Au(l)

A vibrational temperature of NO scattered from Au(l) can be extracted by integrating over all rotational and spin-orbit populations within each vibrational state via [v = 1]/[v = 0] = $\exp[-\Delta E_{vib}/(kT_{vib})]$, where the vibrational energy spacing between NO(v = 0) and NO(v = 1) is ΔE_{vib} = 1876 cm^{-1}. All populations are appropriately corrected for relevant differences in Franck-Condon factors and fluorescence transmission of the UV filter. A two-point Boltzmann plot in Figure 7.3 illustrates the vibrational temperature calculation with a linear fit corresponding to T_{vib} = 708(35) K, i.e. significantly cooler than the 1400(40) K liquid gold surface. This temperature is equivalent to a vibrational excitation probability for (NO(v = 0 → 1) of ~ 0.019.

LIF detection of NO(v = 2) was attempted on the $X^2\Pi(v'' = 2) \leftarrow A^2\Sigma^+(v' = 0)$ transition, however, no peaks were detected in this region. The signal was integrated over the range of expected signal to determine an upper limit of [v = 2]/[v = 0] $\leq 1.5 \times 10^{-3}$. This LIF detection limit is indicated on Figure 7.3 by the gray dashed line. As illustrated in Figure 7.3, an

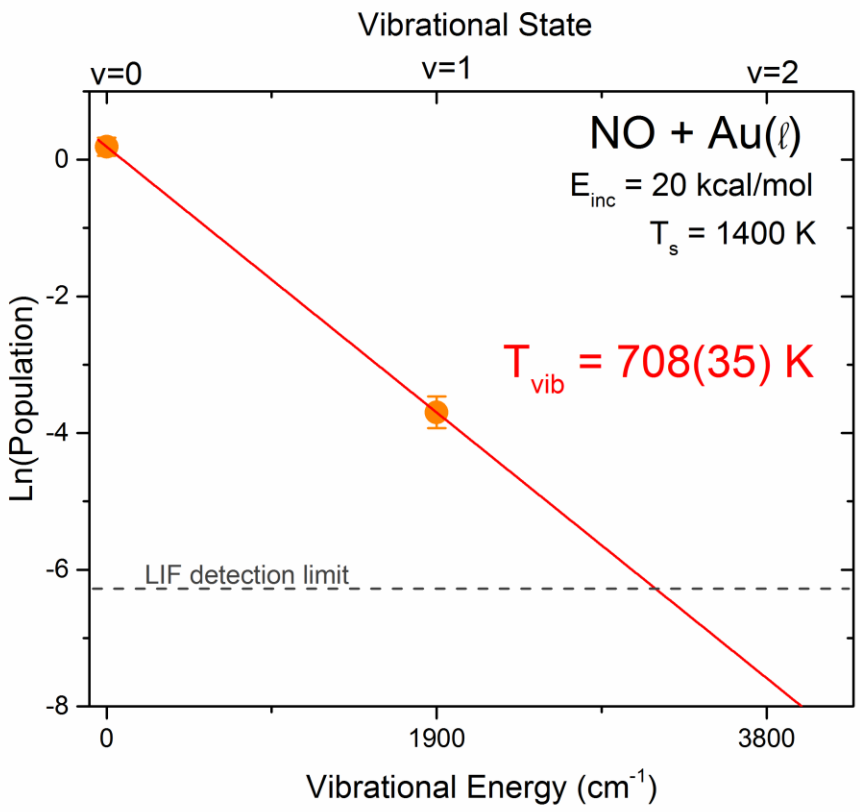

Figure 7.3 Vibrational Boltzmann plot of NO scattered from Au(l). The natural log of NO(v = 0) and NO(v = 1) populations are plotted against vibrational energy. The slope of the linear fit corresponds to a vibrational temperature of T_{vib} = 708 (35) K, from the equation $[v = 1]/[v = 0] = \exp[-\Delta E_{vib}/(kT_{vib})]$. No population in the v = 2 state was detected, although an extrapolation of the fit shows the expected population below the LIF detection limit of this experiment, i.e. $[v = 2]/[v = 0] \leq 1.5 \times 10^{-3}$.

extrapolation of the linear fit from the [v = 0] and [v = 1] populations reveals the expected [v = 2] population to lie below the detection sensitivity of this experiment.

We now consider the rovibronic distributions of NO scattered from Au(l). In Figure 7.4, rotational Boltzmann distributions of NO(v = 0) are displayed for scattering at low (E_{inc} = 2 kcal/mol) and high (E_{inc} = 20 kcal/mol) collision energies, where the ln[Population(J)/(2J+1)] is plotted vs. rotational energy. These rotational distributions also exhibit nonlinear curvature and are fit to double exponential or two-temperature fits. At higher collision energies (E_{inc} = 20

kcal/mol), the rotational distribution fit yields temperatures of T_{cold} = 360(30) K and T_{hot} = 1420(80) K, i.e., within uncertainty of the 1400 K surface temperature. At E_{inc} = 2 kcal/mol, slightly colder temperatures of T_{cold} = 170(40) K and T_{hot} = 830(20) K are observed. These data are from the excited $^2\Pi_{3/2}$ spin-orbit states, which exhibit the same trends/quantities observed from the ground $^2\Pi_{1/2}$ spin-orbit state; moreover, since the incident beam is populated only by the $^2\Pi_{1/2}$ spin-orbit state, the colder component of these $^2\Pi_{3/2}$ rotational distributions is clearly not due to incident beam contamination.

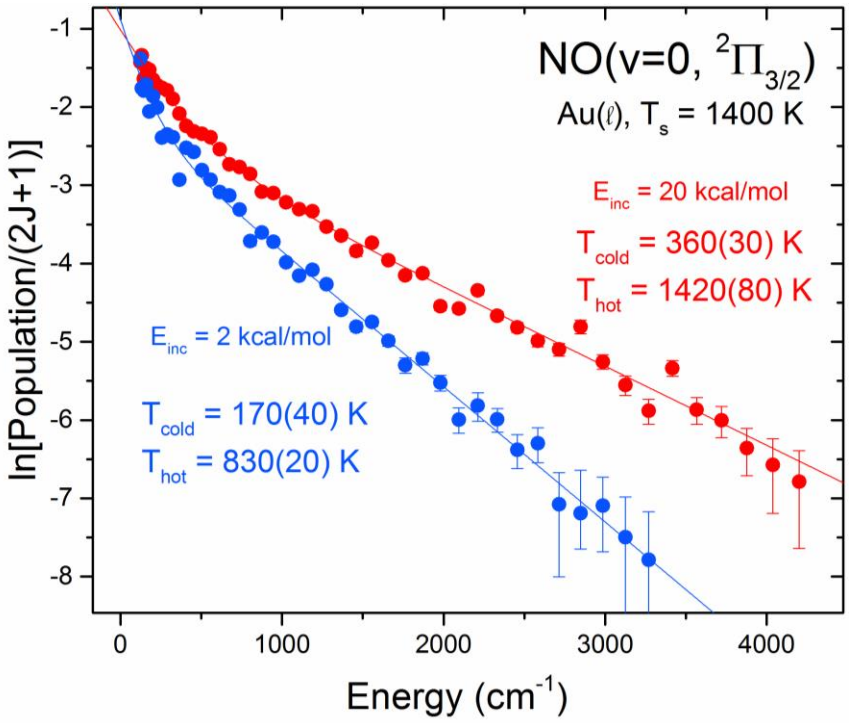

Figure 7.4 Rotational Boltzmann plot of scattered NO(v = 0) from Au (T_S =1400 K) at E_{inc} = 2 and 20 kcal/mol. Two-temperature fits to both rotational distributions are also displayed.

In previous molecular scattering experiments from liquid surfaces, a two-temperature fit has been used to describe a colder, thermal desorption (TD) scattering pathway, with rotational temperatures near the surface temperature, and a rotationally hotter, impulsive scattering (IS)

channel. At lower surface temperatures, this physically motivated model has been useful in characterizing rotational distributions. However, at higher surface temperatures, i.e. T_s = 1400 K, while the rotational distributions are well fit a two-temperature model, the rotational temperatures may not necessarily lend themselves to a simple TD/IS scattering picture. The reason for this is due to a combination of high temperatures and weak gas-liquid surface interaction strengths. Thus, the colder rotational temperatures derived from these fits could represent weaker interactions of NO molecules with the molten metals surfaces, whereby NO scatters away with little rotational excitation. Meanwhile, in the high E_{inc} case, the rotationally hotter NO molecules may either thermally accommodate with the Au surface in the rotational degree of freedom or the excess of incident translational energy may be excited into rotation in the collisional process.

In order to investigate potential rotational accommodation with the liquid surface further, we now consider the rotational distributions of vibrationally excited NO(v = 1) in Figure 7.5, again for incident collision energies at both E_{inc} = 2 and 20 kcal/mol. There is considerably more scatter in these rotational populations relative to NO(v = 0) as the NO(v = 1) state is ~50 times less populated, i.e., [v = 1]/[v = 0] = 0.019. These rotational distributions are fit to a single temperature, yielding equivalent rotational temperatures at both collision energies: T_{rot} = 980(70) K at high E_{inc} and T_{rot} = 970(70) K at low E_{inc}. Especially striking is the observation of vibrationally excited NO at E_{inc} = 2 kcal/mol, where the collision energy is less than the vibrational energy spacing, i.e. E_{inc} = 700 cm^{-1} < ΔE_{vib} = 1876 cm^{-1}, and therefore insufficient to excite NO vibrations. This suggests an excitation process dominated by thermal electron hole pair formation in the metals that is insensitive to incident collision energy. While phonon modes in the metal have also been considered to vibrationally excite NO, they are an unlikely source as

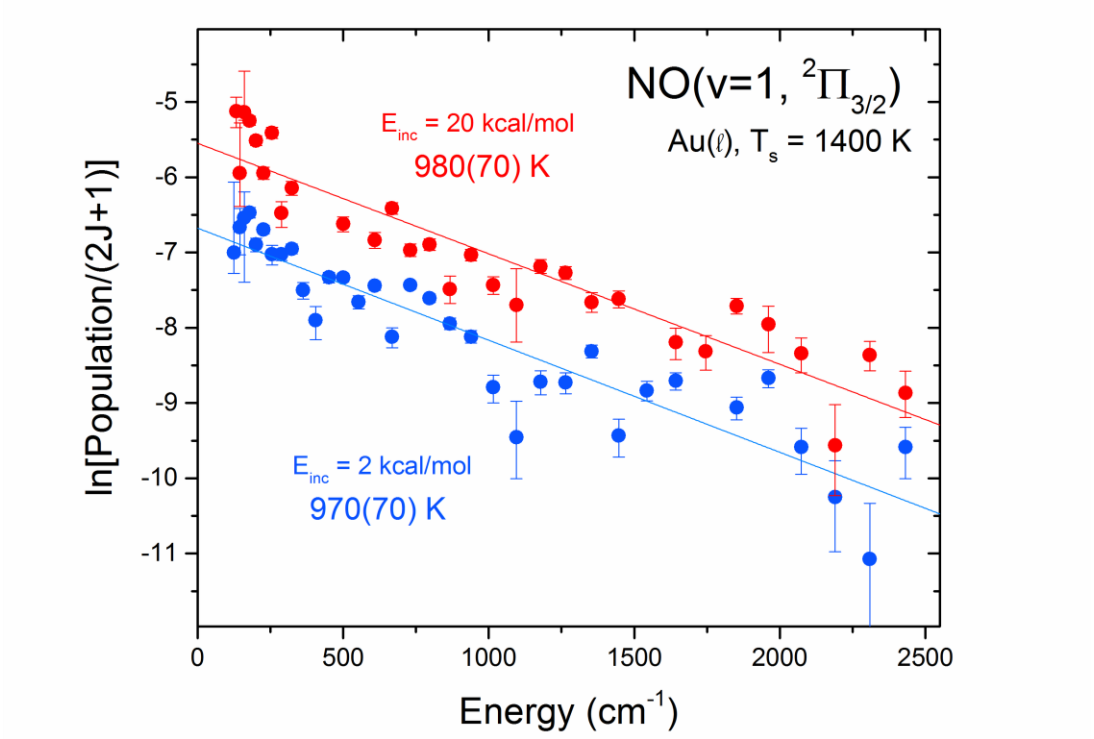

Figure 7.5 Rotational distributions of vibrationally excited NO(v = 0 → 1) from collisions with an Au(l), 1400 K surface for E_{inc} = 2 and 20 kcal/mol. Single-temperature fits reveal similar rotational temperatures at both collision energies that are ~ 400 K cooler than the liquid gold surface.

a multiphonon process between NO + metal would require interactions times on the order of 50 ps to excite molecular vibrations. Vibrational excitation via a nonadiabatic, electron hole pair mediated excitation process will be explored further in section 7.4.1.

7.3.2 NO scattered from Ga(l)

Molecular scattering of NO from liquid gallium at T_s = 873(30) K has also been investigated at both low and high collision energies (E_{inc} = 2 and 20 kcal/mol) where vibrationally excited NO(v = 1) is also detected. Rotational Boltzmann distributions are displayed in Figure 7.5 for both NO(v = 0) and NO(v = 1) at collision energies E_{inc} = 2 and 20 kcal/mol. Broadly summarized, the shapes of these rotational distributions are qualitatively very

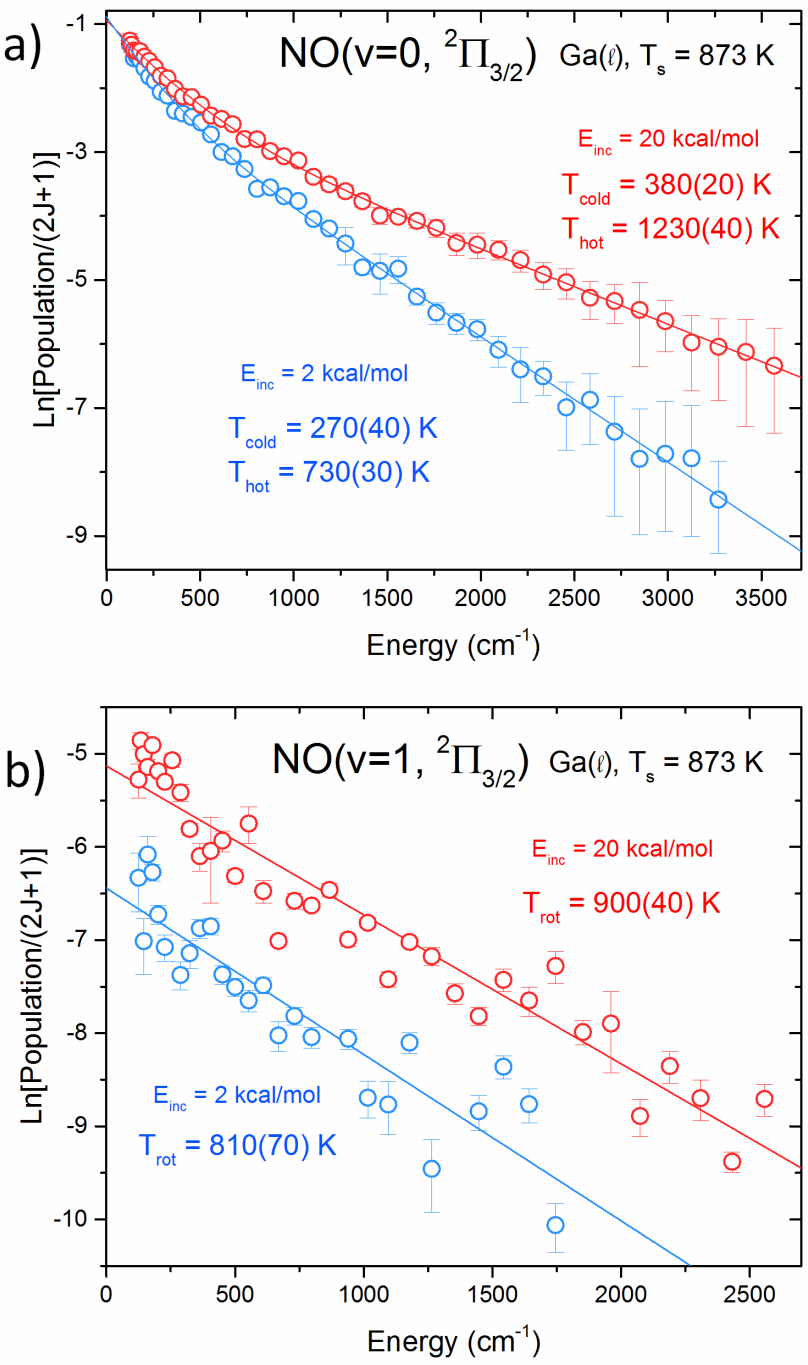

Figure 7.6 Boltzmann rotational distribution of NO scattered from Ga (T_s = 873(30) K) at both low and high collision energies. a) Two-temperature fits to NO(v = 0) rotational distributions and b) single-temperature fits to vibrationally excited NO(v = 1), with T_{rot} at both low and high collision energies within uncertainty of T_s.

similar to those observed for NO + Au(l) (Figures 7.4 and 7.5); two-temperature fits to NO(v = 0) show clear differences between the two collision energies, while NO(v = 1) rotational distributions are fit to single-temperature linear fits that are remarkably similar for both E_{inc}.

The double exponential fits to the rotational distributions of NO(v = 0) at low collisions yield T_{cold} = 270(40) K and T_{hot} = 730(30) K while at higher collision energies T_{cold} = 380(20) K and T_{hot} = 1230(40) K. The single temperature fits of vibrationally excited NO are 810(70) K and 900(40) K for the respective E_{inc} = 2 and 20 kcal/mol scattering conditions. Both of these rotational temperatures are within uncertainty of the 873 K liquid gallium surface, suggestive of rotational thermal accommodation with the surface in the fractional scattering pathways leading to vibrationally excited NO. This thermal accommodation of the rotational degree of freedom is unlike scattering from the significantly hotter 1400 K gold surface, which yielded rotational temperature some 400 K cooler than the surface temperature for NO(v = 1).

7.4 Discussion

7.4.1 Temperature Dependence of NO scattered from Ga(l)

As a way to test the nature of collisional NO vibrational excitation at molten metal surfaces, we now investigate scattering dynamics as a function of the liquid gallium surface temperature. LIF spectra containing all rotational and spin-orbit states populated within NO(v = 0) and NO(v = 1) were taken at T_s = 873 K, from which the Boltzmann rotational populations shown above were derived. In order to extract a vibrational temperature as a function of T_s, however, a smaller piece of the spectrum with lines from a wide range of rotational states is sufficent. Here, the P_{12} branch was scanned over for both vibrational states over the bandhead containing peaks from J = 1.5 - 19.5, which yields representative vibrational state populations.

This band is isolated at the lower energy end of each spectrum and is integrated over for NO scattered from gallium, at surface temperatures ranging from T_s = 600 – 1000 K. The extracted vibrational temperatures vs. surface temperature are displayed in Figure 7.7. These data reveal increasing vibrational excitation with surface temperature, yet with subthermal temperatures, in accordance with molecular scattering results of NO scattered from solid crystalline surfaces.[15]

In previous scattering experiments of NO from crystalline surfaces, an Arrhenius surface temperature dependence of vibrational excitation has been interpreted as characteristic evidence for nonadiabatic, electron hole pair mediated energy transfer between NO and metal surfaces.[1, 11, 12, 16, 24] In Figure 7.8, the vibrational excitation probability, P_v = [v = 1]/[v = 0], is considered as a

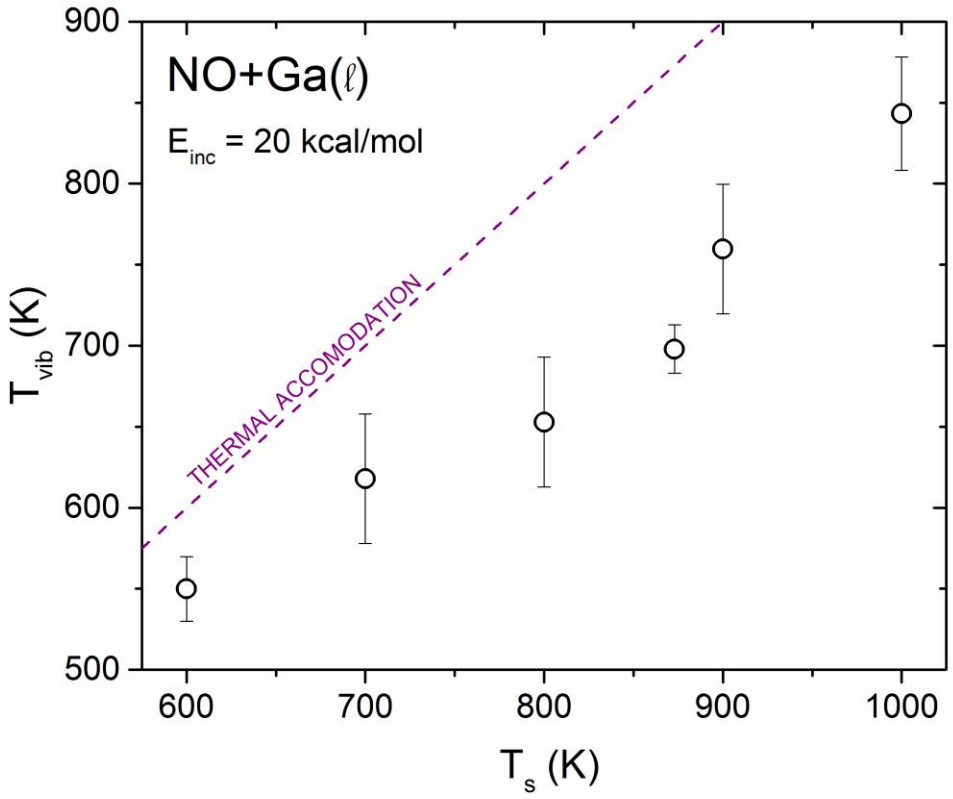

Figure 7.7 Vibrational excitation of NO(v = 0 → 1) scattered from Au(l) (T_s = 1400 K). The vibrational temperature is calculated from [v=1]/[v=0] = exp[-ΔE_{vib}/(kT_{vib})] where ΔE_{vib} ~ 1876 cm^{-1}.

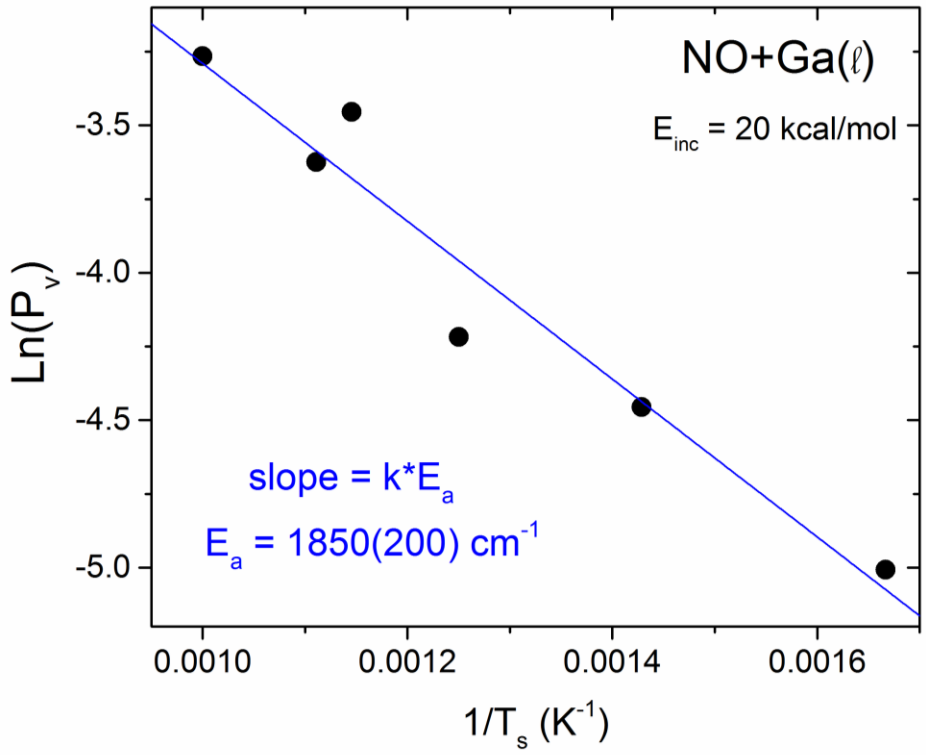

Figure 7.8 Natural log of the vibrational excitation probability of NO(v = 0) + Au(l) → NO(v = 1) vs. inverse surface temperature. The blue line represents the linear fit with E_a = 1850(200) cm^{-1}, i.e. within uncertainty of the vibrational energy spacing of 1876 cm^{-1}.

function of the inverse surface temperature following the equation: $P_v = A*\exp[-E_a/kT_s]$. The data reveal linear behavior with varied surface temperature and an activation energy of E_a = 1850(200) cm^{-1}, i.e., clearly in excellent agreement with the v = 0 → 1 vibrational energy spacing ΔE_{vib} = 1876 cm^{-1}. This suggests strong electronic coupling between NO + liquid metal surface and these results represent first evidence of electron hole pair mediated vibrational excitation of NO at *liquid* metal surfaces.

Wodtke, Tully and coworkers have contributed extensively toward understanding these nonadiabatic, electron hole pair mediated collision dynamics occurring at NO + Au(111) surfaces.[5, 9, 12, 13, 25-28] Evidence has been presented that suggests vibrational excitation and deexcitation of NO molecules at a metal surface are mediated by the formation of electron hole

pairs in the metal. In this mechanism, as a NO molecule nears the surface, an electron from the lowest unoccupied molecular orbital (LUMO) of the metal can 'hop' onto the NO molecule forming a transient anion that is stabilized by a Coulomb image charge in the metal. As the NO molecule leaves the surface, the electron hops back to the metal and during this process vibrational modes in the NO molecule can be excited (or relaxed).

7.4.2 Energy Transfer at the NO + Ga(l)/Au(l) Interfaces

The data in Figure 7.9 summarize the final energy distributions of NO scattered from both Au(l) (T_s = 1400 K) and Ga(l) (T_s = 873 K) at low (E_{inc} = 2 kcal/mol) and high (E_{inc} = 20 kcal/mol) collision energies. The electronic, rotational and vibrational temperatures plotted are calculated as follows: (i) The spin-orbit/electronic temperatures are computed via $[^2\Pi_{3/2}]/[^2\Pi_{1/2}] = \exp(-E_{so}/kT_{elec})$ where E_{so} = 123 cm^{-1}, (ii) average rotational temperatures are presented for each vibrational state, and (iii) vibrational temperatures are calculated by integrating over all rotational and spin-orbit states populated with each vibrational state via $[v=1]/[v=0] = \exp[-\Delta E_{vib}/(kT_{vib})]$, as done in Figure 7.3. Most visible in the Au(l) scattering data in Figure 7.9(a) is the lack of thermal accommodation for the NO molecular degrees of freedom (i.e. rotational, electronic, vibrational) with the molten gold surface at both collision energies studied. Similar trends are observed for scattered NO from a cooler 873 K gallium surface, with the exception of some rotational thermal accommodation. Broadly speaking, these scattering data from Au(l) and Ga(l) reveal more energy transfer into NO internal rotation and electronic degrees of freedom for faster incident speeds, whereas, in contrast, there is no effect of collision energy on the efficiency of vibrational excitation. The higher incident collision energies introduce more

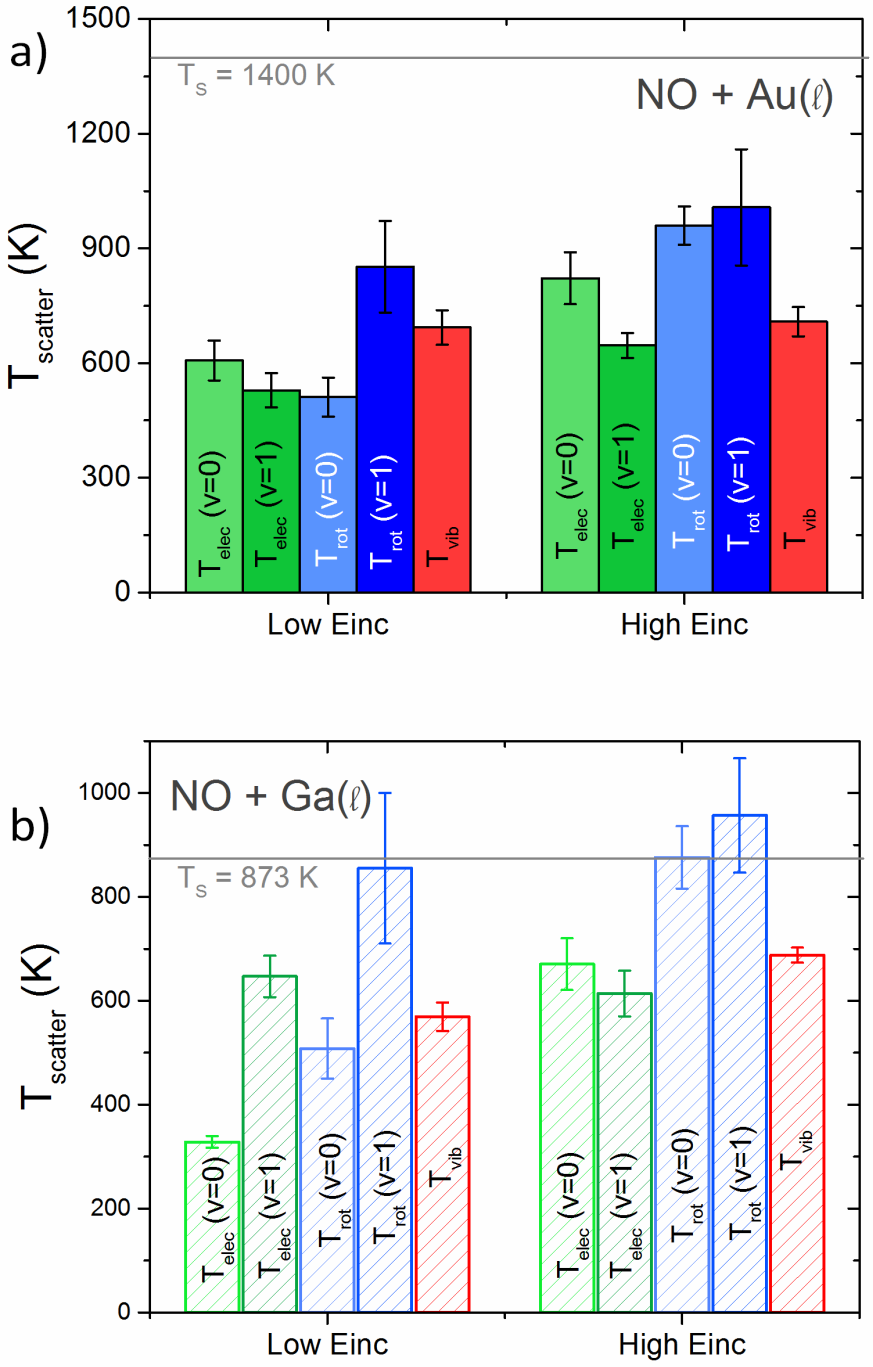

Figure 7.9 Summary of rovibronic temperatures for NO scattered at E_{inc} = 2 and 20 kcal/mol from a) Au(l) T_s =1400 K and b) Ga(l) T_s = 873 K.

available energy into the system, resulting in increased translational to rotational/spin-orbit energy transfer.

As noted earlier, the detection of NO(v = 1) scattered at E_{inc} = 2 kcal/mol signifies that the bulk of the energy must be coming from the metal as $E_{inc} < E_{vib}$, i.e. incident translational energy is insufficient to vibrationally excite NO(v = 1). Also noteworthy is that the vibrational temperatures are nearly identical for both collision energies. This is in contrast to the temperatures observed in the spin-orbit and rotational degree of freedom, which are highly dependent on collision energy, especially for NO(v = 0 → 0) collisions. A closer look at the rotational and spin-orbit temperatures for NO scattering from Au(l) reveals an increase of ~200 K from T_{elec}(v = 0) at low E_{inc} relative to high E_{inc}, however, there is only < 100 K difference in the spin-orbit temperatures of the two collision energies for the vibrationally excited NO distributions. This same trend is observed in the rotational energies, revealing ~ 500 K difference in T_{rot} between the two collision energies for NO(v = 0), while only ~ 100 K for NO(v = 1). These data trends, which are reiterated in the Ga(l) results, indicate that for vibration-conserving collisions, energy transfer from the translational to rotational/spin-orbit degree of freedom is more prominent. However, for collisions where NO is vibrationally excited, NO(v = 0 → 1) the rotational and spin-orbit distributions are less sensitive to incoming incident speeds, where the energy for excitation is provided by the liquid metal surface.

7.5 Conclusion

Quantum state resolved molecular beam scattering techniques are utilized to investigate collision dynamics of NO at molten gold and gallium surfaces. The results presented in this chapter represent the first detection of NO vibrationally excited from collisions at liquid metal

surfaces. Additionally, the surface temperature dependence of NO ($v = 0 \rightarrow 1$) vibrational excitation probabilities exhibit activation energies equivalent to the vibrational energy spacing, suggestive of electron hole pair mediated vibrational excitation. Rovibronic distributions of NO reveal strong collision energy dependence for vibrationally unexcited NO($v = 0 \rightarrow 0$) where more rotational and spin-orbit excitation is found for increasing E_{inc}. Higher incident translational energies bring more energy into the system that can be redistributed into internal rotational and electronic degrees of freedom. The fraction of vibrationally excited NO, however, is relatively insensitive to collision energy for both liquid gold and gallium. Moreover, the rotational and spin-orbit distributions are remarkably similar for NO($v = 1$) scattered from low and high collision energies for both Ga(l) and Au(l), indicating that these internal NO modes are excited by thermal electron hole pairs in the metal surface. These results are consistent with strong NO-metal coupling and electron hole pair mediated excitation of NO internal degrees of freedom.

References for Chapter 7

1. C. T. Rettner, F. Fabre, J. Kimman and D. J. Auerbach, *Phys. Rev. Lett.*, 1985, **55**, 1904-1907.

2. N. Bartels, K. Golibrzuch, C. Bartels, L. Chen, D. J. Auerbach, A. M. Wodtke and T. Schafer, *J. Chem. Phys.*, 2014, **140**, 54710.

3. N. Bartels, K. Golibrzuch, C. Bartels, L. Chen, D. J. Auerbach, A. M. Wodtke and T. Schafer, *P. Natl. Acad. Sci. USA*, 2013, **110**, 17738-17743.

4. H. Hou, C. T. Rettner, D. J. Auerbach, Y. Huang, S. J. Gulding and A. M. Wodtke, *Faraday Discuss.*, 1999, **113**, 181-200.

5. Y. Huang, A. M. Wodtke, H. Hou, C. T. Rettner and D. J. Auerbach, *Phys. Rev. Lett.*, 2000, **84**, 2985-2988.

6. J. D. White, J. Chen, D. Matsiev, D. J. Auerbach and A. M. Wodtke, *Nature*, 2005, **433**, 503-505.

7. A. M. Wodtke, Y. H. Huang and D. J. Auerbach, *J. Chem. Phys.*, 2003, **118**, 8033-8041.

8. I. Rahinov, R. Cooper, D. Matsiev, C. Bartels, D. J. Auerbach and A. M. Wodtke, *Phys. Chem. Chem. Phys.*, 2011, **13**, 12680-12692.

9. Y. H. Huang, C. T. Rettner, D. J. Auerbach and A. M. Wodtke, *Science*, 2000, **290**, 111-114.

10. J. L. Larue, J. D. White, N. H. Nahler, Z. Liu, Y. Sun, P. A. Pianetta, D. J. Auerbach and A. M. Wodtke, *J. Chem. Phys.*, 2008, **129**.

11. E. K. Watts, J. L. W. Siders and G. O. Sitz, *Surf. Sci.*, 1997, **374**, 191-196.

12. D. Matsiev, Z. S. Li, R. Cooper, I. Rahinov, C. Bartels, D. J. Auerbach and A. M. Wodtke, *Phys. Chem. Chem. Phys.*, 2011, **13**, 8153-8162.

13. R. Cooper, I. Rahinov, Z. S. Li, D. Matsiev, D. J. Auerbach and A. M. Wodtke, *Chem. Sci.*, 2010, **1**, 55-61.

14. D. A. Mantell, Y. F. Maa, S. B. Ryali, G. L. Haller and J. B. Fenn, *J. Chem. Phys.*, 1983, **78**, 6338-6339.

15. M. Asscher, W. L. Guthrie, T. H. Lin and G. A. Somorjai, *J. Chem. Phys.*, 1983, **78**, 6992-7004.

16. Q. Ran, D. Matsiev, D. J. Auerbach and A. M. Wodtke, *Phys. Rev. Lett.*, 2007, **98**.

17. M. Manning, J. A. Morgan, D. J. Castro and G. M. Nathanson, *J. Chem. Phys.*, 2003, **119**, 12593-12604.

18. W. R. Ronk, D. V. Kowalski, M. Manning and G. M. Nathanson, *J. Chem. Phys.*, 1996, **105**, 4397-4397.

19. A. Muis and J. R. Manson, *J. Chem. Phys.*, 1999, **111**, 730-736.

20. M. P. Ziemkiewicz, J. R. Roscioli and D. J. Nesbitt, *J. Chem. Phys.*, 2011, **134**, 234703.

21. F. C. Hurlbut and D. E. Beck, *U.C. Eng. Proj. Report HE-150-166*, 1959.

22. A. Zutz and D. J. Nesbitt, *J. Phys. Chem. C*, 2015, **119**, 8596-8607.

23. M. Ziemkiewicz, M. Wojcik and D. J. Nesbitt, *J. Chem. Phys.*, 2005, **123**, 224307.

24. B. D. Kay, T. D. Raymond and M. E. Coltrin, *Phys. Rev. Lett.*, 1987, **59**, 2792-2794.

25. N. Shenvi, S. Roy and J. C. Tully, *J. Chem. Phys.*, 2009, **130**, 174107.

26. N. Shenvi, S. Roy and J. C. Tully, *Science*, 2009, **326**, 829-832.

27. A. M. Wodtke, D. Matsiev and D. J. Auerbach, *Prog. Surf. Sci.*, 2008, **83**, 167-214.

28. A. M. Wodtke, J. C. Tully and D. J. Auerbach, *Int. Rev. Phys. Chem.*, 2004, **23**, 513-539.

Bibliography

Abbatt, J. P. D., *Chem. Rev.*, 2003, **103**, 4783-4800.

Alcock, C. B., Itkin, V. P. and Horrigan, M. K., *Can. Metall. Quart.*, 1984, **23**, 309-313.

Alexander, M. H., *J. Chem. Phys.*, 1999, **111**, 7426-7434.

Alexander, M. H., *J. Chem. Phys.*, 1993, **99**, 7725-7738.

Alexander, M. H., Andresen, P., Bacis, R., Bersohn, R., Comes, F. J., Dagdigian, P. J., Dixon, R. N., Field, R. W., Flynn, G. W., Gericke, K. H., Grant, E. R., Howard, B. J., Huber, J. R., King, D. S., Kinsey, J. L., Kleinermanns, K., Kuchitsu, K., Luntz, A. C., Mccaffery, A. J., Pouilly, B., Reisler, H., Rosenwaks, S., Rothe, E. W., Shapiro, M., Simons, J. P., Vasudev, R., Wiesenfeld, J. R., Wittig, C. and Zare, R. N., *J. Chem. Phys.*, 1988, **89**, 1749-1753.

Aliaga, C., Baker, G. A. and Baldelli, S., *J. Phys. Chem. B*, 2008, **112**, 1676-1684.

Andreae, M. O. and Merlet, P., *Global Biogeochem. Cycles*, 2001, **15**, 955-966.

Anthony, J. L., Anderson, J. L., Maginn, E. J. and Brennecke, J. F., *J. Phys. Chem. B*, 2005, **109**, 6366-6374.

Anthony, J. L., Maginn, E. J. and Brennecke, J. F., *J. Phys. Chem. B*, 2002, **106**, 7315-7320.

Armand, M., Endres, F., MacFarlane, D. R., Ohno, H. and Scrosati, B., *Nat. Mater.*, 2009, **8**, 621-629.

Asscher, M., Guthrie, W. L., Lin, T. H. and Somorjai, G. A., *J. Chem. Phys.*, 1983, **78**, 6992-7004.

Bai, Y., Cao, Y. M., Zhang, J., Wang, M., Li, R. Z., Wang, P., Zakeeruddin, S. M. and Gratzel, M., *Nat. Mater.*, 2008, **7**, 626-630.

Bara, J. E., Noble, R. D. and Gin, D. L., *Ind. Eng. Chem. Res.*, 2009, **48**, 4607-4610.

Bartels, N., Golibrzuch, K., Bartels, C., Chen, L., Auerbach, D. J., Wodtke, A. M. and Schafer, T., *P. Natl. Acad. Sci. USA*, 2013, **110**, 17738-17743.

Bartels, N., Golibrzuch, K., Bartels, C., Chen, L., Auerbach, D. J., Wodtke, A. M. and Schafer, T., *J. Chem. Phys.*, 2014, **140**, 54710.

Blanchard, L. A., Gu, Z. Y. and Brennecke, J. F., *J. Phys. Chem. B*, 2001, **105**, 2437-2444.

Blanchard, L. A., Hancu, D., Beckman, E. J. and Brennecke, J. F., *Nature*, 1999, **399**, 28-29.

Bodo, E., Gontrani, L., Caminiti, R., Plechkova, N. V., Seddon, K. R. and Triolo, A., *J. Phys. Chem. B*, 2010, **114**, 16398.

Bowers, J., Vergara-Gutierrez, M. C. and Webster, J. R. P., *Langmuir*, 2004, **20**, 309-312.

Bradley, A. E., Hardacre, C., Holbrey, J. D., Johnston, S., McMath, S. E. J. and Nieuwenhuyzen, M., *Chem. Mater.*, 2002, **14**, 629-635.

Brown, L. S. and Sibener, S. J., *J. Chem. Phys.*, 1988, **89**, 1163-1169.

Brzozowski, J., Elander, N. and Erman, P., *Phys. Scripta*, 1974, **9**, 99-103.

Caporali, S., Bardi, U. and Lavacchi, A., *J. Electron Spectrosc.*, 2006, **151**, 4-8.

Carvalho, P. J., Freire, M. G., Marrucho, I. M., Queimada, A. J. and Coutinho, J. A. P., *J. Chem. Eng. Data*, 2008, **53**, 1346-1350.

Cavanagh, R. R. and King, D. S., *Phys. Rev. Lett.*, 1981, **47**, 1829-1832.

Chorny, I., Benjamin, I. and Nathanson, G. M., *J. Phys. Chem. B*, 2004, **108**, 995-1002.

Cohen, S. R., Naaman, R. and Balintkurti, G. G., *Chem. Phys.*, 1989, **134**, 119-126.

Cohen, S. R., Naaman, R. and Balintkurti, G. G., *Chem. Phys. Lett.*, 1988, **152**, 269-273.

Cohen, S. R., Naaman, R. and Sagiv, J., *J. Chem. Phys.*, 1988, **88**, 2757-2763.

Cooper, R., Rahinov, I., Li, Z. S., Matsiev, D., Auerbach, D. J. and Wodtke, A. M., *Chem. Sci.*, 2010, **1**, 55-61.

Crutzen, P. J., *Annu. Rev. Earth Planet. Sci.*, 1979, **7**, 443-472.

Davidovits, P., Kolb, C. E., Williams, L. R., Jayne, J. T. and Worsnop, D. R., *Chem. Rev.*, 2006, **106**, 1323-1354.

de Souza, R. F., Padilha, J. C., Goncalves, R. S. and Dupont, J., *Electrochem. Commun.*, 2003, **5**, 728-731.

Dentener, F. J. and Crutzen, P. J., *J. Geophys. Res.*, 1993, **98**, 7149-7163.

Dimitriades, B., *Environ. Sci. Technol.*, 1972, **6**, 253.

Dunning, F. B., Hulet, R. G. and Morse, M. D., *Atomic, Molecular, and Optical Physics: Atoms and Molecules*, Academic Press, San Diego, 1996.

Dzyuba, S. V. and Bartsch, R. A., *ChemPhysChem*, 2002, **3**, 161-166.

Ellison, G. B., Tuck, A. F. and Vaida, V., *J. Geophys. Res.-Atmos.*, 1999, **104**, 11633-11641.

Esperanca, J. M. S. S., Lopes, J. N. C., Tariq, M., Santos, L. M. N. B. F., Magee, J. W. and Rebelo, L. P. N., *J. Chem. Eng. Data*, 2010, **55**, 3-12.

Eyles, C. J., Brouard, M., Yang, C. H., Klos, J., Aoiz, F. J., Gijsbertsen, A., Wiskerke, A. E. and Stolte, S., *Nat. Chem.*, 2011, **3**, 597-602.

Faust, J. A. and Nathanson, G. M., *Chem. Soc. Rev.*, 2016, **45**, 3609-3620.

Faust, J. A., Sobyra, T. B. and Nathanson, G. M., *J. Phys. Chem. Lett.*, 2016, **7**, 730-735.

Forsythe, W. E., *Smithsonian Physical Tables*, Knovel, Norwich, N.Y., 9th rev. edn., 2003.

Frenkel, F., Hager, J., Krieger, W., Walther, H., Ertl, G., Segner, J. and Vielhaber, W., *Chem. Phys. Lett.*, 1982, **90**, 225-229.

Garton, D. J., Minton, T. K., Alagia, M., Balucani, N., Casavecchia, P. and Volpi, G. G., *J. Chem. Phys.*, 2000, **112**, 5975-5984.

Gertner, B. J. and Hynes, J. T., *Science*, 1996, **271**, 1563-1566.

Geuzebroek, F. H., Wiskerke, A. E., Tenner, M. G., Kleyn, A. W., Stolte, S. and Namiki, A., *J. Phys. Chem.*, 1991, **95**, 8409-8421.

Gisler, A. W. and Nesbitt, D. J., *Faraday Discuss.*, 2012, **157**, 297-305.

Gorlov, M. and Kloo, L., *Dalton T.*, 2008, 2655-2666.

Gragson, D. E. and Richmond, G. L., *J. Phys. Chem. B*, 1998, **102**, 3847-3861.

Grassian, V. H., *J. Phys. Chem. A*, 2002, **106**, 860-877.

Grassian, V. H., *Int. Rev. Phys. Chem.*, 2001, **20**, 467-548.

Gregurick, S., Alexander, M. H. and Depristo, A. E., *J. Chem. Phys.*, 1994, **100**, 610-621.

Hammer, T., Reichelt, M. and Morgner, H., *Phys. Chem. Chem. Phys.*, 2010, **12**, 11070-11080.

Herzberg, G., *Spectra and Molecular-Structure I. Spectra of Diatomic-Molecules*, Princeton Univ. Press, Princeton, NJ, 1968.

Hewick, R. M., Hunkapiller, M. W., Hood, L. E. and Dreyer, W. J., *J. Biol. Chem.*, 1981, **256**, 7990-7997.

Hoffman, C. H. and Nesbitt, D. J., *J. Phys. Chem. C*, 2016, **120**, 16687–16698.

Hou, H., Rettner, C. T., Auerbach, D. J., Huang, Y., Gulding, S. J. and Wodtke, A. M., *Faraday Discuss.*, 1999, **113**, 181-200.

Hough, W. L., Smiglak, M., Rodriguez, H., Swatloski, R. P., Spear, S. K., Daly, D. T., Pernak, J., Grisel, J. E., Carliss, R. D., Soutullo, M. D., Davis, J. H. and Rogers, R. D., *New J. Chem.*, 2007, **31**, 1429-1436.

Huang, Y., Wodtke, A. M., Hou, H., Rettner, C. T. and Auerbach, D. J., *Phys. Rev. Lett.*, 2000, **84**, 2985-2988.

Huang, Y. H., Rettner, C. T., Auerbach, D. J. and Wodtke, A. M., *Science*, 2000, **290**, 111-114.

Huddleston, J. G., Visser, A. E., Reichert, W. M., Willauer, H. D., Broker, G. A. and Rogers, R. D., *Green Chem.*, 2001, **3**, 156-164.

Huddleston, J. G., Willauer, H. D., Swatloski, R. P., Visser, A. E. and Rogers, R. D., *Chem. Commun.*, 1998, 1765-1766.

Hurlbut, F. C. and Beck, D. E., *U.C. Eng. Proj. Report HE-150-166*, 1959.

Hutson, N. D., Krzyzynska, R. and Srivastava, R. K., *Ind. Eng. Chem. Res.*, 2008, **47**, 5825-5831.

Iimori, T., Iwahashi, T., Kanai, K., Seki, K., Sung, J. H., Kim, D., Hamaguchi, H. O. and Ouchi, Y., *J. Phys. Chem. B*, 2007, **111**, 4860-4866.

Iwahashi, T., Nishi, T., Yamane, H., Miyamae, T., Kanai, K., Seki, K., Kim, D. and Ouchi, Y., *J. Phys. Chem. C*, 2009, **113**, 19237.

Jeon, Y., Sung, J., Bu, W., Vaknin, D., Ouchi, Y. and Kim, D., *J. Phys. Chem. C*, 2008, **112**, 19649-19654.

Jin, D. S., Deshwal, B. R., Park, Y. S. and Lee, H. K., *J. Hazard. Mater.*, 2006, **135**, 412-417.

Jutz, F., Andanson, J. M. and Baiker, A., *Chem. Rev.*, 2011, **111**, 322-353.

Kanai, K., Nishi, T., Iwahashi, T., Ouchi, Y., Seki, K., Harada, Y. and Shin, S., *J. Electron Spectrosc.*, 2009, **174**, 110-115.

Kanakidou, M., Seinfeld, J. H., Pandis, S. N., Barnes, I., Dentener, F. J., Facchini, M. C., Van Dingenen, R., Ervens, B., Nenes, A., Nielsen, C. J., Swietlicki, E., Putaud, J. P., Balkanski, Y., Fuzzi, S., Horth, J., Moortgat, G. K., Winterhalter, R., Myhre, C. E. L., Tsigaridis, K., Vignati, E., Stephanou, E. G. and Wilson, J., *Atmos. Chem. Phys.*, 2005, **5**, 1053-1123.

Kawano, R., Matsui, H., Matsuyama, C., Sato, A., Susan, M. A. B. H., Tanabe, N. and Watanabe, M., *J. Photoch. Photobio. A*, 2004, **164**, 87-92.

Kay, B. D., Raymond, T. D. and Coltrin, M. E., *Phys. Rev. Lett.*, 1987, **59**, 2792-2794.

Kim, D. and Schatz, G. C., *J. Phys. Chem. A*, 2007, **111**, 5019-5031.

Kim, Y. S., Choi, W. Y., Jang, J. H., Yoo, K. P. and Lee, C. S., *Fluid Phase Equilibr.*, 2005, **228**, 439-445.

Kimman, J., Rettner, C. T., Auerbach, D. J., Barker, J. A. and Tully, J. C., *Phys. Rev. Lett.*, 1986, **57**, 2053-2056.

King, K. L., Paterson, G., Rossi, G. E., Iljina, M., Westacott, R. E., Costen, M. L. and McKendrick, K. G., *Phys. Chem. Chem. Phys.*, 2013, **15**, 12852-12863.

King, M. E., Fiehrer, K. M., Nathanson, G. M. and Minton, T. K., *J. Phys. Chem. A*, 1997, **101**, 6556-6561.

King, M. E., Nathanson, G. M., Hanninglee, M. A. and Minton, T. K., *Phys. Rev. Lett.*, 1993, **70**, 1026-1029.

King, M. E., Saecker, M. E. and Nathanson, G. M., *J. Chem. Phys.*, 1994, **101**, 2539-2547.

Kleyn, A. W., Luntz, A. C. and Auerbach, D. J., *Phys. Rev. Lett.*, 1981, **47**, 1169-1172.

Kohler, S. P. K., Allan, M., Kelso, H., Henderson, D. A. and McKendrick, K. G., *J. Chem. Phys.*, 2005, **122**, 24712.

Kolbeck, C., Cremer, T., Lovelock, K. R. J., Paape, N., Schulz, P. S., Wasserscheid, P., Maier, F. and Steinruck, H. P., *J. Phys. Chem. B*, 2009, **113**, 8682-8688.

Kolbeck, C., Lehmann, J., Lovelock, K. R. J., Cremer, T., Paape, N., Wasserscheid, P., Froba, A. P., Maier, F. and Steinruck, H. P., *J. Phys. Chem. B*, 2010, **114**, 17025-17036.

Kubiak, G. D., Hurst, J. E., Rennagel, H. G., McClelland, G. M. and Zare, R. N., *J. Chem. Phys.*, 1983, **79**, 5163-5178.

Lancaster, D. K., Johnson, A. M., Burden, D. K., Wiens, J. P. and Nathanson, G. M., *J. Phys. Chem. Lett.*, 2013, **4**, 3045-3049.

Lancaster, D. K., Johnson, A. M., Kappes, K. and Nathanson, G. M., *J. Phys. Chem. C*, 2015, **119**, 14613-14623.

Larue, J. L., White, J. D., Nahler, N. H., Liu, Z., Sun, Y., Pianetta, P. A., Auerbach, D. J. and Wodtke, A. M., *J. Chem. Phys.*, 2008, **129**.

Lednovich, S. L. and Fenn, J. B., *AIChE J.*, 1977, **23**, 454-459.

Lee, S. Y., Ogawa, A., Kanno, M., Nakamoto, H., Yasuda, T. and Watanabe, M., *J. Am. Chem. Soc.*, 2010, **132**, 9764-9773.

Lewandowski, A. and Swiderska-Mocek, A., *J. Power Sources*, 2009, **194**, 601-609.

Li, X. H., Schatz, G. C. and Nesbitt, D. J., *J. Phys. Chem. B*, 2012, **116**, 3587-3602.

Likens, G. E., Wright, R. F., Galloway, J. N. and Butler, T. J., *Sci. Am.*, 1979, **241**, 43-51.

Lin, R. Y., Taberna, P. L., Fantini, S., Presser, V., Perez, C. R., Malbosc, F., Rupesinghe, N. L., Teo, K. B. K., Gogotsi, Y. and Simon, P., *J. Phys. Chem. Lett.*, 2011, **2**, 2396-2401.

Lockett, V., Sedev, R., Bassell, C. and Ralston, J., *Phys. Chem. Chem. Phys.*, 2008, **10**, 1330-1335.

Lockett, V., Sedev, R., Harmer, S., Ralston, J., Horne, M. and Rodopoulos, T., *Phys. Chem. Chem. Phys.*, 2010, **12**, 13816-13827.

Lovelock, K. R. J., Kolbeck, C., Cremer, T., Paape, N., Schulz, P. S., Wasserscheid, P., Maier, F. and Steinruck, H. P., *J. Phys. Chem. B*, 2009, **113**, 2854-2864.

Lovelock, K. R. J., Villar-Garcia, I. J., Maier, F., Steinruck, H. P. and Licence, P., *Chem. Rev.*, 2010, **110**, 5158-5190.

Luntz, A. C., Kleyn, A. W. and Auerbach, D. J., *J. Chem. Phys.*, 1982, **76**, 737-738.

Luque, J. and Crosley, D. R., *LIFBASE: Database and Spectral Simulation (version 1.5)*, Report SRI International Report MP 99-009, 1999.

Lykke, K. R. and Kay, B. D., *J. Chem. Phys.*, 1990, **92**, 2614-2623.

MacFarlane, D. R., Sun, J., Golding, J., Meakin, P. and Forsyth, M., *Electrochim. Acta*, 2000, **45**, 1271-1278.

Manning, M., Morgan, J. A., Castro, D. J. and Nathanson, G. M., *J. Chem. Phys.*, 2003, **119**, 12593-12604.

Mantell, D. A., Maa, Y. F., Ryali, S. B., Haller, G. L. and Fenn, J. B., *J. Chem. Phys.*, 1983, **78**, 6338-6339.

Martin, L. R., Damschen, D. E. and Judeikis, H. S., *Atmos. Environ.*, 1981, **15**, 191-195.

Martinez, I. S. and Baldelli, S., *J. Phys. Chem. C*, 2010, **114**, 11564-11575.

Martinez-Nunez, E., Rahaman, A. and Hase, W. L., *J. Phys. Chem. C*, 2007, **111**, 354-364.

Massalski, T. B. and Okamoto, H., *Binary Alloy Phase Diagrams*, ASM International, Materials Park, Ohio, 2nd edn., 1990.

Matsiev, D., Li, Z. S., Cooper, R., Rahinov, I., Bartels, C., Auerbach, D. J. and Wodtke, A. M., *Phys. Chem. Chem. Phys.*, 2011, **13**, 8153-8162.

Matsumoto, H., Sakaebe, H. and Tatsumi, K., *J. Power Sources*, 2005, **146**, 45-50.

Mcclelland, G. M., Kubiak, G. D., Rennagel, H. G. and Zare, R. N., *Phys. Rev. Lett.*, 1981, **46**, 831-834.

Mehnert, C. P., Cook, R. A., Dispenziere, N. C. and Afeworki, M., *J. Am. Chem. Soc.*, 2002, **124**, 12932-12933.

Muis, A. and Manson, J. R., *J. Chem. Phys.*, 1999, **111**, 730-736.

Nakajima, K., Ohno, A., Hashimoto, H., Suzuki, M. and Kimura, K., *J. Chem. Phys.*, 2010, **133**.

Narten, A. H., Danford, M. D. and Levy, H. A., *Faraday Discuss.*, 1967, 97.

Nathanson, G. M., *Annu. Rev. Phys. Chem.*, 2004, **55**, 231-255.

Nathanson, G. M., Davidovits, P., Worsnop, D. R. and Kolb, C. E., *J. Phys. Chem.*, 1996, **100**, 13007-13020.

Nogueira, J. J., Homayoon, Z., Vazquez, S. A. and Martinez-Nunez, E., *J. Phys. Chem. C*, 2011, **115**, 23817-23830.

Nogueira, J. J., Vazquez, S. A., Mazyar, O. A., Hase, W. L., Perkins, B. G., Nesbitt, D. J. and Martinez-Nunez, E., *J. Phys. Chem. A*, 2009, **113**, 3850-3865.

Penfold, J. and Thomas, R. K., *J. Phys. Condens. Matter*, 1990, **2**, 1369-1412.

Peng, Y. X., Liu, L., Cao, Z., Li, S., Mazyar, O. A., Hase, W. L. and Yan, T. Y., *J. Phys. Chem. C*, 2008, **112**, 20340-20346.

Pensado, A. S., Malfreyt, P. and Padua, A. A. H., *J. Phys. Chem. B*, 2009, **113**, 14708-14718.

Perkins, B. G. and Nesbitt, D. J., *J. Phys. Chem. B*, 2006, **110**, 17126-17137.

Perkins, B. G. and Nesbitt, D. J., *J. Phys. Chem. A*, 2009, **113**, 4613-4625.

Perkins, B. G. and Nesbitt, D. J., *J. Phys. Chem. B*, 2008, **112**, 507-519.

Perkins, B. G. and Nesbitt, D. J., *J. Phys. Chem. A*, 2008, **112**, 9324-9335.

Perkins, B. G. and Nesbitt, D. J., *Phys. Chem. Chem. Phys.*, 2010, **12**, 14294-14308.

Perkins, B. G. and Nesbitt, D. J., *P. Natl. Acad. Sci. USA*, 2008, **105**, 12684-12689.

Plechkova, N. V. and Seddon, K. R., *Chem. Soc. Rev.*, 2008, **37**, 123-150.

Poole, R. T., Jenkin, J. G., Liesegang, J. and Leckey, R. C. G., *Phys. Rev. B*, 1975, **11**, 5179-5189.

Prybyla, J. A., Heinz, T. F., Misewich, J. A. and Loy, M. M. T., *Surf. Sci.*, 1990, **230**, L173-L179.

Rahinov, I., Cooper, R., Matsiev, D., Bartels, C., Auerbach, D. J. and Wodtke, A. M., *Phys. Chem. Chem. Phys.*, 2011, **13**, 12680-12692.

Ran, Q., Matsiev, D., Auerbach, D. J. and Wodtke, A. M., *Phys. Rev. Lett.*, 2007, **98**.

Rettner, C. T., Fabre, F., Kimman, J. and Auerbach, D. J., *Phys. Rev. Lett.*, 1985, **55**, 1904-1907.

Richmond, G. L., *Annu. Rev. Phys. Chem.*, 2001, **52**, 357-389.

Richmond, G. L., *Chem. Rev.*, 2002, **102**, 2693-2724.

Ridings, C., Lockett, V. and Andersson, G., *Phys. Chem. Chem. Phys.*, 2011, **13**, 17177-17184.

Riisager, A., Fehrmann, R., Haumann, M. and Wasserscheid, P., *Eur. J. Inorg. Chem.*, 2006, 695-706.

Rivera-Rubero, S. and Baldelli, S., *J. Phys. Chem. B*, 2006, **110**, 4756-4765.

Ronk, W. R., Kowalski, D. V., Manning, M. and Nathanson, G. M., *J. Chem. Phys.*, 1996, **105**, 4397-4397.

Roscioli, J. R. and Nesbitt, D. J., *J. Phys. Chem. A*, 2011, **115**, 9764-9773.

Roscioli, J. R. and Nesbitt, D. J., *Faraday Discuss.*, 2011, **150**, 471-479.

Roscioli, J. R. and Nesbitt, D. J., *J. Phys. Chem. Lett.*, 2010, **1**, 674-678.

Saecker, M. E., Govoni, S. T., Kowalski, D. V., King, M. E. and Nathanson, G. M., *Science*, 1991, **252**, 1421-1424.

Saecker, M. E. and Nathanson, G. M., *J. Chem. Phys.*, 1993, **99**, 7056-7075.

Santos, C. S. and Baldelli, S., *Chem. Soc. Rev.*, 2010, **39**, 2136-2145.

Santos, C. S. and Baldelli, S., *J. Phys. Chem. B*, 2009, **113**, 923-933.

Savitzky, A. and Golay, M. J. E., *Anal. Chem.*, 1964, **36**, 1627-&.

Scheingraber, H. and Vidal, C. R., *J. Opt. Soc. Am. B*, 1985, **2**, 343-354.

Scoles, G., *Atomic and Molecular Beam Methods*, Oxford University Press, New York, 1988.

Seddon, K. R., *J. Chem. Technol. Biotechnol.*, 1997, **68**, 351-356.

Serri, J. A., Cardillo, M. J. and Becker, G. E., *J. Chem. Phys.*, 1982, **77**, 2175-2189.

Sheldon, R., *Chem. Commun.*, 2001, 2399-2407.

Shen, Y. R., *Appl. Phys. B*, 1999, **68**, 295-300.

Shenvi, N., Roy, S. and Tully, J. C., *J. Chem. Phys.*, 2009, **130**, 174107.

Shenvi, N., Roy, S. and Tully, J. C., *Science*, 2009, **326**, 829-832.

Sinha, M. and Fenn, J. B., Proc. 5th Int. Symp. Molecular Beams, Nice, 1975.

Smedley, J. E., Corey, G. C. and Alexander, M. H., *J. Chem. Phys.*, 1987, **87**, 3218-3231.

Sweeney, G. M., Watson, A. and McKendrick, K. G., *J. Chem. Phys.*, 1997, **106**, 9172-9181.

Tasic, U. S., Yan, T. Y. and Hase, W. L., *J. Phys. Chem. B*, 2006, **110**, 11863-11877.

Tesa-Serrate, M. A., King, K. L., Paterson, G., Costen, M. L. and McKendrick, K. G., *Phys. Chem. Chem. Phys.*, 2014, **16**, 173-183.

Tesa-Serrate, M. A., Marshall, B. C., Smoll, E. J., Purcell, S. M., Costen, M. L., Slattery, J. M., Minton, T. K. and McKendrick, K. G., *J. Phys. Chem. C*, 2015, **119**, 5491-5505.

Tesa-Serrate, M. A., Smoll, E. J., D'Andrea, L., Purcell, S. M., Costen, M. L., Bruce, D. W., Slattery, J. M., Minton, T. K. and McKendrick, K. G., *J. Phys. Chem. C*, 2016, **120**, 27369-27379.

Tesa-Serrate, M. A., Smoll, E. J., Minton, T. K. and McKendrick, K. G., *Annu. Rev. Phys. Chem.*, 2016, **67**, 515-540.

Tokuda, H., Hayamizu, K., Ishii, K., Susan, M. A. B. H. and Watanabe, M., *J. Phys. Chem. B*, 2005, **109**, 6103-6110.

Triolo, A., Russina, O., Bleif, H. J. and Di Cola, E., *J. Phys. Chem. B*, 2007, **111**, 4641-4644.

Tully, J. C., *Surf. Sci.*, 1994, **299**, 667-677.

Vieceli, J. S. and Tobias, D. J., *Abstr. Pap. Am. Chem. S.*, 2004, **227**, U1003-U1003.

Villar-Garcia, I. J., Fearn, S., De Gregorio, G. F., Ismail, N. L., Gschwend, F. J. V., McIntosh, A. J. S. and Lovelock, K. R. J., *Chem. Sci.*, 2014, **5**, 4404-4418.

Waring, C., Bagot, P. A. J., Slattery, J. M., Costen, M. L. and McKendrick, K. G., *J. Phys. Chem. A*, 2010, **114**, 4896-4904.

Watts, E. K., Siders, J. L. W. and Sitz, G. O., *Surf. Sci.*, 1997, **374**, 191-196.

Welton, T., *Chem. Rev.*, 1999, **99**, 2071-2083.

Wenaas, E. P., *J. Chem. Phys.*, 1971, **54**, 376.

White, J. D., Chen, J., Matsiev, D., Auerbach, D. J. and Wodtke, A. M., *Nature*, 2005, **433**, 503-505.

Wiens, J. P., Nathanson, G. M., Alexander, W. A., Minton, T. K., Lakshmi, S. and Schatz, G. C., *J. Am. Chem. Soc.*, 2014, **136**, 3065-3074.

Wilson, M. A. and Pohorille, A., *J. Phys. Chem. B*, 1997, **101**, 3130-3135.

Winther-Jensen, B., Winther-Jensen, O., Forsyth, M. and MacFarlane, D. R., *Science*, 2008, **321**, 671-674.

Wodtke, A. M., Huang, Y. H. and Auerbach, D. J., *J. Chem. Phys.*, 2003, **118**, 8033-8041.

Wodtke, A. M., Matsiev, D. and Auerbach, D. J., *Prog. Surf. Sci.*, 2008, **83**, 167-214.

Wodtke, A. M., Tully, J. C. and Auerbach, D. J., *Int. Rev. Phys. Chem.*, 2004, **23**, 513-539.

Wu, B. H., Zhang, J. M., Minton, T. K., McKendrick, K. G., Slattery, J. M., Yockel, S. and Schatz, G. C., *J. Phys. Chem. C*, 2010, **114**, 4015-4027.

Yan, T. Y., Hase, W. L. and Barker, J. R., *Chem. Phys. Lett.*, 2000, **329**, 84-91.

Yang, M., Mallick, B. and Mudring, A. V., *Cryst. Growth Des.*, 2013, **13**, 3068-3077.

Yoshimura, D., Yokoyama, T., Nishi, T., Ishii, H., Ozawa, R., Hamaguchi, H. and Seki, K., *J. Electron Spectrosc.*, 2005, **144**, 319-322.

Zacharias, H., Halpern, J. B. and Welge, K. H., *Chem. Phys. Lett.*, 1976, **43**, 41-44.

Zaitsau, D. H., Kabo, G. J., Strechan, A. A., Paulechka, Y. U., Tschersich, A., Verevkin, S. P. and Heintz, A., *J. Phys. Chem. A*, 2006, **110**, 7303-7306.

Zener, C., *Proceedings of the Royal Society of London Series A*, 1932, **137**, 696-702.

Zhang, J. M., Upadhyaya, H. P., Brunsvold, A. L. and Minton, T. K., *J. Phys. Chem. B*, 2006, **110**, 12500-12511.

Ziemkiewicz, M. and Nesbitt, D. J., *J. Chem. Phys.*, 2009, **131**.

Ziemkiewicz, M., Wojcik, M. and Nesbitt, D. J., *J. Chem. Phys.*, 2005, **123**, 224307.

Ziemkiewicz, M. P., *Molecular and Electronic Dynamics in Van der Waals Cluster Spectroscopy, Hydrogen Abstraction Reactions, and Inelastic Collisions at Liquid Surfaces* (Ph.D.). University of Colorado at Boulder, 2012.

Ziemkiewicz, M. P., Roscioli, J. R. and Nesbitt, D. J., *J. Chem. Phys.*, 2011, **134**, 234703.

Ziemkiewicz, M. P., Zutz, A. and Nesbitt, D. J., *J. Phys. Chem. C*, 2012, **116**, 14284-14294.

Zolot, A. M., Dagdigian, P. J. and Nesbitt, D. J., *J. Chem. Phys.*, 2008, **129**, 194705.

Zutz, A. and Nesbitt, D. J., *J. Phys. Chem. C*, 2015, **119**, 8596-8607.

Zutz, A. and Nesbitt, D. J., *AIP Adv.*, 2016, **6**, 105207.

Nitric and Adipic Acid Manufacturing Plants, Report EPA-450/3-91-026, 1991.

Nitrogen Oxides (NOx), Why and How they are Controlled, Report US EPA Technical Bulletin No. EPA-456/F-99-006R, 1999.